

Carbon-Based Smart Materials

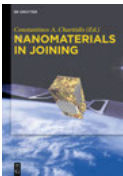
Also of Interest



Nanostructures – Fundamentals

Uwe Hartmann, 2021

ISBN 978-3-11-036218-3, e-ISBN 978-3-11-045955-5



Nanomaterials in Joining

Constantinos A. Charitidis (Ed.), 2015

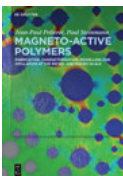
ISBN 978-3-11-033960-4, e-ISBN 978-3-11-033972-7



Nanostructured Materials – Applications, Synthesis and In-Situ Characterization

Huayna Terraschke (Ed.), 2020

ISBN 978-3-11-045829-9, e-ISBN 978-3-11-045909-8



Magneto-Active Polymers – Fabrication, characterisation, modelling and simulation at the micro- and macro-scale

Jean-Paul Pelteret, Paul Steinmann, 2019

ISBN 978-3-11-041951-1, e-ISBN 978-3-11-041857-6



Spintronics – Theory, Modelling, Devices

Tomasz Blachowicz, Andrea Ehrmann, 2019

ISBN 978-3-11-049062-6, e-ISBN 978-3-11-049063-3

Carbon-Based Smart Materials



Edited by
Constantinos A. Charitidis, Elias P. Koumoulos
and Dimitrios A. Dragatogiannis

DE GRUYTER

Editors

Prof. Constantinos A. Charitidis
Department of Materials Science and
Engineering
School of Chemical Engineering
National Technical University of Athens
Heron Polytechniou St. 9
157 73 Athens
Greece
charitidis@chemeng.ntua.gr

Dr. Dimitrios A. Dragatogiannis
Department of Materials Science and
Engineering
School of Chemical Engineering
National Technical University of Athens
Heron Polytechniou St. 9
157 73 Athens
Greece
ddragato@chemeng.ntua.gr

Dr. Elias P. Koumoulos
Department of Materials Science and
Engineering
School of Chemical Engineering
National Technical University of Athens
Heron Polytechniou St. 9
157 73 Athens
Greece
elikoum@chemeng.ntua.gr

ISBN 978-3-11-047774-0

e-ISBN (PDF) 978-3-11-047913-3

e-ISBN (EPUB) 978-3-11-047775-7

DOI <https://doi.org/10.1515/9783110479133>



This work is licensed under a Creative Commons Attribution-NonCommercial-NoDerivatives 4.0 International License. For details go to <http://creativecommons.org/licenses/by-nc-nd/4.0/>.

Library of Congress Control Number: 2019957724

Bibliographic information published by the Deutsche Nationalbibliothek

The Deutsche Nationalbibliothek lists this publication in the Deutsche Nationalbibliografie; detailed bibliographic data are available on the Internet at <http://dnb.dnb.de>.

©2020 Constantinos A. Charitidis, Elias P. Koumoulos and Dimitrios A. Dragatogiannis,
published by Walter de Gruyter GmbH, Berlin/Boston
The book is published with open access at www.degruyter.com.

Cover image: Dmitry/iStock/Getty Images Plus
Typesetting: Integra Software Services Pvt. Ltd.
Printing and binding: CPI books GmbH, Leck

www.degruyter.com

Preface

The research in the field of advanced materials is significantly driven by the development of “smart” materials that are designed to react with environmental conditions and other stimuli. Smart materials that have attracted considerable attention in the last years have now become an intrinsic field in dealing with both societal challenges and significant engineering problems in various sectors such as energy and water consumption, recycling and engineering.

The field of advanced materials benefits from multidisciplinary basic and applied research in physics, chemistry, mathematical modeling and materials engineering. Technical challenges related to developing suitable smart materials and intelligent structures are applicable in a wide range of fields, such as sensors, spintronics, supercapacitors, biomedical applications (drug delivery and hyperthermia therapy), self-healing, flexible memories, construction technologies and other emerging technologies.

Carbon-based materials have gained major attention for replacing other conventional materials as a promising basis for developing novel smart materials due to their abundance and low cost, high-temperature stability and corrosion resistance, high electrical and thermal conductivity and enhanced mechanical properties, particularly in the microscopic and nanoscopic scale.

This book consists of chapters written by expert scientists and engineers from the international carbon-based materials community, who contribute important research work with emphasis to advanced applications. Contributions focus on novel applications of carbon-based smart materials, as well as on functionalization processes and multiscale modeling.

In the first chapter “New class of graphene-based devices for the next generation of nonvolatile memories,” the main scientific works concerning the properties of memories based on graphene layers, graphene oxide, and reduced graphene oxide are reviewed by showing the promising results in terms of writing time and endurance/cyclability compared to existing technologies. Moreover, these materials can potentially allow developing a highly scalable complementary metal-oxide–semiconductor-compatible technology. This chapter suggests that graphene-based memory technology can be exploited for space applications, as it is being insensitive to radiation and easily reprogrammable.

Second chapter is devoted to the research undertaken at the University of Birmingham on the functionalization of carbon-based materials using the active screen plasma (ASP) technology. The chapter entitled “Plasma surface activation and functionalization of carbon-based Materials” exploits the typical physical and chemical phenomena associated with the plasma technology, further optimized by the additional control and degrees of freedom offered by the ASP technology. In this way, the highly reactive species in the plasma were used to reduce graphene oxide films, activate the surface of carbon paper membranes or functionalize the

surface of carbon fibers. All the above seem to be great opportunities to create patterned surfaces using the ASP technology, in combination with other processes, with potential application in multiple fields such as functional materials, sensors and biosensors, electrical, electronic and optoelectronic devices. Without question, the ASP technology remains a valuable enabling technology for the surface functionalization of engineering materials, showing broader prospects of practical applications than ever before.

Modeling of carbon-based smart materials is the subject of the third chapter. A better understanding of the thermophysical behavior of carbon-based polymer nanocomposites at different length- and time-scales could pave the way of discovering novel smart materials and could be facilitated by proper materials modeling. Advanced modeling approaches for the estimation of nanocomposite properties are based on linking and/or coupling various model types that are applicable at different length- and time-scales. This chapter review could be particularly useful for a broader audience of readers, whose research interest is focused on modeling issues in carbon-based materials. Atomistic, mesoscopic and macroscopic simulation tools that allow exploring the main properties of nanocomposites are extensively presented, and future perspectives of advanced modeling of carbon-based smart materials are discussed.

The fourth chapter entitled “Carbon nanotube-based materials for space applications” summarizes the activities performed in three sequential European Space Agency projects, highlighting the introduction of carbon nanotubes (CNTs) into composite materials for space applications. The first activity aimed at proving the feasibility of using CNT skeletons as an alternative to conventionally filled resins, overcoming high viscosity issues, which limits the processability of materials. For the second activity, the aim was to scale up the nanotube structures and integrate them in carbon fiber-reinforced composites. More recently, activities were focused on selecting two applications with highest potential for performance improvements, taking into account all knowledge gained, followed by the development and testing of two demonstrators. This chapter presents the development steps and demonstrator manufacturing and testing for one of these applications, a carbon fiber-reinforced polymer (CFRP) optical mirror. For this mirror demonstrator, a complete assembly consisting of two CFRP skins with outer CNT layers bonded to a carbon-based honeycomb center was manufactured. The principle of producing a highly accurate optical mirror in CFRP-CNT technology is rated as very promising, with important mass savings at required thermoelastic distortion values.

The next chapter deals with molecular dynamics (MD) simulations of graphene-based polymer nanocomposites. The unique, advanced properties of graphene justify why it is widely considered as the material of the future. Within this chapter, graphene’s great potential for new applications is highlighted, and the recent progress in the design of graphene-based polymer nanocomposites from both an experimental and a computational point of view is discussed. The basic concepts of molecular simulations

focusing particularly on the MD technique and simulation results for the structural, conformational and mechanical properties of a test nanocomposite system based on poly(methyl methacrylate) (PMMA) filled with two different types of graphene sheets are also presented: simple (i.e., unfunctionalized) graphene sheets and functionalized (i.e., graphene oxide). This study was driven by recent experimental reports according to which the addition of a small fraction of graphene sheets in a polar polymer matrix such as PMMA can lead to a remarkable enhancement of its elastic constants.

The last chapter “Carbon from waste source for Li-ion battery” suggests that the accomplishment of “12 principles of green chemistry” is a fundamental goal to be pursued by means of designing/optimizing environmentally “conscious” processes, materials and devices to reduce their environmental impact throughout all the phases of their life cycle, thus benefiting the economy, protecting people and achieving the real goal of a truly sustainable world. This goal can be achieved by exploiting carbonized nanocellulosic binders and water-based papermaking coupled with high-performing green composite polymer electrolytes.

The book is useful for everyone who is interested in applications of carbon-based smart materials and is especially oriented to the graduate students and young researchers to facilitate their introduction in this new area. The editors thank all the authors who contributed their work to this book and also acknowledge the superb assistance that the staff of De Gruyter has provided for the publication of this work.

Contents

Preface — V

List of contributing authors — XI

Paolo Bondavalli

1 New class of graphene-based devices for the next generation of nonvolatile memories — 1

Hanshan Dong, Santiago Corujeira Gallo

2 Plasma surface activation and functionalization of carbon-based materials — 17

Rajat Srivastava, Matteo Fasano, Shahin Mohammad Nejad, Hernán Chávez Thielemann, Eliodoro Chiavazzo, and Pietro Asinari

3 Modeling carbon-based smart materials — 33

Marta Martins, Joana F. Guedes, Celeste Pereira, Stefan Forero, Volker Liedtke, Jiří Zelenka, Jan Václavík, Ernst Pfeiffer, Laurent Pambaguian, Advenit Makaya, Nuno Rocha

4 Carbon nanotube-based materials for space applications — 81

Emmanuel N. Skountzos and Vlasis G. Mavrantzas

5 Molecular dynamics simulations of graphene-based polymer nanocomposites — 115

Pravin Jagdale, Gemma Rius, Krishna Rajan, Jijeesh Ravi Nair, Massimo Rovere, Alberto Tagliaferro, Claudio Gerbaldi

6 Carbon from waste source for Li-ion battery — 153

Index — 181

List of contributing authors

Paolo Bondavalli

Thales Research and Technology
1 Av. A. Fresnel
(site de Polytechnique)
Palaiseau Cedex F91767, France
Paolo.Bondavalli@thalesgroup.com

Hanshan Dong

School of Metallurgy and Materials
University of Birmingham
Edgbaston
Birmingham B15 2TT, UK
h.dong.20@bham.ac.uk

Santiago Corujeira Gallo

Deakin University Australia
santiago.corujeiragallos@deakin.edu.au

Pietro Asinari

Politecnico di Torino
Department of Energy
Corso Duca degli Abruzzi, 24
Turin 10129, Italy
pietro.asinari@polito.it

Rajat Srivastava

Politecnico di Torino
Department of Energy
Corso Duca degli Abruzzi, 24
Turin 10129, Italy

Shahin Mohammad Nejad

Politecnico di Torino
Department of Energy
Corso Duca degli Abruzzi, 24
Turin 10129, Italy

Matteo Fassano

Politecnico di Torino
Department of Energy
Corso Duca degli Abruzzi, 24
Turin 10129, Italy

Eliodoro Chiavazzo

Politecnico di Torino
Department of Energy
Corso Duca degli Abruzzi, 24
Turin 10129, Italy

Nuno Rocha

INEGI – Institute of Science and Innovation in
Mechanical and Industrial Engineering
Rua Dr. Roberto Frias 400
Porto 4200-465, Portugal
nuno.rocha@inegi.up.pt

Marta Martins

INEGI – Institute of Science and Innovation in
Mechanical and Industrial Engineering
Rua Dr. Roberto Frias 400
Porto 4200-465, Portugal

Joana F. Guedes

INEGI – Institute of Science and Innovation in
Mechanical and Industrial Engineering
Rua Dr. Roberto Frias 400
Porto 4200-465, Portugal

Celeste Pereira

INEGI – Institute of Science and Innovation in
Mechanical and Industrial Engineering
Rua Dr. Roberto Frias 400
Porto 4200-465, Portugal

Stefan Forero

FutureCarbon
Ritter-von-Eitzenberger-Straße 24
95448 Bayreuth, Germany

Volker Liedtke

AAC – Aerospace & Advanced Composites
Viktor-Kaplan-Straße 2, building F
2700 Wiener Neustadt, Austria

XII — List of contributing authors

Jiří Zelenka

TOSEDA s.r.o.
U Panasonicu 376
530 06 Staré Ččvice (areál TechnoPark
Pardubice), Czech Republic

Jan Václavík

Institute of Plasma Physics of CAS
Za Slovankou 1782/3
Prague 182 00, Czech Republic

Ernst Pfeiffer

HPS GmbH
Hofmannstr. 25-27
81379 München, Germany

Laurent Pambaguian

ESA ESTEC
Keplerlaan 1
2201 AZ Noordwijk, The Netherlands

Advenit Makaya

ESA ESTEC
Keplerlaan 1
2201 AZ Noordwijk, The Netherlands

Emmanuel N. Skountzos

Department of Chemical Engineering
University of Patras
GR 26504 Patras, Greece

Vlasis G. Mavrantzas

Department of Chemical Engineering
University of Patras
GR 26504 Patras, Greece
vlasis@chemeng.upatras.gr

Pravin Jagdale

Department of Applied Science and
technology (DISAT)
Politecnico di Torino
C.so Duca Degli Abruzzi, 24
Torino 10129, Italy

Gemma Rius

Institute of Microelectronics of Barcelona

IMB-CNM-CSIC, Campus UAB
Carrer dels Til.lers s/n
08193 Bellaterra, Spain

Pravin Jagdale

Department of Applied Science and
technology (DISAT)
Politecnico di Torino
C.so Duca Degli Abruzzi, 24
Torino 10129, Italy

Krishna Rajan

Department of Applied Science and
technology (DISAT)
Politecnico di Torino
C.so Duca Degli Abruzzi, 24
Torino 10129, Italy

Jijeesh Ravi Nair

Department of Applied Science and
technology (DISAT)
Politecnico di Torino
C.so Duca Degli Abruzzi, 24
Torino 10129, Italy

Massimo Rovere

Department of Applied Science and
technology (DISAT)
Politecnico di Torino
C.so Duca Degli Abruzzi, 24
Torino 10129, Italy

Alberto Tagliaferro

Department of Applied Science and
technology (DISAT)
Politecnico di Torino
C.so Duca Degli Abruzzi, 24
Torino 10129, Italy

Claudio Gerbaldi

Department of Applied Science and
technology (DISAT)
Politecnico di Torino
C.so Duca Degli Abruzzi, 24
Torino 10129, Italy
alberto.tagliaferro@polito.it

Paolo Bondavalli

1 New class of graphene-based devices for the next generation of nonvolatile memories

1.1 Introduction

Graphene is a one-atom thick layer of carbon atoms arranged in a hexagonal lattice. Graphene potentialities are attracting a lot of researchers to probe opportunities in a number of directions in the “more Moore” or “beyond CMOS” optics in order to identify the new future technologies [1–3]. Another promising utilization of graphene and related nanomaterials is to fabricate nonvolatile memories (NVM) exploiting their “memresistive” behavior storing a value of electrical resistance in a permanent way. This happens when a current passing through the materials changes the level of resistance. Therefore, resistive memory exploits the change in the resistance of a material under the effect of an electric field as an information write/erase principle for nonvolatile data storage. The reading of resistance states is nondestructive, and the memory devices can be operated without transistors in every cell [4, 5], as for flash-type memories [6–10] (see Section 1.2.2), thus achieving a classic cross-bar structure. This kind of memories is called resistive random-access memory (RRAM or ReRAM) and is only one of the possible types of nonvolatile ways to store information in a permanent way. One of the most important advantages of these new classes of 2D materials is that these materials can be implemented in flexible electronics [11–15], in the form of one-thick atom layers as for graphene or in the form of layers of flakes of graphene oxide (GO) or reduced GO (R-GO), thereby reducing the final cost of the final device exploiting roll-to-roll fabrication [16]. Another great advantage of ReRAMs is their potential to implement them by exploiting only two terminals to work (two contacts and not three as a common transistor, which has drain, source and gate, e.g., flash-type memories), which could dramatically reduce the circuitry and allow to implement easily in 3D architectures by using the roll-to-roll fabrication technique. Potentially, this is applied in various fields such as health monitoring [17–21], intelligent packaging [22, 23], cards, labels, badges, value paper and medical disposables. Another potential field is the radiofrequency identification (RFID). This is a technology to electronically record the presence of an object using radio signals. Indeed, an innovative alternative pathway to reduce RFID costs and integrate a memory chip to store data is to eliminate the silicon substrate completely, and produce RFID and memory on the same flexible plastic substrate as the antenna [24–26].

Paolo Bondavalli, Thales Research and Technology, Palaiseau Cedex, France

Thanks to graphitic layers, the antenna and chip can be built on the same low-cost substrate, and attachment costs can be removed.

1.2 Graphene-based NVM

As outlined in the International Technology Roadmap for Semiconductors 2011 section concerning Emerging Research Devices, “ultrathin graphite layers are interesting materials for macromolecular memories thanks to the potential fabrication costs that are considered as the primary driver for this type of memory, while extreme scaling is de-emphasized.” The main drawback is related to the fact that memory operation mechanisms and the physics are still unclear and that a deeper research in this field is necessary to improve the comprehension of the phenomenon and the efficiency of the devices. These are not the same physical mechanisms exploited in memories based on graphene-related materials, which will be discussed in the next paragraphs.

1.2.1 Graphene and graphitic layers

The first paper highlighting the utilization of graphene for resistive NVM exploiting two terminal structures was issued in 2008 by Stadley et al. at Caltech [27]. They reported the development of an NVM element based on graphene break junctions. These junctions were obtained by achieving two-terminal devices, transferring graphene sheets on SiO₂/Si substrate and depositing metal electrodes on them using e-beam lithography process. After applying a specific voltage under ultravacuum condition (10⁻⁷ torr), they were able to create a break in the graphene layer (see Figure 1.1). In these papers, all the measurements were performed under ultravacuum to avoid environmental gas interferences, which strongly reduces the potential utilization of the device.

After cycling the memories, they observed that the resistance values clearly changed as a function of the voltage (see Figure 1.1b): they moved from a high resistance state (off state) to a lower one as a function of the voltage (on state). This effect was nonvolatile and the devices were cycled thousands of writing cycles (10⁵), showing long retention times (more than 24 h, only limited by measurements).

The reproducibility of the switching behavior was very promising. One of the more coherent explanations was related to the fact that the conductance occurred along a small graphene ribbon that bridges the contacts. To better understand the underlying physical mechanism, researchers studied the time-resolved behavior of the switch from the OFF to ON states, shown in Figure 1.2a. The conductance I/V showed well-defined steps, with magnitude $\sim G_Q$. Here G_Q is $2e^2/h$, the conductance quantum, where e is the

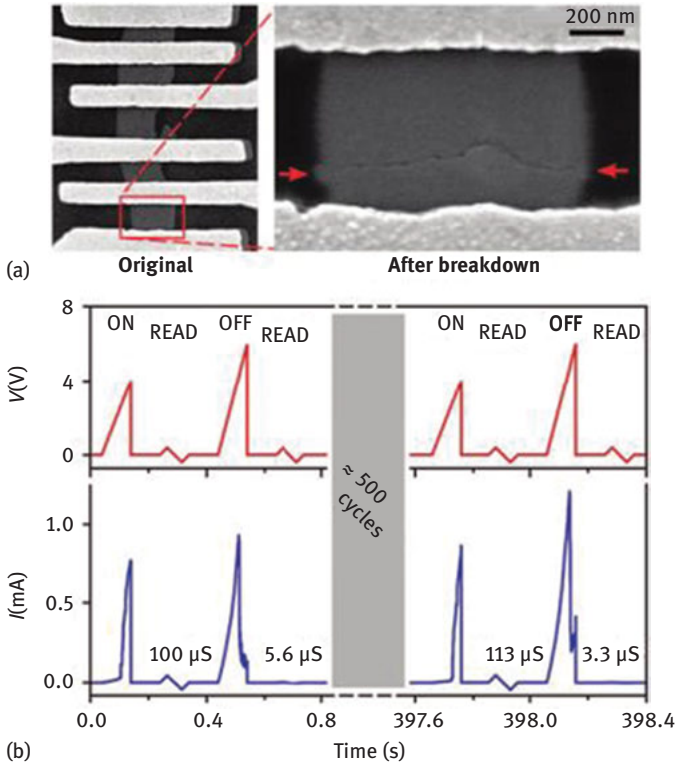


Figure 1.1: (a) SEM image of the device before (left panel) and after breakdown (right panel). The arrows indicate the edges of the break in the graphene layer. (b) Repeatable programming over hundreds of cycles. Upper left panel: Voltage applied to the junction versus time. A ramp with a peak value of ~ 4 V corresponds to an ON pulse, while a ramp with a peak value of ~ 6 V corresponds to an OFF pulse. A small sawtooth-shaped read-out pulse is applied after each write to determine the junction conductance. Lower left panel: Current flow through the junction, with the low-bias conductance labeled above each read-out pulse. Right panels: Similar data taken after approximately 500 intervening cycles, demonstrating the reproducibility of the switching behavior [27].

electron charge and h is Planck's constant. Since G_Q is the conductance of a spin-degenerate one-dimensional conductor, for example, a linear chain of gold atoms [28], observation of steps in the conductance suggests that the conductance states of a device are likely multiples of highly transmitting quantum channels. Authors proposed a model for device operation based on the formation and breaking of carbon atomic chains that bridge the junctions (see Figure 1.2a, right figure). This mode and the results seem to put in evidence the potential for multiresistive states.

The same physical explanation can be evoked for the results obtained in 2009 by Sinitski et al. [29] at Rice when they tested analogue carbon-based structures (see Figure 1.2b). The sensitive layer consists of 10 nm thick graphitic disks

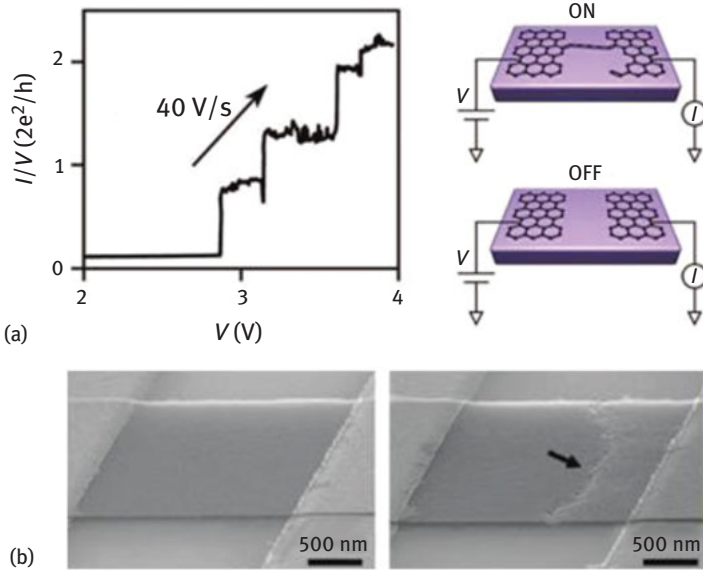


Figure 1.2: (a) Left side: Change in I/V as a function of V pointing out the quantic behavior linked to the formation of atomic chains. Right side: Proposed physical mechanism at the base of the nonvolatile resistive behavior (formation of atomic carbon chains). (b) Tilted-view SEM images of two different devices before and after applying the voltage difference that is necessary to break the layers defined as V_{break} . The arrow shows the fracture across the stripe due to V_{break} [29].

grown by chemical vapor deposition (CVD) process. Researchers evaluated the voltage that is necessary to break the layer. Calculating the Joule heating, researcher obtained that the breakdown voltage, the applied voltage difference necessary to break the layer, was

$$V_{\text{break}} \propto [(C\rho\gamma T_{\text{break}})/\tau]^{1/2} l = A \quad (1.1)$$

where C , ρ , γ are, respectively, the specific heat, the density of CVD-grown graphitic sheets and resistivity, T_{break} is the breakdown temperature of the graphitic layer, A is independent of the devices and l the length of the device. Therefore, the voltage necessary to break the layer is directly proportional to the length. This is very positive because reducing the dimensions will allow to reduce the energy consumption during the writing step.

In 2009, the same team from the University of Rice [30] exploited another approach and grew graphitic layers on a freestanding silicon oxide nanowire (see Figure 1.3a). Indeed they used the nanowire to preserve the mechanical integrity of the device after applying a specific voltage breaking the surficial graphitic layers. The team from Rice fabricated two terminal devices consisting of discontinuous

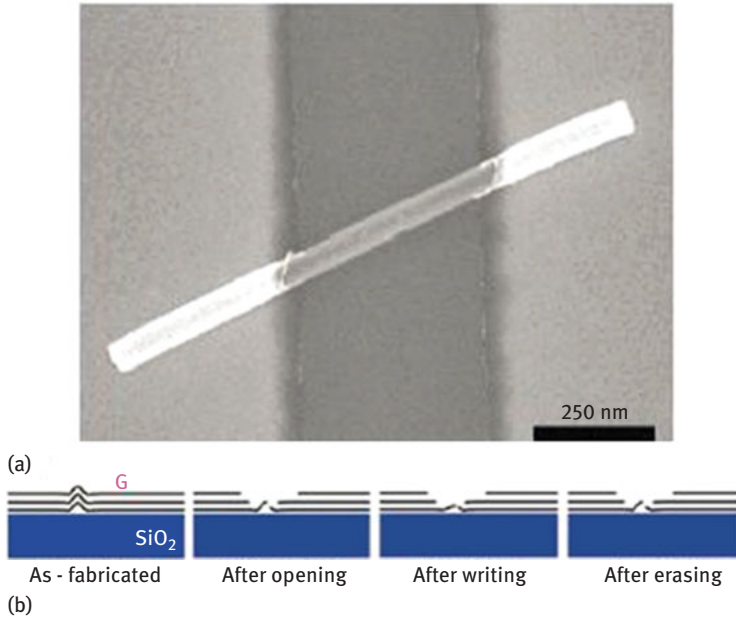


Figure 1.3: (a) Silicon oxide nanowire with graphitic layers grown on its surface and (b) physical principle at the base of the fabrication of nonvolatile graphitic memories exploited by Rice University [30].

5–10 nm thin films of graphitic sheets grown by CVD on nanowires having stable, rewritable, nonvolatile and nondestructive read memories with on/off ratios of up to 10^7 (see Figure 1.4a) and switching times of up to $1 \mu\text{s}$ (tested limit).

All the samples were not tested, as in the previous examples, at ambient conditions but in ultra-vacuum condition (5×10^{-5} torr) and showed an extremely good stability of the performances after several days and also after x-ray exposure (Figure 1.4b).

An interesting work by Wu et al. [31] in 2012 dealt with the electrical properties of graphene sheet suspended on a patterned indium tin oxide (ITO) electrode pair. They measured very interesting on/off ratio of 6 orders and retention time of at less 10^4 s in ambient conditions. In this case, data storage was achieved by applying voltage bias and rewritten after a simple heat treatment. Authors stated that the switch happens only in ambient atmosphere when oxygen changed the injection barrier at the contact. The degassing using a thermal process allowed coming back to the high conduction state.

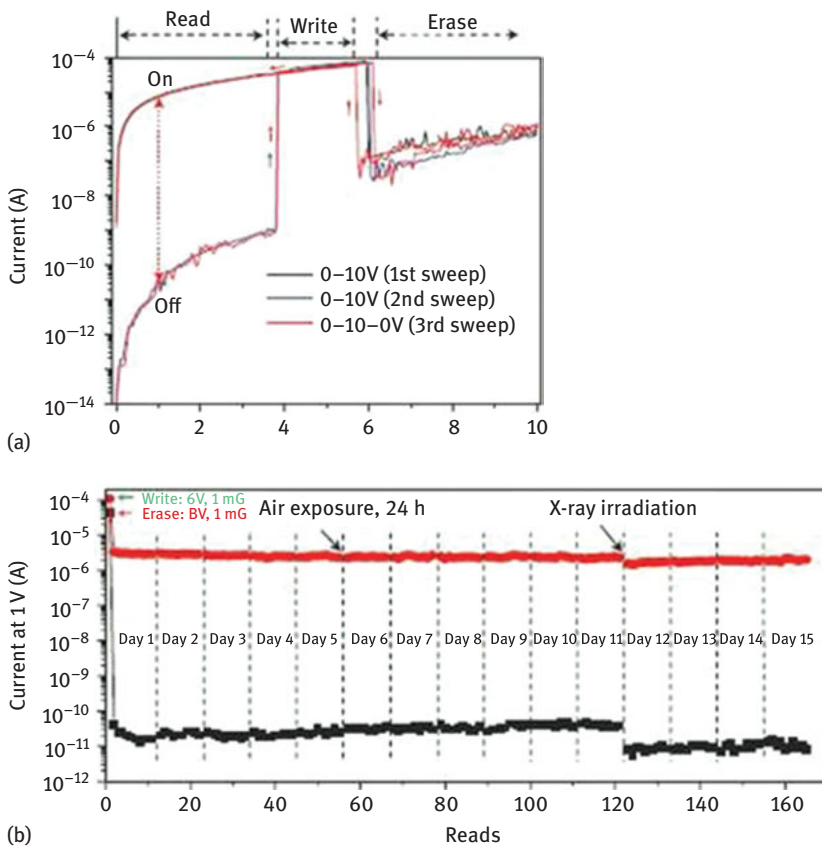


Figure 1.4: (a) The logarithmic I - V behavior of a G-SiO₂ nanoribbon; the “write” or “erase” regions can be achieved through a voltage pulse in the noted regions. After writing or erasing, the high- or low-conductivity state of the system is recorded in the “read.” (b) Data retention by two other G-SiO₂ nanocable devices [30].

1.2.2 Nonvolatile resistive memories based on GO and R-GO oxide layers

Other teams focused their study on GO. GO is a wide band gap material (6 eV) with potential for modulation, thanks to oxidation/reduction process providing tunability of the electronics, mechanical and optical properties. GO [32] is commonly obtained by the oxidation of graphite using the modified Hummer’s method, where the long oxidation time is combined with a highly effective method for the purification of reaction products [33, 34]. A great advantage of this material is its cost, which is at least one-tenth the price of graphene flakes and it is stable in water suspensions. In GO, the memory configuration exploited is similar to cross-bar memories

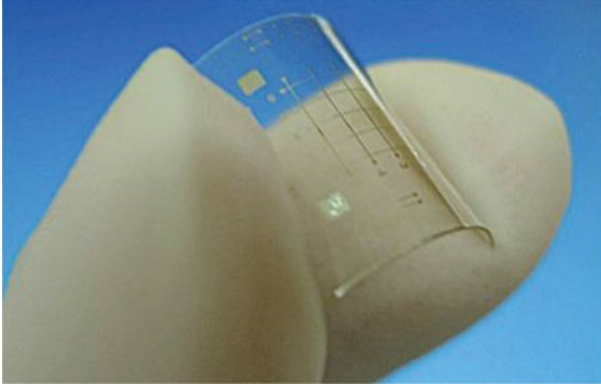


Figure 1.5: Cross-bar memory devices based on GO [39, 40].

[35, 36] (vertical junctions composed by piling up the different layers, sandwiching the active one as metal insulator metal-type structures). We can mention the pioneering work of He et al. in 2009 [37], where reliable and reproducible resistive switching behaviors were observed in GO thin films prepared by vacuum filtration method [38]. They fabricated Cu/GO/Pt structures showing an on/off ratio of about 20, a retention time of more than 10^4 s and switching threshold voltages of less than 1 V. The suggested physical principle at the origin of the switching effect was the desorption/absorption of oxygen-related groups on the GO sheets as well as the diffusion of the top electrodes. One of the major works on GO-based memories was issued in 2010 by Jeong et al. [39, 40]. This team demonstrated the nonvolatile effect on the resistance of a 70 nm layer thick GO in a layered structure composed of Al/GO/Al (Figure 1.5) in a cross-bar configuration.

Jeong et al. were one of the first teams that pointed out the performances of these kinds of layers on flexible substrates. The researchers from KAIST demonstrated that using GO layers they were able to achieve flexible nonvolatile resistive memories with impressive performances under traction and compression [they kept three orders between on (LRS) and off (HRS) levels]. Concerning the physics explanation of the phenomenon, Hong et al. [41, 42] performed a deep analysis of the switching mechanism for this kind of devices and demonstrated that these structures had performances dependent on the origin of the top contacts. For example, in case of Au-based top electrodes, there was no oxygen migration in opposition to Al electrodes. The effect of bottom contacts was also quite important. Indeed if the roughness was too high, the GO layer had such cracks and rough surface that the top electrode material could easily penetrate and then build filaments that hindered the switching operations. This drastically reduced the lifetime of the device (only 100 cycles) because of the formation of a permanent conductive path between the two electrodes. These results were highlighted by X-ray photoelectron spectroscopy measurements that pointed

out the permanent presence of Al near the bottom electrode as the main reason for failure. Evaluating the effect of the migration of oxygen versus the formation of Al-based filaments, Hong and coworkers stated that the formation of conducting filaments was a local phenomenon and that the oxygen migration was the dominant mechanism. Indeed, they discovered that the leakage current between the bottom and lower electrodes was dependent on the cell dimension. In fact when the cells were larger the effect of the oxygen migration or reduction on the conduction was enhanced proportionally to the surface. In order to avoid the failure mechanism linked to the formation of permanent conductive filaments through the material cracks, one suggestion is to exploit deposition techniques that allow a more uniform distribution of the deposited material. One technique is the deposition by spray coating or heating the substrate to avoid the so-called coffee-ring effect [43, 44], which is responsible for the nonuniformity of the deposition [45]. This deposition could potentially prevent the formation of cracks linked to the roughness in the GO layers.

Another interesting study was performed by Vasu et al. at the University of Bangalore (India) in 2011 [46]. They reported very simple unipolar resistive switching device using ultrathin (~20 nm) films of R-GO with on/off ratios reaching five orders of magnitude. The thin films were formed at room temperature simply by drop-casting R-GO from suspension on ITO glass electrode, followed by aluminum or gold deposition (no difference was pointed out after the measurements). A very interesting result was also the switching time that could attain 10 μ s with an on/off ratio of 100. In this case, the formation of nanofilaments of carbon atoms was evoked as the main physical working principle.

1.3 Other approaches to achieve nonvolatile memories using graphitic layers

In the previous sections, we have discussed about the resistive NVM. Other teams have decided to use different approaches to exploit the properties of graphene-based layers to fabricate NVM and have exploited the hysteretic electrical behavior of graphene, or multilayered graphene (MLG), when used as channel in a field effect transistor (FET)-type configuration. This is substantially based on the chemical modification of graphene under an electric field that will enhance environmental interactions. However, the more promising results, in terms of performances but also in terms of potential industrial exploitation, have been obtained in case of the fabrication of flash-type memory [47–48] using graphene or MLG as the floating gate (FG). Basically, a flash memory is an electronic nonvolatile computer storage medium that can be electrically erased and reprogrammed. In flash memory, each cell resembles a standard MOSFET [85], where the transistor has two gates instead of one. Indeed there is the traditional top gate, also called control gate and an FG

embedded in an oxide layer; hence, it is electrically insulated. In FG, which is located between the top gate and the MOSFET channel, any electrons placed on it, activating the top gate, are trapped there and will not discharge for many years. If FG holds a charge, it screens (partially cancels) the electric field from the top gate; therefore, it modifies the threshold voltage (V_T) of the MOSFET. This operation is nonvolatile and is reversible if another adequate voltage is applied on the top gate. The present technology used for flash-type memories employs doped polysilicon as material for the FG. One of the main advantages of graphene/MLG is the reduction of voltage to achieve a correct memory window, which is the shift of the threshold voltage of the transistor when the memory is switched from 0 to 1 state. In the present flash memories, a voltage difference of ± 20 V [49] is necessary to program/erase to achieve a memory window of 1.5 V, which is the industrial standard. Some works have demonstrated, as shown in the next paragraphs that thanks to the higher density of states (DOS) of graphene compared to degenerately doped polysilicon this difference can be reduced up to 6 Volts. Another advantage is the higher work function of graphene [50–52] that is directly linked to the larger barrier height between the FG and the oxide [53–56], which embeds the FG. This potentially allows achieving longer retention time, potentially more than ten years. Finally, the possibility to achieve device using 2D devices with a lower dimensionality that will potentially allow an easier 3D implementation and so a higher memory density.

1.3.1 Graphitic-based nonvolatile memory using a transistor configuration

One of the first papers highlighting the interest of using graphene-based FET for NVM was issued by Wang et al. at the Nanyang Technological University in Singapore in 2010 [57]. Indeed they observed exactly the same phenomenon observed in case of FET with one carbon nanotube as a channel: unhysteretic phenomenon where they observed the formation of a loop of the current value between drain and source, I_{ds} , as a function of the gate voltage, V_{gs} , during the voltage sweep cycle from negative to positive values of V_{gs} and back. This phenomenon is caused by the presence of moisture interacting with the transistor dielectrics. This effect, it has been demonstrated, can be removed in vacuum [58, 59]. Moreover the switching time in case of activation of the hysteretic phenomenon in FET using graphene is of the order of some seconds, which is too high for memory applications.

In 2008, a pioneering work of Echtermeyer et al. of the Advanced Research Center in Aachen (Germany) and of A. K. Geim at the University of Manchester (UK) was performed adopting another point of view compared to the previous studies [60, 61]. Considering the difficulty to achieve nanoribbons with dimensions smaller than 10 nm to open a gap, they exploited another phenomenon. Indeed they

fabricated two-gate transistor structures as shown in Figure 1.6, where the graphene has a width of $10\ \mu\text{m}$ and was covered by an SiO_2 layer.

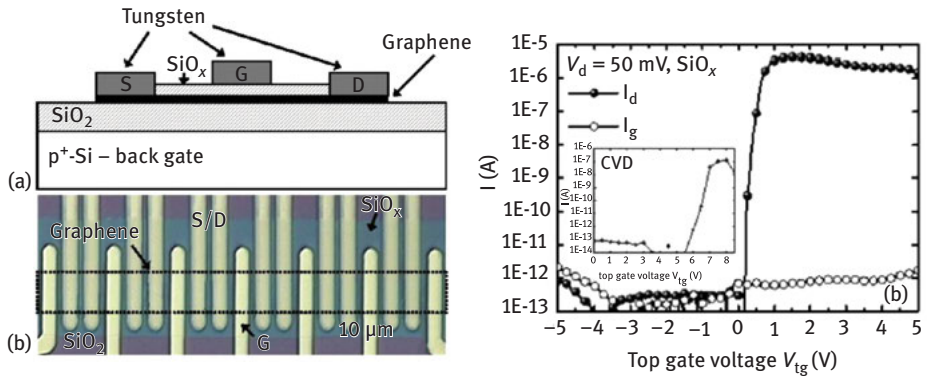


Figure 1.6: (a) Schematic of a double-gated graphene field effect device (FED) and (b) current between drain and source as a function of the top gate voltage value [60, 61].

They observed that applying a voltage spanning from -5 to $+5$ V, for positive voltage there was a strong enhancement in the current of $5/6$ order, hence, a reduction in the resistance that was nonvolatile. Echtermeyer and coworkers suggested that considering that the measurements had been performed in ambient conditions, the water molecules were split in H^+ and OH^- (see Figure 1.6) by the electric field and tended to attach to the graphene, creating graphene or GO (that are insulating materials), passing through the highly porous silicon dioxide layer surface, and so drastically changing the conductivity of the channel in a nonvolatile way. This phenomenon allowed obtaining a strong on/off ratio, quite unusual for graphene (and not graphene nanoribbons) based FET. However, even if the results seem to be very promising, more studies have to be done on the switching time, which intuitively appears to be quite long considering the effects involved. We can add that the graphene layer has been obtained by mechanical cleavage, which is a technique that allows fabricating high-quality samples but that it is not industrially suitable. It is necessary to test this approach, for example, using CVD graphene in order to achieve a potential parallel fabrication of this kind of devices. It has also to be verified if it is fundamental to obtain a single graphene layer or if more stacked layers of graphene can reach the same performances.

1.3.2 Nonvolatile flash-type memories based on graphene/multilayered graphene

Another potential utilization of graphene is FG in flash-type memories. An extremely innovative approach has been proposed by Bertolazzi et al. of the Ecole Polytechnique de Lausanne (EPFL) in Switzerland. They were able to fabricate a flash memory using exactly the same architecture of the existing ones, exploiting only 2D materials [62].

Bertolazzi and coworkers were able to build a flash-type memory using MoS_2 as the channel and few graphene layers as the FG (see Figure 1.7), embedded in HfO_2 oxide, where the charge is trapped. It is clear that this kind of structure is extremely original but some performances especially considering the switching time (the lowest value is 100 ms) are not adequate. Some doubts can be raised on the fabrication technique, which includes three quite complex transfer steps and that are not suitable at the moment for an industrial exploitation. Hong et al. at IBM in Watson

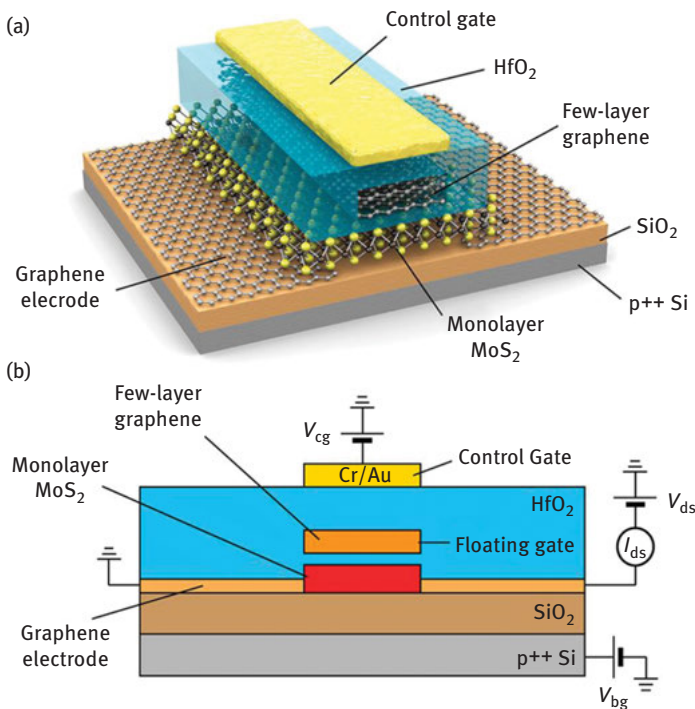


Figure 1.7: MoS₂/graphene heterostructure memory layout. (a) Three-dimensional schematic view of the memory device based on single-layer MoS₂. (b) Schematic view of the flash-type memory cell with a single-layer MoS₂ acting as a semiconducting channel and graphene contacts and multilayered graphene (MLG) as the FG [62].

(USA) fabricated a flash memory [63] using some graphitic layers, grown by CVD on Si as FG. In this case, the technological approach appears potentially scalable, CMOS compatible and so industrially suitable (see Figure 1.8) compared to the previous one. IBM researchers observed a potential retention time of 10 years, with a loss of only 8% of the charges in the FLG but also simulating the potential crosstalk between neighbor cells, who stated that this kind of memories showed negligible interference down to 10 nm (in case of common polysilicon FG, the interference raises dramatically under 25 nm). Briefly, considering the power reduction (as told previously, thanks to the higher DOS compared to common FG fabricated using polysilicon) and the increase in the storage density, Hong and coworkers estimated a potential reduction of 75% in the operating energy of this kind of memory. However, in this work there are no data on the switching time and therefore we cannot compare their performances with existing memories.

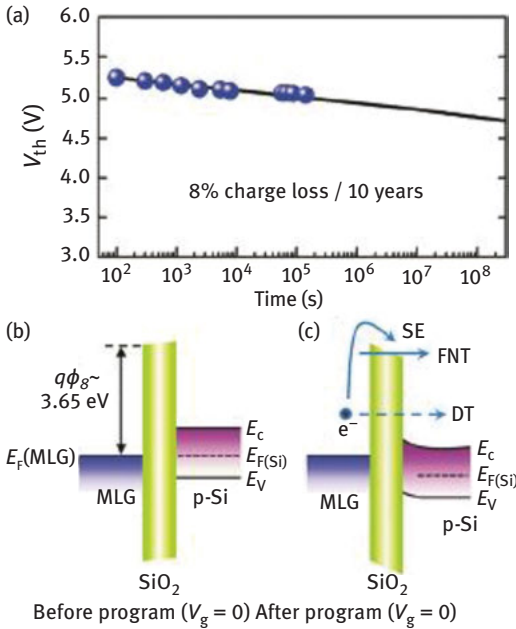


Figure 1.8: Retention characteristics of GFM. (a) Retention measurement of MLG-FM showing only 8% of charge loss in 10 years at room temperature. (b) Energy band diagram of MLG/SiO₂/Si junctions before programming. (c) Energy band diagram after programming, which shows three possible mechanisms for charge loss during retention state: SE, FNT and DT. All three mechanisms depend exponentially on the barrier height (ϕ_B) between the work function of graphene and the SiO₂ tunnel oxide [63].

1.4 Conclusions and potential applications

Graphene-based memories is a completely new technology that needs some time to demonstrate its utility especially in the difficult field of NVM for space application. These memories could constitute a real breakthrough compared to existing technologies also considering the dramatic potential reduction of energy consumption. These memories can be developed to bear harsh environments with a focus on radiation-resistant components. The stability (also in temperature), resilience, nonvolatility and on/off ratio that, in certain cases, can attain 10^7 or the switching time of $1\ \mu\text{s}$ (competitive with flash-type memories), potential switching voltages of 3–4 V, combined with predictable fabrication-controlled I–V behavior, simple two-terminal geometry (no need for a gate and so dramatically reducing circuitry) and access to mass fabrication for the two approaches make them extremely attractive structures for NVM.

Indeed, thanks to thin-film technologies, electronic functionality can be foreseen in very large quantity and at very low cost on substrates such as plastic and paper. Additional functionality is also an attractive feature of carbon-based memories. For example, by using these kinds of materials, we open up the route for memories on flexible substrates, a key building block to enable the success of flexible electronics. Carbon-based resistive memories should also offer the capability for multilevel storage and “memristive-like” behavior, as seen in other resistive memory materials. Multilevel storage allows storing more than one bit per cell, so increasing data storage densities, while memristive-like behavior can be exploited to provide a remarkable range of signal processing/computing-type operations, including implementing logic, providing synaptic and neuron-like “mimics,” and performing, in a very efficient way, analogue signal processing functions (such as multiply accumulate operations).

In case of graphitic-based memories based on other approaches, the transistor-type configuration exploiting the hysteretic effect, in our opinion, has a limited potential compared to new flash-type memories using graphene or MLG as the FG, because their architecture can be unlikely miniaturized and their performances especially considering the switching time are difficult to evaluate. In case of flash-type memories, these last exploit intrinsic characteristics of the materials such as the higher DOS (which allow reducing the voltage for the memory window) or the higher work function (which allows reaching more than 10 years of charge storage) that really allows improving the performances of this kind of memories. Moreover, it has been demonstrated to achieve high-density architecture with limited crosstalk. It is necessary to make an effort on the miniaturization of these devices but the recent works, for example, [51], make us think that this technology can be quite rapidly in competition with existing flash memories, also because it is CMOS compatible and easy to implement in existing production lines.

References

- [1] Ohishi, M. et al. Spin injection into a graphene thin film at room temperature. *Jpn. J. Appl. Phys* 2007, 46, L605–L607
- [2] Cho, S., Chen, Y. F., Fuhrer, M. S. Gate-tunable graphene spin valve. *Appl. Phys. Lett* 2007, 91, 123–105.
- [3] Lee, M. J., Suh, D. S., Seo, S., Jung, R., Ahn, S. E., Lee, C. B., Kang, B. S., Ahn, S. E., Lee, C. B., Seo, D. H., Cha, Y. K., Yoo, I. K., Kim, J. S., Park, B. H. Two series oxide resistors applicable to high speed and high density nonvolatile memory. *Adv. Mater* 2007, 19, (22) 3919–3923, 0935–9648.
- [4] Waser, R., Aono, M. Nanoionics-based resistive switching memories. *Nat. Mater.* 2007, 6 (11) 833, 840, 1476–1122.
- [5] Bez, R., Camerlenghi, E., Modelli, A., Visconti, A., Introduction to Flash memory. *Proceeding of the IEEE.* 2003, 91 (4), 489.
- [6] Aritome, S., Advanced flash memory technology and trends for file storage application. *Tech. Dig. IEDM 2000*, 763.
- [7] Muller, G., Happ, T., Kund, M., Yong Lee, G., Nagel, N., Sezi, R., Status and outlook of emerging nonvolatile memory technologies, In *proceeding of: Electron Devices Meeting, 2004. IEDM Technical Digest. IEEE International.*
- [8] Lai, S., Flash memories: Where we were and where we are going. *IEDM Tech. Dig.* 1998, 971–973.
- [9] Pavan, P., Bez, R., Olivo, P., and Zanoni, E., Flash memory cells – An overview. *Proc. IEEE* 1997, 85, 1248–1271, Aug.
- [10] Pavan, P., Bez, R., The industry standard Flash memory cell, in *Flash Memories*, P. Cappelletti et al., Ed. Norwell, MA: Kluwer, 1999.
- [11] Chao Yan, Jeong Ho Cho, Jong-Hyun Ahn, Graphene-based flexible and stretchable thin film transistors. *Nanoscale* 2012, 4, 48–70.
- [12] Bae, S., Kim, H., Lee, Y., Xu, X., Park, J.-S., Zheng, Y., Balakrishnan, J., Lei, T., Ri Kim, H., Song, Y. I., Kim, Y.-J., Kim, K. S., Ozyilmaz, B., Ahn, J.-H., Hong, B. H., Iijima, S., Roll-to-roll production of 30-inch graphene films for transparent electrodes. *Nat. Nanotechnol* 2010, 5, 574–578.
- [13] Wang, Y., Zheng, Y., Xu, X., Dubuisson, E., Bao, Q., Lu, J., Loh, K. P., Electrochemical delamination of CVD-grown graphene film: toward the recyclable use of copper catalyst. *ACS Nano* 2011, 5, 9927–9933.
- [14] Lock, E. H., Baraket, M., Laskoski, M., Mulvaney, S. P., Lee, W. K., Sheehan, P. E., Hines, D. R., Robinson, J. T., Tosado, J., Fuhrer, M. S., Hernandez, S. C., Walton, S. G., High-quality uniform dry transfer of graphene to polymers. *Nano Lett*, 2011, 12, 102–107
- [15] Xin, Wei, Liu, Zhi-Bo, Sheng, Qi-Wen, Feng, Ming, Huang, Li-Gang, Wang, Peng, Jiang, Wen-Shuai, Xing, Fei, Liu, Yan-Ge, Tian, Jian-Guo, Flexible graphene saturable absorber on two-layer structure for tunable mode-locked soliton fiber laser. *Optics Express*, 2014, 22 (9) DOI:10.1364/OE.22.010239
- [16] Secor, E. B., Prabhurashi, P. L., Puntambekar, K, Geier, M. L., Hersam, M. C., Inkjet printing of high conductivity, flexible graphene patterns. *J Phys Chem Lett*, 2013, 4 (8), 1347–1351.
- [17] Schwartz, G., Tee, B., Mei, J. et al. Flexible polymer transistors with high pressure sensitivity for application in electronic skin and health monitoring. *Nat Commun* 4, 1859 (2013). <https://doi.org/10.1038/ncomms2832>
- [18] Sekitani, T., Zschieschang, U., Klauk, H., Someya, T. Flexible organic transistors and circuits with extreme bending stability. *Nature Mater* 2010, 9, 1015–1022.
- [19] Ramuz, M., Tee, B. C.-K., Tok, J. B.-H., Bao, Z. Transparent, optical, pressure-sensitive artificial skin for large-area stretchable electronics. *Adv Mater*, 2012, 24, 3223–3227.
- [20] Wagner, S. et al. Electronic skin: Architecture and components. *Phys E*, 2004, 25, 326–334.

- [21] Sokolov, A. N., Tee, B. C. K., Bettinger, C. J., Tok, J. B. H., Bao, Z. Chemical and engineering approaches to enable organic field-effect transistors for electronic skin applications. *Acc. Chem. Res.* 2012, 45, 361–371.
- [22] Yam, L., Takhistov, Paul T., Miltz, Joseph, Intelligent packaging: Concepts and application kit. *J Food Sci.* 2005, 70, 1, pages R1–R10, January.
- [23] Kololuoma, Terho K., Tuomikoski, Markus, Makela, Tapio, Heilmann, Jali, Haring, Tomi, Kallioinen, Jani, Hagberg, Juha, Kettunen, Ilkka Kopola, Harri K., Towards roll-to-roll fabrication of electronics, optics, and optoelectronics for smart and intelligent packaging. *Proc. SPIE* 2004, 77, 53–63, Emerging Optoelectronic Applications, (June 25).
- [24] Kim, S., Cook, B., Le, T., Cooper, J., Lee, H., Lakafosis, V., Vyas, R., Moro, R., Bozzi, M., Georgiadis, A., Collado, A., Tentzeris, M M., Inkjet-printed antennas, sensors and circuits on paper substrate, *IET microwaves, antennas & propagation*, 2013, 7 (10), 16 July, 858–868.
- [25] Le, T., Ziyin Lin., Wong, C.P., Tentzeris, M.M., Novel enhancement techniques for ultra-high-performance conformal wireless sensors and “smart skins” utilizing inkjet-printed graphene. *Electronic Components and Technology Conference (ECTC)*, 2013 IEEE 63rd, 2013, 1640, 1643, 28–31 May.
- [26] Pham, H., Xiaochuan Xu, D.T., Chen, M. Y., Hosseini, A., Lu, Xuejun, Chen, R.T., Inkjet-printed two-dimensional phased-array antenna on a flexible substrate. *Antennas and Wireless Propagation Letters, IEEE*, 2013, 12, 170–173.
- [27] Standley, B., Bao, W., Zhang, H. Bruck, J., Ning, Lau C., Bockrath, M., Graphene-based atomic-scale switches. *Nanolett* 2008, 8 (10), 3345–3349.
- [28] Agrait, N., Levy-Yeyati, A., van Ruitenbeek, J. M. Quantum properties of atomic-sized conductor. *Phys Reps* 2003 377, 81–380.
- [29] Sinitskii, A., Tour, J. M., Lithographic graphitic memories. *ACS Nano* 2009, 3 (9), 27–60.
- [30] Li, Y., Sinitskii, A., Tour, J. M., Electronic two-terminal bistable graphitic memories. *Nat Mat* 2008, 7 966.
- [31] Wu, C., Li, F., Zhang, Y., Guo, T. Recoverable electrical transition in a single graphene sheet for application in nonvolatile memories. *Appl Phys Lett* 2012, 100, 042–105.
- [32] Son, D. I., Kim, T. W., Shim, J. H., Jung, J. H., Lee, D. U., Lee, J. M., Park, W. I., Choi, W. K., Flexible organic bistable devices based on graphene embedded in an insulating poly(methyl methacrylate) polymer layer. *Nano Lett* 2010, 10, 2441–2447.
- [33] Dreyer, Daniel R., Park, S., Bielawski, C. W., Ruoff, R. S., The chemistry of graphene oxide. *Chem Soc Rev* 2010, 39, 228–240.
- [34] Hummers, W. S., Offeman, R. E. Preparation of graphitic oxide. *J. Am. Chem. Soc* 1958, 80, 1339.
- [35] Snider, Greg, Kuekes, Philip, Williams, R Stanley, CMOS-like logic in defective, nanoscale crossbars. *Nano Tech* 2004, 15, 881–891.
- [36] Linn, Eike, Rosezin, Roland, Kügeler, Carsten, Waser. Rainer, Complementary resistive switches for passive nanocrossbar memories. *Nat Mater* 2010, 9, 403–406.
- [37] He, C. L., Zhuge, F., Zhou, X. F., Li, M., Zhou, G. C., Nonvolatile resistive switching in graphene oxide thin films. *Appl Phys Lett* 2009, 95, 232101
- [38] Wu, Z., Chen, Z., Du, X., Logan, J. M., Sippel, J., Nikolou, M., Kamaras, K., Reynolds, J. R., Tanner, D. B., Hebard, A. F., Transparent, conductive carbon nanotube films. *Science* 2004, 305, 1273–1276.
- [39] Jeong, H. Y., Yun Kim, O., Won Kim, J., Hwang, J. O., Kim, J-E., Yong Lee J., Yoon, T. H., Cho, B. J., Kim, S. O., Ruoff, R. S., Choi, S-Y. Graphene oxide thin films for flexible nonvolatile memory. *Nanolett* 2010, 10, 4381–4386.
- [40] <http://spectrum.ieee.org/semiconductors/nanotechnology/flexible-graphene-memristors>.
- [41] Hong, S. K., Kim, J. Y., Kim, J. W., Choi, S. Y., Cho, B. J., Flexible Resistive Switching Memory. Device Based on Graphene Oxide. *IEEE Electron Device Lett* 2010, 31, 1005.

- [42] Hong, S. K., Kim, J. E., Kim, S. O., Cho, B. J., Analysis on switching mechanism of graphene oxide resistive memory device. *J Appl Phys* 2010, 31 (1005), 2010
- [43] Deegan, R. D., Bakajin, O., Dupont, T. F., Huber, G., Nagel, S. R. and Witten, T. A., Capillary flows as the cause of ring stains from dried liquid drops, *Nature* 1997, 1, 827.
- [44] Deegan, R. D., Bakajin, O., Dupont, T. F., Huber, G., Nagel, S. R. and Witten, T. A., Contact line deposits in an evaporating drop. *Phys Rev B* 2000 62 (1), 756.
- [45] Bondavalli, P., Delfaure, C., Legagneux, P., Pribat, D., Supercapacitor electrode based on mixtures of graphite and carbon nanotubes deposited using a new dynamic air-brush deposition technique. *J ECS* 2013, 160 (4), A1–A6.
- [46] Vasu, K. S., Sampath, S., Sood, A. K., Nonvolatile unipolar resistive switching in ultrathin films of graphene and carbon nanotubes. *Solid State Communications* 2011, 151 (16), 1084–1087
- [47] Micheloni, Rino, Crippa, Luca, Marelli, Alessia, *Inside NAND Flash Memories*, Springer, e-book, ISBN 978-90-481-9431-5
- [48] Masuoka, F., Iizuka H., US4531203 (A) Semiconductor memory device and method for manufacturing the same.
- [49] Masuoka, F., Momodomi, M., Iwata, Y., Shirota, R., New ultra high density EPROM and flash EEPROM with NAND structure cell. *Electron Devices Meeting, 1987 International* 1987, IEEE.
- [50] Van Houdt, J., Degraeve, R., Groeseneken, G., Maes, H. E., Nonvolatile memory technologies with emphasis on flash: A comprehensive guide to understanding and using NVM devices, Published Online: 23 MAR 2007 DOI: 10.1002/9780470181355.ch4
- [51] Kingon, Angus, Device physics: Memories are made of . . . , *Nature*, 1999, 401, 658–659.
- [52] Cheng Yuhua, Chenming Hu, MOSFET Classification and Operation. *MOSFET Modeling & BSIM3 User's Guide*. Springer. 1999, 13, ISBN 0-7923-8575-6.
- [53] Song, Seung Min., Park, Jong Kyung., Sul, One Jae., Cho, Byung Jin. Determination of work function of graphene under a metal electrode and its role in contact resistance. *Nano Letters* 2012, 12 (8), 3887–3892.
- [54] Yu, Y., Zhao, Y., Ryu, S., Brus, L. E., Kim, K. S., Kim, P., Tuning the graphene work function by electric field effect. *Nano Lett.* 2009, 9, 3430–3434.
- [55] Yan, L., Punckt, C., Aksay, I. A., Mertin, W., Bacher, G., Local voltage drop in a single functionalized graphene sheet characterized by Kelvin probe force microscopy. *Nano Lett* 2011, 11, 3543–3549.
- [56] Filleter, T., Emtsev, K. V., Seyller Th., Bennewitz R., Local work function measurements of epitaxial graphene. *Appl. Phys. Lett.* 2008, 93, 133–117.
- [57] Wang, Haomin., Wu, Yihong., Chunxiao, Cong., Jingzhi, Shang., Yu, Ting., Hysteresis of electronic transport in graphene transistors. *ACS Nano* 2010, 4 (12), 7221–7228. DOI:10.1021/nn101950n
- [58] Kim, W., Javey, A., Vermesh, O., Wang, Q., Li, Y., Dai, H., Hysteresis caused by water molecules in carbon nanotube field-effect transistors. *Nano Lett* 2003, 3, 193–198.
- [59] Bondavalli, P., Legagneux, P., Pribat, D., CNTFET based gas sensors: State of the art and critical review. *Sensors Actuat B* 140, 1, 304–318.
- [60] Echtermeyer, T., Lemme, M., Baus, M., Szafranek, B., Geim, A., Kurz, H. Nonvolatile switching in graphene field-effect devices. *IEEE Electron Device Lett.* 2008, 29, 8, 952–954.
- [61] Echtermeyer, T. J., Lemme, M. C., M. Baus, B., Szafranek, N., Geim, A. K., and Kurz, H., A graphene-based electrochemical switch. arXiv:0712.2026v1.
- [62] Bertolazzi, S., Krasnozhan, D., Kis, A. Nonvolatile memory cells based on MoS₂/Graphene heterostructures. *ACS Nano* 2013, 7 (4), 3246–3252.
- [63] Hong, Augustin J., Song, Emil B., Yu, Hyung Sk., Matthew, J., Allen, J Kim., Fowler, J. D., Wassei, Jonathan K. , Park, Youngju., Wang, Yong., Zou, Jin., Kaner, R. B., Weiller, B. H., Wang, L., Graphene flash memory. *ACS Nano* 2011, 5 (10), 7812–7817.

Hanshan Dong, Santiago Corujeira Gallo

2 Plasma surface activation and functionalization of carbon-based materials

2.1 Introduction

Carbon-based materials have been extensively researched for an increasing number of applications because of their abundance and low cost, ease of processability, high-temperature stability and corrosion resistance, high electrical conductivity and good mechanical properties, particularly in the microscopic and nanoscopic scale [1]. The uses of carbon-based materials are very diverse, going from mechanical reinforcement in polymer matrix composites [2] to electrodes in supercapacitors and fuel cells [1]. However, their chemical inertness poses a common challenge in most applications, and several surface activation and surface functionalization methods have been developed to improve their performance, their compatibility with other materials or their interaction with the service environment [3].

The chemical inertness of carbon-based materials is attributed to the presence of graphene planes on the surface, having a low density of dangling bonds [5]. Graphene, carbon nanotubes (CNTs) and buckyballs are extreme examples of this microstructure, as they are composed of a single or a small number of graphene layers with a regular arrangement [6]. On the other hand, carbon fibers and amorphous carbon exhibit a turbostratic structure, with a higher degree of disorder and a larger number of dangling bonds on the surface (Figure 2.1). Several surface engineering techniques have been developed to activate and/or functionalize carbon-based materials [7]. These processes aim at increasing the number of dangling bonds and attaching functional groups to them to make the carbon-based material more compatible with the polymeric matrix in a composite, or to improve the wettability by an electrolyte in a supercapacitor and increase the charge exchange rate at the electrode.

The conventional surface engineering methods include wet chemical processes [8, 9], thermochemical [10] or electrochemical treatments [11]. Even though these methods are effective, they can be difficult to control and, in some cases, they raise environmental concerns. Therefore, recent studies have focused on the development of plasma processes for surface activation and functionalization of carbon-based materials [12, 13]. Plasma processes are conducted under vacuum or at atmospheric pressure and use highly reactive ionized gas molecules to create active sites and

Hanshan Dong, The University of Birmingham, UK
Santiago Corujeira Gallo, Deakin University, Australia

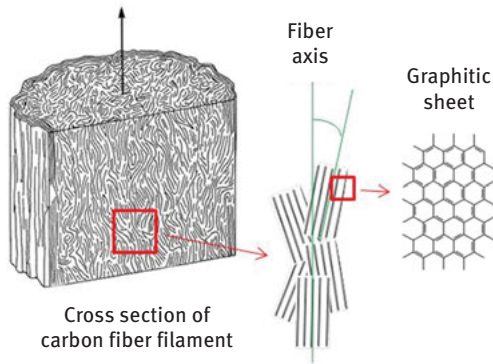


Figure 2.1: Turbostratic microstructure of carbon fibers, with inert graphene basal planes on their surface. Reprinted with permission from [4].

attach functional groups on the surface of carbon-based materials. In general, these processes are easier to control than conventional treatments, and they offer technical and environmental benefits.

2.2 Active screen plasma surface engineering

Active screen plasma (ASP) is a low-temperature and low-pressure plasma technology of surface engineering, which was developed at the University of Birmingham in the early 2000s [14–16]. The technology was initially applied to the thermochemical treatment of steels, but its potential for the functionalization of other materials was recognized immediately [17]. The schematic diagram in Figure 2.2 illustrates the main features of the ASP reactor in contrast to a conventional DC plasma reactor. The benefits of the ASP technology are mainly attributed to the creation of ions and active species on an auxiliary surface, the so-called *active screen*, as opposed to the surface of the treated material [18]. This allows more control over the type of plasma–surface interactions and the severity of the physical and chemical processes [3].

The active screen is a metallic mesh negatively biased to form ions and other active species from gas molecules, most typically N_2 , H_2 , Ar, CH_4 . The surfaces to be treated can be simply left at floating potential¹ and exposed to the flow of active

¹ Floating potential is the electric potential that an insulated object develops when exposed to the plasma. An object immersed in the plasma will be exposed to ions and electrons, but the electrons move much faster than the ions because of the difference in mass, so the number of electrons arriving at the surface of the object is higher than the number of ions. If the object is electrically insulated, the negative charge of the electrons accumulates, developing a self-induced bias that attracts positive ions and repels the less energetic electrons, until an equal number of ions and electrons arrive at the surface at any given time, that is, zero net current.

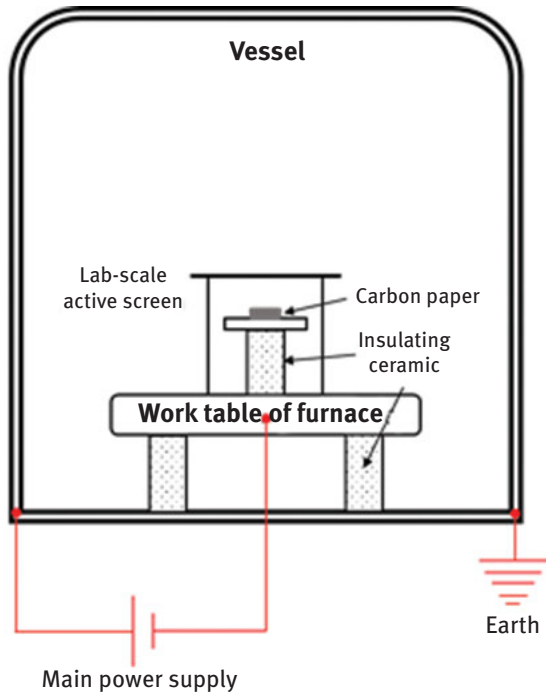


Figure 2.2: Schematic diagram of an active screen plasma reactor. Reprinted with permission from [19].

species, in which case the plasma–surface interactions are mainly of chemical nature, for example, attachment of functional groups. In other cases, a moderate bias is applied on the treated surface in order to attract the active species with increasing energy, making the physical action of the ions more pronounced. This ion bombardment can create new active sites and change the surface roughness. Alternatively, the material from the active screen can be sputtered² and deposited on the surfaces exposed to the plasma. This approach is particularly useful to functionalize surfaces with metallic materials.

In summary, the ASP technology has an additional degree of freedom compared to other plasma reactors, making it possible to create highly reactive ions and excited species on the *active screen*, and attracting them toward the work table with varying levels of energy (bias) to control the type of plasma–surface interaction, thus favoring physical or chemical phenomena. The following sections illustrate some of the recent

² Sputtering refers to the ejection of material from a solid surface by the physical action of impacting ions.

uses of the ASP treatments to activate and functionalize carbon-based materials with a wide range of microstructures, from the highly ordered structure of graphene to the disordered microstructure of carbon paper.

2.3 Reduction of graphene oxide for optoelectronic devices

Graphene has attracted significant attention for optoelectronic devices, and graphene oxide (GO) is an interesting precursor for graphene coatings of high-quality and over large-surface areas [6, 20]. GO has a nanosheet-layered structure similar to graphene but contains different oxygen groups [21, 22]. The GO coatings can be produced by chemical methods [23], dissolving graphene powder and other salts in sulfuric acid, subsequently dispersing and exfoliating the GO nanosheets by sonication, and finally casting it onto the substrate. A reduction process is then required to remove the oxygen functionalities and obtain a graphene coating of high quality, and the ASP technology was used for this purpose [24]. The ASP treatments were conducted at 400 Pa in pure H_2 or N_2-H_2 mixtures, at temperatures between 100 and 200 °C for 1 h.

The appearance of coatings changed from a light brown color to silver-gray after the plasma reduction in pure hydrogen and nitrogen–hydrogen mixtures, and this change was accompanied by a decrease in optical transparency and electrical resistance of the coating (Figure 2.3). The reduction process with the plasma technology was more effective than the heat treatment of GO in a reducing atmosphere, and the results varied with the treatment temperature (100–200 °C) and the gas mixture (H_2 or H_2-N_2). The X-ray diffraction (XRD) traces revealed that the GO peak disappeared after the reduction process, and the Raman spectra indicated an increase in the ratio of disordered to graphitic bands (D/G), which was attributed to the introduction of defects in the graphene planes during the reduction process. The X-ray photoelectron spectroscopy (XPS) data showed a marked decrease in oxygen functional groups attached to the carbon network, with the carboxylic oxygen ($O-C=O$) being the most unstable functional group compared to other oxygen bonds. The XPS data also revealed the presence of Fe, Cr and Mo doping elements in a partially oxidized state. These metallic dopants are transferred from the mesh of the active screen equipment to the GO-coated substrates, particularly when using nitrogen containing gas mixtures. A small amount of nitrogen was also incorporated into the coatings.

The oxygen to carbon ratio (O/C), reported in Table 2.1, reflects the efficiency of each process to reduce the GO coating. The plasma treatment in pure hydrogen was the most effective, resulting in an extensive decomposition of carboxyl functionalities and the creation of carbonyl groups. On the other hand, the use of nitrogen in the gas mixture increased the doping of the GO coating with metal atoms from the active screen, with a marked drop in electric resistance. The level of doping can be

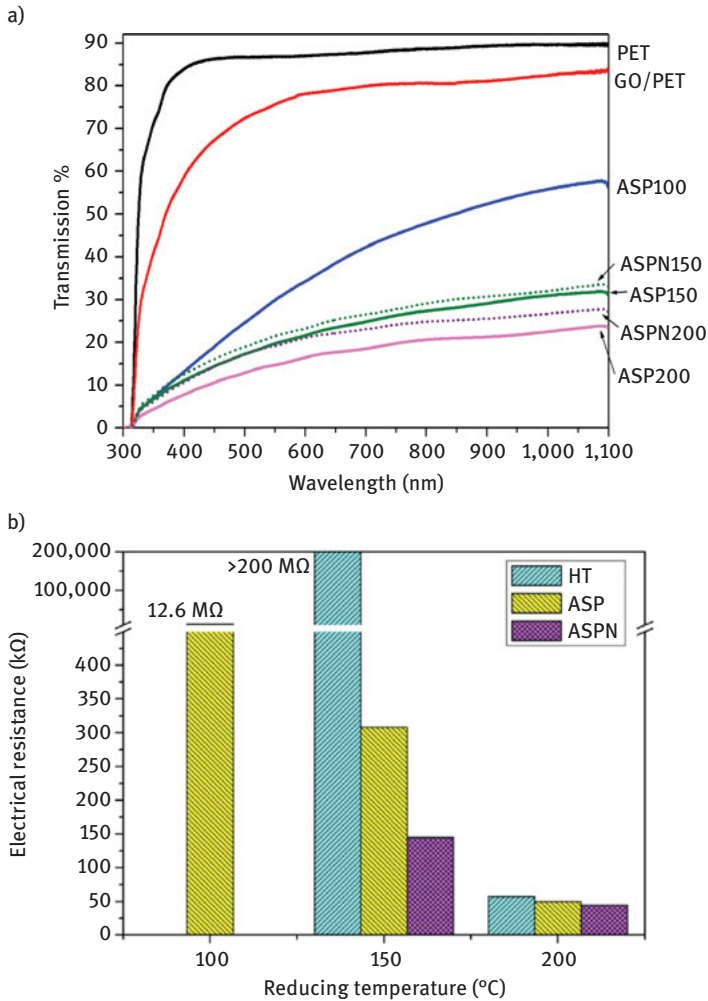


Figure 2.3: Properties of the untreated and reduced GO coatings: (a) optical transparency and (b) electrical resistance. Reprinted with permission from [24].

PET: poly(ethylene terephthalate) substrate; GO: graphene oxide coating; ASP: active screen plasma surface treatment.

controlled by varying the processing conditions (composition of the active screen, gas mixture, electric bias applied on the treated surface and duration of the process), opening new pathways to reduce and functionalize GO coatings.

Table 2.1: Chemical analysis from XPS: O components and O/C ratio. Reprinted with permission from [24].

Sample	Treatment	Gas	Temperature	O–Si	O–Me	O–C=O	O–C	O/C
GO	Untreated	N/A	N/A	2.6	0.0	9.2	9.0	0.235
HT200	Heat treated	H ₂	200 °C	4.3	0.0	7.4	5.7	0.154
ASP150	ASP	H ₂	150 °C	5.6	6.7	6.9	1.5	0.122
ASPN150	ASP	H ₂ –N ₂	150 °C	2.1	7.4	7.4	1.3	0.125
ASP200	ASP	H ₂	200 °C	1.7	6.2	6.2	1.1	0.102
ASPN200	ASP	H ₂ –N ₂	200 °C	2.4	6.8	6.8	1.1	0.115

2.4 Functionalization of carbon nanofibers for supercapacitors

Carbon nanofibers (CNF) are good candidate materials for electrodes in energy storage devices because of the intrinsic properties of carbon (thermal and chemical stability, electric conductivity) and the ability to form controlled porous structures with the nanofibers [1]. This combination allows researchers to create stable electrodes with a very large surface area, and recent efforts have focused on increasing the surface conductivity and the charge exchange efficiency with the electrolyte. Silver and nickel are among the proposed electroactive materials, capable of increasing the pseudocapacitance and double-layer energy storage mechanisms,³ and the ASP technology was used for this purpose [25]. CNFs were dispersed in isopropanol, the suspension was placed in Petri dishes and the solvent was left to evaporate before the plasma treatments.

The ASP treatments did not change the size or the structure of the CNFs, but their surface was covered with nickel and silver nanoparticles, respectively. The metal nanoparticles were approximately 10–50 nm in diameter (Figure 2.4), and their size and density increased with the ASP treatment time, which was reflected on the nickel and silver contents detected by energy-dispersive X-ray spectroscopy and XRD. The ASP functionalization with silver produced a rough surface, even after 120 min of plasma treatment, which is beneficial to increase the surface area. On the other hand, nickel tended to form a continuous coating on the CNFs after only 45 min of ASP treatment, thus limiting the amount of material and the morphology of the particles that could be deposited on CNFs.

³ Electrical double layer capacitors are based on non-Faradaic mechanisms, in which the electric charge is stored in the double layer formed at the interface between the inert electrode material and the electrolyte, without involving redox reactions. On the other hand, the pseudocapacitors rely on reversible redox reactions (Faradaic), which take place on the surface of the active electrode material in contact with the electrolyte [1].

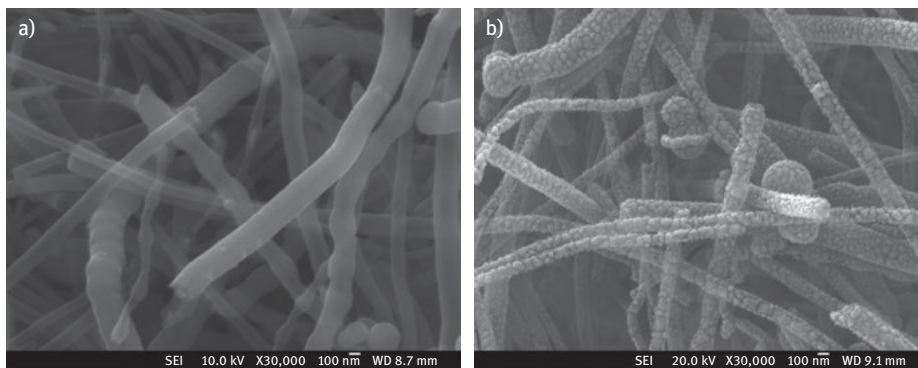


Figure 2.4: Surface morphology of carbon nanofibers: (a) untreated and (b) ASP functionalized with nickel. Reprinted with permission from [25] Copyright (2017) American Chemical Society.

The cyclic voltammetry (CV) tests conducted in 1 M sodium sulfate solution revealed a significant increase in the loop area after the ASP treatments, particularly with silver (Figure 2.5). More importantly, the CNFs functionalized with silver retained the rectangular shape of the CV curves, which was attributed to the high surface conductivity and ion transport efficiency. On the other hand, the nickel-functionalized CNFs showed severe distortions, particularly at higher scan rates, between 100 and 200 mV/s. The differences were also observed in the cyclic charge–discharge curves, with the nickel-functionalized CNF electrodes showing a twofold increase in capacitance and the silver-functionalized CNF electrodes exhibiting a fourfold increase in capacitance compared to the untreated CNFs. The electrochemical impedance spectra indicated that the increase in capacitance was mainly due to the double layer mechanism, rather than pseudocapacitance. However, recent reports have indicated that vanadium and other transition metal nitrides can improve both Faradaic and non-Faradaic charge storage mechanisms, which make them promising electrode materials for supercapacitors. This finding opens good prospects for the ASP technology, considering that it has been extensively used to form nitrides and carbides for surface functionalization and hardening.

2.5 Surface activation of carbon paper gas diffusion layers in fuel cells

Carbon paper is used as gas diffusion layer (GDL) in direct methanol fuel cells [26]. The electrocatalysts, which consist of reaction layers of precious metals with nanometer-size features, are frequently deposited directly on the GDL. These deposition processes are typically conducted in an aqueous environment and the poor

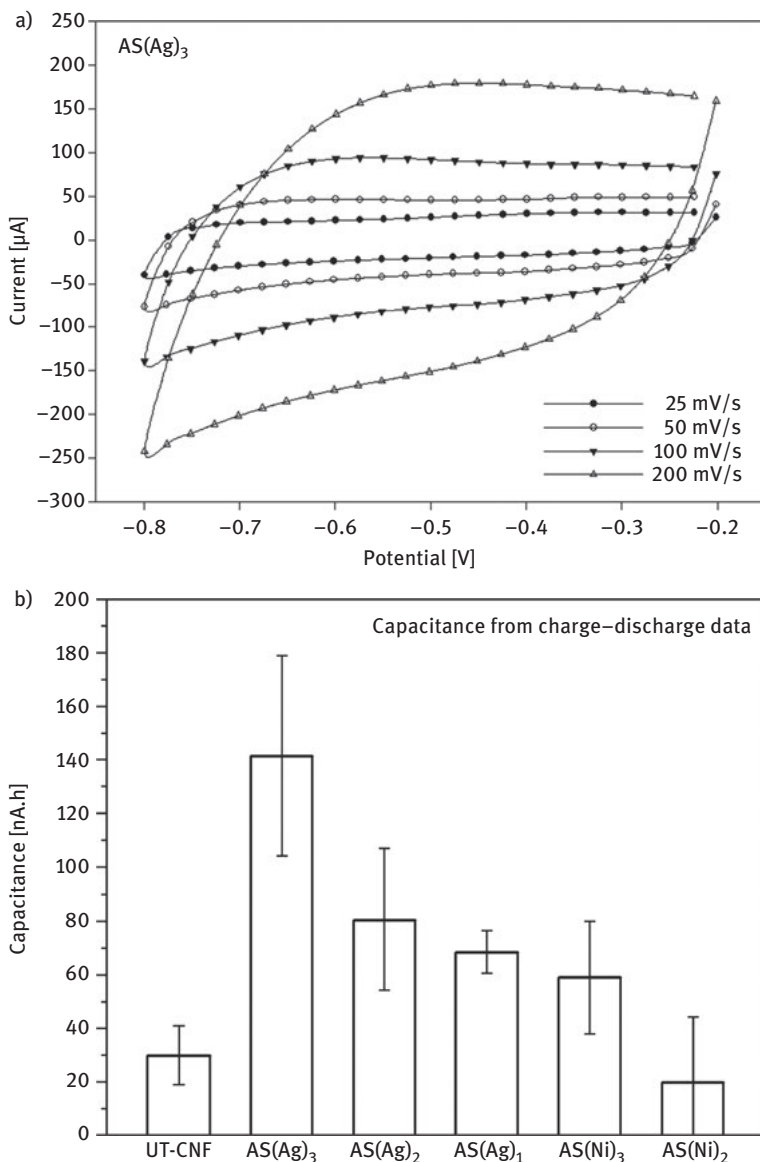


Figure 2.5: Cyclic voltammety of carbon nanofibers functionalized with silver (a) and capacitance (b) calculated from charge–discharge experiments. Reprinted with permission from [25] Copyright (2017) American Chemical Society.

wettability of the hydrophobic carbon paper results in aggregation and uneven growth of the electrocatalyst, which reduces efficiency and increases cost [27, 28]. Therefore, the ASP technology was used to activate the surface of SIGRACET®

GDL 35BC carbon paper [19]. The activation treatment was conducted in a gas mixture of 25% N₂ and 75% H₂ at a pressure of 400 Pa. The temperature ranged from 100 to 210 °C and the duration of the treatment was between 10 and 30 min. After the activation treatment, the carbon papers were rinsed in ethanol and immersed in an aqueous solution of H₂PtCl₆ and formic acid to grow the platinum nanowires (2 mg/cm²), and finally rinsed in water/ethanol/water and dried at 40 °C for 24 h. These carbon papers were then used as integrated cathodes in single cell tests, with a Nafion 117 membrane and the commercial JM anode (PtRu 4 mg/cm²). The electrodes were then hot-pressed against the Nafion 117 membrane at 135 °C for 2 min under a constant pressure of 5 MPa. The reference cells were fabricated with Nafion 117 membrane, commercial JM cathode (Pt 4 mg/cm²) and JM anode (PtRu 4 mg/cm²). These electrode assemblies were sandwiched between two graphite flow field plates to form a single cell with an active electrode area of 5 cm².

The CV tests conducted on a single cell revealed that all the carbon papers activated with the ASP technology for 10 min had higher electrochemical surface area (ECSA) than the untreated carbon paper. What is more, the ECSA increased with the ASP treatment temperature up to 150 °C, and then decreased with further temperature increments (Figure 2.6). The maximum ECSA value of 25.8 m²/g corresponded to the carbon paper activated at 150 °C with the ASP technology, which was 65% higher than the ECSA value of the untreated carbon paper. The polarization curves also revealed maximum power densities for moderate ASP treatment temperatures in the order of 120 and 150 °C. The highest power density measured in these experiments was 63.9 mW/cm², which was three times higher than the power density obtained with the untreated carbon paper.

This remarkable improvement in the performance of the single cells was attributed to the different surface morphology observed at high magnification. The surface of the untreated carbon paper was only partially covered by Pt nanowires, and they formed rather large cubic-shaped clusters. The uneven surface morphology was a result of the super hydrophobic nature of the untreated carbon paper and its poor wettability (Figure 2.7). In contrast, the surface of the ASP-activated carbon paper showed a more uniform distribution of the Pt nanowires, with a decreasing number of aggregates as the ASP treatment temperature increased up to 150 °C. At temperatures higher than 150 °C, the morphology of the Pt nanowires changed, becoming shorter and, consequently, reducing the ECSA and the cell performance. Longer ASP activation times, that is, 30 min, had a detrimental effect on the surface morphology of the catalyst layer and, consequently, on the cell performance. In summary, the ASP activation at moderate temperature (120–150 °C) and for a short time (10 min) can effectively promote the growth of the electroactive layer of Pt nanowires on the carbon paper, improving the utilization of this expensive catalyst and, ultimately, increasing the ECSA and the power density of the fuel cell.

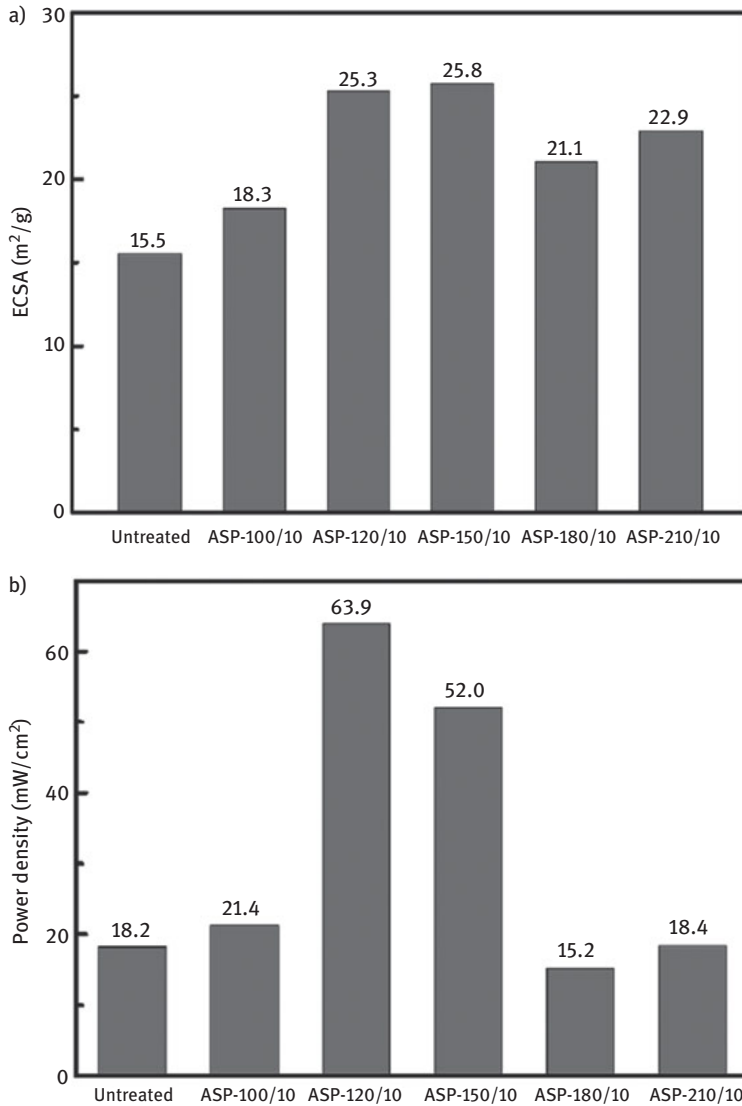


Figure 2.6: (a) Electrochemical surface area (ECSA) and (b) power density from polarization tests. Reprinted with permission from [19].

2.6 Improving the bond strength of carbon fibers in composite materials

Carbon fibers are exceptional reinforcements for polymer matrix composite materials, particularly because of their high strength, high stiffness and lightweight [29].

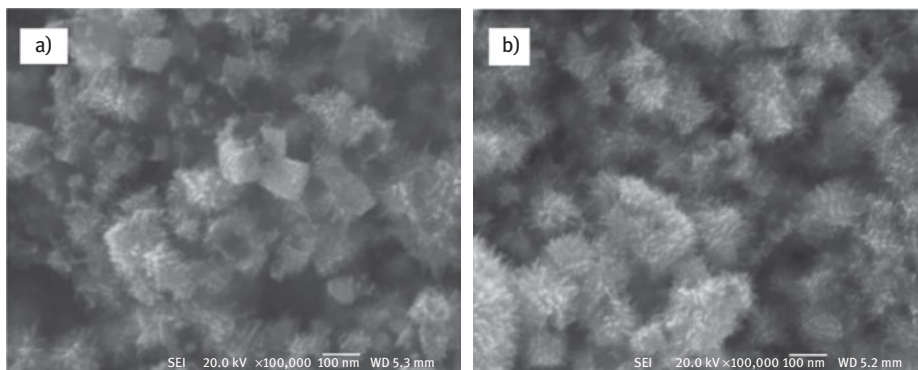


Figure 2.7: Surface morphology of the electrocatalyst layer deposited on the (a) untreated and (b) ASP functionalized carbon paper (ASP treatment conducted at 120 °C for 10 min) [19].

However, the graphitic basal planes present on the surface of the carbon fibers make them relatively inert and this reduces the wettability and the bond strength with the polymeric matrix, frequently an epoxy resin [3]. Plasma treatments have been used to introduce polar functional groups on the surface of carbon fibers. These functional groups help to modify the bond strength with the polymeric matrix and to tailor the mechanical properties of the composite material, particularly the strength and toughness [30, 31]. The ASP technology offers good control over the treatment conditions to avoid damaging the fibers, thus retaining their strength.

Carbon fibers were ASP treated in a gas mixture of 75% H₂ and 25% N₂ at a pressure of 50 Pa. This atmosphere was selected to introduce –NH_x functional groups on the surface of the carbon fibers [32]. These functional groups are known to create strong chemical bonds with the epoxy resins used in these composites, and the physical etching creates a microroughness on the carbon fibers, which increases the mechanical interlocking with the matrix. Optical emission spectroscopy studies conducted during the ASP treatments revealed NH_x species in the plasma phase, and NH groups were also identified on the surface of the functionalized carbon fibers using XPS (Figure 2.8). The relative intensity of the NH species in the plasma decreased with increasing applied power, and this change correlated with a reduction in the nitrogen content on the surface of the functionalized fibers. A similar trend was observed on the contact angle of glassy carbon disks, functionalized alongside with the carbon fibers. All the ASP-treated carbon disks showed contact angles significantly lower (<60°) than the untreated disks (80°), but the lowest contact angle (40°) corresponded to the disk treated at low power and for short time.

Further wettability measurements were conducted on carbon disks immediately after the ASP treatment and over the subsequent 4 weeks. It was found that the contact angle dropped remarkably after the plasma treatments to values as low as 10°. However, the contact angle increased rapidly over the subsequent 7 days

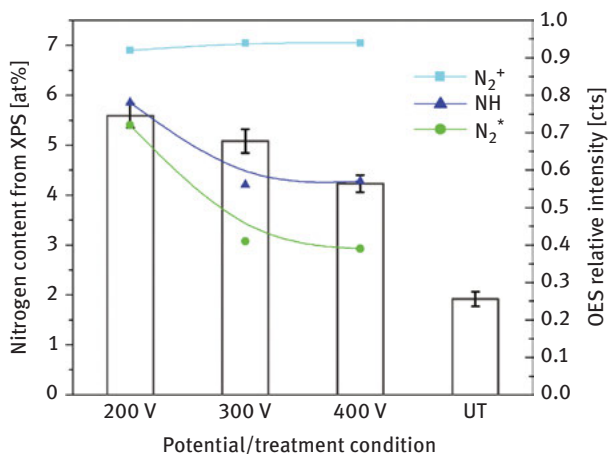


Figure 2.8: Correlation of active species in the plasma phase with functional groups on the surface of the carbon fibers as a function of the ASP treatment conditions (potential). Reprinted with permission from [30]. Copyright 2017, American Vacuum Society.

and remained relatively constant for the remaining 3 weeks (Figure 2.9). The chemical analysis by XPS showed a small but consistent reduction in the nitrogen content (from 5.8 to 5.1 at.%) over a period of 28 days. However, the initial XPS analysis was only conducted 3–4 weeks after the ASP treatment, so the wettability measurements could not be correlated with the XPS data. The change in the nitrogen content and in the wettability was consistent with an exponential decay, which could be attributed to a degradation of the nitrogen functionalities by oxidative scissions and evaporative loss upon their exposure to air. The elucidation of the degradation mechanism requires further study.



Figure 2.9: Evolution of the contact angle of an ASP-treated carbon surface with time. Reprinted with permission from [30]. Copyright 2017, American Vacuum Society.

2.7 Synthesis and deposition of carbon nanotube films

CNTs exhibit extraordinary electrical, thermal and mechanical properties, similar to CNFs. CNTs are frequently synthesized by arc discharges, laser ablation or chemical vapor deposition (CVD) [33–35]. The latter method is capable of producing vertically

aligned CNT (VACNT), but the process requires prior deposition of metal nanoparticles on the substrate to act as catalysts and nucleation sites. In addition, the high temperature required for conventional CVD processes can be detrimental for the substrate. It is known that plasma-enhanced CVD (PE-CVD) can reduce the deposition temperature, but the energy of the ions needs to be carefully controlled to enhance rather than suppress the growth of CNT [36]. A multistep process to deposit metal nanoparticles and grow CNTs at low temperatures has been recently developed based on the ASP technology [33].

Silicon wafers (100) were used as substrates for the PE-CVD process with RF excitation (13.56 MHz, 30 W) and a modified active screen experimental setup (Figure 2.10). Metal nanoparticles with different compositions were deposited on the silicon wafers by changing material of the active screen, in this case nickel and stainless steel. The size, morphology and uniformity of the metal particles were critical for the success of the process, the density and vertical alignment of the CNTs. VACNTs were grown in the same active screen experimental arrangement using a gas mixture of acetylene, argon and hydrogen at 100 Pa (Figure 2.11). Transmission electron microscopic observations revealed a tip-growth mode, in which the metal nanoparticles were detached from the silicon wafer and remained at the tip (growing front) of the CNTs. For a given treatment time (100 min), the length of the CNTs increased with the processing temperature from 0.6 μm at 400 $^{\circ}\text{C}$ to 6 μm at 500 $^{\circ}\text{C}$, and their diameter decreased from 28 to 16 nm, respectively (Figure 2.11). The structure of the CNTs did not change significantly with

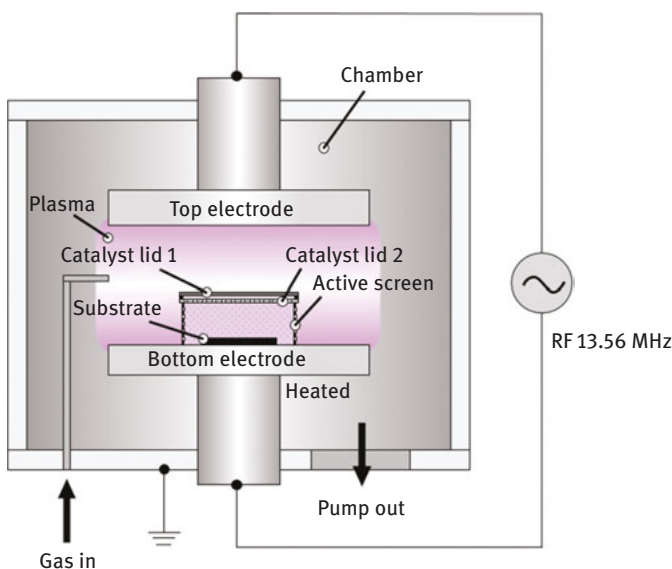


Figure 2.10: Schematic diagram of the active screen setup used for PE-CVD of vertically aligned carbon nanotubes. Reprinted with permission from [33].

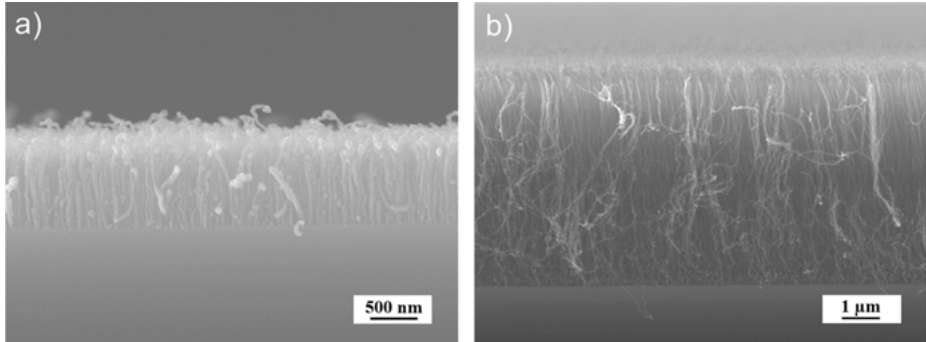


Figure 2.11: SEM images of CNTs grown at (a) 400 °C and (b) 500 °C. Reprinted with permission from [33].

the deposition temperature, but the ratio of D and G bands (I_D/I_G) in the Raman spectra changed from 0.7 to 0.97 with increasing content of acetylene in the gas mixture.

The multistep PE-CVD process, based on the ASP technology with RF excitation, could successfully deposit a layer of metal nanoparticles on a silicon wafer and subsequently grow vertically aligned CNTs. The size, morphology and microstructure of the VACNTs could be controlled by changing key processing parameters, such as size, distribution and uniformity of metal nanoparticles, gas mixture and processing temperature. This process represents a simple and cost-effective method to functionalize the surface of a wide range of substrates with CNTs.

2.8 Summary and future perspectives

This chapter presents a summary of the research undertaken at the University of Birmingham on the functionalization of carbon-based materials using the ASP technology. This research exploits the typical physical and chemical phenomena associated with the plasma technology, further optimized by the additional control and degrees of freedom offered by the ASP technology. In this way, the highly reactive species in the plasma were used to reduce GO films, activate the surface of carbon paper membranes or functionalize the surface of carbon fibers. In addition, the sputtering of material from the active screen and its deposition on the surfaces exposed to the plasma was used to increase the conductivity and surface area of CNFs and to create nucleation sites for CNTs. In all cases, the treatment conditions could be optimized, targeting specific plasma–surface interactions, to achieve the desired properties.

Future efforts will focus on expanding the range of gases and active screen materials used to functionalize temperature-sensitive substrates, as well as combining the ASP technology with pre- and post-treatments. There are also challenges related to the

uniformity of the ASP treatment of porous and three-dimensional structures due to shadowing effects that need to be addressed. In addition, the interaction between active species in the plasma and different microstructures of carbon-based materials deserves further study, together with the evolution of the ASP functionalized surfaces over time. Lastly, there seem to be good opportunities to create patterned surfaces using the ASP technology, in combination with other processes with potential application in multiple fields such as functional materials, sensors and biosensors, electrical, electronic and optoelectronic devices. Without question, the ASP technology remains to be a valuable enabling technology for the surface functionalization of engineering materials, showing broader prospects of practical applications than ever before.

Acknowledgments: The research leading to these results has received funding from the European Union for Multi-Surf (Project ID 327750), FIBRALSPEC (GA604248) and MODCOMP (GA685844). The authors would like to thank their former and current colleagues Dr Xiaoying Li, Prof Jian Chen, Dr Kaijie Lin, Dr Shaojun Qi and Mr Xiaochao Ji for the reproduction of their original work.

References

- [1] Pandolfo, A. G., A. F. Hollenkamp, Carbon properties and their role in supercapacitors. *J Power Sources* 2006, 157 (1), 11–27.
- [2] Karger-Kocsis, J., Mahmood, H., Pegoretti, A., Recent advances in fiber/matrix interphase engineering for polymer composites. *Prog. Mater. Sci* 2015, 73, 1–43.
- [3] Corujeira-Gallo, S., Dong, H., Effect of microstructure on the plasma surface treatment of carbon fibres. *J Compos Mater* 2017, 51 (23), 3239–3256.
- [4] Behr, M. J., et al., Structure-property model for polyethylene-derived carbon fiber. *Carbon* 2016, 107, 525–535.
- [5] Hoecker, F., Karger-Kocsis, J., Surface energetics of carbon fibers and its effects on the mechanical performance of CF/EP composites. *J Appl Polym Sci* 1996, 59 (1), 139–153.
- [6] Novoselov, K. S., et al., A roadmap for graphene. *Nature* 2012, 490, 192.
- [7] Tang, L. G., Karoos, J. L., A review of methods for improving the interfacial adhesion between carbon fiber and polymer matrix. *Polym Compos* 1997, 18 (1), 100–113.
- [8] Zielke, U., Hüttinger, K. J., Hoffman, W. P., Surface oxidized carbon fibers: II. Chemical modification. *Carbon* 1996, 34 (8), 999–1005.
- [9] Severini, F., et al., Chemical modification of carbon fiber surfaces. *Carbon* 2002, 40, (5), 735–741.
- [10] Solís-Fernández, P., et al., A comparison between physically and chemically driven etching in the oxidation of graphite surfaces. *J Colloid Interf Sci* 2010, 344 (2), 451–459.
- [11] Donnet, J. B., Guilpain, G., Surface treatments and properties of carbon fibers. *Carbon* 1989, 27 (5), 749–757.
- [12] Käßler, I., Hund, R. D., Cherif, C., Surface modification of carbon fibres using plasma technique. *AUTEX Res J* 2014, 14 (1), 34–38.
- [13] Tiwari, S., et al., Influence of cold remote nitrogen oxygen plasma treatment on carbon fabric and its composites with specialty polymers. *J Mater Sci* 2011, 46, (4), 964–974.

- [14] Li, C. X., Bell, T., and Dong, H., A study of active screen plasma nitriding. *Surf Eng*, 2002, 18 (3), 174–181.
- [15] Cheng, Z., et al., Study of the active screen plasma nitriding. *Cailiao Rechuli Xuebao/ Transactions of Materials and Heat Treatment* 2004, 25 (5), 330–333.
- [16] Georges, J., Nitriding process and nitriding furnace therefor, U.P. Office, Editor. 1999: United States of America.
- [17] Li, C. X., Bell, T., Potential of plasma nitriding of polymer for improved hardness and wear resistance. *J. Mater. Process. Technol* 2005, 168 (2), 219–224.
- [18] Corujeira Gallo, S., H. Dong, Study of active screen plasma processing conditions for carburising and nitriding austenitic stainless steel. *Surf Coat Tech* 2009, 203 (24), 3669–3675.
- [19] Lin, K., et al., The effect of active screen plasma treatment conditions on the growth and performance of Pt nanowire catalyst layer in DMFCs. *Int. J. Hydrog. Energy* 2016, 41 (18), 7622–7630.
- [20] Lee, Y., Ahn, J.-H., Graphene-based transparent conductive films. *Nano* 2013, 08 (03), 1330001.
- [21] Gómez-Navarro, C., et al., Atomic Structure of Reduced Graphene Oxide. *Nano Letters* 2010, 10 (4), 1144–1148.
- [22] Dreyer, D. R., et al., The chemistry of graphene oxide. *Chem. Soc. Rev* 2010, 39 (1), 228–240.
- [23] Marcano, D. C., et al., Improved Synthesis of Graphene Oxide. *ACS Nano* 2010, 4, (8), 4806–4814.
- [24] Chen, J., et al., Reducing and multiple-element doping of graphene oxide using active screen plasma treatments. *Carbon* 2015, 95, 338–346.
- [25] Corujeira Gallo, S., et al., Carbon nanofibers functionalized with active screen plasma-deposited metal nanoparticles for electrical energy storage devices. *ACS Appl Mater Inter* 2017, 9, 27, 23195–23201.
- [26] Schweiss, R. and Öttinger, O., The importance of carbon materials in micro-porous layer in gas diffusion layers for proton exchange membrane fuel cells. *Carbon* 2015, 93, 1079.
- [27] Rajalakshmi, N., Dhathathreyan, K. S., Nanostructured platinum catalyst layer prepared by pulsed electrodeposition for use in PEM fuel cells. *Int. J. Hydrog. Energy* 2008, 33 (20), 5672–5677.
- [28] Du, S., Pollet, B. G., Catalyst loading for Pt-nanowire thin film electrodes in PEFCs. *Int. J. Hydrog. Energy*, 2012, 37 (23), 17892–17898.
- [29] Sharma, M., et al., Carbon fiber surfaces and composite interphases. *Compos Sci Technol*, 2014, 102, 35–50.
- [30] Corujeira Gallo, S., Charitidis, C., Dong, H., Surface functionalization of carbon fibers with active screen plasma. *J Vac Sci Technol A: Vacuum, Surfaces and Films* 2017, 35 (2), 021404-1-10.
- [31] Corujeira Gallo, S., et al. Active screen plasma treatment and characterisation of carbon fibres – A feasibility study. *Carbon* 2015, Dresden.
- [32] Pittman Jr, C. U., et al., Chemical modification of carbon fiber surfaces by nitric acid oxidation followed by reaction with tetraethylenepentamine. *Carbon*, 1997, 35 (3), 317–331.
- [33] Ji, X., et al., A novel hybrid method combining ASP with PECVD for in-situ low temperature synthesis of vertically aligned carbon nanotube films. *Diam. Relat. Mater* 2017, 77, 16–24.
- [34] Thess, A., et al., Crystalline ropes of metallic carbon nanotubes. *Science* 1996, 273 (5274), 483–487.
- [35] Iijima, S., Helical microtubules of graphitic carbon. *Nature* 1991, 354, 56.
- [36] Jang, I., et al., Characteristics of carbon nanotubes grown by mesh-inserted plasma-enhanced chemical vapor deposition. *Carbon* 2007, 45 (15), 3015–3021.

Rajat Srivastava, Matteo Fasano, Shahin Mohammad Nejad,
Hernán Chávez Thielemann, Eliodoro Chiavazzo,
and Pietro Asinari

3 Modeling carbon-based smart materials

3.1 Introduction

Smart materials show changes in their properties in a predictable manner upon application of external stimuli, such as chemical, electrical, thermal, mechanical, magnetic and light ones. Our knowledge about smart materials exists from the era of Roman Empire: there are several evidences that building materials used at that time, mainly mixtures of several compounds including limestone, had self-healing capabilities, since they were able to repair cracks by the simple action of rainwater [1]. Modern smart materials are opening up new opportunities in several fields, for instance, healthcare, defense, waste management and packaging. In fact, these materials are widely used in applications such as sensors, actuators, robots, artificial muscles and drug delivery. Smart materials can be classified based on their responses to the external stimuli, that is, shape memory, piezoelectric, photoresponsive, electroresponsive, magneto-responsive and thermochromic materials.

Shape memory materials have the unique capability of remembering their original shape after deformation, thereby returning to it upon application of external stimuli such as thermal, mechanical or magnetic variations [2, 3]. These materials have found application in automobiles, aircraft, biomedical devices, robots, civil structures and textiles [3–8]. Shape memory materials can be made out of alloys, ceramics, polymers, hybrid materials or gels. The first shape memory material dates back to 1932, when Arne Ölander first discovered a solid cadmium–gold alloy that, when deformed in a cold state, returned to its original shape upon heating [9]. Nickel–titanium (NiTi) was then a popular shape memory alloy (SMA) discovered by Buehler et al. [10] in 1963, which spread the use of SMA to the first industrial applications. NiTi alloys are preferable in most applications due to their good ductility, corrosion resistance, mechanical stability and biocompatibility [11, 12]. In recent years, carbon-based shape memory polymers attracted attention due to their capability of handling high strain and temperature, their lower density and recovery temperature and their flexibility and recyclability [13–15]. All these superior properties make them interesting shape memory materials, particularly for aerospace and biomedical fields.

Rajat Srivastava, Matteo Fasano, Shahin Mohammad Nejad, Hernán Chávez Thielemann, Eliodoro Chiavazzo, Pietro Asinari, Department of Energy, Politecnico di Torino, Torino, Italy

For example, Zhang et al. [16] fabricated multistimuli-responsive shape memory materials based on polymer composites reinforced by graphene nanoplatelets (GNPs), which could be triggered by electrical and infrared stimuli. Figure 3.1 shows the shape memory mechanism actuated by photothermal effect: after a deformation at low temperature (*Shape 2*), the original shape of the GNP-based polymeric material (*Shape 1*) can be recovered upon exposure to infrared radiation [16]. Recently, carbon-based shape memory polymer nanocomposites seem promising candidates for electrical actuators. In fact, polymer nanocomposites filled with carbon nanotubes (CNTs) have shown low electrical resistivity while fast thermal response to applied voltage. These composites can be tailored to specific actuation requests, since a desired shape recovery can be attained by printing CNTs with a specified pattern throughout the polymeric matrix [17].

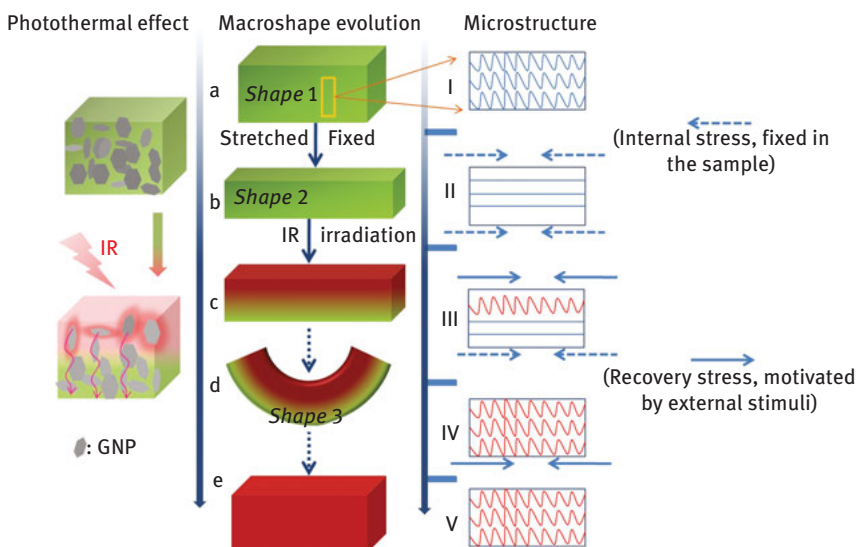


Figure 3.1: Schematic illustration of infrared radiation-actuated shape memory effect of GNP-based polymer blend. Reproduced from Ref. [16] with permission from the Royal Society of Chemistry.

Piezoelectric materials are capable of converting mechanical deformation into electricity, and vice versa [18, 19]. These materials are widely used as sensors, actuators, structural health detectors and energy generators [19–22]. Particularly, there is a growing demand of wearable sensors for monitoring physiological and biomechanical signals in sports and medical applications. However, bulky batteries are currently needed to power these sensors; therefore, smart garments generating their own power by human body motion would be highly beneficial (see Figure 3.2). This requirement can be, for instance, fulfilled by polymeric fiber-based piezoelectric generators, which are flexible and durable as well [23–25].

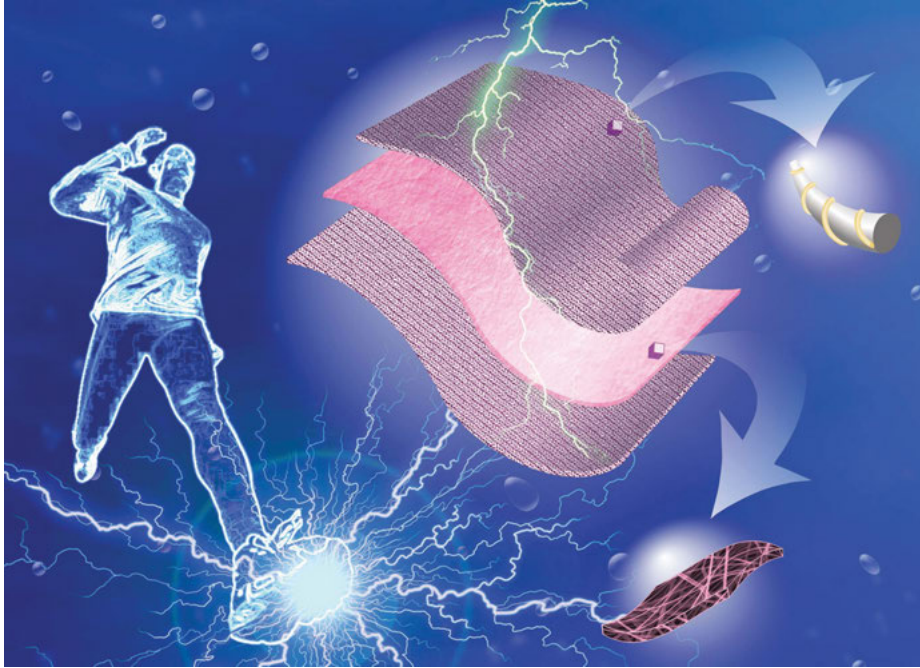


Figure 3.2: Sketch showing power generation from human movement using fiber-based piezoelectric generator. Reproduced from Refs. [23, 26] with permission from the Royal Society of Chemistry.

Zhong et al. [24] fabricated a piezoelectric fiber using cotton threads coated with CNTs and dipped into an aqueous suspension of polytetrafluoroethylene. This carbon-based polymeric piezoelectric fiber utilizes the biomechanical energy from human motion to generate electrical energy, with an average power output of $\sim 0.1 \mu\text{W}/\text{cm}^2$, which would be enough to energize wearable sensors or smart shirts (see Figure 3.3).

Photoresponsive materials show changes in their physical and chemical behavior when exposed to light. Usages of these smart materials include anticounterfeiting applications [27], chemical sensors [28], optical switches [29], flexible rewritable optical memories [30] and toys (e.g., doll whose skin get tanned under the sun [31]). The most widely used photoactive agents are azobenzene, spiropyrans, spirooxazines, diarylethenes and fulgides, which are summarily depicted in Figure 3.4.

Recently, Renuka et al. [29] developed an optical switch using multiwalled CNTs (MWCNTs) and azo-based chromophores (Figure 3.5). The electrical conduction of the composite is controlled by azo-based system, which shrinks when exposed to UV irradiation (*cis* isomer), thereby increasing the electrical conduction, because of the reduced tunneling barriers through the MWCNTs. The conduction drops down again when UV irradiation stops, because azo molecules return to their *trans* isomer configuration.



Figure 3.3: Schematic diagram of a smart shirt. Reprinted from Ref. [24] with permission from American Chemical Society.

Lately, *electroactive polymers* (EAPs) are gaining interest because of their unique property to change geometrical/structural properties in response to the application of an electric field. Due to this capability, EAPs can be employed in artificial muscles, sensors, robots, biomedical devices and energy storage systems [33, 34]. *Magneto-responsive materials*, instead, can be shaped upon the application of a magnetic field. Magneto-responsive fluids, for instance, can be used to construct dampers with adaptive response and thus enhanced suppression of vibrations. These can be fitted to buildings and bridges to mitigate the detrimental effect of strong winds or earthquakes. Among other applications, magneto-responsive materials can be used also in nanomedicine [35, 36]. Finally, *thermochromic materials* change color in response to different temperatures. They have been used, for example, in bath plugs that change their color when water is too hot.

Carbon-based polymer nanocomposites seem to be among the most promising candidates for the development of smart materials. However, significant efforts are still needed to design smart materials with specific thermal, mechanical and electrical properties. Since these properties derive by mechanisms coupled from nano- to macroscale, multiphysics simulations could support a more rational research of smart materials with tailored properties. For example, the overall piezoelectric response of carbon-based polymeric smart materials is influenced by several mechanisms, including tunneling of electrons and formation of percolating networks of carbon fillers in the polymer composite [37–39], and should therefore be addressed by linking atomistic to mesoscopic models. In the following sections, the atomistic,

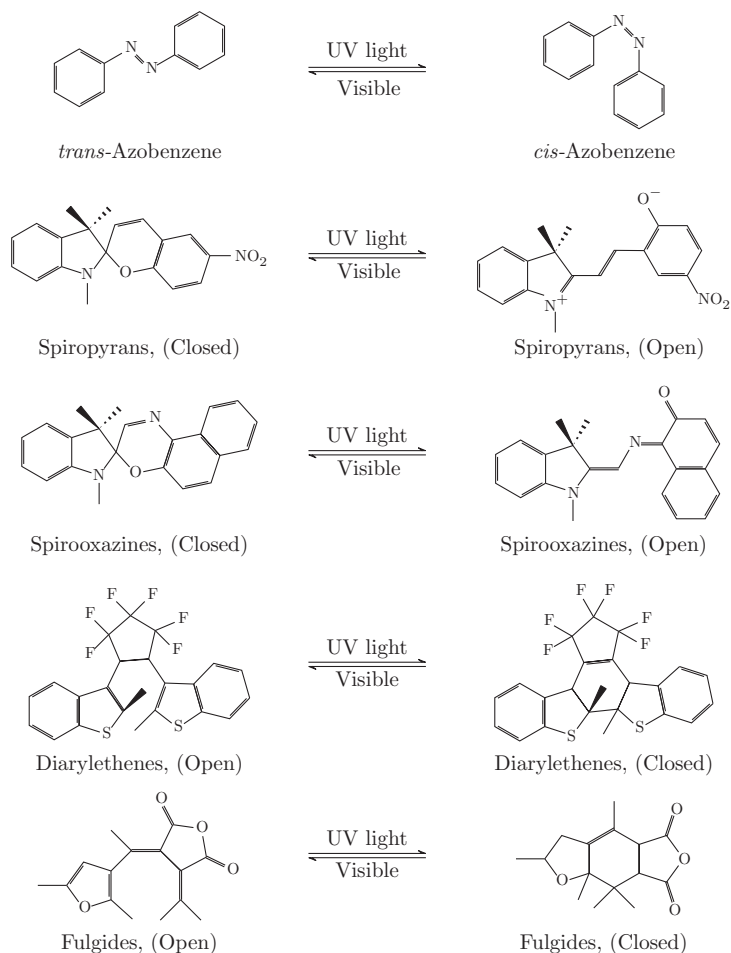


Figure 3.4: Chemical structure of photoresponsive molecules [32].

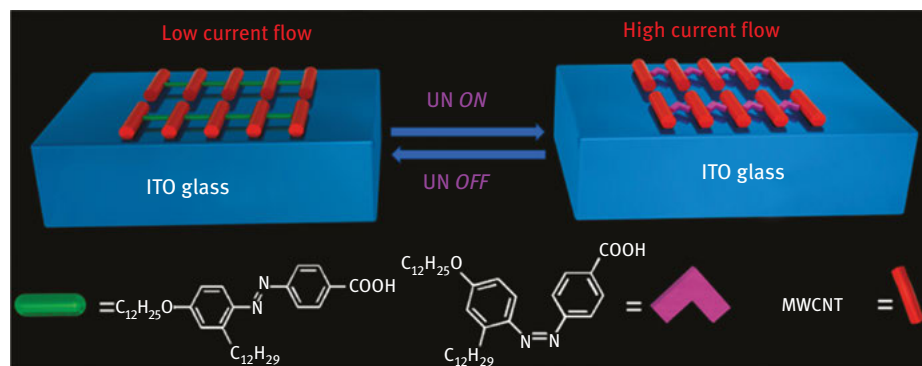


Figure 3.5: Schematic diagram of an optical switch based on MWCNT/azo composite. Reprinted from Ref. [29] with permission from American Chemical Society.

mesoscopic and macroscopic simulation tools that allow to explore the main properties of nanocomposites are extensively presented, and future perspectives of advanced modeling of carbon-based smart materials are discussed.

3.2 Multiphysics modeling

A better understanding of the thermophysical behavior of carbon-based polymer nanocomposites at different length- and timescales could ease the discovery of novel smart materials, and could be facilitated by proper material modeling approaches [40–47]. Advanced modeling approaches to the properties of nanocomposites are based on linking and/or coupling various model types that are applicable at different length- and timescales (see Figure 3.6).

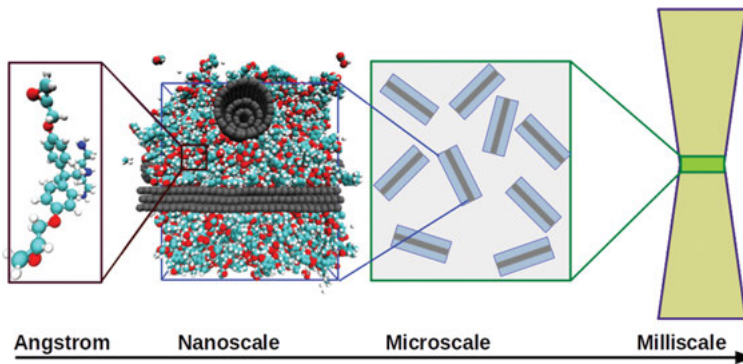


Figure 3.6: Schematic diagram of advanced modeling of polymer nanocomposite across multiple scales.

This situation is ubiquitous in many sectors, where modeling can support the effective development of advanced materials, but the heterogeneity of modeling techniques may prevent to highlight the computational synergies. For this reason, the European Commission published a Review of Materials Modelling (RoMM), now in its sixth edition [48], which provides a classification of materials modeling that enables a coherent description of model types and a standardized documentation of modeling data (called “MODA”) of materials. Furthermore, the RoMM contains several examples of MODA documentation applied to a compendium of applications from EU H2020 LEIT NMBP Materials projects. Based on the above review, the European Materials Modelling Council (EMMC, <http://www.emmc.info>) proposed a CEN Workshop Agreement about “Materials modelling – terminology, classification and metadata” [49], endorsed by more than 15 European organizations with the objective of standardization of terminology, classification and documentation of materials

modeling and simulation. Moreover, the EMMC already proposed a European Materials Modelling Ontology (EMMO) [50]. The EMMO aims at addressing the granularity levels of materials modeling (atomistic, electronic, mesoscopic and continuum), which do not really depend on the scale they are applied to. This is why multiscale modeling is somehow confusing and it would be better to talk about multiphysics modeling.

In particular, at atomistic/molecular level, molecular dynamics (MD) simulations allow understanding the behavior of the constitutive elements of nanocomposites (such as carbon fillers and polymer matrices) and, most importantly, their interaction at the interface [51]. The structural and interfacial characteristics of the constitutive elements of nanocomposites at molecular level are successively employed in coarser modeling descriptions (mesoscopic models). The mesoscopic structure of a smart composite is modeled by a representative volume element (RVE) of the material, and the properties computed at mesoscale can be finally homogenized to evaluate the effective thermophysical properties at macroscopic (continuum) level.

3.2.1 Atomistic models

Thermophysical properties of carbon-based nanocomposite materials are mainly governed by the interaction between nanofillers and surrounding matrix at molecular level. MD simulations are typically the most adequate tool to study such atomistic phenomena. In this section, the process of building the molecular geometry of nanocomposite is first discussed; then, the MD protocols for assessing thermal, mechanical and electrical properties are described, and main results from the literature are presented.

Building the atomistic setup

While the atomistic structure of carbon nanofillers (e.g., nanotubes, nanoplatelets and nanoribbons) can be conveniently generated by tools available in the literature [52–54], one of the major challenges in simulating polymer-based nanocomposites at the molecular level is to accurately describe the structure of polymeric matrix. Curing is a chemical reaction that happens between the components of thermosetting plastics (e.g., epoxy resins), namely the resin and hardener, which result in a final cross-linked (cured) structure. MD methods possess an inherent advantage over continuum approaches, since they are able to accurately simulate the mechanisms underlying curing reaction. Schulz and Frisch [55] first attempted to model curing procedure at the molecular level. They employed a lattice Monte Carlo simulation method to understand the reaction kinetics of curing process in terms of degree of polymerization and molecular weight distribution. Later works also included topological information

of polymer networks in the description of curing process, therefore allowing the simulation of thermomechanical properties of epoxy resins by MD simulations [56–64].

Protocols for simulating the curing process and creating the atomistic setup of epoxy resins can be classified into two groups: (1) single-step methods, where all the potential chemical bonds between reactive sites within a specified cut-off distance are formed at once; (2) multistep approaches, where reactive pairs within a spatial distance are cross-linked together and the resulting structure relaxed by MD, iteratively, until the desired curing degree is met. Generally, single-step approaches lead to large artificial strains in the cured structure; whereas, multistep methods – even though they are more computationally expensive – provide structures closer to real curing reactions, since they operate through intermediate MD relaxations.

Jang et al. [64] compared the performance of these two approaches on a system consisting of bisphenol A diglycidyl ether (DGEBA) epoxy and poly(oxypropylene) diamine (POP) curing agent. In the single-step method, a Monte Carlo algorithm was adopted to allocate cross-linking bonds. For the multistep algorithm, an initial cut-off radius of 10 Å was assigned, and covalent bonds between all pairs of potentially reactive atoms within the cut-off radius generated. After that, the partially cured system was relaxed in the NPT and NVE ensembles, respectively. In addition, the partial charges of atoms were adjusted to neutralize the net charge in the system. Finally, in the case that no reactive pairs remained within the current cut-off radius, the reaction cut-off radius was increased iteratively. The thermal (thermal expansion, heat capacity and glass transition temperature), structural (dihedral angle distributions, radial distribution functions, minimum inter-nitrogen contour length distributions and fragment molecular weight distribution) and mechanical (Young's modulus) properties of the systems cured by either single- or multistep approach were then compared. Results showed that the fragment molecular weight distribution was different in the two cases, since fewer and larger fragments were obtained with the single-step approach; nevertheless, the other properties had no significant dependency on the choice of cross-linking method.

Thermal properties

Thermal conductivity

The thermal conductivity (λ) of nanostructured materials can be estimated by either equilibrium MD (EMD) or nonequilibrium MD (NEMD) simulations. It is noteworthy to mention that EMD simulations are best to study homogeneous systems, whereas NEMD techniques are more suitable for heterogeneous systems [65]. Green-Kubo formulation underlies EMD simulations, since it relates λ with the fluctuations of thermal current via the fluctuation-dissipation theorem [66, 67]:

$$\lambda = \frac{1}{Vk_B T^2} \int_0^\infty \langle \mathbf{J}(t)\mathbf{J}(0) \rangle dt, \quad (3.1)$$

where k_B is the Boltzmann constant, T and V are the temperature and volume of the system, respectively. In addition, $\mathbf{J}(t)$ is the heat current vector at time t and $\langle \mathbf{J}(t)\mathbf{J}(0) \rangle$ is the heat current autocorrelation function. In terms of MD entities, the heat current vector is commonly defined as

$$\mathbf{J}(t) = \frac{d}{dt} \sum_{i=1}^N E_i \mathbf{r}_i, \quad (3.2)$$

being \mathbf{r}_i and E_i the position and total energy of atom i , respectively. E_i can be computed by summing up kinetic and potential energies of the atom, namely

$$E_i = \frac{1}{2} m_i |\mathbf{v}_i|^2 + \frac{1}{2} \sum_{j \neq i}^N U_p(r_{ij}), \quad (3.3)$$

where m_i and \mathbf{v}_i indicate mass and velocity of atom i , respectively. $U_p(r_{ij})$ is the total potential energy of atom i , which depends on the type of bonded and non-bonded interaction potentials used in the simulations and r_{ij} is the distance between atoms i and j .

For example, Kumar et al. [68] used EMD to study the correlation between λ of cross-linked epoxies (DGEBA resin, 4,4'-diaminodiphenyl sulfone - DDS hardener) and temperature. Results demonstrate that the inclusion of long-range Coulomb interaction corrections leads to a better agreement between modeling and experimental results. Sirk et al. [69], instead, employed MD simulations to study the effect of epoxy composition on its thermal, structural and volumetric properties. Different cross-linked networks including DGEBA resin and various mixtures of flexible (POP) and stiff (MCA, 4,4'-Methylenebis(cyclohexylamine)) curing agents were built. They found out that the flexibility of cross-linker has considerable impact on the thermal and volumetric characteristics of the cross-linked network, especially at temperatures close to glass transition. Fasanella and Sundararaghavan [70] adopted the EMD approach to study the effect of temperature and functionalization on λ of DGEBA + DDS epoxy, possibly reinforced by single-walled CNTs (SWCNTs). In particular, the thermal conductivity was computed both perpendicularly and along the main axis of the nanotube. Results showed that, for what concerns the direction perpendicular to the CNT axis, the λ of pristine SWCNT/epoxy nanocomposites is lower than the neat epoxy one, whereas an improved thermal performance is shown for functionalized SWCNT/epoxy nanocomposites (see Figure 3.7). In addition, a significant enhancement in the λ along nanotube axis has been observed in the case of pristine SWCNT/epoxy in comparison to both neat epoxy and functionalized SWCNT/epoxy nanocomposite (see the inset in Figure 3.7).

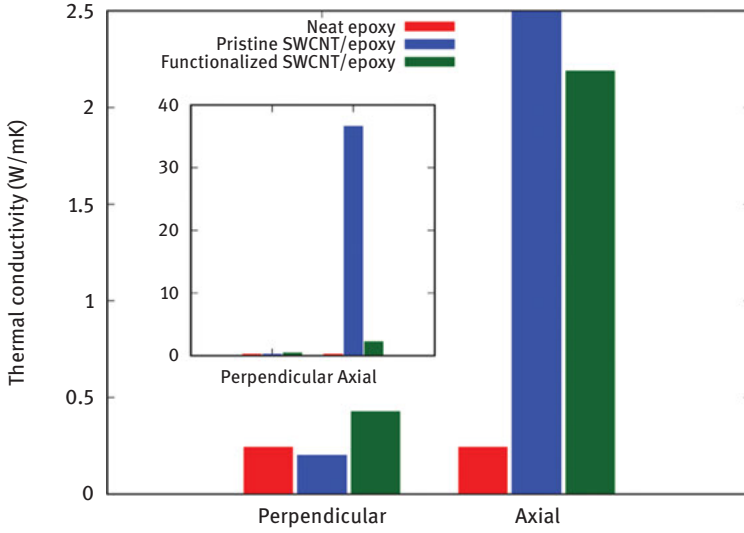


Figure 3.7: Average thermal conductivity in the temperature range of 220–420 K in the perpendicular and axial directions with respect to the nanotube axis for different simulated nanocomposites. Adapted with permission from Springer Nature [70].

NEMD methods for computing thermal conductivity of nanostructured materials are based on Fourier’s law. For example, the thermal conductivity of an isotropic system with temperature gradient along z direction can be found as [71]

$$\lambda_z = -\frac{q_z}{dT/dz}, \quad (3.4)$$

where $q_z = Q_z/A$ is the specific heat flux, namely, the heat flux Q_z transferred through the surface A along the direction z . In addition, dT/dz is the steady-state temperature gradient along z -axis. The temperature profile throughout the simulation domain can be computed after dividing the box into N slabs (depending on the system size) along the desired direction. Equation (3.4) can be exploited in nonequilibrium simulations to compute λ according to two possible approaches.

The first approach is typically called NEMD (see an example in Figure 3.8), where a temperature gradient is imposed across the extremities of computational system. This is achieved by a proper design of regions with either high (red atoms in Figure 3.8) or low (blue atoms in Figure 3.8) controlled temperature. To sustain the temperature gradient during the simulation, energy is constantly supplied and extracted from the high- and the low-temperature regions by thermostats, respectively. Such addition or extraction of energy in the hot or cold regions is generally carried out by modifying the kinetic energy of atoms through a velocity rescaling procedure. The instantaneous local kinetic temperature (T_i) in each slab can be computed as

$$T_i = \frac{1}{3N_i k_B} \sum_{k=1}^{N_i} m_k |\mathbf{v}_k|^2, \quad (3.5)$$

where N_i is the number of atoms in the i th slab and m_k the mass of the k th atom. The energy exchange between hot and cold regions at steady state causes a specific thermal flux (q_z) through the system, which can be calculated as

$$q_z = \frac{Q_z}{2A} = \frac{1}{2A\Delta t} \left\langle \frac{1}{2} \sum_{k=1}^{N_B} m_k (|\mathbf{v}'_k|^2 - |\mathbf{v}_k|^2) \right\rangle, \quad (3.6)$$

where N_B is the number of atoms in the thermostated region. Besides, \mathbf{v}_k and \mathbf{v}'_k represent the atomic velocities in the thermostated regions (hot or cold regions) before and after rescaling, respectively. Note that, in the considered geometry (Figure 3.8), the heat flux in eq. (3.6) is divided by 2 due to the symmetrical simulation box.

The second approach is named as reverse NEMD (RNEMD), and it was originally conceived by Müller-Plathe [72]. The main difference between RNEMD and NEMD methods is that the former generates nonequilibrium conditions through the computational domain by fixing heat flux (which gives rise to temperature gradient), while the latter by fixing the temperature gradient (which gives rise to heat flux). In case of RNEMD, the heat flux is induced by interchanging the atomic velocities between hot and cold regions. In the hot region, the coldest atom is selected and its velocity (v_{cold} , red region in Figure 3.8) is exchanged with the velocity of hottest

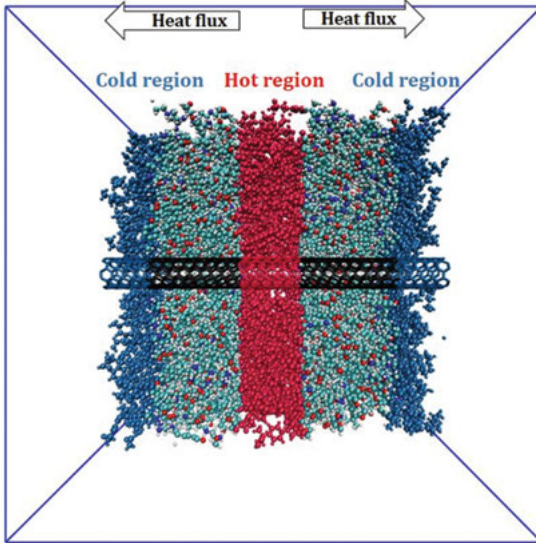


Figure 3.8: Specification of hot and cold baths for computing the thermal conductivity of a carbon-based nanocomposite by NEMD simulations.

atom in the cold region (v_{hot} , blue regions in Figure 3.8). This process eventually leads to an artificial specific heat flux (q_z) flowing from cold to hot regions. All velocity interchange procedure (i.e., *transfers*) follows the total energy conservation law; therefore, at steady state, equal amount of energy per area and time is induced from hot to cold regions via heat conduction, namely

$$q_z = \frac{1}{2A\Delta t} \sum_{\text{transfers}} \frac{m}{2} (|v_{\text{hot}}|^2 - |v_{\text{cold}}|^2). \quad (3.7)$$

The most significant advantage of RNEMD over classical NEMD is the fact that heat flux, which is a slowly converging quantity with respect to temperature, is fixed from the beginning of simulation. Therefore, in general, RNEMD approaches provide faster convergence of λ computation with respect to classical NEMD ones.

Interestingly, Varshney et al. [73] evaluated the thermal conductivity of a cross-linked network of EPON-862 and curing agent W (diethyltoluenediamine, DETDA) using both EMD and NEMD approaches. In the case of EMD, a cubic simulation box ($53.6 \times 53.6 \times 53.6 \text{ \AA}^3$) was employed; in the case of NEMD, a thin slab with large aspect ratio along the heat flow direction ($21.4 \times 21.4 \times 373.3 \text{ \AA}^3$) was considered instead. The results obtained by both methods were in good agreement with experiments, even though EMD led to a slight overestimation of λ . Mortazavi et al. [74] employed NEMD to estimate the thermal conduction in graphene-reinforced nanocomposites. In their study, epoxy consisted of DGEBA resin and DETA (diethylenetriamine) or DDS curing agents. They found that the thermal conductivity of a single-layer graphene immersed in the epoxy matrix at atmospheric pressure and room temperature decreases by around 30% with respect to the value of pristine graphene, while the type of hardener has no considerable effect. Furthermore, they also investigated the impact of pressure and epoxy-graphene covalent bonds on λ of graphene: no significant change in the λ of graphene was observed by increasing the pressure up to 14 GPa, while the formation of 5% covalent bonds led to 65% reduction in the thermal conductivity of graphene. Clearly, such methodologies can be successfully adopted in a large variety of polymeric matrices: for example, Alaghemandi et al. [75] used RNEMD to investigate the λ of SWCNT–polyamide (PA) nanocomposites along both parallel and perpendicular directions with respect to the nanotube axis, finding a good agreement with experiments [76, 77].

Thermal boundary resistance

The thermal boundary resistance, also known as Kapitza resistance or interfacial thermal resistance (R_k) [78], at filler–filler and filler–matrix interfaces is one of the most significant bottlenecks in the overall thermal conduction through polymer nanocomposites [79, 80]. This thermal resistance arises mainly from the weak van der Waals interactions between adjacent fillers, and between fillers and the surrounding matrix.

Such weak interactions considerably hinder the specific heat flux (q) across the interface due to phonon scattering, which in turn results in a localized interfacial temperature jump (ΔT). The inverse of thermal boundary resistance, also known as thermal boundary conductance, $G_k = 1/R_k$, is defined as

$$G_k = \frac{q}{\Delta T}. \quad (3.8)$$

MD simulations are typically used to investigate thermal boundary resistance, since it arises from atomistic details of interfaces. Generally, two NEMD approaches have been used in the literature to study interfacial thermal properties of nanocomposites [81].

In the first approach, the simulated system is divided into multiple slabs according to the geometrical characteristics of the box. On the one side, a constant heat flux is added to the atoms of nanofiller (heat source); on the other side, a constant heat flux is removed from the outermost region of the computational domain occupied by the matrix (heat sink). This thermal power could be extracted or introduced by means of a velocity rescaling procedure, which must conserve the total linear momentum of the system. As an example, this method was adopted to compute the thermal boundary resistance between the CNT and octane liquid depicted in Figure 3.9. In those simulations [81], the continuous addition (CNT) and extraction (outermost region occupied by octane) of a constant heat flux leads to a steady-state temperature profile throughout the system, where the average temperature in each

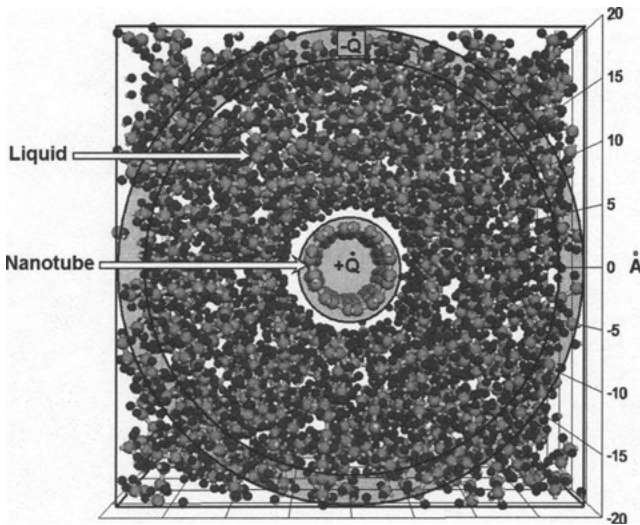


Figure 3.9: Schematic of division of carbon nanotube/octane system into concentric cylindrical slabs to investigate thermal interfacial effects. Reprinted from Ref. [81] with the permission of AIP Publishing.

slab can be computed by eq. (3.5). An example of temperature profile measured in this system is shown in Figure 3.10: the average temperature of the CNT is around 575 K, while the liquid temperature ranges from 320 K (close to the CNT surface) down to 300 K (heat sink). The significant temperature drop at the nanotube–octane interface proves the existence of Kapitza resistance, which is then computed by eq. (3.8) since both q and ΔT can be extracted from simulations.

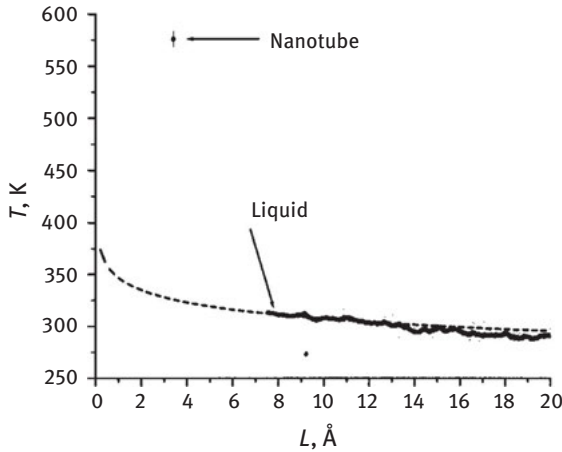


Figure 3.10: Relation between the temperature gradient and distance from the center of CNT at constant heat flow (see configuration in Figure 3.9). Reprinted from Ref. [81] with the permission of AIP Publishing.

In the second approach, the whole system is first equilibrated at the initial temperature $T(0)$; after that, the filler is heated up to a predetermined temperature $T_f(0) = T(0) + \Delta T(0)$, while the matrix temperature is kept constant at the $T_m(t) = T(0)$ value. Such a temperature gradient can be determined by a proper distribution of thermostats in the computational domain. The system is then allowed to relax without any heat source or sink. As depicted in Figure 3.11, the temperature difference between the filler and the surrounding matrix ($\Delta T(t) = T_f(t) - T_m(t)$) tends to decay exponentially with time according to the Newton's law of cooling, namely

$$\Delta T(t) = \Delta T(0) \exp\left(-\frac{t}{\tau}\right). \quad (3.9)$$

If the conduction resistance of the filler is considerably lower than the matrix one (which is typically the case of carbon nanofillers), the characteristic decay time (τ) can be related to the area of filler–matrix interface (A_{int}), the filler heat capacity (c) and the (R_k) at filler–matrix interface as [82]

$$R_k = \frac{A_{int}\tau}{c}. \quad (3.10)$$

Due to the paramount importance of heat transfer across nanoscale interfaces on the effective thermal properties of nanocomposites, several researches have used MD simulations to achieve a mechanistic understanding of the parameters that could affect thermal boundary resistance, such as curing degree of polymeric matrix, surface functionalization of fillers and presence of covalent or noncovalent bonds between fillers and the surrounding matrix [83–100].

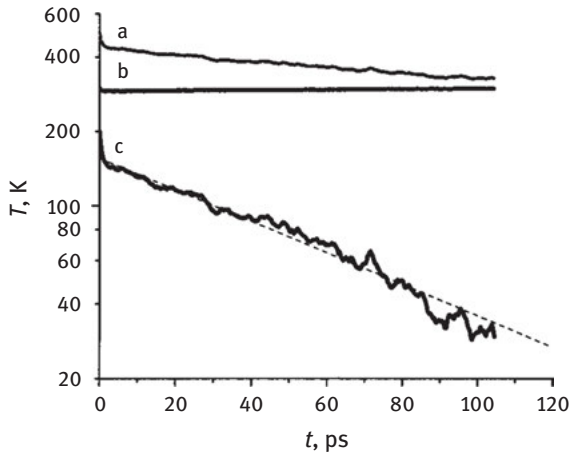


Figure 3.11: Instantaneously heated nanotube at a desired temperature is allowed to relax without heat source or sink, then (a) the temperature of the CNT, (b) liquid temperature and (c) difference between the temperature of CNT and liquid as a function of time are shown (see configuration in Figure 3.9). Reprinted from Ref. [81] with the permission of AIP Publishing.

As an example, Varshney et al. [83] analyzed by MD simulations a nanocomposite made of epoxy polymer (EPON-862/DETDA) reinforced with SWCNTs. They reported a 20% enhancement in the G_k at filler–matrix interface by increasing the curing degree of epoxy. Such behavior was explained by the increased structural rigidity and non-bonded interactions of the cured epoxies, since the curing process generates a denser matrix structure. Huang et al. [94], instead, investigated the impact of covalent bonds (cross-links) between SWCNT and PEK (poly ether ketone) on the thermal boundary conductance at their interface. Considering a simulation domain similar to the one in Figure 3.9, the number of cross-links between SWCNT and PEK was changed in the range 0–80 (0% – 6.25% functionalization degree), and the G_k was then computed in each case. Results in Figure 3.12 show that the temperature jump at CNT–PEK interface decreases with the number of cross-links; thus, G_k increases from 23.58 (no cross-links) to 236.44 MW/m² K (80 cross-links). Finally, Wang et al. [89] employed RNEMD to determine how different surface functionalizations of graphene could affect the

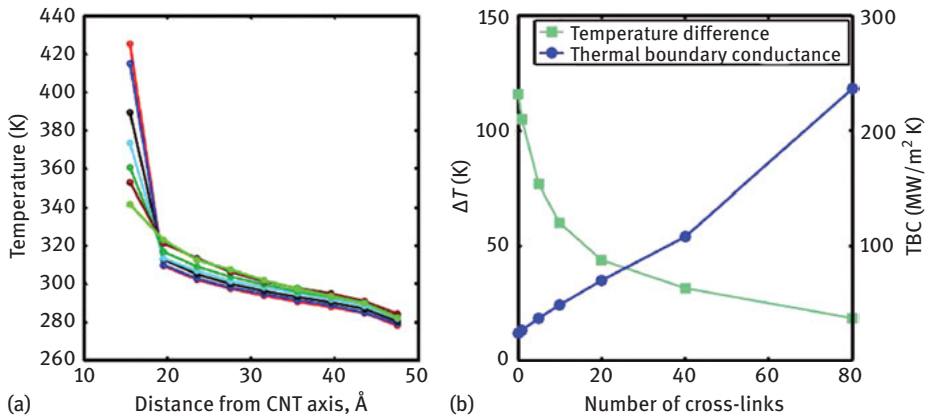


Figure 3.12: (a) Radial temperature distribution in the system under steady-state condition for seven simulated cases: no cross-links (red, 0%), 1 cross-link (blue, 0.08%), 5 cross-links (black, 0.39%), 10 cross-links (cyan, 0.78%), 20 cross-links (dark green, 1.56%), 40 cross-links (brown, 3.12%) and 80 cross-links (green, 6.25%). (b) Temperature difference and thermal boundary conductance at the CNT-PEK interface for different studied cases. Reprinted from Ref. [94] with the permission of AIP Publishing.

interfacial thermal resistance at graphene-polymer interface. To this aim, various types of covalent (butyl, carboxyl and hydroxyl) and noncovalent (1-pyrenebutyl, 1-pyrenebutyric acid and 1-pyrenebutylamine) functional groups were considered at different coverages, namely, the ratio between the number of functional groups to the total number of carbon atoms in the graphene sheet. Furthermore, the effect of isotope doping and acetylenic linkage in graphene was also assessed. Simulation results for covalent and noncovalent functionalizations are reported in Figures 3.13 and 3.14, respectively. It is noteworthy to mention that the thermal boundary resistance values in these figures are normalized using the value of R_k in the case of no functionalization on graphene, that is, $R_{k0} = (0.713 \pm 0.036) \times 10^{-8} \text{ m}^2 \text{ K/W}$. While both increasing covalent and noncovalent functionalizations led to R_k decrease, no significant effects were instead observed with isotope doping or acetylenic linkages in the graphene filler [89].

Mechanical properties

MD simulations are also useful to compute mechanical properties of composite materials, such as the elastic moduli and the whole stress-strain response of a nanometric specimen [101, 102]. Discrepancies between MD and experimental results may be due to the faster strain rate simulated, the effect of dislocations at higher scales, the local high variability of temperature and the possible unwanted residual stresses from cross-link process [103].

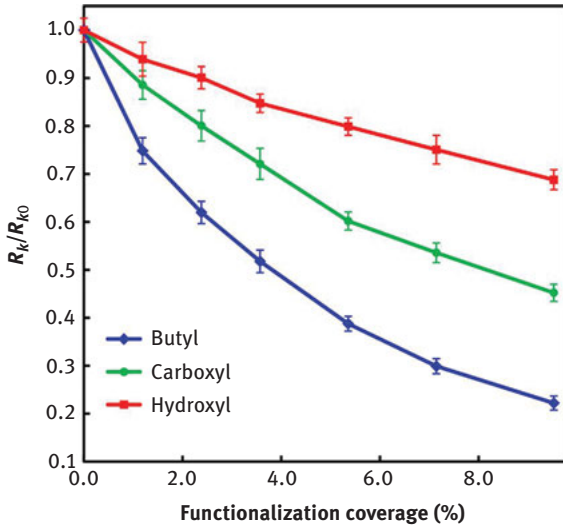


Figure 3.13: Dependence of the relative thermal boundary resistance on coverage percentage of different covalent functional molecules. Reprinted from Ref. [89] with the permission of American Chemical Society.

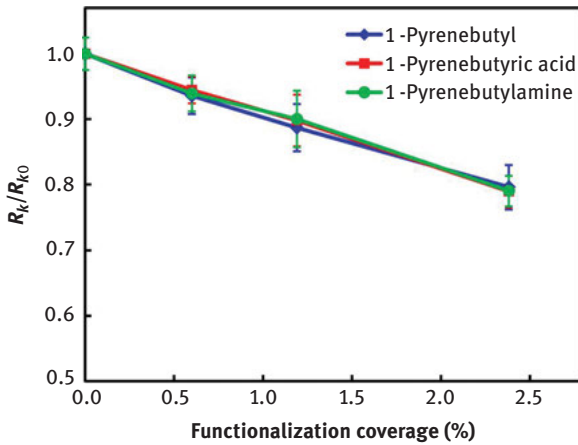


Figure 3.14: Dependence of the relative thermal boundary resistance on coverage percentage of different noncovalent functional molecules. Reprinted from Ref. [89] with the permission of American Chemical Society.

In general, the elastic properties of a material along one specific direction can be quantified by the Young's modulus (E_m) as

$$\sigma = E_m \varepsilon, \quad (3.11)$$

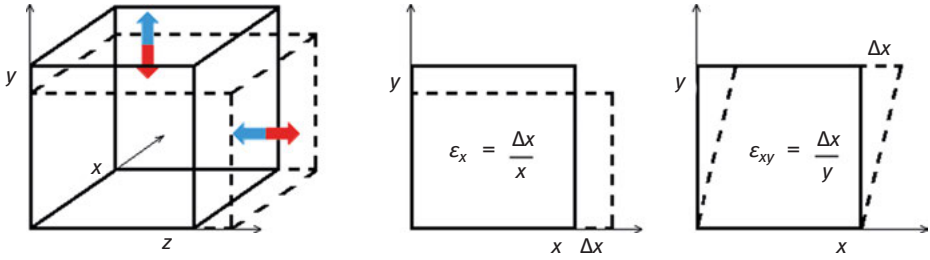


Figure 3.15: Longitudinal and shear deformation of a simple volume of material.

where the stress (σ) is a measure of the average force applied over an equivalent area (F/A), and the strain (ε) is the ratio of deformation with respect to the initial length (see Figure 3.15). Such relation can be generalized to three-dimensional space to relate all the components of the stress and strain tensors (generalized Hooke's law):

$$\sigma_{ij} = C'_{ijkl} \varepsilon_{kl}, \quad (3.12)$$

where C'_{ijkl} are the components of the fourth-order stiffness tensor of the considered material. Note that the C' tensor is symmetric ($\sigma_{ij} = \sigma_{ji}$ and thus $C'_{ijkl} = C'_{jikl}$, similarly for the strain tensor), and that the Voigt's notation [104] is typically adopted to simplify eq. (3.12):

$$\sigma_i = C'_{ij} \varepsilon_j, \quad (3.13)$$

with $i, j = 1, 2, \dots, 6$. Therefore, for any linearly elastic material, the stiffness matrix can be written as

$$C' = \begin{bmatrix} C'_{11} & C'_{12} & C'_{13} & C'_{14} & C'_{15} & C'_{16} \\ C'_{21} & C'_{22} & C'_{23} & C'_{24} & C'_{25} & C'_{26} \\ C'_{31} & C'_{32} & C'_{33} & C'_{34} & C'_{35} & C'_{36} \\ C'_{41} & C'_{42} & C'_{43} & C'_{44} & C'_{45} & C'_{46} \\ C'_{51} & C'_{52} & C'_{53} & C'_{54} & C'_{55} & C'_{56} \\ C'_{61} & C'_{62} & C'_{63} & C'_{64} & C'_{65} & C'_{66} \end{bmatrix} \quad (3.14)$$

MD simulations can be used to apply a deformation $\varepsilon = [\varepsilon_{11} \ \varepsilon_{22} \ \varepsilon_{33} \ 2\varepsilon_{23} \ 2\varepsilon_{13} \ 2\varepsilon_{12}] = [\varepsilon_1 \ \varepsilon_2 \ \varepsilon_3 \ \varepsilon_4 \ \varepsilon_5 \ \varepsilon_6]$ to a representative unit cell of the material under investigation, and then to measure the respective residual stress in each direction [105]. Given these values, eq. (3.13) allows then to obtain the 6×6 elastic stiffness matrix (C') of the simulated material.

The expression of C' is simpler in materials characterized by symmetry, since some of its coefficients are equal to zero. For example, the elastic stiffness tensor of orthotropic materials can be reduced to

$$C' = \begin{bmatrix} C'_{11} & C'_{12} & C'_{13} & 0 & 0 & 0 \\ C'_{21} & C'_{22} & C'_{23} & 0 & 0 & 0 \\ C'_{31} & C'_{32} & C'_{33} & 0 & 0 & 0 \\ 0 & 0 & 0 & C'_{44} & 0 & 0 \\ 0 & 0 & 0 & 0 & C'_{55} & 0 \\ 0 & 0 & 0 & 0 & 0 & C'_{66} \end{bmatrix} \quad (3.15)$$

namely to nine different stiffness coefficients ($C'_{12} = C'_{21}$, $C'_{13} = C'_{31}$, $C'_{23} = C'_{32}$). Instead, the elastic properties of homogeneous isotropic linear elastic materials are determined by two moduli only, namely λ_m and μ_m :

$$\mu_m = \frac{1}{3}(C'_{44} + C'_{55} + C'_{66}) \quad (3.16)$$

and

$$\lambda_m = \frac{1}{3}(C'_{11} + C'_{22} + C'_{33}) - \frac{2}{3}(C'_{44} + C'_{55} + C'_{66}), \quad (3.17)$$

and thus

$$\lambda_m + 2\mu_m = \frac{1}{3}(C'_{11} + C'_{22} + C'_{33}).$$

In this case, the elastic stiffness tensor simplifies to [103]

$$C' = \begin{bmatrix} \lambda_m + 2\mu_m & \lambda_m & \lambda_m & 0 & 0 & 0 \\ \lambda_m & \lambda_m + 2\mu_m & \lambda_m & 0 & 0 & 0 \\ \lambda_m & \lambda_m & \lambda_m + 2\mu_m & 0 & 0 & 0 \\ 0 & 0 & 0 & \mu_m & 0 & 0 \\ 0 & 0 & 0 & 0 & \mu_m & 0 \\ 0 & 0 & 0 & 0 & 0 & \mu_m \end{bmatrix} \quad (3.18)$$

Once λ_m and μ_m are determined, the following relations for homogeneous isotropic linear elastic materials hold:

$$G_m = \mu_m \quad (3.19)$$

$$K_m = \lambda_m + \frac{2}{3}\mu_m \quad (3.20)$$

$$\nu = \frac{\lambda_m}{2(\lambda_m + \mu_m)} \quad (3.21)$$

$$E_m = \mu_m \frac{3\lambda_m + 2\mu_m}{\lambda_m + \mu_m}, \quad (3.22)$$

where G_m is the shear modulus, which regards forces parallel to one surface of the material; K_m is the bulk modulus, which regards the isobaric compression of the material; ν is the Poisson's ratio, which relates the expansion of the material in one direction while it is compressed in another; E_m represents the Young's modulus, which is a measure of the linear elastic stiffness of the material.

MD can be also used to mimic the experimental tensile test of nanomaterials. Typically, the system is first equilibrated; then, a small strain is applied along one longitudinal direction of the computational box with a ramped function of time (see Figure 3.16), and the resulting strain measured [106, 107].



Figure 3.16: Longitudinal deformation of a simulation box.

Electrical properties

Polymeric materials are typically characterized by very low (or no) electrical conductivity; however, the insertion of carbon fillers – such as graphene sheets, CNTs or carbon fibers (CFs) – can improve the electrical properties of the resulting polymer nanocomposites.

A limited volume fraction of CFs has been observed to significantly improve electrical conductivity of polymer nanocomposites [108, 109]. This is due to the formation of continuous conductive networks of CFs in the polymer matrix, thus allowing a transition from nonconductive to conductive electrical properties. The percolation threshold is the critical volume fraction of conductive fillers in the nanocomposite above which conductive pathways in the system always occur. This threshold determines the transition from electrical insulating to conducting behavior, and it is therefore the crucial figure of merit to understand the electrical features of nanocomposites. Furthermore, researchers have reported that the conductive behavior of nanocomposites depends on the spatial distribution of CFs as well. On the one hand, high volume fractions of fibers poorly dispersed in the polymer matrix may lead to fiber agglomeration, which possibly results in electrical conductivity enhancement (but degraded mechanical properties). On the other hand, spatially uniform

distributions of fibers at low volume fractions are unfavorable for the electrical conductance of nanocomposites.

Molecular simulation is an efficient tool to study the electrical properties and percolation mechanism in nanocomposites, since it allows determining whether CFs are forming conductive networks within the polymeric matrix or not. According to the electric tunneling theory, two carbon fillers can be considered as electrically connected to each other if their shortest distance is less than a critical gap, which is known as tunneling distance. The electrical resistance offered by the thin (i.e., less than the tunneling distance) insulating polymer matrix between the conductive fibers is therefore known as tunneling resistance.

The generalized formula for electric tunnel effect through a potential barrier between electrodes separated by a thin insulating film was derived by Simmons in 1963 [110]. Hence, if the thickness of insulating film between the conductive fibers is treated as uniform, the curvature of fibers is neglected, the potential barrier is taken as rectangular and the image forces are included, the current density (j , considered in A/cm^2) flowing through the thin film of polymer matrix between the fibers is given as [110]

$$j = \frac{6.2 \times 10^{10}}{\Delta s^2} [\phi \exp(-1.025 \Delta s \phi^{1/2}) - (\phi + U) \exp(-1.025 \Delta s (\phi + U)^{1/2})], \quad (3.23)$$

where

$$\phi = \phi_0 - (U/2s)(s_1 + s_2) - \frac{5.75}{\kappa \Delta s} \ln \frac{s_2(s - s_1)}{s_1(s - s_2)}, \quad (3.24)$$

s is the thickness of the insulating polymer film (in Å), $\Delta s = (s_2 - s_1)$ is the difference of the limits of barrier at Fermi level (in Å), κ is the dielectric constant of insulating polymer film, U is the voltage across the insulating polymer film (in V) and ϕ_0 is the height of potential barrier (or work function) (in V). If $U < \phi_0$, then

$$s_1 = 6/\kappa\phi_0$$

$$s_2 = s[1 - 46/(3\phi_0\kappa s + 20 - 2U\kappa s)] + 6/\kappa\phi_0. \quad (3.25)$$

Moreover, the voltage across the insulating polymer film can be calculated as

$$U = e/C = \frac{es}{A_c \kappa \epsilon_0}, \quad (3.26)$$

where e , C , A_c and ϵ_0 are electron charge, capacitance, area of the insulating film in contact and permittivity of free space, respectively. The electric tunneling resistance can be finally computed as

$$R_{tunnel} = \frac{U}{j A_c}. \quad (3.27)$$

Li et al. [111] performed Monte Carlo simulations to understand the effect of tunneling resistance between CNTs on the electrical conductivity of the whole polymer nanocomposite. Their results indicate that the tunneling resistance increases with the thickness of insulating polymer film (see Figure 3.17). They also reported that the conductivity of nanocomposites drops below 10^{-12} S/m, namely the nanocomposite behaves as an electrical insulator, when the tunneling resistance is larger than 10^{19} Ω . The thickness of polymeric film corresponding to this Ω value is found to be 1.8 nm, which is then considered as the maximum tunneling distance.

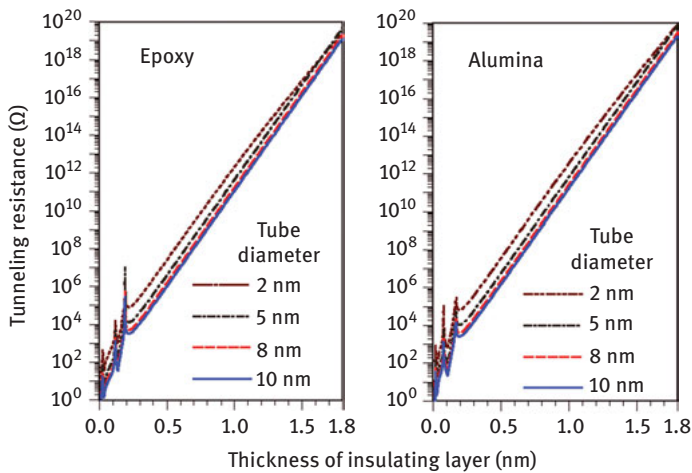


Figure 3.17: Tunneling resistance as a function of the thickness of insulating polymer film between carbon nanotube fillers in a nanocomposite. Different diameters of nanotubes and matrix materials are reported. Reprinted from Ref. [111] with the permission of AIP Publishing.

Hu et al. [112] studied the effect of CNT aspect ratio on the electrical properties of nanocomposites by means of three-dimensional statistical percolation modeling. They reported that the higher aspect ratio of CNTs leads to larger aggregates of fillers in the nanocomposite, which ease the creation of paths with high electrical conductivity. As a result, both lower percolation threshold and higher electrical conductivity of nanocomposites are reported for larger aspect ratio of fillers [112]. Furthermore, the electrical percolation threshold is found to be significantly influenced by the intertube van der Waals interaction and tunneling resistance for nanocomposites with low CNT aspect ratio (i.e., length/diameter ratio <200), whereas negligible effects are observed with high aspect ratio [113].

Researchers agree that the tunneling resistance, which shows values several orders of magnitude larger than the intrinsic resistance of carbon fillers, plays a dominating

role in controlling the electrical behavior of nanocomposites [111–114]. Thus, to enhance computational efficiency and simulate larger domains, the intrinsic resistance of nanofillers is often neglected in simulations of nanocomposites with well-dispersed fillers [114].

3.2.2 Mesoscopic models

Thermal properties

The most popular approaches to study effective thermal properties of composites at mesoscale are off-lattice Monte Carlo, dissipative particle dynamics (DPD) and lattice Boltzmann method (LBM).

Duong and coworkers [115] developed an off-lattice Monte Carlo simulation approach to investigate the effective thermal conductivity (λ_{eff}) of CNT-reinforced nanocomposites, taking into account also the thermal boundary resistance (R_k) at CNT–matrix interface. In their model, heat transfer comes from the random motion of a large number of discrete thermal walkers. The proposed model has been widely utilized to investigate the impact of fibers distribution, morphology, volume fraction as well as R_k value at fiber–matrix interface on the λ_{eff} of nanocomposites [116–119], nanofluids [120, 121] and aerogels [122] based on CNTs, with a good capability to reproduce experiments. Kui et al. [123] modified Duong’s model to evaluate the thermal properties of composite materials reinforced by graphene sheets. Later, Gong et al. [124–127] extended the initial model to evaluate the thermal conductivity of multiphase composite materials as well. As an example, they studied the λ_{eff} of a polymer composite consisting of polyether ether ketone (PEEK) matrix reinforced by SWCNT fibers and tungsten disulfide (WS_2) nanoparticles [125]. They explored the impact of interfacial thermal resistance at CNT–PEEK and WS_2 –PEEK interfaces, CNT morphology (i.e., diameter and aspect ratio of SWCNTs) and SWCNT orientation (i.e., random, parallel or perpendicular to heat flux) on the effective thermal conductivity of composites. According to their findings, λ_{eff} increases with SWCNT concentration, while it decreases with larger Kapitza resistances at the different interfaces. Regarding SWCNT orientation, fibers parallel and perpendicular to the heat flux direction show the best and the worst effect on the overall thermal performance, respectively. They also reported that SWCNTs with higher aspect ratio and smaller diameter generate higher thermal conductivity enhancements at given mass fraction of fillers.

In DPD, the simulated particles (beads) represent whole molecules or fluid regions [128]. For instance, Zhou et al. [129] coupled DPD and smoothed particle hydrodynamics (SPH) to study, at mesoscopic level, the λ_{eff} of polymer composites reinforced by CNTs. This numerical model was used to investigate the impact of different parameters, such as filler dispersion, volume fraction, length and matrix

characteristics, on λ_{eff} of nanocomposites. Their results show that λ_{eff} changes quadratically with the volume fraction of fillers, with both random and aligned distributions of fibers.

LBM is another method that can be used to study the thermal properties of composite materials at mesoscopic level. The most significant advantage of LBM is the easy implementation of different interparticle interactions and complex boundary conditions [130]. Wang and coworkers [131] developed a three-dimensional LBM model to calculate the thermal conductivity of composites reinforced by CFs, in good agreement with experimental evidence. Chiavazzo and Asinari [132], instead, computed through LBM the λ_{eff} of composites made of polypropylene polymer (matrix) and graphite particles (fillers). Fang et al. proposed a multiple relaxation time LBM to predict numerically the λ_{eff} of anisotropic heterogeneous materials, such as polymers reinforced by braiding yarns [133]. The model has been afterward applied to compute longitudinal and perpendicular λ_{eff} of computational domains with different volume fractions of fillers, considering the interfacial thermal resistance between components as well.

Mechanical properties

Atomistic simulation methods are well established for computing the interfacial properties of polymer composites at the molecular level (nanoscale). However, the considerable computational resources required limit the maximum length- and timescale of feasible simulations [134, 135]. While sophisticated strategies for speeding up complex MD simulations of systems that undergo significant configuration changes have been recently suggested on the basis of the equation-free method [136, 137], coarse-grained (CG) models have been specifically developed to simulate polymers [138–140] and carbon fillers (CNTs and graphene) [141, 142].

CG MD overcomes the complexity of atomistic simulations by reducing the degrees of freedom of particle–particle interactions, so that larger length- and timescales (from nanoscale to mesoscale) can be afforded [138, 143]. For the development of CG molecular models, chemically connected atoms are grouped together to form superatoms or CG beads that contain sufficient information to reproduce the chemical features of the molecular structure (see, for instance, Figure 3.18) [139]. Moreover, several methods have been proposed to parametrize the force field among CG beads starting from their respective atomistic details [134, 138, 139]. Arash et al. [143, 144] developed a CG model of CNT/polymer systems, with the aim to compute the mechanical behavior of polymer nanocomposites. Their results confirm that CNT reinforcement significantly enhances the Young's modulus of the composite, and that CG models provide comparable accuracy and lower computational cost than atomistic simulations. Later, Mousavi et al. [145] introduced nonbonded interactions between polymer chains, CNTs and polymer matrix in the CG model to investigate the influence of cross-linking, weight fraction and distribution of CNTs on the elastic properties of polymer nanocomposites.

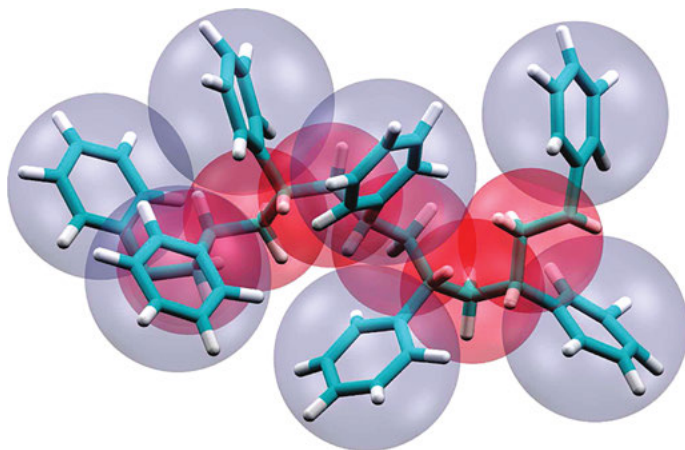


Figure 3.18: Coarse-grained model of polystyrene (red and gray beads) from atomistic details (white and cyan sticks). Reprinted from Ref. [139] with permission of American Chemical Society.

The effect of dispersion, alignment and morphology of nanofillers on the properties of polymer composites can be studied by DPD as well. Zhou et al. [146] studied the dispersion and alignment of CNTs using DPD simulations. Numerical experiments demonstrated that CNTs tend to align themselves in the polymer matrix with increasing nanotube length and volume fraction, especially in well-dispersed systems. Instead, a DPD study on graphene/PMMA (Poly(methyl methacrylate)) composite showed that, while pristine graphene and PMMA are immiscible, high concentrations of graphene functionalizations lead to better filler dispersions in the PMMA matrix [147]. Furthermore, when the volume fraction of fillers is larger, graphene needs to be functionalized more to reach good dispersion. Similar results were obtained by Lin et al. [148], who reported better dispersions of covalently functionalized graphene fillers in PMMA matrix compared to nonfunctionalized ones.

Electrical properties

The RVE concept is also applicable to predict the mesoscale electrical properties of nanocomposites. The electrical conductivity of carbon-based polymer nanocomposites mainly depends on [149–151]:

- the intrinsic electrical conductance of CFs;
- the normal transport through conductive networks of carbon fillers in contact with each other within the polymeric matrix;
- the hopping transport due to the tunneling of electrons between CFs separated by polymer matrix of thickness less than the tunneling distance.

To compute the electrical conductivity of nanocomposites at mesoscale, CFs should be first randomly distributed within a RVE of polymer nanocomposite. These simulations typically assume that fibers have low electrical resistance and thus act as conductors, whereas polymeric matrix is considered as a highly resistive material with low electrical conduction. Therefore, the most conductive path for a given composite is the one minimizing the relative distance between CFs [151, 152]. Different algorithms are available to find the shortest path in a given configuration (e.g., Dijkstra algorithm [153]), which can be thus employed to calculate the electrical conductivity of the simulated nanocomposites at mesoscale. This procedure is typically repeated over different random distributions of fibers in the matrix to reduce statistical fluctuations in terms of composite conductivity.

In a cuboid RVE with dimensions (L_x, L_y, L_z) containing randomly distributed fibers in a polymer matrix [154], each fiber can be modeled as a line segment in spherical coordinates (see Figure 3.19):

$$\begin{aligned}x_i^e &= x_i^s + l_i \sin \theta_i \cos \varphi_i, \\y_i^e &= y_i^s + l_i \sin \theta_i \sin \varphi_i, \\z_i^e &= z_i^s + l_i \cos \theta_i,\end{aligned}\tag{3.28}$$

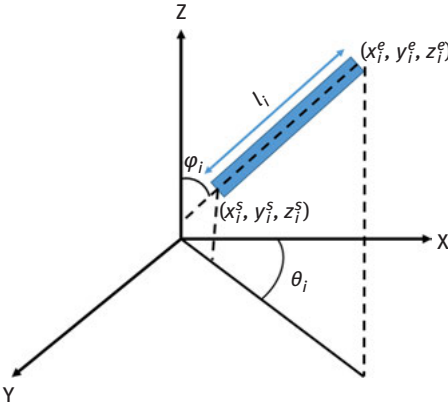


Figure 3.19: Fiber modeled as a line segment in spherical coordinates.

where i is the index of the i^{th} fiber, (x_i^s, y_i^s, z_i^s) and (x_i^e, y_i^e, z_i^e) are the start and end point coordinates of the fiber. The length, polar and azimuthal angle of the i^{th} fiber are denoted as l_i , θ_i and φ_i , respectively.

The start point coordinates, the polar angles and the azimuthal angles of each fiber can be generated randomly as

$$\begin{aligned}x_i^s &= L_x \xi, & y_i^s &= L_y \xi, & z_i^s &= L_z \xi \\ \theta_i &= 2\pi \xi, & \varphi_i &= \cos^{-1}(2\xi - 1)\end{aligned}\tag{3.29}$$

where ξ is an uniformly generated random number in the range $[0, 1]$. To better represent experimental variability, the simulated length of fibers can follow a Weibull distribution [155]. It should be noted that the end points of fibers might initially lie outside the RVE cuboid: in that case, periodic boundary conditions are applied to relocate them inside the cuboid.

The electrical conductivity of nanocomposites can be estimated once the series of resistances in the percolating network is computed, including both intrinsic resistance of fibers (R_{ij}) and their contact resistance ($R_{contact}$). According to the Drude model, the R_{ij} of a fiber (i, j) with l_{ij} length, D diameter and σ_e^{fiber} intrinsic electrical conductivity (see Figure 3.20) can be calculated as [154]

$$R_{ij} = \frac{4l_{ij}}{\sigma_e^{fiber} \pi D^2}. \quad (3.30)$$

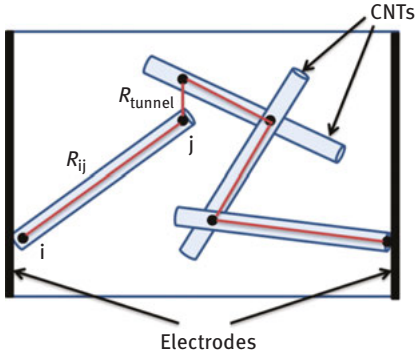


Figure 3.20: Network of electrical resistors in the RVE of a nanocomposite reinforced by nanofillers, for example, CNTs. Reprinted from Ref. [151] with permission from Elsevier.

Considering a marginal effect of temperature, the contact resistance $R_{contact}$ between two fibers can be instead estimated as [150]

$$R_{contact} = \frac{h}{2e^2 M \tau_p}, \quad (3.31)$$

being h the Planck constant, e the electron charge, M the number of conduction channels and τ_p the transmission probability for the electron to tunnel through the polymer layer between fibers. According to Bao et al. [150], the transmission probability τ_p can be estimated by the Wentzel–Kramers–Brillouin approximation [156] as follows:

$$\tau_p = \begin{cases} \exp\left(-\frac{d_{vdW}}{d_{tunnel}}\right) & 0 \leq d \leq D + d_{vdW} \\ \exp\left(-\frac{d-D}{d_{tunnel}}\right) & D + d_{vdW} \leq d \leq D + d_{cut} \end{cases} \quad (3.32)$$

where d is the minimum distance between adjacent fibers, d_{vdW} is the van der Waals separation distance and d_{tunnel} is the tunneling length. The latter can be described as [150]

$$d_{tunnel} = \frac{\hbar}{\sqrt{8m_e\Delta E}}, \quad (3.33)$$

where $\hbar = h/2\pi$ is the reduced Planck constant, m_e the mass of electron and ΔE the energy barrier. Note that in eq. (3.32), tunneling effects are neglected if the thickness of polymer matrix between contiguous fibers is larger than d_{cut} , namely, the considered cut-off distance.

Bao et al. [150] studied the effect of CNT alignment in polymer matrix on the critical percolation threshold, and their results revealed that the maximum electrical conductivity is obtained in nanocomposites with partially aligned CNTs. Similarly, Monte Carlo simulations by Zeng et al. [157] reported a clear dependence of the electrical percolation threshold on CNT length, waviness, distribution anisotropy and volume fraction. Improved three-dimensional percolating network theories can also be used to understand how the deformation of CNTs at crossed nanotube junctions influences the electrical conductivity of nanocomposites [158]. In detail, the study by Gong and colleagues [158] suggests that CNT deformation at crossed nanotube junctions determines a large increase in the intrinsic resistance of the nanotube while only a limited decrease in the CNT–CNT contact resistance, therefore, leading to enhanced overall resistance at the junction. Furthermore, numerical simulations based on the Dijkstra algorithm showed that increased contents of MWCNTs in polymer nanocomposites result in higher electrical conductivities, in good quantitative agreement with experiments (see Figure 3.21)

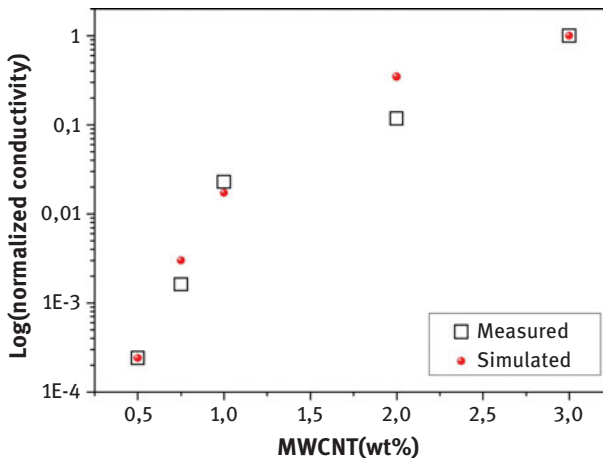


Figure 3.21: Simulation and experimental results of electrical conductivity of CNT-based polymer composites as a function of weight percentage of MWCNTs. Reprinted from Ref. [152] with permission from Elsevier.

[152]. Finally, Rahatekar et al. [159] performed DPD simulations to explore the influence of aspect ratio and fiber alignment on the electrical percolation threshold of nanocomposites.

3.2.3 Continuum models

Thermal properties

The effective thermal conductivity (λ_{eff}) of polymer nanocomposites at macroscale can be predicted by two approaches, namely analytical or simulation ones. Analytical models, for example, effective medium approximation, generally provide quick evaluations of the properties of composites, but cannot take into account neither the interactions between adjacent inclusions nor the actual morphology of composite. Further details on the analytical models for effective thermal conductivity of nanocomposites can be found in a recent review article by Zhai et al. [160].

Due to the current improvement of computational tools and numerical algorithms, finite element method (FEM) has been increasingly utilized to compute the thermal conductivity of composite materials at continuum level. FEM calculates the λ_{eff} of nanocomposites by solving numerically the Fourier's law for conduction at steady state, and this procedure is – in principle – capable to consider different morphologies (e.g., fiber distribution) of the composite material by proper meshing strategies. FEM simulations of composites are typically limited to an RVE of the system. The RVE is built in such a manner that the smallest constituent that can influence the first-order macroscopic behavior of the system is consistent with the simulated length scale; then, the results obtained from the RVE are extended to develop a full-scale model. For example, Figure 3.22 depicts 3D cubic RVEs of composites with different inclusions, namely cylindrical, platelet-like and spherical fillers. The major drawback of FEM in comparison with analytical approaches remains the high computational cost, as well as the modeling complexity given by systems including fibers with high volume fraction or aspect ratio.

Ramani and Vaidynathan [162] carried out an automated finite element analysis to compute λ_{eff} of composite materials. The employed FEM model allowed to study the effect of various parameters, such as fiber aspect ratio, volume fraction, dispersion, orientation and fiber–matrix interfacial thermal resistance on the resulting thermal behavior of composites. Numerical results were compared to analytical models and experiments, finding a good agreement especially at high volume fractions. Ahmed and Masud [163] employed FEM to study the effect of geometrical parameters on the λ_{eff} of polymer composites reinforced by MWCNTs. Their study revealed that the λ of nanocomposites increases with the aspect ratio of nanotubes, whereas interface thermal resistances do not have a prime contribution in lowering the thermal conductivity at the macroscopic scale. Instead, Li et al. [164] quantified

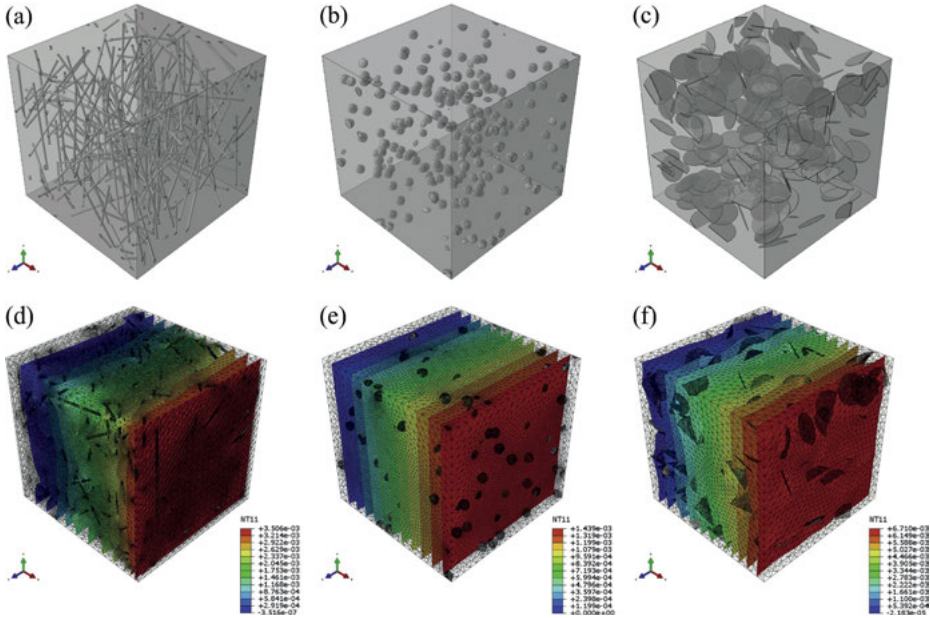


Figure 3.22: Temperature fields in 3D representative volume elements of different composites simulated by FEM method. Reprinted from Ref. [161] with permission from Elsevier.

the influence of SWCNT–matrix interfacial thermal resistance (R_{CNT-m}) on λ_{eff} of SWCNT/polymer composites. Their results showed that the λ_{eff} of composite can be lower than the one of pristine polymer matrix if R_{CNT-m} is greater than a critical value.

Mechanical properties

The FEM can be used to understand the macroscale mechanical properties of nanocomposites, for example, the elastic moduli. At molecular level, the RVE of a generic nanocomposite is a heterogeneous medium consisting of polymer matrix, carbon nanofibers and interface region. However, at continuum level, such heterogeneous RVE should be homogenized to compute the effective material properties through micromechanical analyses (see Figure 3.23). Notice that the homogenization procedure of RVEs to calculate the effective elastic moduli of nanocomposites is equivalent to average the mechanical properties of heterogeneous nanocomposites [165].

The constituents of the RVE can then be assumed as isotropically symmetric within the nanocomposite [166], and the constitutive relation given by the generalized Hooke's law:

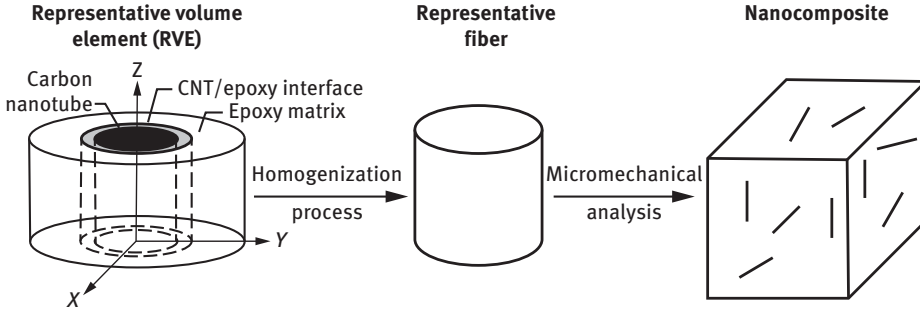


Figure 3.23: Homogenization of a representative volume element of nanocomposite, which includes the nanofiller (CNT), the CNT/epoxy interface and part of the surrounding epoxy matrix into a representative, homogeneous fiber of the composite to be considered for micromechanical analysis. Adapted from Ref. [166] with permission from Elsevier.

$$\sigma_{ij} = C'_{ijkl} \varepsilon_{kl}, \quad i, j, k, l = 1, 2, 3 \quad (3.34)$$

being C'_{ijkl} the elastic stiffness tensor of the RVE, σ_{ij} and ε_{kl} the stress and strain tensors, respectively. The effective stiffness coefficient (C'^e_{ijkl}) of the homogenized multi-constituent nanocomposite can thus be written as

$$\bar{\sigma}_{ij} = C'^e_{ijkl} \bar{\varepsilon}_{kl}, \quad (3.35)$$

being $\bar{\sigma}_{ij}$ and $\bar{\varepsilon}_{kl}$ the stress and strain tensors averaged over the RVE volume (V_{RVE}), respectively, that is:

$$\bar{\sigma}_{ij} = \frac{1}{V_{RVE}} \int_{V_{RVE}} \sigma_{ij} dV, \quad (3.36)$$

$$\bar{\varepsilon}_{kl} = \frac{1}{V_{RVE}} \int_{V_{RVE}} \varepsilon_{kl} dV. \quad (3.37)$$

The effective elastic moduli of nanocomposite are finally calculated using the averaged stress and strain tensors as follows:

$$C'^e_{ijkl} = \frac{\bar{\sigma}_{ij}}{\bar{\varepsilon}_{kl}}, \quad i = j = k = l \quad (\text{Young's modulus}) \quad (3.38)$$

$$C'^e_{ijkl} = \frac{\bar{\sigma}_{ij}}{2\bar{\varepsilon}_{kl}}, \quad (i = k) \neq (j = l) \quad (\text{Shear modulus}) \quad (3.39)$$

Instead, the Poisson's ratio of nanocomposite is computed as

$$\nu_{ij} = -\frac{\bar{\varepsilon}_{jj}}{\bar{\varepsilon}_{ii}}. \quad (3.40)$$

Odegard et al. [167] proposed a method to transform the discrete molecular structures of nanotube fillers, polymer matrix and CNT/polymer interface at nanoscale into an equivalent continuum model of composite. Liu and Chen [168] computed the effective mechanical properties of CNT-reinforced composites using a nanoscale RVE and the FEM. They showed that the stiffness of composite increases several times with volume fractions of CNT nanofillers up to 5%. Instead, an equivalent continuum modeling study by Huang and Rodrigue [169] found that both aspect ratio and length of CNT fillers have a significant influence on the mechanical properties of polypropylene-based composites. In a similar study, Kumar and Srivastava [170] reported that the elastic stiffness of polymer matrix was improved by carbon-based filler reinforcements. This study also concluded that graphene reinforcements provided the best in-plane stiffness properties of nanocomposite, whereas CNTs the best out-of-plane ones. Finally, a continuum simulation using multiscale homogenization procedure was applied by Golestanian and Gahruei [171] to understand the effect of CNT waviness on the elastic properties of CNT-reinforced polymer composites. The simulation study revealed that wavier CNTs reduce elastic modulus of nanocomposite along the longitudinal direction, while they increase elastic modulus along the transverse one.

Electrical properties

The effective electrical properties of nanocomposites at the micro- and macroscale are substantially affected by phenomena at molecular level, such as tunneling mechanism and formation of conductive networks.

In case of a 1D conductor with l length and A_c cross section, the effective electrical conductivity of composite (σ_e) can be computed by measuring the electric current (I) flowing through the computational domain, given a certain electric potential (U), that is

$$\sigma_e = \frac{Il}{A_c U}. \quad (3.41)$$

Instead, in case of 3D anisotropic materials, a more general expression should be considered:

$$\mathbf{j} = \sigma_e \mathbf{E}, \quad (3.42)$$

where \mathbf{j} being the current density vector, $\mathbf{E} = -\nabla U$ the electric field vector under electrostatic conditions and σ_e the effective conductivity tensor. Typically, FEM analysis with micromechanical corrections is adopted to compute effective electrical properties of nanocomposites at continuum level as, for example, depicted in Figure 3.24.

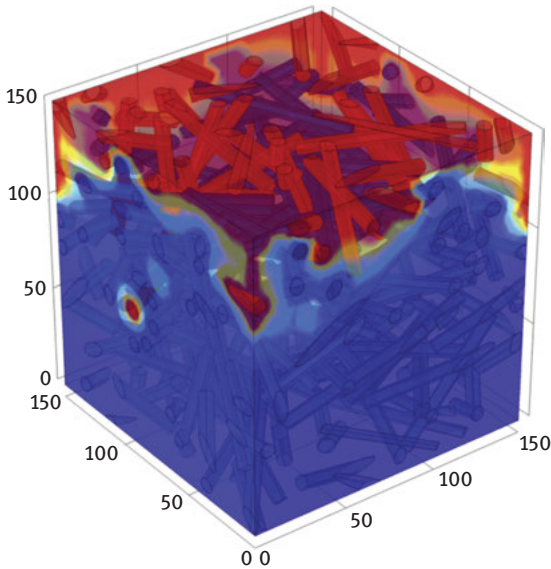


Figure 3.24: Electrical potential within a nanocomposite evaluated by FEM analysis. Reprinted from Ref. [172] with permission from Elsevier.

Seidel and Lagoudas [173] developed a micromechanical model to estimate the electrical properties of CNT–polymer nanocomposites. They reported that the large increment in the σ_e of MWCNT-based nanocomposites at low nanotube concentrations is mainly due to formation of conductive networks, whereas in SWCNT-based nanocomposites, both electron hopping and conductive network formation play a relevant role [173, 174]. The macroscale piezoresistive properties of CNT–polymer composites along both transverse and axial directions were studied instead by Ren and Seidel [37], considering both electric tunneling and inherent piezoresistivity of CNT in the selected RVEs. In that study, the macroscale piezoresistive response of different mesoscale CNT dispersion scenarios in the nanocomposite was predicted using computational micromechanics techniques based on the finite element analysis. The authors found that the electric tunneling mechanism dominates the overall piezoresistive properties of CNT–polymer composites along both transverse and axial directions, whereas the inherent piezoresistivity contribution is more evident along the axial direction rather than along the transverse one [37]. The influence of electric tunneling was found to be negligible in composites with well-dispersed distributions of CNTs, where the intertube distance was larger than the tunneling distance; conversely, agglomerated CNT dispersions eased electric tunneling mechanism.

3.3 Perspectives

The idea to combine different materials to develop an engineered material having unique capabilities, distinct from their constituent materials, is very fascinating, and it has been well known by long time. Nowadays, the possibilities offered by materials processing and, sometimes, nanotechnology have revamped the emphasis on composite materials. In particular, carbon-based composites have already proved to provide remarkable improvements in terms of stiffness, durability, strength and lightweight characteristics in some industrial sectors, for example, automotive.

In spite of the previous successes, some industrial challenges remain for composite materials. According to a recent commentary by *Materials Today* [175], mass production of composites is a key aspect that must still be developed before composites will prove to be useful for many new applications. The lack of mass production/automation techniques sometimes reveals the lack of knowledge of the composite manufacturing process, which forces to rely on try and error in developing new products [175]. Clearly, this approach, which is still dominant in many applications, cannot be properly standardized. Hence, the lack of standardization, design standards and good technical support/backup from suppliers tends to reduce the composite acceptance in an industrial context [175]. Composite materials without a warranty are not well accepted by engineers, who have to deal with high-fidelity standards in the design and production of complex products. Things become even worse in case of recycling CFs, as envisioned by circular economy. End-of-life fiber-reinforced composites are particularly challenging for implementing circular economy, even though some large-scale demonstration has been already funded by the European Commission [176]. All the above factors significantly increase the price of carbon-based composites with regard to their competitors, namely steel, concrete and thermoplastics, and this induces a loss of market share [175]. Price reduction can hardly be achieved by combining raw materials, because this intrinsically requires some additional processing costs. However, one promising alternative option consists in increasing the value chain by adding new functionalities for composite materials. This leads to the so-called smart materials (see Table 3.1 and references therein). Materials with self-sensing and structural health monitoring capabilities, devices with fast triggering shape memory, thermally driven actuators and high-performance all-solid-state supercapacitors are good examples of this strategy. On the other hand, this strategy leads necessarily to even more scientific challenges, because high precision and reproducibility of the arrangement of CFs into the composites are required.

The previous discussion reveals that the exploitation of carbon-based composites requires addressing many scientific challenges, which could benefit from systematic and state-of-the-art materials modeling. Essentially, modeling should address two main issues: (i) elucidating the atomistic details of interface between CF and polymer and (ii) taking into account properly the extreme variability in the CF orientation within the composite.

Table 3.1: Modeling methods for computing thermophysical properties of carbon-based nanocomposites of interest as smart materials. PDMS is polydimethylsiloxane; PVDF is polyvinylidene fluoride.

Material	Modeling method	Properties	Applications as smart material
CNT/PDMS composite	FEM	Structural, mechanical and thermal properties	Thermally driven actuator [181]
CNT/polymer composite	Multiphysics modeling	Electromechanical properties	Strain sensor [182]
CNT/polymer	Percolation network model	Electrical conductivity	High accuracy sensor [183, 184]
PVDF/carbon fiber composite	Multiphysics micromechanics and FEM	Mechanical and piezoelectric properties	Self-sensing and structural health monitoring [39]
CNT sponge/shape memory polymer nanocomposite	FEM	Electrical properties	Fast triggering shape memory material [185]
Graphene oxide (GO)/reduced GO/water	Quantum/MD simulations	Capacitance	High-performance all-solid-state supercapacitors [186]

The first issue is very well known and is also largely explored from the experimental point of view. For example, CF-reinforced thermoplastic composites gained recent interest due to ease of production and recycling compared to that of thermoset composites, but surface treatments are used to increase the concentration of surface functional groups and hence the fiber–polymer interfacial adhesion [177]. Similarly, different methods of preparation for thermoset composites rely on functionalizing the interface between various nanofillers and epoxy, which is typically characterized by several experimental techniques [178]. Remarkably, nowadays both experimental and modeling techniques are used in order to investigate the relationships between interfacial characteristics and composite properties, for example, with regard to the advantages and disadvantages of covalent and noncovalent functionalization of CFs [179].

The second issue where materials modeling can provide some useful insights is due to the extreme variability in the microscopic structure of composites. Different arrangements of CFs within the composite, shape and orientation of the CF aggregates and dynamics response of the microstructure due to the applied loads are just examples of phenomena that require modeling at scales much larger than that of individual fiber. This may appear simply as a geometrical problem, but it leads immediately to (i) a significant increase in the computational demand and to (ii) a problem of model reduction in postprocessing the modeling results. The second problem is

particularly severe, because it may hinder the opportunity to use materials modeling for increasing the understanding of composites under realistic conditions. In fact, understanding requires squeezing a large amount of information in very simple design guidelines. Moreover, this second problem has an indirect effect on the first problem about affordable computational demand as well. In fact, the possibility to develop simple interpolation models, which can summarize the outcome of more complex models, is essential for any coupling and/or linking strategy. Concerning the latter point, analytical simplified models, which can describe the transfer of energy, mechanical stresses and electricity between neighboring fibers, are highly desirable for developing reliable predictions about percolating networks within the composites. Nowadays, machine learning techniques and artificial intelligence offer solutions for developing analytical interpolating functions, which can be tuned on underlying detailed models and are suitable as input for up-scaled models for predicting macroscopic properties of the materials. These analytical functions keep some insights into the investigated phenomena and, at the same time, are very fast and transferable in up-scaled models, which can describe large portions of the material under investigation. This is a clear advantage with regard to previous techniques based on neural networks. Hence, we envision a huge impact of such techniques in dealing with realistic simulations of carbon-based composites for engineering applications.

Finally, last but not least, carbon-based composites still raise some concerns in terms of their toxicity, particularly when nanofibers are involved. These concerns are about the manufacturing processes of composites, the release of nanoparticles during operation and the end-of-life waste management. Clearly, the fact that some nanofibers, for example, CNTs, are similar in shape and size to asbestos raises further concern [180]. Even though materials modeling may help in assessing some guidelines and in clarifying some scenarios, quantitative and predictive computational nanotoxicology is still far from being mainstream. However, it represents a very interesting approach, which is currently under development in many different fields for assessing preliminarily the impact of new nanotechnologies, and we envision that also carbon-based composites will benefit from it.

Acknowledgments: This work partially received funding from the European Union's Horizon 2020 research and innovation programs, through MODCOMP (grant agreement no. 685844) and SMARTFAN (grant agreement no. 760779) projects.

References

- [1] van der Zwaag, S., *Self Healing Materials: An Alternative Approach to 20 Centuries of Materials Science*, Springer Netherlands: Springer Series in Materials Science, 2007.
- [2] Robinson, A. L., *Metallurgy: Extraordinary alloys that remember their past*. *Science* 1976, 191, 4230, 934–936.

- [3] Jani, J. M., Leary, M., Subic, A., and Gibson, M. A., A review of shape memory alloy research, applications and opportunities. *Mater. Des* 2014, 56, 1078–1113.
- [4] Calkins, F. T., and Mabe, J. H., Shape memory alloy based morphing aerostructures. *ASME. J. Mech. Des* 2010, 132, 11, 111012.
- [5] Baer, G., Wilson, T. S., Matthews, D. L., and Maitland, D. J., Shape memory behavior of thermally stimulated polyurethane for medical applications. *J. Appl. Polym. Sci* 2007, 103, 6, 3882–3892.
- [6] Kim, S., Hawkes, E., Choy, K., Joldaz, M., Foley, J., and Wood, R., “Micro artificial muscle fiber using NiTi spring for soft robotics,” in 2009 IEEE/RSJ International Conference on Intelligent Robots and Systems, pp 2228–2234, Oct 2009.
- [7] Song, G., Ma, N., and Li, H.-N., Applications of shape memory alloys in civil structures. *Eng. Struct* 2006, 28, 9, 1266–1274.
- [8] Gök, M. O., Bilir, M. Z., and Gürcüm, B. H., “Shape-memory applications in textile design,” *Procedia - Social and Behavioral Sciences*, vol. 195, pp. 2160–2169, 2015. World Conference on Technology, Innovation and Entrepreneurship.
- [9] Olander, A., An electrochemical investigation of solid cadmium-gold alloys. *J. Am. Chem. Soc* 1932, 54, 10, 3819–3833.
- [10] Buehler, W. J., Gilfrich, J. V., and Wiley, R. C., Effect of low-temperature phase changes on the mechanical properties of alloys near composition TiNi. *J. Appl. Phys* 1963, 34, 5, 1475–1477.
- [11] Otsuka, K., and Ren, X., Physical metallurgy of Ti–Ni-based shape memory alloys. *Prog. Mater Sci* 2005, 50, 5, 511–678.
- [12] van Humbeeck, J., Shape memory materials: State of the art and requirements for future applications. *J. Phys. IV France* 1997, 07, C5, C5–3–C5–12.
- [13] Ratna, D., and Karger-Kocsis, J., Recent advances in shape memory polymers and composites: a review. *J. Mater. Sci* 2008, 43, 254–269.
- [14] Gong, X., Liu, L., Liu, Y., and Leng, J., An electrical-heating and self-sensing shape memory polymer composite incorporated with carbon fiber felt. *Smart Mater. Struct* 2016, 25, 035036.
- [15] Liu, Y., Zhao, J., Zhao, L., Li, W., Zhang, H., Yu, X., and Zhang, Z., High performance shape memory epoxy/carbon nanotube nanocomposites. *ACS Appl. Mater. Interfaces* 2016, 8, 1, 311–320.
- [16] Zhang, Z.-X., Dou, J.-X., He, J.-H., Xiao, C.-X., Shen, L.-Y., Yang, J.-H., Wang, Y., and Zhou, Z.-W., Electrically/infrared actuated shape memory composites based on a bio-based polyester blend and graphene nanoplatelets and their excellent self-driven ability. *J. Mater. Chem. C* 2017, 5, 4145–4158.
- [17] Wang, X., Sparkman, J., and Gou, J., Electrical actuation and shape memory behavior of polyurethane composites incorporated with printed carbon nanotube layers. *Compos. Sci. Technol* 2017, 141, 8–15.
- [18] Yang, E., Xu, Z., Chur, L. K., Behroozfar, A., Baniasadi, M., Moreno, S., Huang, J., Gilligan, J., and Minary-Jolandan, M., Nanofibrous smart fabrics from twisted yarns of electrospun piezopolymer. *ACS Appl. Mater. Interfaces* 2017, 9, 28, 24220–24229.
- [19] Yuan, X., Zhu, S., Li, X., Chen, C., Zhou, K., and Zhang, D., Mechanical performance of piezoelectric fiber composites and electroelastic field concentration near the electrode edges. *Mater. Des* 2017, 128, Supplement C, 71–79.
- [20] Chen, Q., Sun, Y., Qin, L., and Wang, Q. M., Piezoelectric fiber-composite-based cantilever sensor for electric-field-induced strain measurement in soft electroactive polymer. *IEEE Trans. Ultrason. Ferroelectr. Freq. Control* 2013, 60, 2142–2153.

- [21] Lin, X., Huang, S., Zhou, K., and Zhang, D., The influence of structural parameters on the actuation performance of piezoelectric fiber composites. *Mater. Des* 2016, 107, Supplement C, 123–129.
- [22] Yang, Y., Tang, L., and Li, H., Vibration energy harvesting using macrofiber composites. *Smart Mater. Struct* 2009, 18, 11, 115025.
- [23] Zeng, W., Tao, X.-M., Chen, S., Shang, S., Chan, H. L. W., and Choy, S. H., Highly durable all-fiber nanogenerator for mechanical energy harvesting. *Energy Environ. Sci* 2013, 6, 2631–2638.
- [24] Zhong, J., Zhang, Y., Zhong, Q., Hu, Q., Hu, B., Wang, Z. L., and Zhou, J., Fiber-based generator for wearable electronics and mobile medication. *ACS Nano* 2014, 8, 6, 6273–6280.
- [25] Lu, X., Qu, H., and Skorobogatiy, M., Piezoelectric micro- and nanostructured fibers fabricated from thermoplastic nanocomposites using a fiber drawing technique: Comparative study and potential applications. *ACS Nano* 2017, 11, 2, 2103–2114.
- [26] Back cover. *Energy Environ. Sci* 2013, 6, 2778.
- [27] Wang, J., Gao, Y., Zhang, J., and Tian, H., Invisible photochromism and optical anti-counterfeiting based on d-a type inverse diarylethene. *J. Mater. Chem. C* 2017, 5, 4571–4577.
- [28] Ye, J.-T., Wang, L., Wang, H.-Q., Chen, -Z.-Z., Qiu, Y.-Q., and Xie, H.-M., Spirooxazine molecular switches with nonlinear optical responses as selective cation sensors. *RSC Adv* 2017, 7, 642–650.
- [29] Renuka, K. D., Lekshmi, C. L., Joseph, K., and Mahesh, S., Sustainable electronic materials: Reversible phototuning of conductance in a noncovalent assembly of MWCNT and bioresource-derived photochromic molecule. *ACS Appl. Mater. Interfaces* 2017, 9, 2, 1167–1172.
- [30] Wei, J., Jiao, X., Wang, T., and Chen, D., Electrospun photochromic hybrid membranes for flexible rewritable media. *ACS Applied Materials & Interfaces* 2016, 8, 43, 29713–29720.
- [31] William J, S., “Doll or the like,” Oct. 27 1953. US Patent 2656647 A.
- [32] Ercole, F., Davis, T. P., and Evans, R. A., Photo-responsive systems and biomaterials: photochromic polymers, light-triggered self-assembly, surface modification, fluorescence modulation and beyond. *Polym. Chem* 2010, 1, 37–54.
- [33] Manouras, T., and Vamvakaki, M., Field responsive materials: photo-, electro-, magnetic- and ultrasound-sensitive polymers. *Polym. Chem* 2017, 8, 74–96.
- [34] Fasano, M., Chiavazzo, E., and Asinari, P., Water transport control in carbon nanotube arrays. *Nanoscale research letters* 2014, 9, 1, 559.
- [35] Gizzatov, A., Key, J., Aryal, S., Ananta, J., Cervadoro, A., Palange, A. L., Fasano, M., Stigliano, C., Zhong, M., Di, M. D., Guven, A., Chiavazzo, E., Asinari, P., Liu, X., Ferrari, M., Wilson, L. J., and Decuzzi, P., Hierarchically structured magnetic nanoconstructs with enhanced relaxivity and cooperative tumor accumulation. *Adv. Funct. Mater* 2014, 24, 29, 4584–4594.
- [36] Chiavazzo, E., Fasano, M., Asinari, P., and Decuzzi, P., Scaling behaviour for the water transport in nanoconfined geometries. *Nat. Commun* 2014, 5, 3565.
- [37] Ren, X., and Seidel, G. D., Computational micromechanics modeling of piezoresistivity in carbon nanotube–polymer nanocomposites. *Compos. Interfaces* 2013, 20, 9, 693–720.
- [38] Ren, X., Burton, J., Seidel, G. D., and Lafdi, K., Computational multiscale modeling and characterization of piezoresistivity in fuzzy fiber reinforced polymer composites. *Int. J. Solids Struct* 2015, 54, 121–134.
- [39] Greminger, M., and Haghighashtiani, G., Multiscale modeling of PVDF matrix carbon fiber composites. *Modell. Simul. Mater. Sci. Eng* 2017, 25, 4, 045007.
- [40] Toth, R., Santese, F., Pereira, S. P., Nieto, D. R., Pricl, S., Fermeglia, M., and Posocco, P., Size and shape matter! A multiscale molecular simulation approach to polymer nanocomposites. *Journal of Materials Chemistry* 2012, 22, 12, 5398–5409.

- [41] Posocco, P., Pricl, S., and Fermeglia, M., Multiscale modeling approach for polymeric nanocomposites. *Modeling and Prediction of Polymer Nanocomposite Properties* 2013, 95–128.
- [42] Fermeglia, M., Posocco, P. and Pricl, S., Nano tools for macro problems: multiscale molecular modeling of nanostructured polymer systems. *Composite Interfaces* 2013, 20, 6, 379–394.
- [43] Subramanian, N., Rai, A., and Chattopadhyay, A., Atomistically informed stochastic multiscale model to predict the behavior of carbon nanotube-enhanced nanocomposites. *Carbon* 2015, 94, 661–672.
- [44] Laurini, E., Posocco, P., Fermeglia, M., and Pricl, S., Modena nanotools: An integrated multiscale simulation workflow to predict thermophysical properties of thermoplastic polyurethanes. *Journal of Computational Science* 2016, 15, 24–33.
- [45] Khromov, K. Y., Knizhnik, A., Potapkin, B., and Kenny, J., Multiscale modeling of electrical conductivity of carbon nanotubes based polymer nanocomposites. *Journal of Applied Physics* 2017, 121, 22, 225102.
- [46] Laurini, E., Marson, D., Fermeglia, M., and Pricl, S., Multimodel approach for accurate determination of industry-driven properties for polymer nanocomposite materials. *Journal of computational science* 2018, 26, 28–38.
- [47] Li, Y., and Seidel, G., Multiscale modeling of the interface effects in CNT-epoxy nanocomposites. *Computational Materials Science* 2018, 153, 363–381.
- [48] De Baas, A., “What makes a material function? let me compute the ways . . .,” *Modeling in FP7 NMP Programme, European Commission*, vol. 6th edition, 2017.
- [49] The CEN Workshop Agreement, “CEN/WS MODA - Materials modelling - terminology, classification and metadata.” CWA, vol. 17284, 2018. ftp://ftp.cencenelec.eu/CEN/Sectors/TCandWorkshops/Workshops/WS%20MODA/CWA_17284.pdf.
- [50] Ghedini, E., Hashibon, A., Friis, J., Goldbeck, G., Schmitz, G., and de Baas, A., “EMMO the European Materials Modelling Ontology,” in *EMMC Workshop on Interoperability in Materials Modelling*, 2017. https://emmc.info/wp-content/uploads/2017/12/EMMC_IntOp2017-Cambridge_Ghedini_Bologna.pdf.
- [51] Sáenz Ezquerro, C., Laspalas, M., Chiminelli, A., Serrano, F., and Valero, C., Interface characterization of epoxy resin nanocomposites: A molecular dynamics approach. *Fibers* 2018, 6, 3, 54.
- [52] Humphrey, W., Dalke, A., and Schulten, K., VMD: Visual molecular dynamics. *J. Mol. Graphics* 1996, 14, 1, 33–38.
- [53] Hanwell, M. D., Curtis, D. E., Lonie, D. C., Vandermeersch, T., Zurek, E., and Hutchison, G. R., Avogadro: an advanced semantic chemical editor, visualization, and analysis platform. *J. Cheminf. Aug* 2012, 4, 17.
- [54] Fasano, M., Crisafulli, A., Cardellini, A., Bergamasco, L., Chiavazzo, E., and Asinari, P., Thermally triggered nanorocket from double-walled carbon nanotube in water. *Molecular Simulation* 2019, 45, 4–5, 417–424.
- [55] Schulz, M., and Frisch, H. L., Monte Carlo studies of interpenetrating polymer network formation. *J. Chem. Phys* 1994, 101, 11, 10008–10022.
- [56] Doherty, D., Holmes, B., Leung, P., and Ross, R., Polymerization molecular dynamics simulations. i. cross-linked atomistic models for poly (methacrylate) networks. *Comput. Theor. Polym. Sci* 1998, 8, 1–2, 169–178.
- [57] Yarovsky, I., and Evans, E., Computer simulation of structure and properties of crosslinked polymers: application to epoxy resins. *Polymer* 2002, 43, 3, 963–969.
- [58] Li, C., and Strachan, A., Molecular simulations of crosslinking process of thermosetting polymers. *Polymer* 2010, 51, 25, 6058–6070.

- [59] Jang, C., Lacy, T. E., Gwaltney, S. R., Toghiani, H., and Pittman, C. U. Jr, Relative reactivity volume criterion for cross-linking: Application to vinyl ester resin molecular dynamics simulations. *Macromolecules* 2012, 45, 11, 4876–4885.
- [60] Varshney, V., Patnaik, S. S., Roy, A. K., and Farmer, B. L., A molecular dynamics study of epoxy-based networks: Cross-linking procedure and prediction of molecular and material properties. *Macromolecules* 2008, 41, 18, 6837–6842.
- [61] Lin, P.-H., and Khare, R., Molecular simulation of cross-linked epoxy and epoxy-POSS nanocomposite. *Macromolecules* 2009, 42, 12, 4319–4327.
- [62] Rottach, D. R., Curro, J. G., Budzien, J., Grest, G. S., Svaneborg, C., and Everaers, R., Molecular dynamics simulations of polymer networks undergoing sequential cross-linking and scission reactions. *Macromolecules* 2007, 40, 1, 131–139.
- [63] Wu, C., and Xu, W., Atomistic molecular modelling of crosslinked epoxy resin. *Polymer* 2006, 47, 16, 6004–6009.
- [64] Jang, C., Sirk, T. W., Andzelm, J. W., and Abrams, C. F., Comparison of crosslinking algorithms in molecular dynamics simulation of thermosetting polymers. *Macromol. Theory Simul* 2015, 24, 3, 260–270.
- [65] Maiti, A., Mahan, G., and Pantelides, S., Dynamical simulations of nonequilibrium processes—heat flow and the Kapitza resistance across grain boundaries. *Solid State Commun* 1997, 102, 7, 517–521.
- [66] Kubo, R., Toda, M., and Hashitsume, N., *Statistical physics II: nonequilibrium statistical mechanics*, Vol. 31. Springer Science & Business Media, 2012.
- [67] Evans, D. J., and Morriss, G. P., 4 - The Green–Kubo relations, In: *Statistical Mechanics of Nonequilibrium Liquids* (D. J. Evans and G. P. Morrisseds.), 77–93, Academic Press, 1990.
- [68] Kumar, A., Sundararaghavan, V., and Browning, A., Study of temperature dependence of thermal conductivity in cross-linked epoxies using molecular dynamics simulations with long range interactions. *Modell. Simul. Mater. Sci. Eng* 2014, 22, 2, 025013.
- [69] Sirk, T. W., Karim, M., Khare, K. S., Lenhart, J. L., Andzelm, J. W., and Khare, R., Bi-modal polymer networks: composition-dependent trends in thermal, volumetric and structural properties from molecular dynamics simulation. *Polymer* 2015, 58, 199–208.
- [70] Fasanella, N. A., and Sundararaghavan, V., Atomistic modeling of thermal conductivity of epoxy nanotube composites. *JOM* 2016, 68, 5, 1396–1410.
- [71] Anderson, C. V., and Tamma, K. K., An overview of advances in heat conduction models and approaches for prediction of thermal conductivity in thin dielectric films. *Int. J. Numer. Methods Heat Fluid Flow* 2004, 14, 1, 12–65.
- [72] Müller-Plathe, F., A simple nonequilibrium molecular dynamics method for calculating the thermal conductivity. *J. Chem. Phys* 1997, 106, 14, 6082–6085.
- [73] Varshney, V., Patnaik, S. S., Roy, A. K., and Farmer, B. L., Heat transport in epoxy networks: A molecular dynamics study. *Polymer* 2009, 50, 14, 3378–3385.
- [74] Mortazavi, B., Benzerara, O., Meyer, H., Bardon, J., and Ahzi, S., Combined molecular dynamics-finite element multiscale modeling of thermal conduction in graphene epoxy nanocomposites. *Carbon* 2013, 60, 356–365.
- [75] Alaghemandi, M., Müller-Plathe, F., and Böhm, M. C., Thermal conductivity of carbon nanotube–polyamide-6,6 nanocomposites: Reverse nonequilibrium molecular dynamics simulations. *J. Chem. Phys* 2011, 135, 18, 11B606.
- [76] Shen, Z., Bateman, S., Wu, D. Y., McMahon, P., Dell’Olio, M., and Gotama, J., The effects of carbon nanotubes on mechanical and thermal properties of woven glass fibre reinforced polyamide-6 nanocomposites. *Compos. Sci. Technol* 2009, 69, 2, 239–244.

- [77] Du, F., Guthy, C., Kashiwagi, T., Fischer, J. E., and Winey, K. I., An infiltration method for preparing single-wall nanotube/epoxy composites with improved thermal conductivity. *J. Polym. Sci., Part B: Polym. Phys* 2006, 44, 10, 1513–1519.
- [78] Tascini, A. S., Armstrong, J., Chiavazzo, E., Fasano, M., Asinari, P., and Bresme, F., Thermal transport across nanoparticle-fluid interfaces: the interplay of interfacial curvature and nanoparticle-fluid interactions. *Phys. Chem. Chem. Phys* 2017, 19, 3244–3253.
- [79] Fasano, M., Bigdeli, M. B., Sereshk, M. R. V., Chiavazzo, E., and Asinari, P., Thermal transmittance of carbon nanotube networks: Guidelines for novel thermal storage systems and polymeric material of thermal interest. *Renewable Sustainable Energy Review* 2015, 41, 1028–1036.
- [80] Bigdeli, M. B., and Fasano, M., Thermal transmittance in graphene based networks for polymer matrix composites. *Int. J. Therm. Sci* 2017, 117, 98–105.
- [81] Shenogin, S., Xue, L., Ozisik, R., Koblinski, P., and Cahill, D. G., Role of thermal boundary resistance on the heat flow in carbon-nanotube composites. *J. Appl. Phys* 2004, 95, 12, 8136–8144.
- [82] Lervik, A., Bresme, F., and Kjølstrup, S., Heat transfer in soft nanoscale interfaces: the influence of interface curvature. *Soft Matter* 2009, 5, 2407–2414.
- [83] Varshney, V., Roy, A. K., Michalak, T. J., Lee, J., and Farmer, B. L., Effect of curing and functionalization on the interface thermal conductance in carbon nanotube–epoxy composites. *Jom* 2013, 65, 2, 140–146.
- [84] Shenogin, S., Bodapati, A., Xue, L., Ozisik, R., and Koblinski, P., Effect of chemical functionalization on thermal transport of carbon nanotube composites. *Appl. Phys. Lett* 2004, 85, 12, 2229–2231.
- [85] Clancy, T. C., and Gates, T. S., Modeling of interfacial modification effects on thermal conductivity of carbon nanotube composites. *Polymer* 2006, 47, 16, 5990–5996.
- [86] Liu, C., and Fan, S., Effects of chemical modifications on the thermal conductivity of carbon nanotube composites. *Appl. Phys. Lett* 2005, 86, 12, 123106.
- [87] Shen, X., Wang, Z., Wu, Y., Liu, X., and Kim, J.-K., Effect of functionalization on thermal conductivities of graphene/epoxy composites. *Carbon* 2016, 108, 412–422.
- [88] Luo, T., and Lloyd, J. R., Enhancement of thermal energy transport across graphene/graphite and polymer interfaces: a molecular dynamics study. *Adv. Funct. Mater* 2012, 22, 12, 2495–2502.
- [89] Wang, Y., Yang, C., Pei, Q.-X., and Zhang, Y., Some aspects of thermal transport across the interface between graphene and epoxy in nanocomposites. *ACS Appl. Mater. Interfaces* 2016, 8, 12, 8272–8279.
- [90] Zheng, Q., Xue, Q., Yan, K., Gao, X., Li, Q., and Hao, L., Effect of chemisorption on the interfacial bonding characteristics of carbon nanotube–polymer composites. *Polymer* 2008, 49, 3, 800–808.
- [91] Varshney, V., Patnaik, S. S., Roy, A. K., and Farmer, B. L., Modeling of thermal conductance at transverse cnt-cnt interfaces. *J. Phys. Chem. C* 2010, 114, 39, 16223–16228.
- [92] Clancy, T. C., Frankland, S.-J. V., Hinkley, J. A., and Gates, T. S., Multiscale modeling of thermal conductivity of polymer/carbon nanocomposites. *Int. J. Therm. Sci* 2010, 49, 9, 1555–1560.
- [93] Varshney, V., Roy, A. K., and Baur, J. W., Modeling the role of bulk and surface characteristics of carbon fiber on thermal conductance across the carbon-fiber/matrix interface. *ACS Appl. Mater. Interfaces* 2015, 7, 48, 26674–26683.
- [94] Huang, H., Chen, L., Varshney, V., Roy, A. K., and Kumar, S., Investigation of phonon transport and thermal boundary conductance at the interface of functionalized swcnt and poly(ether-ketone). *Journal of Applied Physics* 2016, 120, 9, 095102.

- [95] Wang, Y., Zhan, H., Xiang, Y., Yang, C., Wang, C. M., and Zhang, Y., Effect of covalent functionalization on thermal transport across graphene–polymer interfaces. *J. Phys. Chem. C* 2015, 119, 22, 12731–12738.
- [96] Kim, B., Choi, J., Yang, S., Yu, S., and Cho, M., Multiscale modeling of interphase in crosslinked epoxy nanocomposites. *Composites Part B: Engineering* 2017, 120, 128–142.
- [97] Kuang, Y., and Huang, B., Effects of covalent functionalization on the thermal transport in carbon nanotube/polymer composites: a multi-scale investigation. *Polymer* 2015, 56, 563–571.
- [98] Zhang, J., Jiang, C., Jiang, D., and Peng, H.-X., Nano-engineering thermal transport performance of carbon nanotube networks with polymer intercalation: a molecular dynamics study. *Phys. Chem. Chem. Phys* 2014, 16, 9, 4378–4385.
- [99] Hida, S., Hori, T., Shiga, T., Elliott, J., and Shiomi, J., Thermal resistance and phonon scattering at the interface between carbon nanotube and amorphous polyethylene. *Int. J. Heat Mass Transfer* 2013, 67, 1024–1029.
- [100] Carlborg, C. F., Shiomi, J., and Maruyama, S., Thermal boundary resistance between single-walled carbon nanotubes and surrounding matrices. *Phys. Rev. B* 2008, 78, 20, 205406.
- [101] Chawla, R., Mechanical and tribological properties of graphene reinforced natural rubber composites: A molecular dynamics study. *MRS Advances* 2018, 3, 10, 525–530.
- [102] Weerasinghe, A., Lu, C.-T., Maroudas, D., and Ramasubramaniam, A., Multiscale shear-lag analysis of stiffness enhancement in polymer–graphene nanocomposites. *ACS applied materials & interfaces* 2017, 9, 27, 23092–23098.
- [103] Theodorou, D. N., and Suter, U. W., Atomistic modeling of mechanical properties of polymeric glasses. *Macromolecules* 1986, 19, 139–154.
- [104] Weiner, J. H., *Statistical mechanics of elasticity*, New York: Wiley, 1983.
- [105] Li, Y., Wang, S., and Wang, Q., A molecular dynamics simulation study on enhancement of mechanical and tribological properties of polymer composites by introduction of graphene. *Carbon* 2017, 111, 538–545.
- [106] Zaminpayma, E., Molecular dynamics simulation of mechanical properties and interaction energy of polythiophene/polyethylene/poly (pphenylenevinylene) and CNTs composites. *Polymer Composites* 2014, 35, 11, 2261–2268.
- [107] Sul, J.-H., Prusty, B. G., and Kelly, D. W., Application of molecular dynamics to evaluate the design performance of low aspect ratio carbon nanotubes in fibre reinforced polymer resin. *Composites Part A: Applied Science and Manufacturing* 2014, 65, 64–72.
- [108] Coleman, J. N., Curran, S., Dalton, A. B., Davey, A. P., McCarthy, B., Blau, W., and Barklie, R. C., Percolation-dominated conductivity in a conjugated-polymer-carbon-nanotube composite. *Phys. Rev. B* Sep 1998, 58, R7492–R7495.
- [109] Ahmad, K., Pan, W., and Shi, S.-L., Electrical conductivity and dielectric properties of multiwalled carbon nanotube and alumina composites. *Appl. Phys. Lett* 2006, 89, 13, 133122.
- [110] Simmons, J. G., Generalized formula for the electric tunnel effect between similar electrodes separated by a thin insulating film. *J. Appl. Phys* 1963, 34, 6, 1793–1803.
- [111] Li, C., Thostenson, E. T., and Chou, T.-W., Dominant role of tunneling resistance in the electrical conductivity of carbon nanotube–based composites. *Appl. Phys. Lett* 2007, 91, 22, 223114.
- [112] Hu, N., Masuda, Z., Yan, C., Yamamoto, G., Fukunaga, H., and Hashida, T., The electrical properties of polymer nanocomposites with carbon nanotube fillers. *Nanotechnology* 2008, 19, 21, 215701.
- [113] Lu, W., Chou, T.-W., and Thostenson, E. T., A three-dimensional model of electrical percolation thresholds in carbon nanotube-based composites. *Appl. Phys. Lett* 2010, 96, 22, 223106.

- [114] Yu, Y., Song, G., and Sun, L., Determinant role of tunneling resistance in electrical conductivity of polymer composites reinforced by well dispersed carbon nanotubes. *J. Appl. Phys* 2010, 108, 8, 084319.
- [115] Duong, H. M., Papavassiliou, D. V., Lee, L. L., and Mullen, K. J., Random walks in nanotube composites: Improved algorithms and the role of thermal boundary resistance. *Appl. Phys. Lett* 2005, 87, 1, 013101.
- [116] Duong, H. M., Papavassiliou, D. V., Mullen, K. J., and Maruyama, S., Computational modeling of the thermal conductivity of single-walled carbon nanotube–polymer composites. *Nanotechnology* 2008, 19, 6, 065702.
- [117] Duong, H. M., Yamamoto, N., Papavassiliou, D. V., Maruyama, S., and Wardle, B. L., Inter-carbon nanotube contact in thermal transport of controlled-morphology polymer nanocomposites. *Nanotechnology* 2009, 20, 15, 155702.
- [118] Bui, K., Grady, B. P., and Papavassiliou, D. V., Heat transfer in high volume fraction CNT nanocomposites: Effects of inter-nanotube thermal resistance. *Chem. Phys. Lett* 2011, 508, 4, 248–251.
- [119] Bui, K., Grady, B. P., Saha, M. C., and Papavassiliou, D. V., Effect of carbon nanotube persistence length on heat transfer in nanocomposites: A simulation approach. *Appl. Phys. Lett* 2013, 102, 20, 203116.
- [120] Duong, H. M., Papavassiliou, D. V., Mullen, K. J., Wardle, B. L., and Maruyama, S., Calculated thermal properties of single-walled carbon nanotube suspensions. *J. Phys. Chem. C* 2008, 112, 50, 19860–19865.
- [121] Duong, H. M., Papavassiliou, D. V., Mullen, K. J., Wardle, B. L., and Maruyama, S., A numerical study on the effective thermal conductivity of biological fluids containing single-walled carbon nanotubes. *Int. J. Heat Mass Transfer* 2009, 52, 23, 5591–5597.
- [122] Gong, F., Tam, Y. S., Nguyen, S. T., and Duong, H. M., Prediction of thermal resistances and heat conduction of carbon nanotube aerogels in various permeated gases. *Chem. Phys. Lett* 2015, 627, 116–120.
- [123] Bui, K., Duong, H. M., Striolo, A., and Papavassiliou, D. V., Effective heat transfer properties of graphene sheet nanocomposites and comparison to carbon nanotube nanocomposites. *J. Phys. Chem. C* 2011, 115, 10, 3872–3880.
- [124] Gong, F., Papavassiliou, D. V., and Duong, H. M., Off-lattice Monte Carlo simulation of heat transfer through carbon nanotube multiphase systems taking into account thermal boundary resistances. *Numerical Heat Transfer, Part A* 2014, 65, 11, 1023–1043.
- [125] Gong, F., Bui, K., Papavassiliou, D. V., and Duong, H. M., Thermal transport phenomena and limitations in heterogeneous polymer composites containing carbon nanotubes and inorganic nanoparticles. *Carbon* 2014, 78, 305–316.
- [126] Gong, F., Hongyan, Z., Papavassiliou, D. V., Bui, K., Lim, C., and Duong, H. M., Mesoscopic modeling of cancer photothermal therapy using single-walled carbon nanotubes and near infrared radiation: insights through an off-lattice Monte Carlo approach. *Nanotechnology* 2014, 25, 20, 205101.
- [127] Gong, F., Duong, H. M., and Papavassiliou, D. V., Inter-carbon nanotube contact and thermal resistances in heat transport of three-phase composites. *J. Phys. Chem. C* 2015, 119, 14, 7614–7620.
- [128] Gooneie, A., Schuschnigg, S., and Holzer, C., A review of multiscale computational methods in polymeric materials. *Polymers* 2017, 9, 1, 16.
- [129] Zhou, B., Luo, W., Yang, J., Duan, X., Wen, Y., Zhou, H., Chen, R., and Shan, B., Thermal conductivity of aligned CNT/polymer composites using mesoscopic simulation. *Composites Part A: Applied Science and Manufacturing* 2016, 90, 410–416.

- [130] Raabe, D., Overview of the Lattice Boltzmann method for nano-and microscale fluid dynamics in materials science and engineering. *Modell. Simul. Mater. Sci. Eng* 2004, 12, 6, R13.
- [131] Wang, M., Kang, Q., and Pan, N., Thermal conductivity enhancement of carbon fiber composites. *Appl. Therm. Eng* 2009, 29, 2, 418–421.
- [132] Chiavazzo, E., and Asinari, P., Reconstruction and modeling of 3d percolation networks of carbon fillers in a polymer matrix. *Int. J. Therm. Sci* 2010, 49, 12, 2272–2281.
- [133] Fang, W.-Z., Chen, L., Gou, J.-J., and Tao, W.-Q., Predictions of effective thermal conductivities for three-dimensional four-directional braided composites using the Lattice Boltzmann method. *International Journal of Heat and Mass Transfer* 2016, 92, 120–130.
- [134] Reith, D., Meyer, H., and Müller-Plathe, F., Mapping atomistic to coarse-grained polymer models using automatic simplex optimization to fit structural properties. *Macromolecules* 2001, 34, 7, 2335–2345.
- [135] Rzepiela, A. J., Louhivuori, M., Peter, C., and Marrink, S. J., Hybrid simulations: combining atomistic and coarse-grained force fields using virtual sites. *Phys. Chem. Chem. Phys* 2011, 13, 10437–10448.
- [136] Chiavazzo, E., Covino, R., Coifman, R. R., Gear, C. W., Georgiou, A. S., Hummer, G., and Kevrekidis, I. G., Intrinsic map dynamics exploration for uncharted effective free-energy landscapes. *Proceedings of the National Academy of Sciences* 2017, 114, 28, E5494–E5503.
- [137] Georgiou, A. S., Bello-Rivas, J. M., Gear, C. W., Wu, H.-T., Chiavazzo, E., and Kevrekidis, I. G., An exploration algorithm for stochastic simulators driven by energy gradients. *Entropy* 2017, 19, 7, 294.
- [138] Dirk, R., Mathias, P., and Florian, M., Deriving effective mesoscale potentials from atomistic simulations. *J. Comput. Chem* 2003, 24, 13, 1624–1636.
- [139] Fritz, D., Harmandaris, V. A., Kremer, K., and van der Vegt, N. F. A., Coarse-grained polymer melts based on isolated atomistic chains: Simulation of polystyrene of different tacticities. *Macromolecules* 2009, 42, 19, 7579–7588.
- [140] Hsu, D. D., Xia, W., Arturo, S. G., and Keten, S., Systematic method for thermomechanically consistent coarse-graining: A universal model for methacrylate-based polymers. *J. Chem. Theory Comput* 2014, 10, 6, 2514–2527.
- [141] Zhao, J., Jiang, J.-W., Wang, L., Guo, W., and Rabczuk, T., Coarse-grained potentials of single-walled carbon nanotubes. *J. Mech. Phys. Solids* 2014, 71, 197–218.
- [142] Ruiz, L., Xia, W., Meng, Z., and Keten, S., A coarse-grained model for the mechanical behavior of multi-layer graphene. *Carbon* 2015, 82, 103–115.
- [143] Arash, B., Park, H. S., and Rabczuk, T., Mechanical properties of carbon nanotube reinforced polymer nanocomposites: A coarse-grained model. *Composites Part B: Engineering* 2015, 80, 92–100.
- [144] Arash, B., Park, H. S., and Rabczuk, T., Tensile fracture behavior of short carbon nanotube reinforced polymer composites: A coarse-grained model. *Compos. Struct* 2015, 134, 981–988.
- [145] Mousavi, A. A., Arash, B., Zhuang, X., and Rabczuk, T., A coarse-grained model for the elastic properties of cross linked short carbon nanotube/polymer composites. *Composites Part B: Engineering* 2016, 95, 404–411.
- [146] Zhou, B., Luo, W., Yang, J., Duan, X., Wen, Y., Zhou, H., Chen, R., and Shan, B., Simulation of dispersion and alignment of carbon nanotubes in polymer flow using dissipative particle dynamics. *Comput. Mater. Sci* 2017, 126, 35–42.
- [147] Ju, S.-P., Wang, Y.-C., Huang, G.-J., and Chang, J.-W., Miscibility of graphene and poly(methyl methacrylate) (PMMA): molecular dynamics and dissipative particle dynamics simulations. *RSC Adv* 2013, 3, 8298–8307.

- [148] Lin, F., Yang, C., Zeng, Q., and Xiang, Y., Morphological and mechanical properties of graphene-reinforced PMMA nanocomposites using a multiscale analysis. *Comput. Mater. Sci* 2018, 150, 107–120.
- [149] Kilbride, B. E., Coleman, J. N., Fraysse, J., Fournet, P., Cadec, M., Drury, A., Hutzler, S., Roth, S., and Blau, W. J., Experimental observation of scaling laws for alternating current and direct current conductivity in polymer-carbon nanotube composite thin films. *J. Appl. Phys* 2002, 92, 7, 4024–4030.
- [150] Bao, W., Meguid, S., Zhu, Z., Pan, Y., and Weng, G., A novel approach to predict the electrical conductivity of multifunctional nanocomposites. *Mech. Mater* 2012, 46, Supplement C, 129–138.
- [151] Grabowski, K., Zbyrad, P., Uhl, T., Staszewski, W. J., and Packo, P., Multiscale electro-mechanical modeling of carbon nanotube composites. *Comput. Mater. Sci* 2017, 135C, 169–180.
- [152] Castellino, M., Rovere, M., Shahzad, M. I., and Tagliaferro, A., Conductivity in carbon nanotube polymer composites: A comparison between model and experiment. *Composites Part A* 2016, 87, Supplement C, 237–242.
- [153] Dijkstra, E., A note on two problems in connexion with graphs. *Numer. Math* 1959, 1, 1, 269–271.
- [154] Bao, W. S., Meguid, S. A., Zhu, Z. H., and Weng, G. J., Tunneling resistance and its effect on the electrical conductivity of carbon nanotube nanocomposites. *J. Appl. Phys* 2012, 111, 9, 093726.
- [155] Wang, S., Liang, Z., Wang, B., and Zhang, C., Statistical characterization of single-wall carbon nanotube length distribution. *Nanotechnology* 2006, 17, 3, 634.
- [156] Bohm, D., *Quantum Theory*, Dover Publications: Dover Books on Physics, 1989.
- [157] Zeng, X., Xu, X., Shenai, P. M., Kovalev, E., Baudot, C., Mathews, N., and Zhao, Y., Characteristics of the electrical percolation in carbon nanotubes/polymer nanocomposites. *J. Phys. Chem. C* 2011, 115, 44, 21685–21690.
- [158] Gong, S., Zhu, Z. H., and Haddad, E. I., Modeling electrical conductivity of nanocomposites by considering carbon nanotube deformation at nanotube junctions. *J. Appl. Phys* 2013, 114, 7, 074303.
- [159] Rahatekar, S. S., Hamm, M., Shaffer, M. S. P., and Elliott, J. A., Mesoscale modeling of electrical percolation in fiber-filled systems. *J. Chem. Phys* 2005, 123, 13, 134702.
- [160] Zhai, S., Zhang, P., Xian, Y., Zeng, J., and Shi, B., Effective thermal conductivity of polymer composites: Theoretical models and simulation models. *Int. J. Heat Mass Transfer* 2018, 117, 358–374.
- [161] He, B., Mortazavi, B., Zhuang, X., and Rabczuk, T., Modeling Kapitza resistance of two-phase composite material. *Compos. Struct* 2016, 152, Supplement C, 939–946.
- [162] Ramani, K., and Vaidyanathan, A., Finite element analysis of effective thermal conductivity of filled polymeric composites. *J. Compos. Mater* 1995, 29, 13, 1725–1740.
- [163] Ahmed, S., and Masud, A., “Evaluation of effective thermal conductivity of multiwalled carbon nanotube reinforced polymer composites using finite element method and continuum model,” *Procedia Eng.*, vol. 90, pp.129–135, 2014. 10th International Conference on Mechanical Engineering, ICME 2013.
- [164] Li, X., Fan, X., Zhu, Y., Li, J., Adams, J. M., Shen, S., and Li, H., Computational modeling and evaluation of the thermal behavior of randomly distributed single-walled carbon nanotube/polymer composites. *Comput. Mater. Sci* 2012, 63, 207–213.
- [165] Srivastava, A., and Kumar, D., A continuum model to study interphase effects on elastic properties of CNT/GS-nanocomposite. *Mater. Res. Express* 2017, 4, 2, 025036.
- [166] Wernik, J., and Meguid, S., Multiscale micromechanical modeling of the constitutive response of carbon nanotube-reinforced structural adhesives. *Int. J. Solids Struct* 2014, 51, 14, 2575–2589.

- [167] Odegard, G., Gates, T., Wise, K., Park, C., and Siochi, E., Constitutive modeling of nanotube-reinforced polymer composites. *Compos. Sci. Technol* 2003, 63, 11, 1671–1687.
- [168] Liu, Y., and Chen, X., Evaluations of the effective material properties of carbon nanotube-based composites using a nanoscale representative volume element. *Mech. Mater* 2003, 35, 1, 69–81.
- [169] Huang, J., and Rodrigue, D., Equivalent continuum models of carbon nanotube reinforced polypropylene composites. *Materials & Design* 2013, 50, 936–945.
- [170] Kumar, D., and Srivastava, A., Elastic properties of CNT-and graphene-reinforced nanocomposites using RVE. *Steel and Composite Structures* 08 2016, 21, 1085–1103.
- [171] Golestanian, H., and Gahruei, M. H., Effective mechanical properties of nanocomposites reinforced with wavy carbon nanotubes. *Mater. Sci. Technol* 2013, 29, 8, 913–920.
- [172] Nilsson, F., Krüchel, J., Schubert, D. W., Chen, F., Unge, M., Gedde, U. W., and Hedenqvist, M. S., Simulating the effective electric conductivity of polymer composites with high aspect ratio fillers. *Compos. Sci. Technol* 2016, 132, 16–23.
- [173] Seidel, G. D., and Lagoudas, D. C., A micromechanics model for the electrical conductivity of nanotube-polymer nanocomposites. *J. Compos. Mater* 2009, 43, 9, 917–941.
- [174] Feng, C., and Jiang, L., Micromechanics modeling of the electrical conductivity of carbon nanotube (CNT)-polymer nanocomposites. *Compos. A Appl. Sci. Manuf* 2013, 47, Supplement C, 143–149.
- [175] Jacob, A., “What is the biggest challenge facing the composites industry today?,” *Plastics magazine, Materials Today*, 2013. <https://www.materialstoday.com/composite-industry/comment/what-is-the-biggest-challenge-facing-the-composite/>.
- [176] FiberEUUse, “Large scale demonstration of new circular economy value chains based on the reuse of end-of-life fiber reinforced composites,” *CORDIS Europe*, vol. 730323, 2017–2021. https://cordis.europa.eu/project/rcn/210178_en.html.
- [177] Yao, S.-S., Jin, F.-L., Rhee, K. Y., Hui, D., and Park, S.-J., Recent advances in carbon-fiber-reinforced thermoplastic composites: A review. *Composites Part B: Engineering* 2017, 142, 241–250.
- [178] Gantayat, S., Rout, D., and Swain, S. K., Carbon nanomaterial-reinforced epoxy composites: A review. *Polymer-Plastics Technology and Engineering* 2018, 57, 1, 1–16.
- [179] Chen, J., Yan, L., Song, W., and Xu, D., Interfacial characteristics of carbon nanotube-polymer composites: A review. *Composites Part A: Applied Science and Manufacturing* 2018, 114, 149–169.
- [180] Chernova, T., Murphy, F. A., Galavotti, S., Sun, X.-M., Powley, I. R., Grosso, S., Schinwald, A., Zacarias-Cabeza, J., Dudek, K. M., Dinsdale, D., Quesne, J. L., Bennett, J., Nakas, A., Greaves, P., Poland, C. A., Donaldson, K., Bushell, M., Willis, A. E., and MacFarlane, M., Long-fiber carbon nanotubes replicate asbestos-induced mesothelioma with disruption of the tumor suppressor gene *Cdkn2a (ink4a/Arf)*. *Current Biology* 2017, 27, 21, .e6, 3302–3314.
- [181] Zhang, W., Chen, L., Zhang, J., and Huang, Z., Design and optimization of carbon nanotube/polymer actuator by using finite element analysis. *Chinese Physics B* 2017, 26, 4, 048801.
- [182] Grabowski, K., Blacha, I., Staszewski, W. J., Uhl, T., and Packo, P., Optimization of multi-scale modelling of CNT/polymer composite strain sensors, In: *Health Monitoring of Structural and Biological Systems 2017*, Vol. 10170, 101700R, International Society for Optics and Photonics, 2017.
- [183] Gong, S., Wang, Y., Xiao, Z., Li, Z., Wang, Z. X., Lei, R. S., and Zhu, Z. H., Effect of temperature on the electrical property of epoxy composites with carbon nanotube. *Compos. Sci. Technol* 2017, 149, 48–54.

- [184] Gong, S., Wu, D., Li, Y., Jin, M., Xiao, T., Wang, Y., Xiao, Z., Zhu, Z., and Li, Z., Temperature-independent piezoresistive sensors based on carbon nanotube/polymer nanocomposite. *Carbon* 2018, 137, 188–195.
- [185] Zhou, G., Zhang, H., Xu, S., Gui, X., Wei, H., Leng, J., Koratkar, N., and Zhong, J., Fast triggering of shape memory polymers using an embedded carbon nanotube sponge network. *Sci. Rep* 2016, 6, 24148.
- [186] Gao, Y., Wan, Y., Wei, B., and Xia, Z., Capacitive enhancement mechanisms and design principles of high-performance graphene oxide-based all-solid-state supercapacitors. *Adv. Funct. Mater* 2018, 28, 17, 1706721.

Marta Martins, Joana F. Guedes, Celeste Pereira, Stefan Forero,
Volker Liedtke, Jiří Zelenka, Jan Václavík, Ernst Pfeiffer,
Laurent Pambaguian, Advenit Makaya, Nuno Rocha

4 Carbon nanotube-based materials for space applications

4.1 Introduction

Carbon nanomaterials embedded in carbon fiber-reinforced composite materials can improve specific performance characteristics such as electrical conductivity, resistance to mechanical fatigue and crack propagation, structural damping, Passive Intermodulation (PIM) reduction, Electromagnetic compatibility (EMC) shielding, re-machining and coating capabilities. Some of these improvements were investigated and demonstrated in the ESA projects “NACO-1” and “NACO-2” performed between 2007 and 2013. This chapter outlines the work performed during these activities for the development of carbon fiber-reinforced polymer (CFRP) composites integrating carbon nanotube (CNT) buckypapers (BP) to be used in space applications.

The ranking of space applications potentially benefitting CNT technology has been reviewed throughout these activities. The final activity is aimed at finally selecting an application with highest potential for performance improvements. For that, an optical CFRP mirror with comparable characteristics of conventional Zerodur-based mirrors featuring the inclusion of 3D nanotube structures was selected and manufactured.

Although CFRP composites are being used for reflectors in Space applications, due to its outstanding mechanical and thermal properties at low mass, optical mirroring properties are limited by the surface properties of the CFRP. One should note that each composite layer is composed of 1D and/or 2D patterns of continuous carbon fibers, each one of them having about 10 μm of diameter, which are combined in tows of thousands of carbon fibers leading to a tow a few millimeters large. This configuration creates an undesired composite surface roughness, in a phenomenon usually known as print-through effect (Figure 4.1).

CFRP surface roughness limits its reflective properties. To afford further mirroring characteristics, polishing and metal coatings strategies can be followed. However, the

Marta Martins, Joana F. Guedes, Celeste Pereira, Nuno Rocha, INEGI – Institute of Science and Innovation in Mechanical and Industrial Engineering, Porto, Portugal

Stefan Forero, FutureCarbon, Bayreuth, Germany

Volker Liedtke, AAC – Aerospace & Advanced Composites, Wiener Neustadt, Austria

Jiří Zelenka, TOSEDA s.r.o., Staré Čívce, Czech Republic

Jan Václavík, Institute of Plasma Physics of CAS, Prague, Czech Republic

Ernst Pfeiffer, HPS GmbH, München, Germany

Laurent Pambaguian, Advenit Makaya, ESA ESTEC, Noordwijk, Netherlands

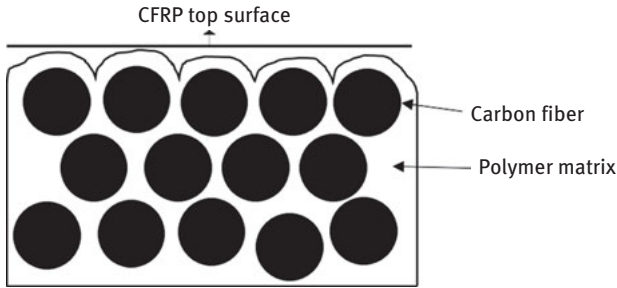


Figure 4.1: Representative image of print-through effect in a CFRP.

former is inherently limited by the continuous form of the carbon fibers, whereas the latter is also limited by the print-through characteristics of the CFRP. To overcome this limitation, inclusion of carbon nanotubes (CNT) at the top surface of the composites has been proposed as a solution to reduce its print-through behavior. In addition, the nearly isotropic nature of the CNT top layer is expected to ease polishing and metal coating processing. A material configuration in which a top layer of resin rich in CNT is added in the CFRP lay-up allows the reduction of the print-through effect on the manufactured CFRP and improves the reflective properties of the top surface.

The potential of CNTs is considered as tremendous; their intrinsic properties make them very attractive for Space applications where the characteristics of the materials often represent a limit to the development of technologies. Much of the development efforts have been focused on retaining CNTs large aspect ratio, achieving good interfacial stress transfer (surface modification), good dispersion and alignment in the polymer matrix during processing, all for maximizing the nanotubes effect. As a result, a growing number of companies already supply CNT-based masterbatches or compounds to be used in plastic/composite processing. Nevertheless, these materials are expensive, limited in the type of dispersing resin systems and on the CNT weight loading, and very difficult to incorporate in the conventional processes due to the very high viscosities.

In fact, one of the main difficulties that have been associated with the manufacturing of CFRP materials containing nanotubes is the poor processability of the resin systems modified with CNT, due to the extremely high viscosities. It is practically impossible to obtain a surface with quality when using high viscosity systems.

CNT BP consist of a 3D structure (skeleton) of CNTs either being single-walled (SWNT) or multiwalled or carbon nanofibers (CNF), which show a unique combination of inherent CNT/CNF properties while maintaining their lengths in a mat-like or 3D structure. These structures can be an alternative to overcome dispersion issues usually associated with the use of CNTs in resin masterbatches. In addition, higher CNT contents can also be attained by the use of three-dimensional CNT structures; therefore, CNT in the form of BP is a promising choice for boosting CFRP properties.

4.2 Preparation of epoxy nanocomposites based on high CNT content buckypapers

The main objective of the first study was to develop and characterize highly loaded CNT-based nanocomposites, by infiltrating nanotube skeletons with either organic or inorganic matrix. We herein present the main results obtained with an organic thermoset (epoxy) resin.

A new approach was used to produce these CNT nanocomposites, where the CNT skeletons or papers were infiltrated with a low-viscosity epoxy resin in a closed mold. The CNT were first produced in thin papers called BP to form networks of elongated nanotubes. The impregnation was performed by infiltrating the resin along all the 3D CNT structure. The level of impregnation of the final structure was assessed by physical measurements and observations under scanning electron microscopy (SEM). The results showed that the proposed processing approach is capable of producing well-dispersed nanocomposites with high CNT loading (more than 12 wt% in resin weight), which are important for developing high-performance structures based on CNT with good thermal and electrical conductivity.

4.2.1 Materials

CNT thin papers, with 80 mm of diameter, functionalized (-COOH) and solvent (hexane or ethanol, EtOH) were produced by Future Carbon, GmbH. The properties of the nanotubes used for the preparation of the skeletons are described in Table 4.1.

Table 4.1: Properties of the CNTs used for the development of buckypapers.

Property	
Diameter (nm)	10–20
Length (μm)	20–40
Purity (min wt% C)	>98%
Number of walls	5–15

The epoxy resin used to infiltrate the CNT skeleton was SR 8100 with SD 8824 hardener from SICOMIN. This system has low viscosity at room temperature (110 mPa s), facilitating the resin flow and impregnation of the skeletons. The gel time of about 1 h at 40 °C is suitable for a low-pressure infiltration. The recommended cure and postcure cycles for this system are 24 h at room temperature and 8 h at 60 °C, respectively.

4.2.2 Sample manufacturing

The impregnation of the CNT BP was performed at room temperature using a closed mold, as represented in Figure 4.2. For this mold, two spacers are available: one of 0.5 mm used for one layer composites and the other of 1 mm used for two layer composites. Three runs were performed using CNT papers with different chemical treatments, namely hexane or ethanol.

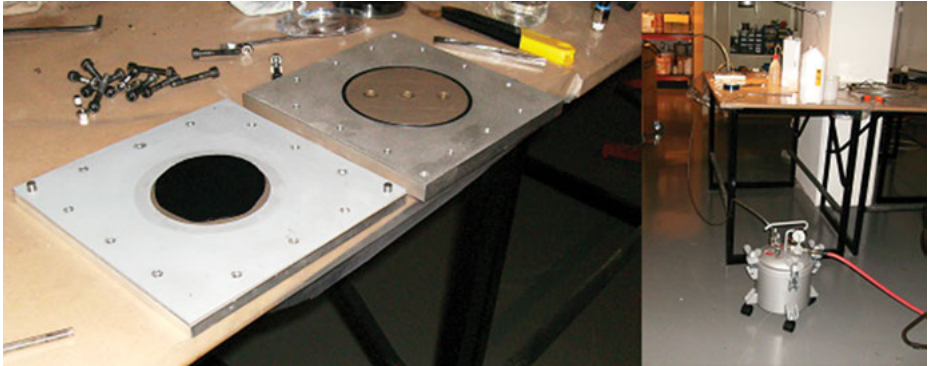


Figure 4.2: (Left) CNT skeleton positioned in the closed mold, before resin infiltration; (right) resin trap, placed before the vacuum pump, used to store eventual excess resin from the infiltration process.

The procedure used for the infiltration process can be roughly divided into the following steps:

1. Prepare the mold with the application of release agent
2. Put spacer in place
3. Place the CNT BP in the bottom mold
4. Close the mold
5. Connect the resin entry and the vacuum pump outlet
6. Turn on vacuum pump and verify if mold is completely sealed
7. Prepare the resin
8. Infiltrate the resin

The vacuum level used during the infiltration process was of 0.2 bar; the resin was injected in the mold at room temperature and the mold itself was kept at room temperature. The skeletons were allowed to cure 24 h at room temperature inside the mold, followed by demolding and postcure cycle in an electrical oven.

4.2.3 Characterization

CNT papers and composite samples were visual inspected, measured and weighted before and after infiltration. Fractured surfaces of samples were observed under a high-resolution SEM for the level of impregnation and surface quality assessment, as well as for measurements of the nanotube and resin layer thicknesses.

4.2.4 Results and discussion

4.2.4.1 Physical characterization

Figure 4.3 shows an SEM image of the BP surface (a), appearance of a CNT paper before (b) and after (c) infiltration. CNT papers have good strength and flexibility to allow handling like carbon fiber mat. The SEM image (a) shows that CNT possess diameters in the range of 10–20 nm and lengths in the range of 20–40 μm . CNT are produced solely by catalytic chemical vapor deposition as described elsewhere [1]. The number of walls is between 5 and 15.

Table 4.2 summarizes the main physical characteristics of the CNT papers used and of the nanocomposites obtained, namely the thickness and mass values. The CNT BP papers used in the manufacturing of samples 1 and 2 are hexane treated and the one used for sample 3 is ethanol treated. The thickness of the CNT papers is uniform, ranging from 350 to 375 μm .

After resin infiltration, the CNT BP thicknesses increase more than doubling its value. This increase is, however, very close to all samples, in the range of 405–430 μm . The mass of the obtained nanocomposites ranges between 3.11 and 3.98 g and the CNT weight content calculated directly (from the variation of mass before and after infiltration) is between 11.6% and 15.4% [2]. The higher CNT content was obtained for sample 1, with hexane-treated nanotubes. From these results we cannot conclude about a relation between solvent treatment and CNT content in the composite. Sample 2 is the one that has higher mass and consequently lower CNT content. This is due to the higher amount of resin that infiltrated the paper. The infiltration process shall be controlled in order to achieve highly loaded CNT composites, the reproducibility of the process and thus be able to conclude on the effect of the paper solvent treatment on composite properties.

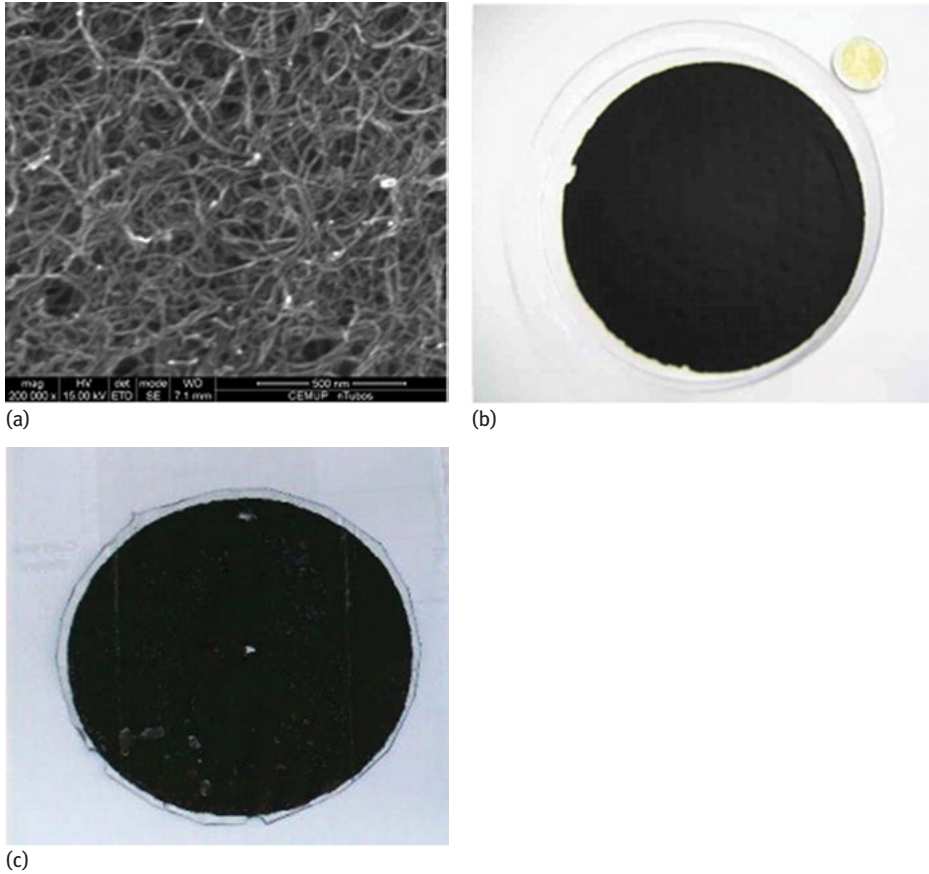


Figure 4.3: SEM image of the buckypaper surface (a) and the aspect of the buckypaper before (b) and after infiltration (c).

Table 4.2: Summary of the CNT papers and nanocomposite characteristics.

Sample	CNT paper			Nanocomposite		
	Solvent	Thickness (mm)	Mass (g)	Thickness (mm)	Mass (g)	CNT wt%
1	Hexane	0.350	0.4798	0.760	3.11	15.4
2	Hexane	0.370	0.4616	0.803	3.98	11.6
3	Ethanol	0.375	0.4576	0.780	3.27	14.0

4.2.4.2 Structure observations

In Figure 4.4, two microscopic pictures are presented, which are obtained under two magnifications and from different locations along the thickness of the sample 1. It is

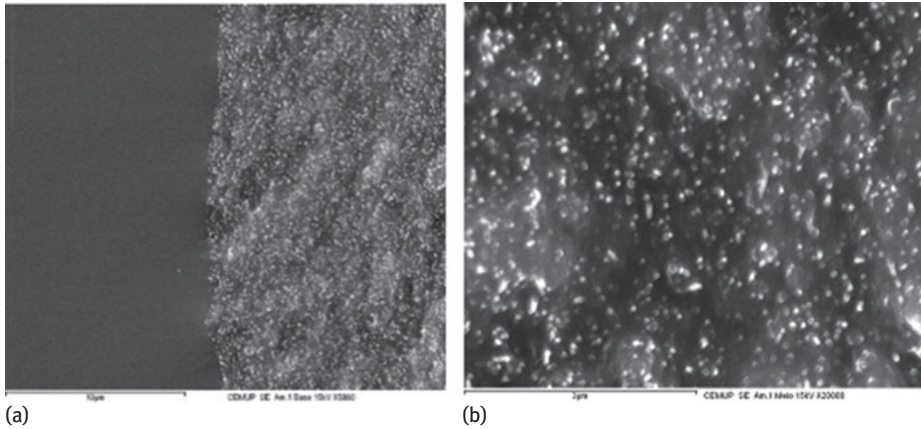


Figure 4.4: SEM pictures of sample 1 (a) in the bottom side of the composite and (b) in the middle of the composite.

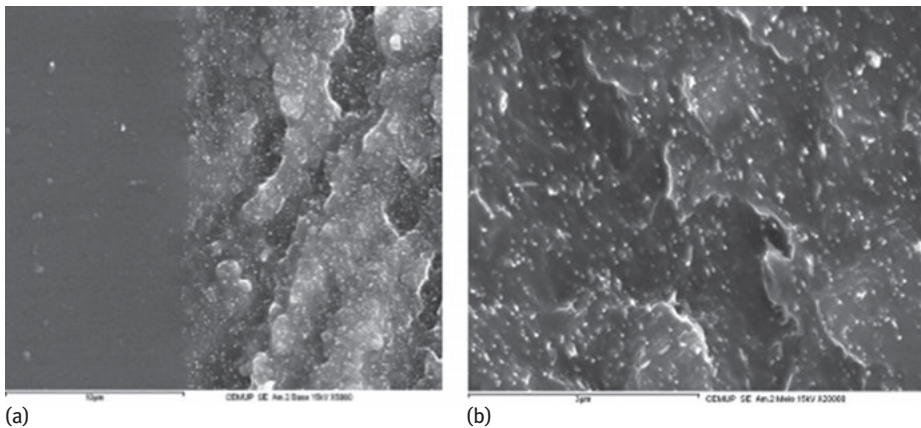


Figure 4.5: SEM pictures of sample 2 (a) in the bottom side of the composite and (b) in the middle of the composite.

possible to observe a thick layer of resin (more than 0.2 mm) located in the bottom side of the sample and nanotubes well impregnated by resin in the middle of the sample.

Figure 4.5 presents two microscopic pictures for sample 2. As for sample 1, a rich resin layer is observed in the bottom side (lower than 0.2 mm) and upper side (lower than 0.100 mm) of the sample, and a good matrix infiltration in the middle is witnessed.

Figure 4.6 shows the pictures obtained for the third run sample. It is observed that the BP does not maintain the initial form (appearing slightly curved in the images) and their thickness is variable along the diameter. Once again, a thick layer of

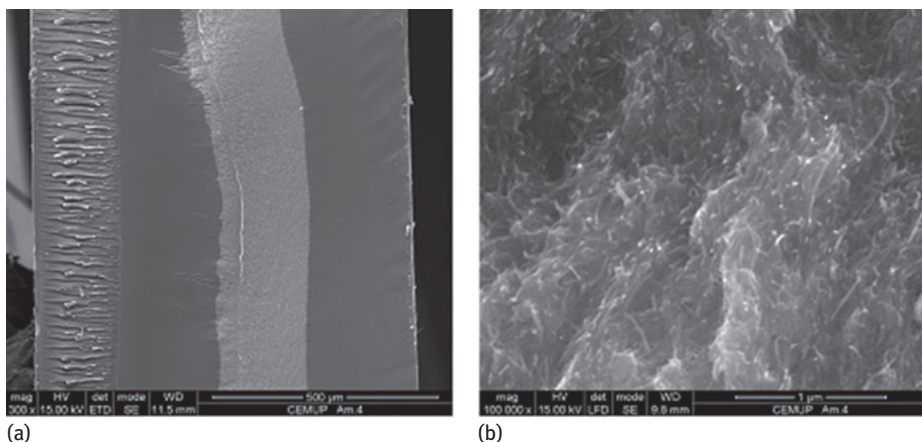


Figure 4.6: Composite SEM pictures of the third run sample: (a) along the thickness of the composite and (b) in the middle of the composite.

resin is covering the paper. In fact, it is possible to see that the thickness of the resin layer is much higher than the CNT BP one. Once more, a good matrix infiltration in the middle is observed.

Table 4.3 summarizes the measurements of the top and bottom resin-rich layers and CNT paper thicknesses, after the infiltration process, measured from the SEM observations. It is observed that the thickness of the paper does not remain unchangeable, since it swells for samples 1 and 2 and shrinks considerably for sample 3.

Table 4.3: Resume of the characteristics of CNT papers and CNT nanocomposites.

Sample	Nanocomposite			
	CNT thickness before resin infiltration (mm)	CNT thickness after resin infiltration (mm)	Thickness of resin layers (top + bottom)	CNT wt% (eliminating resin-rich layers)
1	0.350	0.428	0.366	34.8
2	0.370	0.462	0.282	17.4
3	0.375	0.220	0.624	47.4

Two possible explanations for this can be prompted: the first one is that the solvent treatment has an effect on the resin behavior – contraction or expansion – during the cure [3]; the second is that the solvent treatment increases or decreases the infiltration of the resin into the paper, either by changing the wettability or the permeability of the CNT papers [4]. P.E. Lopes and coauthors [5] studied the wettability (by contact

angle measurements) of CNT BP with different treatments. However, the CNT treatments studied were heat, carboxyl or nonfunctionalized, which are different than the ones reported here.

A rough estimation of the possible CNT content that could be achieved, if the resin-rich layers were eliminated, calculated and presented in Table 4.3. The most surprising results are the differences between samples 1 and 2, which have the same CNT treatment. The second sample has the lower CNT content and confirms the high portion of resin in the composite. Once more, we conclude that the infiltration process should be well controlled, and a release film must be used in the surfaces of the CNT papers intended for reducing the thickness of top and bottom layers of resin and the permeability of the CNT papers accessed. The resin content is a critical aspect of this CNT composites, since the excess of resin can affect negatively some properties, namely the thermal and electrical conductivity as well the mechanical properties [6–8].

These extrapolated results of CNT content (presented in Table 4.3) are more in agreement with those reported in literature [9]. Wang and coworkers have prepared SWNT BP/epoxy resin nanocomposites by using very thin papers (0.1–0.5 mm) stacked together in a hot press machine. The resin was infiltrated in papers after being diluted with acetone due to its high viscosity (2,700 mPa.s). They produced nanocomposites with SWNT loadings as high as 39% with nanopore sizes in the BP in the range of 100–200 nm.

4.2.5 Conclusions

It was the purpose of this experimental work to produce CNT/epoxy resin composites by infiltrating a low-viscosity epoxy resin in membranes of nanotube networks called BP, supplied by Future Carbon. The CNT content achieved in the composites is between 11.6% and 15.4% in weight. In all the SEM observations of the composites produced, there is evidence that there is a good level of impregnation, yet the resin layer around the CNT BP is very thick. The process must be optimized in order to obtain composites without excess of resin in the surfaces, since the resin affects negatively some properties of the composites, namely the thermal and electrical conductivity as well the mechanical properties.

4.3 Manufacturing process scale-up and integration into CFRP composite structures

The main purpose of project NACO2 was the scale-up processing of CNT BP and their integration on CFRP composites. In order to find the most suitable manufacturing method, a number of tests were planned taking into account critical aspects of the

manufacturing parameters (such as mold materials, vacuum and pressure levels during curing and resin impregnation temperature) [9]. Based on this, several manufacturing runs were experimentally performed, aiming to obtain high-quality CNT–CFRP composites. From these runs, it was concluded that the use of a steel mold coated with Teflon release films, combined with manual resin impregnation at room temperature and cure in the autoclave under vacuum and pressure lead to improved materials. At the end of the project, a CNT–skeleton composite demonstrator was obtained; herein we present the manufacturing details of that demonstrator.

4.3.1 Materials

Oxidized CNT skeletons in paper containing binder were used. The epoxy resin system used was: Araldite LY556, Aradur HY906 and Accelerator DY070, manufactured by HUNTSMAN, Switzerland. A Style 450/T300 Plain Weave 140 g/m² carbon fiber fabric of Cramer Fabrics, Germany, was used for the manufacturing of the demonstrator. Table 4.4 presents the characteristics and suppliers of the raw materials used for manufacturing the polymer demonstrator.

Table 4.4: Resume of the materials used in CNT–polymer demonstrator.

Materials	Main characteristics	Supplier
CNT skeleton	Oxidized CNTs, paper form, with binder	Future Carbon
Resin	Epoxy system (LY556 + HY906 + DY070); pot-life: 50–55 h at 25 °C; viscosity: 1,900–2,100 mPa S	Huntsman
Carbon fiber	CF Style 450/T300 Plain Weave 140 g/m ²	CC Fabrics

The CNT skeleton was produced by tape casting and has a binder amount of 29% in weight. The thickness is about 70 μm, as measured by optical microscopy and the size was 107 × 11 cm².

4.3.2 Sample manufacturing

The demonstrator was produced by hand lay-up followed by vacuum bagging in the autoclave and using Teflon as release film. The resin was applied at room temperature between all the reinforcement layers, and the CNT BP was applied as the top layer. The “striped” surface of the CNT skeleton (BP side that was cast in the release film) was faced toward the CFRP material during the impregnation. No resin in the top layer (on the BP) was applied. The pressure used in the autoclave was of 3 bar, the vacuum level was of 150–250 mbar and the temperature program was 2 h at 120 °C + 2 h at 180 °C. Figure 4.7 shows the different stages of the demonstrator manufacturing.

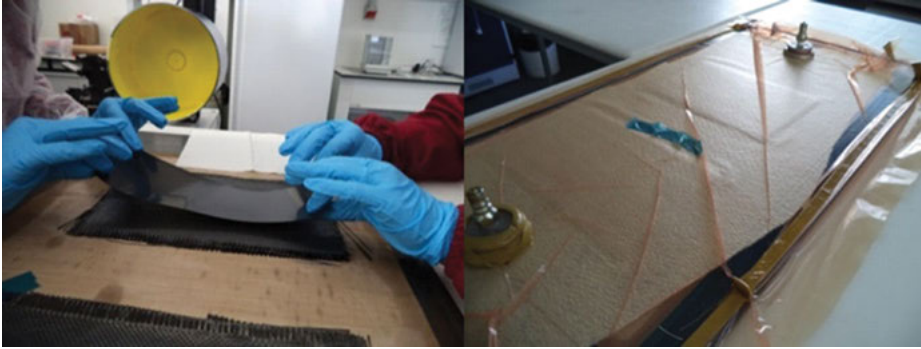


Figure 4.7: Different stages of the manufacturing process of the demonstrator.

4.3.3 Results and discussion

4.3.3.1 CNT skeleton handling

Since the CNT skeleton used had a very low thickness ($70\ \mu\text{m}$), it was important that the material is very well conditioned. Also, due to its large size, it is crucial to be easy to manipulate so the composite manufacturing process is feasible. The CNT skeleton used in the demonstrator was packaged between two polymer substrate foils. The upper substrate foil was very easy to remove; however, the lower foil was completely “glued” to the BP. The cutting of the structure was easily performed with the use of supporting plates to maintain the CNT BP immobile and fully supported. Figure 4.8 shows two pictures of the conditioning and handling of the skeleton.

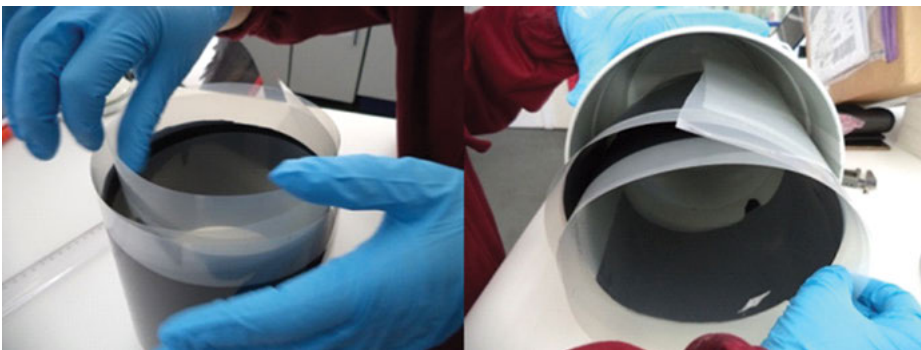


Figure 4.8: Conditioning, handling and aspect of BP used for manufacturing the demonstrator.

4.3.3.2 CNT skeleton preparation

As mentioned earlier, the BP was “glued” to the supporting foil. The procedure for removing the CNT paper, used in the demonstrator, from the casting substrate is given as follows:

1. cutting of the edges with the aid of supporting plates;
2. face the supporting film upward;
3. release a film tip with the aid of a tweezer;
4. separate the film from the BP using a metallic roller, while pulling the film upward and
5. continue until both materials are completely separated.

Figure 4.9 shows the sequence of procedures performed to separate the CNT skeleton from the supporting foil. It can be seen that the face of the BP that was “glued” to the polymer foil showed a different aspect, where a “striped” pattern is clearly visible. This stripped surface was faced toward the CFRP material during the impregnation run.

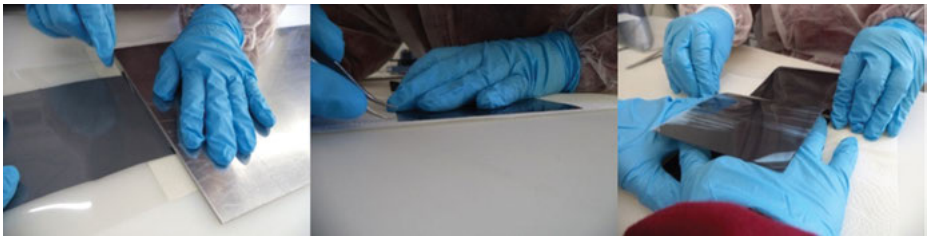


Figure 4.9: Procedure used for cutting and removing the supporting film from the buckypaper.

4.3.3.3 Visual inspections

Figure 4.10 shows the aspect of the whole sample after curing cycle and demolding, as well as samples already cut and ready for characterization tests. Some cracks in the BP were visible in the corners of the samples, after the cutting procedure. This can be due to either (i) lack of adhesion of the BP to the CFRP and/or (ii) the poor impregnation of the BP.

4.3.3.4 Structure observations

Figure 4.11 shows the resulting SEM pictures of the demonstrator. The SEM images show that, in some extent, the BP is separated from the CFRP laminate. The level of impregnation of the fibers seems good, and only a small resin layer (50–90 μm) is



Figure 4.10: Polymer demonstrator photographs.

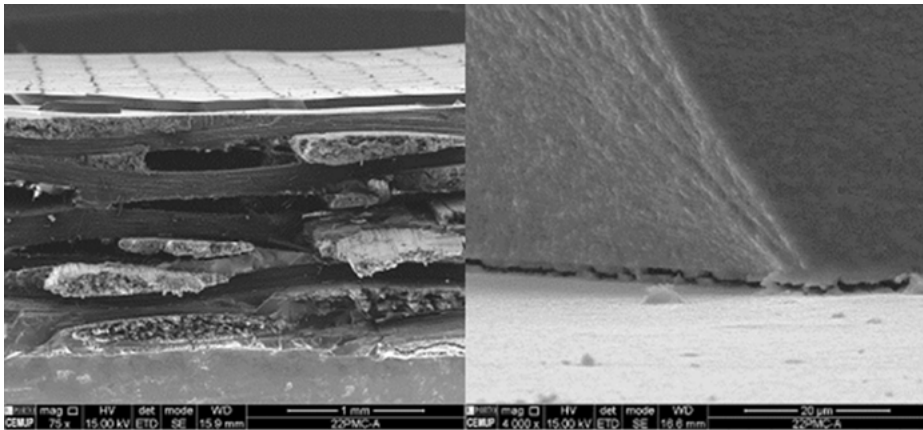


Figure 4.11: Polymer demonstrator photographs.

visible on the bottom surface. As previously mentioned, it is visible that the BP is not bonded to the laminate.

4.3.4 Conclusions

A small demonstrator was manufactured with the main following objectives:

1. to evaluate the quality of packaging;
2. to assess the hand ability of large and thin BP;
3. to determine the effect of the autoclave cycle on the BP's binder;
4. to verify the level of wettability and quality of impregnation of the BP of drop of resin and
5. to demonstrate that the manufacturing of large composites with large and very thin CNT layers is feasible.

The main conclusions from this activity can be summarized as follows [10, 11]:

- The CNT paper packaged between two polymer substrate foils and rolled inside a metallic container is effectively protected.
- BP can be easily manipulated when confined between the substrate foils. However, the removal of the lower substrate requires additional caution.
- The most significant change on the BP after autoclave cycle is the appearance of a layer of polymer (binder) in the surfaces of the skeleton.
- The resin spreads quite easily in the surface (nonstriped) and is able to enter into the material.
- The manufacturing of large composites with large and very thin CNT layers is feasible. However, some improvements or additional studies must be done, since the BP and the laminate were poorly bonded.

4.4 Technology demonstration in CFRP mirrors for space applications

The aim of NATAP activity was to identify, develop and test two selected demonstrators with functional CNT layers. Due to the high variety of options for adapting material properties, an initial trade-off was conducted to identify various space products, where the effect and the possibility of implementation would be maximized. Based on previous development activities, a large number of applications have been investigated in detail with respect to the likelihood to be used in the near future and with potential for improvement of weight, cost, performance and resistance to environmental impacts. From these, an optical mirror with comparable characteristics of conventional Zerodur-based mirrors was selected [12]. The realized demonstrator (28 cm diameter) consists of a sandwich structure, composed of CFRP honeycomb, CFRP face sheet and an infiltrated CNT BP, which serves as a “grindable surface” for highest accuracy. This surface was finally coated with a metal layer (by vapor deposition of aluminum coating and top protective SiO/SiO₂ coating layer) for optical reflectivity in the appropriate wavelength.

4.4.1 Materials

FutureCarbon was in charge of providing a dense CNT-based paper or nonwoven structure to be used as top carbon layer on the concave (optical) side of the mirror surface. From the manufacturing point of view, the CNT paper was the first layer on the mold surface. The CNT papers were manufactured using a filtration process, which resulted in 4–5 wt% of –COOH groups on the nanotube surface, aiming to provide covalent bonding with the resin system. CNT papers with a thickness of approx. 200–300 μm were manufactured, with diameters in the range of 31–32 cm [13].

TOSEDA supplied cyanate ester-based preregs, using a pitch carbon fiber fabric (UD) [Granoc PF(S)-YSH 50A-75 (Mitsui, JP)]. The prepreg sheets used have Fibre Volume Fraction (FVF) of about 50% and were manufactured using a solvent-based process [14].

The honeycomb used was UCF-126-3/8-2.0 RS3 with YSH50 fibers and cyanate ester resin, supplied by Ultracore (Table 4.5).

Table 4.5: Resume of the materials used [15].

Materials	Main characteristics	Supplier
CNT skeleton	–COO groups, 6,96–7,42 mg/cm ² , 31–32 cm diameter	FutureCarbon
Resin	CE Primaset DT4000 (included as prepreg matrix)	Lonza
Carbon fiber	Granoc PF(S)-YSH50A-75 75 g/m ² (included as prepreg reinforcement)	Nippon
Honeycomb	4 pieces 100 × 200 mm ² , UCF-126-3/8-2.0 RS3	Ultracore
Adhesive film	Redux 312L	Hexcel
Prepregs	Average carbon fabric volume concentration in prepreg 51 vol%	Toseda

The mold used for manufacturing the CNT–CFRP mirror was made from Invar, with a nickel surface treatment. The active surface of the mold, however, was machined with sharp tolerances to give the mirror the best surface accuracy possible before the polishing operations.

The preregs manufacturing process includes the following steps:

- Impregnation of Granoc fabric with cyanate ester resin diluted to 35% in acetone
- Air-drying of the impregnated preregs to remove the solvent (acetone concentration < 3%)
- Cutting the air dried pre-preg sheets into the requested size followed
- Marking one corner of the prepreg sheets to keep the same orientation of the carbon fabric fibers (warp and weft)
- Placement of the preregs between PP foils for protection against bonding during storage and transport.

4.4.2 Sample manufacturing

After several manufacturing methodologies used (mainly deriving from the presence of cracks on the CNT surface, which are presented below), the procedure for manufacturing the mirror demonstrator was defined as follows:

1. Cut the CNT BP using a clean sharp tool, with the aid of metal plates, if necessary (Figure 4.12).
2. Dry the CNT BP during 16 h at 110 °C before stacking the materials.

3. If necessary, cut the prepregs in the appropriate dimensions (the warp and weft directions of the prepregs are identified).
4. Register the weight, area and thickness of the materials.
5. Place the Teflon release film in the mold and hold the materials by applying an adhesive tape in the corners (Figure 4.13).
6. Prepare the vacuum bag.
7. Place the CNT-BP in the Teflon release film inside the vacuum bag (Figure 4.14).
8. Lay up the two first prepregs layers, taking into account fabric warp and weft directions (Figure 4.15).
9. Close the vacuum bag and apply vacuum during 10 min with a vacuum level of 800 mbar with a Teflon release film between the prepreg layers and the vacuum bag (Figure 4.16).
10. Repeat the prepreg lay-up procedure until completion.
11. Place the demolding release film as top layer, use breather to eventually absorb excess resin and close the vacuum bag.
12. Apply the vacuum pressure (Figure 4.17). If necessary, the materials can remain under vacuum overnight.
13. Place the materials in the autoclave with the proper curing schedule.

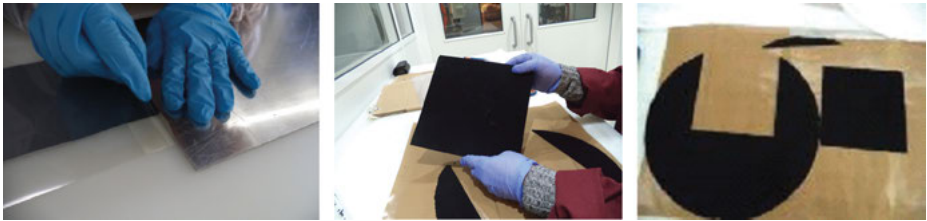


Figure 4.12: Cutting the CNT-BP with the proper size.

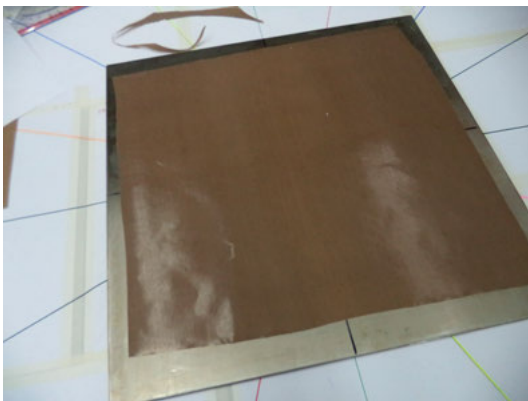


Figure 4.13: Teflon release film.

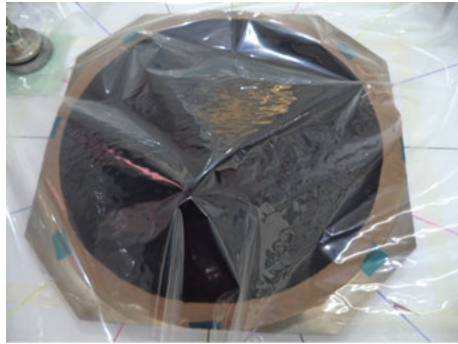
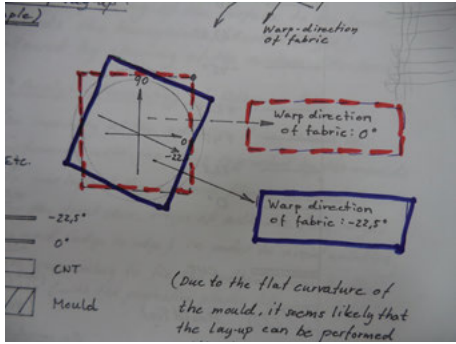


Figure 4.14: CNT-BP facing the mold.

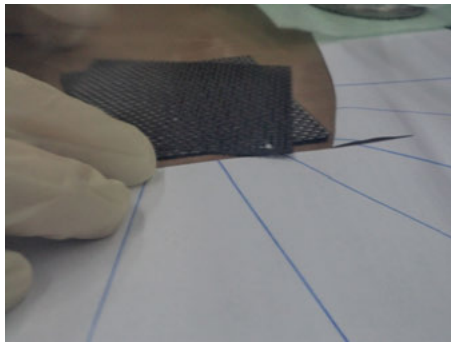
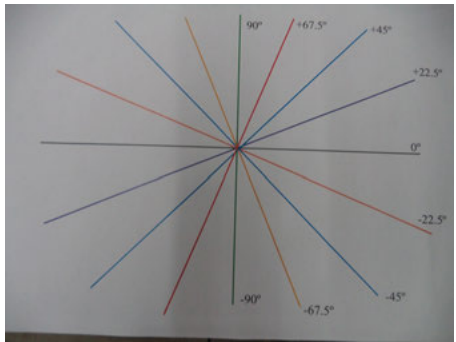


Figure 4.15: Prepreg orientations.

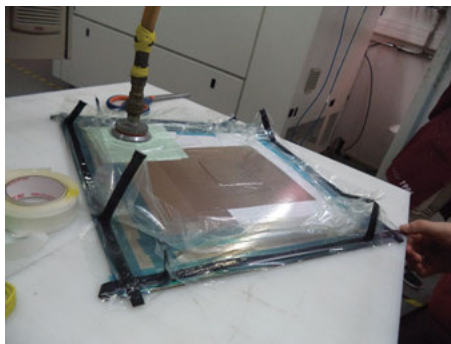
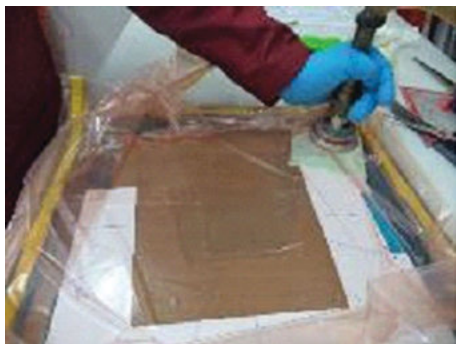


Figure 4.16: Vacuum application.

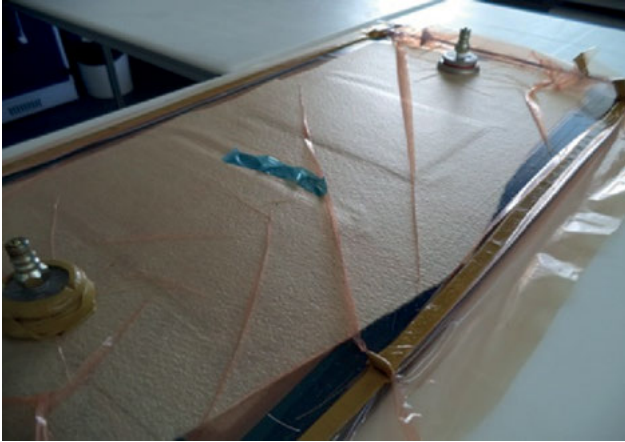


Figure 4.17: Final vacuum-bagged sample, before curing in the autoclave.

4.4.3 Results and discussion

4.4.3.1 Requirement definitions

For specifying the optical mirror properties, the nominal requirements for optical surfaces (not superpolished) were used as baseline. The usual base materials for classical optical mirrors are materials like Zerodur (lithium aluminosilicate glass-ceramic produced by Schott AG), Astrosital glass, ULE (ultralow expansion titaniasilicate glass), fused silica, SiC or nickel Canigen. Table 4.6 lists out the requirements [16]:

Table 4.6: CNT–CFRP optical mirror requirements.

Property	Requirement
Mass	At least 20% less than conventional mirrors
Reflectivity	$R > 0.93$
Surface form tolerance	$RMS < 70 \text{ nm}$
Operating temperatures	$-65 \text{ }^\circ\text{C}/+45 \text{ }^\circ\text{C}$
Nonoperating temperatures	$\pm 120 \text{ }^\circ\text{C}$
Outgassing	According to ECSS [17]
CME	24 ppm
CTE	$< 1 \times 10^{-6}$
Thermal conductivity	$> 0.75 \text{ W/mK}$
Electrical conductivity	$> 10^3 \text{ S/m}$

4.4.3.2 Mirror design

The design of the mirror demonstrator was performed taking into account both the requirements and material properties. The active surface of the mirror is parabolic, circular symmetric, in order to ease the machining operations. The design (Figure 4.18) is based on a sandwich with a flat skin and a front skin with low curvature, rotationally symmetrical with a radius of curvature of 3,360 mm [18].

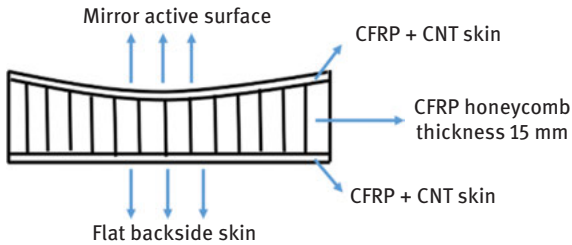


Figure 4.18: CNT-CFRP overall mirror design.

The detailed design also includes the following considerations:

- The reflector sandwich is fully symmetrical in thickness direction.
- Each skin is composed of 16 layers fabric prepreg with surface weight of 75 g/m^2 (without resin) together with a CNT layer.
- The honeycomb is made of CFRP using YSH50A carbon fibers.
- The CNT-CFRP skins are further metalized with vacuum deposit aluminum and protected with a SiO_2 layer.
- The adhesive film bonding the CFRP and the honeycomb is based on cyanate ester resin.
- The CTE of the combined skin + CNT + adhesive film shall be zero.
- The CTE of the CFRP honeycomb shall be zero.
- A design of the complete sandwich as close as possible to CTE zero is necessary.

In order to create a very accurate quasi-isotropic lay-up, the following lay-up of the CNT-CFRP layers is proposed. All orientations are based on warp fabric direction, explained in Figure 4.19.

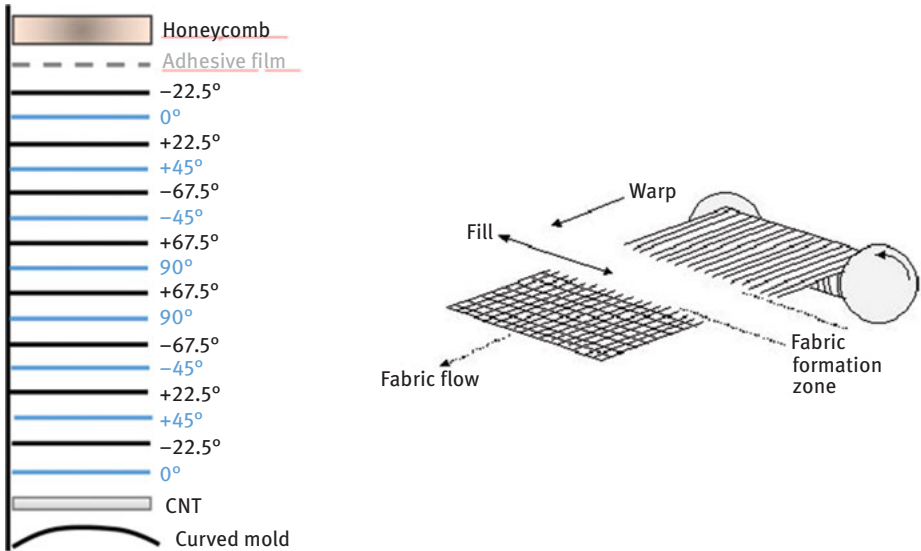


Figure 4.19: CNT-CFRP mirror design: detail of CNT-CFRP skins.

4.4.3.3 Manufacturing trials

NATAP sample manufacturing was performed in several phases. These phases and main objectives of each one are presented in Figure 4.20 [19].

From batch 1 and 2 sample manufacturing, the following conclusions were taken [20]:

- The preimpregnated fiber sheets and BP are easy to manipulate during the manufacturing process – including the production of curved samples – therefore, no major risks are attributed to draping for the expected geometries for the final applications.
- Prepregs prepared for batch 2 with 51% of FVF were found to be a good approach for manufacturing the demonstrator, since the resin amount present is enough to guarantee a good BP impregnation without the need to add additional resins. The CFRP layers were found to be well compacted, reducing the risk of having dry CFRP layers.
- Theoretical calculations also show that these new prepregs result in a final FVF of approximately 65%, which is a good balance between high fiber volume fraction for increased performance and enough resin to guarantee an homogenous structure of the CFRP structure (if previous prepregs with higher FVF were used, it was expected that composite was significantly dry – with 71–78 vol% of fiber).

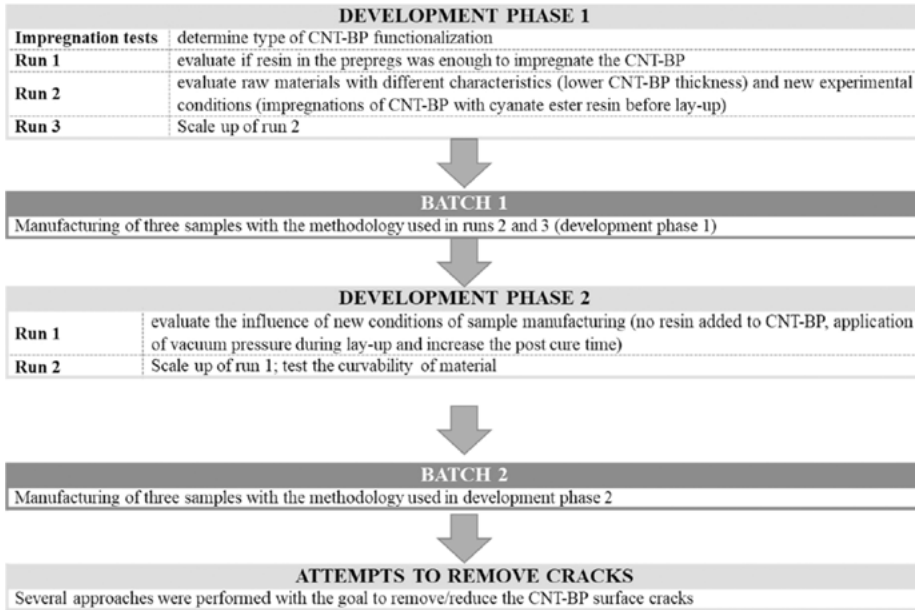

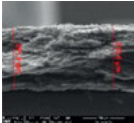
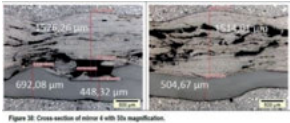
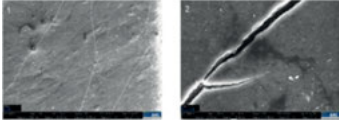
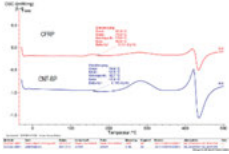
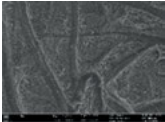
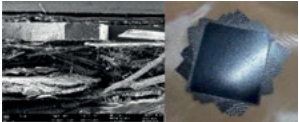


Figure 4.20: NATAP project phases and main objectives of each one.

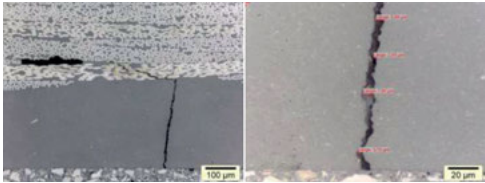
- The vacuum pressure applied during lay-up is an important step to improve cohesion between layers.
- Curved samples can be manufactured without significant additional effort, however, they were found to be more difficult to demold. It is recommended to coat the curved mold with a Teflon release film with extended length (larger than the mold) to ease the demolding process;
- In batch 2, two main problems were detected: samples warping after cure cycle (only detected during demolding) and some marks on the surface. Warping can be attributed to the formation of tension forces formed during the cure cycle (at high temperatures and due to the geometry of the samples) and, therefore, the prepregs lay-up sequence may be reviewed for specific geometries;
- The existence of a surface pattern is should not be a problem, since the marks are expected to disappear after polishing and metalization processes.

Sample characterizations performed throughout the project allowed to detect some issues are shown below. The actions taken to avoid/eliminate those issues are also presented.

As referred before, some changes were made in both the characteristics of the raw materials used and experimental conditions during sample manufacturing. Figure 4.21 summarizes the experimental conditions, changes in the methodology used and problems encountered in the different stages of NATAP.

Project phase	Issue	Characterization
Development phase 1: Run 1	Dry CNT structure, only bonded to CFRP at the ends	 <p>Detail showing the adherence only in the edges of the CNT layer and the carbon fiber; the CNT structure is dry</p>
Batch 1	CNT BP thickness after impregnation was higher than expected (BP expands with resin addition)	 <p>Cross-sectional view performed by INEGI (nonimpregnated CNT BP average thickness 300 μm)</p>  <p>Cross-sectional view performed by AAC (BP-impregnated average thickness 430 μm)/ nonimpregnated CNT BP average thickness</p>
Batch 1	Presence of cracks in the CNT BP structure	 <p>SEM images of coated surface mirror sample of batch 1 provided by AAC, showing the existence of cracks</p>
Batch 1	Glass transition temperature lower than expected	 <p>T_g measurements performed by AAC</p>
Development phase 2: Run 1	Lack of resin	 <p>BP surface (before impregnation) – marks are visible</p>  <p>Cross-sectional SEM picture, showing that the structure is dry (low resin content); bright surface shows that the BP is well impregnated</p>

(continued)

Project phase	Issue	Characterization
Batch 2	Cracks on CNT-BP structure	 <p>Cross-sectional view performed by AAC. Cracks are visible.</p>

4.4.3.4 Mirror demonstrator manufacturing

The main steps taken in the demonstrator manufacturing are summarized as follows [15]:

1. Mold preparation
2. Back skin manufacturing
3. Front skin manufacturing
4. Bonding honeycomb to front skin
5. Honeycomb machining
6. Back skin bonding to honeycomb (final assembly)
7. Final machining

Back and front skins were prepared according to the stacking sequence previously presented. Figure 4.22 shows the aspect of both CNT–CFRP skins after demolding (Figures 4.23–4.25).

The first assembly step consisted in bonding the honeycomb to the front skin. The CNT–CFRP skin was placed in the mold and prepared for the adhesive and honeycomb settlement. Afterward, the assembly was placed in the oven under vacuum pressure and temperature cycles.

After the first assembly, the honeycomb was machined on the free side in order to have a flat surface, for further bonding with the back skin bonding. A flat disk installed in a defined position in the turning machine was used for the in-house machining process.

The final assembly consisted in bonding the back skin to the first assembly. The back skin, containing adhesive, was placed on the top of the machined honeycomb. The entire assembly was then placed in the oven under vacuum pressure and temperature cycles.

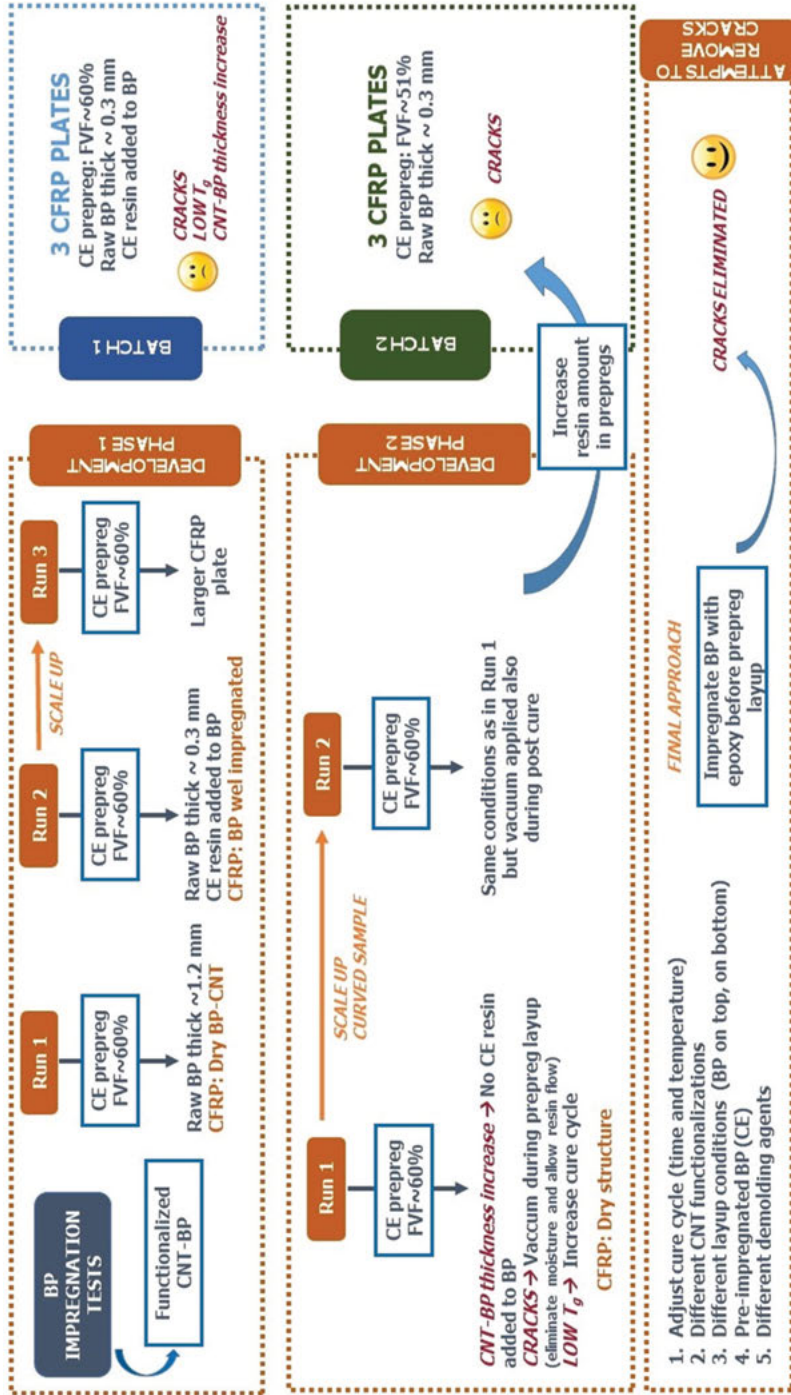


Figure 4.21: Conditions of each stage of sample manufacturing, problems and actions to solve them.

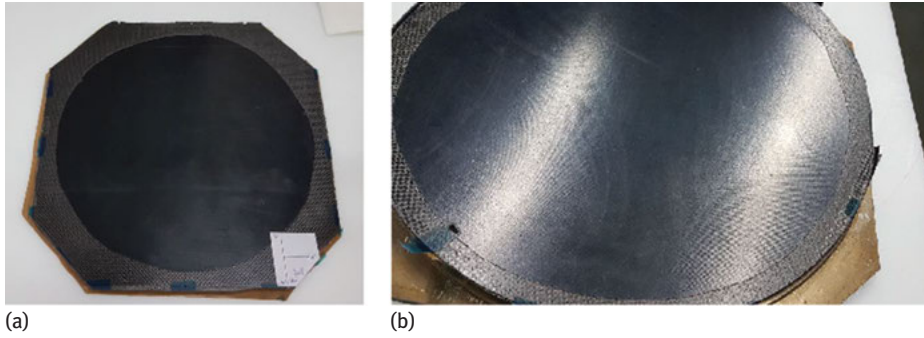


Figure 4.22: (a) Mirror back skin and (b) mirror front skin.

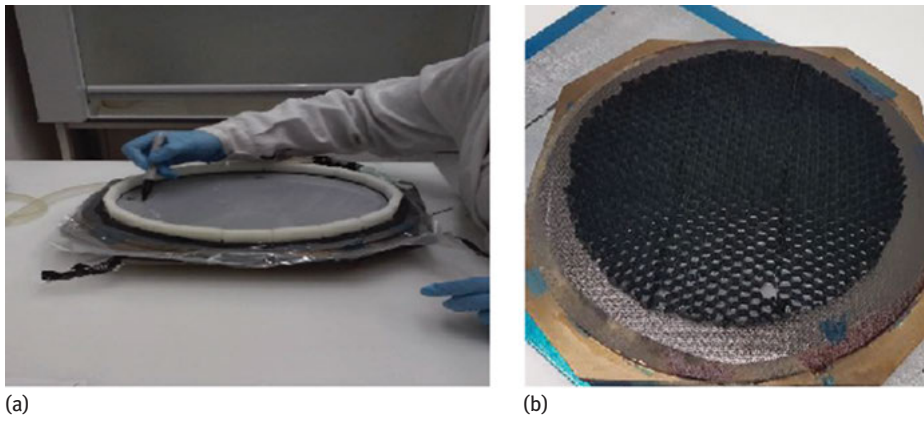


Figure 4.23: (a) Application of adhesive and (b) view of the honeycomb bonded to front skin.

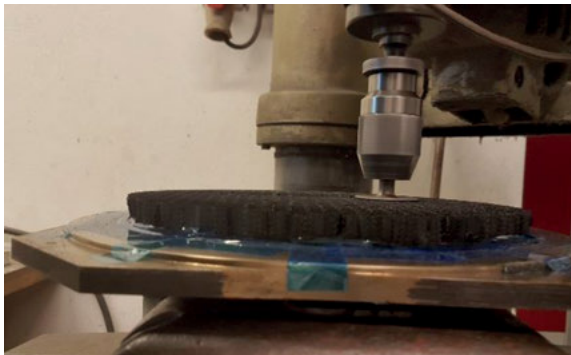


Figure 4.24: Honeycomb machining to obtain a flat surface.

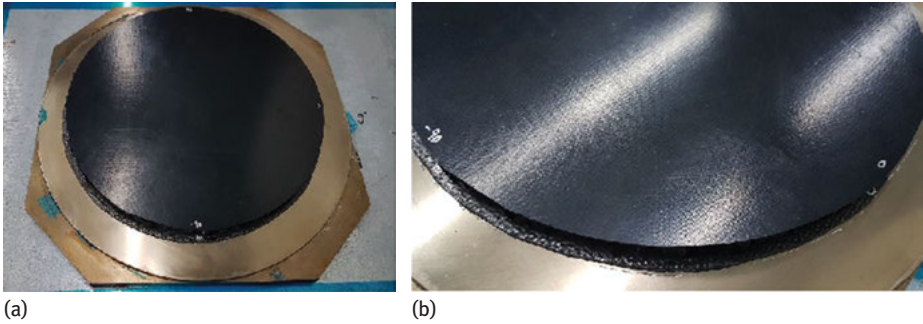


Figure 4.25: (a) Assembly after curing with the back skin in the top. (b) Detail of the back surface, where no cracks are visible after all the assembly operations.

4.4.3.5 Mirror polishing and metalization

One of the project goals was to determine the most suitable polishing process conditions applicable on CNC polishing machines and allowing to achieve targeted microroughness R_q (S_q) of 10–15 nm on the optical mirror surface. The individual work steps are summarized as follows [21]:

4.4.3.6 Polishing

- Machining outside diameter
- Smoothing an optical surface
- Surface form correction
- Roughness correction

4.4.3.7 Metalization

- By vacuum deposition using e-beam evaporator unit.

The selected technologies were:

- Polishing by two-step process using CeO_2 polishing slurry and polyurethane pad
- Metalization by physical vapor deposition (PVD) technology (e-beam evaporator)

Figure 4.26 shows the surface appearance of a CNT–CFRP skin after the polishing procedure and the surface microroughness of that surface measured using an interferometer, showing that the surface root mean square height (S_q) value is 11.82 nm.

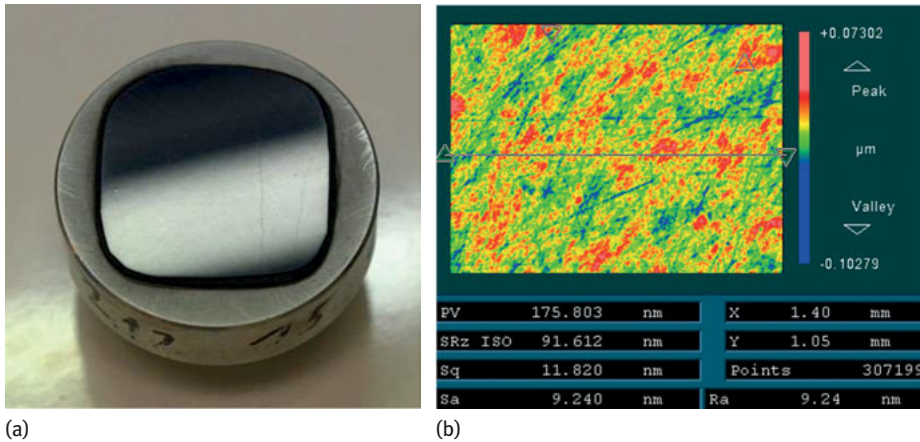


Figure 4.26: (a) Surface appearance of CNT-CFRP skin after polishing and (b) interferometer results after polishing.

The polished CNT surface of the optical mirror was coated by combination of Al (100–120 nm) and SiO₂ (70 nm) protective layer without loss of adhesion. This combination is a standard type of coating for optical mirrors. SiO₂ greatly increases durability of the surface (protection of the Al coating against oxidation). Resulting mirror surface has good abrasion resistance, but the top CNT layer of the composite is soft (compared to ceramics and glasses); hence, the optical mirror surface can be damaged due to damage of the CNT layer.

The achieved RMS value of 412 nm, which included the outer border, does not reach the target value of 70 nm. A reduction of the effective area to exclude the edge effect enhances the RMS to ~230 nm, which still is not sufficient for the targeted quality.

Nevertheless, the quality is well passing the necessary surface quality for the backup option of the radiometer example MetOp, where 1,000 nm is targeted.

Further improvements on RMS quality will be possible when the print-through of the backing structure as well as the cracks in the CNT layer can be reduced or, respectively, avoided.

An enhancement of hardness of the top layer could improve the local roughness, which has been measured to be in the range of 10 nm [22].

4.4.3.8 Mechanical characterization

The mechanical properties have been determined at ambient temperature before thermal cycling (RT) and after thermal cycling (RT, TC), and at the maximal (120 °C) and minimal (–120 °C) nonoperational temperatures foreseen for the respective

application. The summary of determined mechanical properties for the mirror is shown in Table 4.7. The measured density of the material was $1.493 \pm 0.015 \text{ g/cm}^3$.

Table 4.7: Summary of mirror mechanical properties [19].

Temperature (°C)	3-Point bending strength (MPa)	Young's modulus (GPa)	4-Point bending strength (MPa)	Young's modulus (GPa)	Interlaminar shear strength (MPa)
-120	282.8 ± 12.9	24.9 ± 1.4	324.7 ± 16.7	27.7 ± 1.5	29.1 ± 1.6
RT	284.6 ± 9.9	31.9 ± 1.6	270.5 ± 5.5	29.1 ± 1.1	26.2 ± 1.4
+120	262.2 ± 5.9	24.9 ± 2.7	236.6 ± 6.3	32.4 ± 1.3	23.6 ± 1.1
RT, TC	251.2 ± 11.1	28.6 ± 1.6	254.5 ± 9.2	27.0 ± 0.5	27.1 ± 1.2

Summarizing all the above presented results, the mechanical properties of the materials are considered suitable for the application with sufficient safety margin.

4.4.3.9 Electrical characterization

A total of four measurement points were performed onto the antenna polished and metallized surface; three to be placed at the outer circumference of the antenna and one into the center (Table 4.8).

Table 4.8: Radial positions for electrical measurements.

Position	Code	Details
1	FS-R1 to FS-C	Front side radial-1 to front side-center
2	FS-R2 to FS-C	Front side radial-2 to front side-center
3	FS-R3 to FS-C	Front side radial-3 to front side-center
4	FS-R1 to FS-R2	Front side radial-1 to front side-2
5	FS-R1 to FS-R3	Front side radial-1 to front side-3
6	FS-R2 to FS-R3	Front side radial-2 to front side-3

The DC resistance using a Metrohit Multimeter was measured from each of the three radial positions (FS-R1 to FS-R3) to the center FS-C (Figures 4.27 and 4.28).

The results of this test are shown in Table 4.9. The standard deviation of the measurements before thermal cycling is very high. A reason for this can be a capacitor effect of the honeycomb structure under the surface.

The electrical conductivity after the thermal tests was much higher than before the thermal cycling. The reason for this can be the many small cracks of the metalized surface; therefore, the insulating silica top layer was probably fractured, exposing

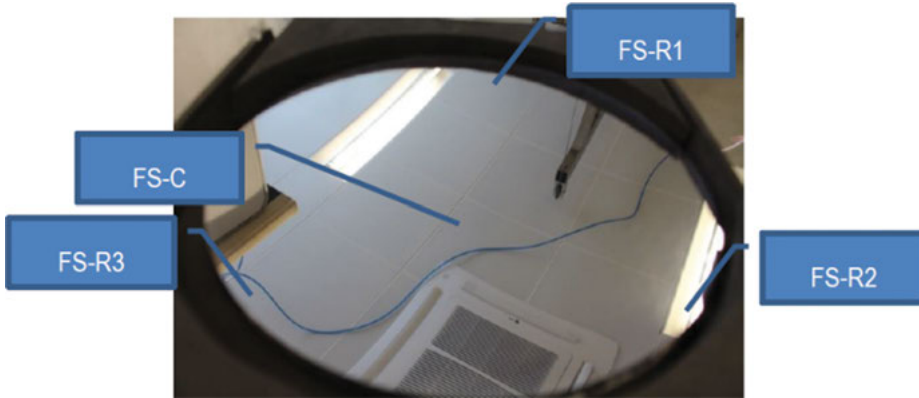


Figure 4.27: Electrical surface resistance test.

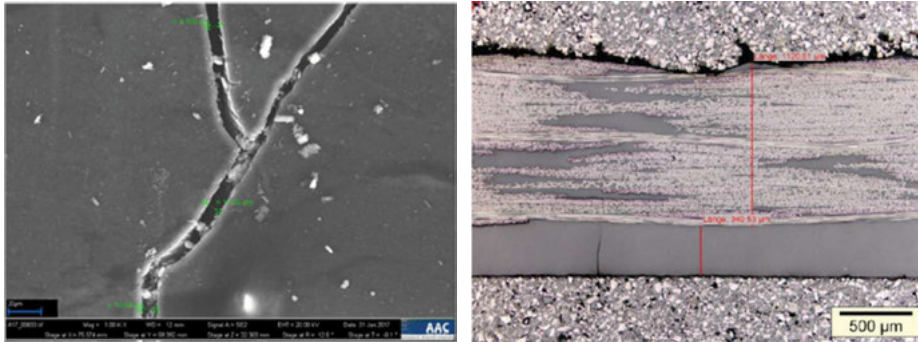


Figure 4.28: Surface crack in mirror sample after thermal cycling (left), Cross section of mirror sample (right).

Table 4.9: Summary of electrical measurement results.

Code	Before thermal cycling			After thermal cycling	
	Average (Ω)	Standard deviation	Conductivity (S/m)	Average (Ω)	Standard deviation
FS-R1 to FS-C	9,166.7	1040.8	9,92E-04	21.7	7.2
FS-R2 to FS-C	6,166.7	1040.8	1.47E-03	13.0	4.2
FS-R3 to FS-C	3,600.0	1216.6	2.53E-03	21.3	4.6
FS-R1 to FS-R2	2,066.7	378.6	2.42E-03	27.1	5.8
FS-R1 to FS-R3	2,000.0	435.9	2.50E-03	23.3	2.5
FS-R2 to FS-R3	2,566.7	907.4	1.95E-03	22.7	3.0

either the aluminum or the CNT layer, and we could measure the electrically conductive surface through the top layer.

The requirement of 10^3 S/m, that is, “metallic” electrical conductivity, could not be reached. The as-received surface conductivity was 4.28 S/m for the CNT side and 2.59 S/m for the CFRP side. Careful roughening the surface with Grit 1200 sandpaper improved the surface conductivity substantially to 4.28 S/m for the CNT side, and 16.18 S/m for the CFRP side where carbon fibers were apparently contacted.

4.4.3.10 Thermo-optical properties

Thermo-optical properties were tested at ZAE Würzburg, each for the CNT and for the CFRP side. The thermo-optical properties do not differ from CFRP to CNT side (Table 4.10).

Table 4.10: Summary of mirror absorbance values.

Sample	Visual absorbance	Solar absorbance	UV absorbance
CFRP face	0.92 ± 0.02	0.91 ± 0.02	0.93 ± 0.02
CNT face	0.94 ± 0.02	0.94 ± 0.02	0.94 ± 0.02

4.4.3.11 Structure observations

The mirror samples consisted of about 1.1–1.2 mm CFRP, and a CNT layer of about 350 μm . The surface shows cracks after thermal cycling.

Table 4.11 summarizes the main results achieved with the CNT–CFRP mirror, highlighting that mass, CTE and thermal conductivity properties achieved are in high-performance levels; however, specific heat, surface accuracy and reflectivity values are below the requirement definitions.

4.4.4 Conclusions

The selected demonstrator – a CFRP-based mirror – was manufactured using two CFRP skins based on cyanate ester preregs, with BP on the top surface. The CNT structure was incorporated as top layer of the skin during preregs lay-up and then impregnated with the resin from preregs. These CFRP skins were assembled with a CFRP honeycomb for obtaining the final part, further polished and metalized. Mirror mass was significantly improved at very good thermoelastic distortion values, but the CNT surfaces have many cracks, which further propagated after thermal cycling.

Table 4.11: Optical mirror demonstrator – major results.

Property	Results	Performance level
Mass	More than 20% mass saving in relation to a conventional optical mirror can be achieved. The mirror demonstrator's mass was only 270 g.	++
CTE	$-0.706 \times 10^{-6}/K$ in X/Y-direction (requirement: $<\pm 1 \times 10^{-6}/K$)	++
Thermal conductivity	0.84 W/(m*K), better than required (>0.75 W/(m*K))	+
Specific heat	0.73 J/(kg*°C) acceptable in relation to Zerodur 0.85 J/(kg*°C)	-
Surface accuracy	0.135 μm has been reached, not far away from requirements ($<0.1 \mu\text{m}$)	-
Surface quality	Not reached – presence of many cracks	--
Reflectivity	0.7 (after cycling), required value (>0.93) not reached due to cracks in surface	--
Temperature range	$-120 \text{ }^\circ\text{C} \rightarrow +100 \text{ }^\circ\text{C}$	

Several development steps were performed, aiming to eliminate or reduce the formation of cracks, such as the study of the influence of the lay-up, curing conditions and mold conditions, but none of the proposed approaches was effective. After all physical parameters being tested, the chemical influence of the resin was investigated. The cracks were eliminated by replacing the CTE for an epoxy resin in the CNT layer.

In fiber-reinforced composites, the CTE is affected primarily by the carbon fibers, while on the CNT layer, the resin CTE has the dominant effect. CTE disproportion can generate fatal stresses.

4.5 Conclusions

In this chapter, we presented a brief overview of the activities performed under three ESA projects, as well as the main results, targeting the use of CNT structures in the space sector. The first project was intended to prove the feasibility of CNT structures – BP – to be infiltrated with an organic matrix, potentially as an alternative to poorly dispersed and high viscosity nanotube-filled resin systems. Focus was given on assessing the morphology of the developed materials, by using high-resolution

microscopic analyses. The results show the proposed processing approach as capable of producing well-dispersed nanocomposites with high CNT loading (more than 15 wt% CNT by composite weight), which are important for developing high-performance structures based on CNT with good thermal and electrical conductivity.

The main objective of this activity was to scale up the material developments and thereby increase the Technology readiness level (TRL) to 2 for CNT skeleton-based polymer composites. The developed materials are used for manufacturing and testing of demonstrators for typical space applications. Several experimental trials were performed, trying to optimize process conditions such as mold tools, curing conditions or the use of different methods for BP impregnation. In a first step, the manufacturing process for obtaining CNT-skeletons with well-defined and reproducible characteristics was followed. In a second step, the composite manufacturing processes were further developed on sample level and in parallel the dimensions of the CNT-skeletons were scaled up to $0.1 \text{ m} \times 1 \text{ m}$ with thickness ranging from few tens of micrometers up to few centimeters. In the third step, the CNT-reinforced composite manufacturing was stabilized on scaled-up dimensions, suitable for manufacturing technological demonstrators. It was possible to obtain CFRP/CNT skeleton composites based on small papers in a controlled manner, with high CNT content, no defects and voids and without excess of resin in top, interlayer and bottom surfaces.

The final activity targeted a space application, and a demonstrator was manufactured and tested during the project. The selected application was an optical mirror, in which the CNT structures were intended to improve the surface characteristics of the material, facilitating the polishing and metalization steps. Extensive mechanical, thermal and optical characterizations were performed at sample and demonstrator level. The CNT-CFRP mirror resulted in more than 20% of mass savings, when compared to a conventional mirror, with a final mass of only 270 g. The measured surface accuracy was of $0.135 \text{ }\mu\text{m}$, not much distant of requirements ($< 0.1 \text{ }\mu\text{m}$). The main issue of the optical mirror is related to the presence of several cracks on the CNT layer, limiting the surface quality and the reflectivity values obtained. Nevertheless, the principle of producing a highly accurate optical mirror based on a CFRP/CNT is rated as promising, with good thermoelastic distortion values. It is estimated that a TRL level between 3 and 4 has been reached.

Acknowledgments: The authors thank the financial support from the European Space Agency (ESA) under the frame of the following projects:

- Non-conventional Matrix/CNT Reinforced Composite for Applications in Space (NACO), Contract 20521/06/NL/SFe
- Non-conventional Matrix/CNT Reinforced Composite 2, Contract 4000104354/11/NL/RA
- Carbon Nanotube Technology and Material Engineering for Various Space Applications (NATAP), Contract 4000116757/16/NL/LvH/fg

References

- [1] NACO-FCA-TN-06, Optimization Procedures and CNT Network Characteristics
- [2] NACO-INE-TN, *Production of CNT-PMC at INEGI- first trials*
- [3] Abdalla, M., Dean, D., Robinson, P. and Nyairo, E., “Cure behavior of epoxy/MWCNT nanocomposites: the effect of nanotube surface modification”, *Polymer* 49 (2008), 3310–3317
- [4] Wang, Z., Liang, Z., Wang, B., Zhang, C. and Kramer, L., “Processing and property investigation of single-walled carbon nanotube (SWNT) buckypaper/epoxy resin matrix nanocomposites”; *Composites: Part A* 35 (2004) 1225–1232
- [5] Lopes, P.E. et al. *Composite Structures* 92 (2010) 1291–1298
- [6] Gojny F., Wichmann, M.H.G., Fiedler, B., Bauhofer, W., Windle, A. H., Schulte, K. *Polymer* 47 (2006), 2036–2045
- [7] Hernández-Pérez, A., Avilés, F., May-Pat, A., Valadez-González, A., Herrera-Franco, P. J. and Bartolo-Pérez, P., “Effective properties of multiwalled carbon nanotube/epoxy composites using two different tubes”, *Composites Science and Technology* 68 (2008) 1422–1431
- [8] Gonnet, P., Liang, Z., Choi, E. S., Kadambala, R. S., Zhang, C., Brooks, J. S., Kramer, L., “Thermal conductivity of magnetically aligned carbon nanotube buckypapers and nanocomposites”, *Current Applied Physics*, 6 (2006), 119–122
- [9] Non-Conventional Matrix/CNT Reinforced Composite 2, NACO2-INE-TN-240, *Polymer CNT-Composite 1 Development and Test*
- [10] Non-Conventional Matrix/CNT Reinforced Composite 2, NACO2-HPS-RP-100, *Summary Report*
- [11] Non-Conventional Matrix/CNT Reinforced Composite 2, NACO2-INE-TN-312, *Polymer Demonstrator Report*
- [12] Carbon Nanotube Technology and Material Engineering for Various Space Applications (NATAP), NATAP-HPS-TN-110, *Selection of Space Applications and Associated Requirements*
- [13] Carbon Nanotube Technology and Material Engineering for Various Space Applications (NATAP), NATAP-FC-TN-211 *Production of Composite Samples and Breadboards Batch 1 & 2*
- [14] Carbon Nanotube Technology and Material Engineering for Various Space Applications (NATAP), NATAP-TOS-E-TN215, *Production of composite samples and breadboards: Batch 1 & 2*
- [15] Carbon Nanotube Technology and Material Engineering for Various Space Applications (NATAP), NATAP-HPSP-TN-351, *Mirror Demonstrator Manufacturing*
- [16] Carbon Nanotube Technology and Material Engineering for Various Space Applications (NATAP), NAT-KTO-RS-001, *Mirror Specifications*
- [17] ECSS-Q-ST-70-02C, Thermal vacuum outgassing test for the screening of space materials, 15 November 2008
- [18] Carbon Nanotube Technology and Material Engineering for Various Space Applications (NATAP), NATAP-HPS-TN-120, *Preliminary concept for demonstrator optical mirror*
- [19] Carbon Nanotube Technology and Material Engineering for Various Space Applications (NATAP), NATAP-HPS-RP-200, *Final Report*
- [20] Carbon Nanotube Technology and Material Engineering for Various Space Applications (NATAP), NATAP-INE-TN2.1.3, *Production of Material and Subelement Specimens 2*
- [21] Carbon Nanotube Technology and Material Engineering for Various Space Applications (NATAP), NATAP-TOS-E-TN351, *Demonstrator 1 Manufacturing*
- [22] Carbon Nanotube Technology and Material Engineering for Various Space Applications (NATAP), NATAP-AAC-TN-400, *Test Report Demonstrator Manufacturing*

Emmanuel N. Skountzos and Vlasios G. Mavrantzas

5 Molecular dynamics simulations of graphene-based polymer nanocomposites

5.1 Introduction

5.1.1 Carbon-based materials – the case of graphene

During the last decades, carbon has attracted a great deal of scientific and industrial attention due to the discovery of several allotropes (graphene, fullerene, carbon nanotubes [CNTs]), which are characterized by unprecedented physical and chemical properties such as high mechanical strength, extremely high electrical and thermal conductivity, high optical transparency and excellent gas barrier properties. Because of these unique features, carbon materials are widely used as nanofillers for the fabrication of composite materials with applications in several fields (biology, energy storage, transport and aviation, optoelectronics, pharmaceuticals, medicine and many others). Fullerenes, for example, are used as electron acceptors for the fabrication of organic solar cells based on semiconducting polymers such as poly-3-hexyl thiophene, which has significantly improved the efficiency of the corresponding devices, reaching values comparable to those of inorganic solar cells. Graphene-based biosensors characterized by remarkable detection efficiency toward certain target molecules have also been manufactured by exploiting the excellent electrical and optical properties of graphene even when present at very low concentrations. The very high specific surface area of CNTs combined with their low electrical resistance and high charge transport capability have allowed the production of high-performance supercapacitors with increased energy storage, power-delivery capabilities and rather long-life cycle compared to conventional batteries.

From the broad family of the carbon-based nanoparticles (NPs), the one that has attracted the most significant attention is graphene, a one-atom-thick planar sheet of sp²-bonded carbon atoms densely packed in a honeycomb crystal lattice. Graphene is the basic building block for graphitic materials of all other dimensionalities (Figure 5.1), because it can be wrapped up into 0D fullerenes, rolled into 1D nanotubes or stacked into 3D graphite [1].

Emmanuel N. Skountzos, Department of Chemical Engineering, University of Patras, Patras, Greece; Foundation of Research and Technology Hellas, Institute of Chemical Engineering Sciences (FORTH/ICE-HT), Rio-Patras, Greece

Vlasios G. Mavrantzas, Department of Chemical Engineering, University of Patras, Patras, Greece; Foundation of Research and Technology Hellas, Institute of Chemical Engineering Sciences (FORTH/ICE-HT), Rio-Patras, Greece; Particle Technology Laboratory, Department of Mechanical and Process Engineering, ETH Zürich, Switzerland

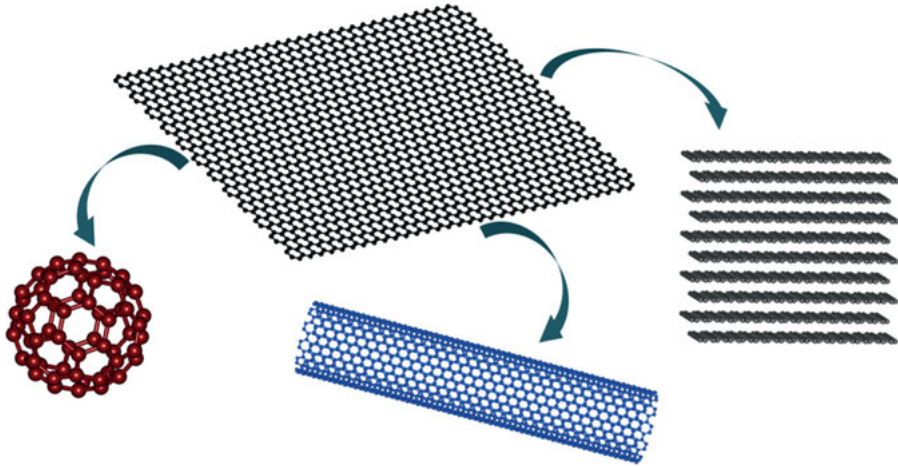


Figure 5.1: Graphene, the building block of all graphitic forms.

Until 2004, the production of single-layer (SL) graphene sheets (GS) was considered impossible, since theoretical calculations had predicted that GS would be completely unstable. The successful isolation of SL, defect-free GS using the “scotch tape method” [2] led to a rapid expansion of the field. The discovery was made by Prof. Sir Kostya Novoselov and Prof. Sir Andre Geim, who were awarded the Nobel Prize in Physics in 2010.

The impact of graphene on the scientific community has been enormous. Thousands of scientific articles (experimental and theoretical) are published every year and hundreds of these are heavily cited, while the paper describing the simple method to produce perfect GS has been characterized as “one of the most cited recent papers in the field of Physics” according to the ISI citation index. Apart from the great scientific interest in this exotic material, a significant impact on the largest technological industries of the world has also emerged after its discovery. Every year, thousands of patents are filed around the world on the design of new materials and new devices with important implications for practically all aspects of modern life (medicine, transportation, electronics, etc.), which explains why graphene has been characterized as the material of the future.

5.1.2 Graphene and graphene-based polymer nanocomposites

Numerous excellent reviews have been written in the last few years on the production, properties and applications of graphene [3–7] and graphene-based nanocomposites [8–13]; hence, here we will limit ourselves only to a brief overview of its

unique structural and physicochemical properties, and for more details we refer the interested reader to the original articles.

Production of graphene

After a long and tenacious series of unsuccessful attempts to produce SL graphene, the publication of a simple method was presented in 2004 [2] known today as the “scotch tape method.” By repeatedly cleaving a graphite crystal flake with an adhesive tape to its limit, and then transferring the thinned-down graphite onto an oxidized silicon wafer with the appropriate color, a 2D carbon lattice is produced.

In general, production methods of graphene fall into two main categories:

- Bottom-up methods
- Top-down methods

In bottom-up processes, graphene is synthesized by a variety of methods such as

1. Epitaxial growth on metal carbides [14–16]
2. Chemical vapor deposition (CVD) [17–18]
3. Unzipping CNTs [19–20]

In top-down processes, it is synthesized from a bulk material (e.g., graphite), which is broken down into smaller pieces using mechanical, chemical or other forms of energy. Typical examples of the top-down production processes include

1. the micromechanical exfoliation of graphite [2];
2. the direct sonication of graphite [21–22];
3. the chemical reduction of organically treated graphite oxide [23] and
4. the thermal exfoliation/reduction of graphite oxide [24].

In principle, with bottom-up approaches, large-sized, defect-free monolayer graphene is produced, a perfect material for the subsequent studies. The only drawback with these methods is that they afford only the production of tiny amounts of graphene. Top-down processes, on the other hand, are suitable for the large-scale production of graphene as (for example) required for the fabrication of graphene-based polymer nanocomposites.

Properties of graphene

The rapid adoption of graphene as the material of interest lies primarily in the excellent spectrum of properties (mechanical, electrical, thermal, optical, etc.) characterizing monolayer, few-layer graphene and graphene oxide (GO). The goal of many research efforts nowadays is to exploit these extraordinary properties for applications

in nanotechnology by fabricating materials with improved mechanical, electrical, thermal and optical performance.

Carbon-based nanomaterials such as graphite, diamond and CNTs have their own record in terms of mechanical strength, hardness or Young's modulus. The newest member of the family, graphene, is no exception despite that its mechanical behavior has not been investigated as much as its electronic and optical properties. The reported stiffness of about 300–400 N/m (with a breaking strength of about 42 N/m) represents the intrinsic strength of a defect-free sheet [25] while estimates of the Young's modulus are on the order of 0.5–1.0 TPa [25]. Interestingly, and despite their defects, suspended GO sheets retain to a large extent their mechanical performance, characterized by a Young's modulus of 0.25 TPa [26]. These features, combined with the relatively low cost for the production of thin graphite and the ease of processes for blending GO into matrices [11], render these materials as ideal candidates for electrical and mechanical reinforcement [27, 28].

Regarding electrical properties of graphene, we mention that its electrical resistivity at room temperature is about $1 \mu\Omega \text{ cm}$; as a result, graphene is about 35% less resistant than silver, the lowest resistivity material known today at room temperature. In semiconductors, a different measure is used to quantify electronic motion known as mobility. Mobility is often expressed as the conductivity of the material per electronic charge carrier. This implies that high mobility is advantageous also for chemical or biochemical sensing applications in which a charge signal (e.g., a molecule adsorbed on a device) is translated into an electrical signal, thanks to the changing conductivity of the device. Thermal vibrations of atoms set the upper limit to electron mobility in graphene, which is $\sim 200,000 \text{ cm}^2/\text{V s}$ [29–30] at room temperature, which should be compared to $\sim 100,000 \text{ cm}^2/\text{V s}$ [31] in CNTs.

Chen et al. [32–33] showed that although the room temperature limit of mobility in graphene can be as high as $200,000 \text{ cm}^2/\text{V s}$, in present-day samples the actual mobility is lower (around $10,000 \text{ cm}^2/\text{V s}$) leaving significant room for improvement. Because graphene is only one-atom thick, current samples must be supported by a substrate, typically silicon dioxide. Trapped electrical charges in silicon dioxide (a sort of atomic-scale dirt) can interact with electrons in graphene, which can cause a reduction in mobility.

In addition to being considered as a promising material for applications in chemical and biochemical sensing, its low resistivity and extremely thin nature render graphene a very promising material also for use in thin, mechanically tough, electrically conducting, transparent films that are needed in many applications in electronics (ranging from touch screens to photovoltaic cells).

Apart from its excellent mechanical and electrical properties, graphene exhibits amazing performance as a thermal conductor. Balandin et al. [34] reported values of thermal conductivity for SL graphene at room temperature in the range of 4,840–5,300 W/m K. These extremely high values of thermal conductivity suggest that graphene can outperform CNTs in heat conduction [35–36]. However, when

graphene is in contact with a substrate, its thermal transport properties can be significantly affected. Seol et al. [37] showed experimentally that the value of thermal conductivity of monolayer graphene exfoliated on a silicon dioxide support is still as high as about 600 W/m K near room temperature, exceeding those of metals such as copper. It is lower, however, than that of suspended graphene because of phonons leaking across the graphene–support interface and strong interface scattering of flexural modes, which make a large contribution to thermal conductivity for suspended graphene. In general, the superb thermal conduction properties of graphene have established it as an excellent material for thermal management.

Production of graphene-based polymer nanocomposites

In recent years, a variety of processing methods have been proposed for dispersing GS into polymer matrices. Many of these procedures are like those used for other nanocomposite systems (e.g., CNT/polymer nanocomposites) [38], while others apply only to graphene-based polymer nanocomposites.

A crucial step in the production of any polymer nanocomposite is the dispersion of the nanofiller. A well-dispersed state ensures a maximized reinforced surface area, which directly affects all properties of the nanocomposite. Efforts are therefore focused on achieving a well-dispersed, homogeneous system by developing either covalent or noncovalent functionalization of the filler surface, an issue that will be discussed in some more detail in the following sections.

Most polymer/graphene composites are produced today with one of the following three strategies: (1) solvent processing, (2) in situ polymerization and (3) melt processing with each one of them having its own advantages and disadvantages. In the solvent processing method, GS are initially dispersed in a suitable solvent, a procedure typically assisted by ultrasonication [11, 39]. Then, the polymer is added in the solvent/graphene blend, and the solvent is finally removed by evaporation or distillation. It is a rather simple method, used widely to prepare polymer/graphene composites. Its most important drawback is that common organic solvents adsorb on GS stronger than most of the polymers.

In the in situ polymerization method, GS are mixed with the targeted monomers, and by adjusting parameters (such as temperature and pressure), the polymerization reaction proceeds [40–41]. The advantages of the method are twofold: (a) it provides a strong interaction between the polymer matrix and the surface of GS and (b) it leads to highly homogeneous dispersions. However, an increase in the viscosity of the blend is usually recorded as a side effect, which affects processability (especially at high GS loadings).

Melt processing is commercially the most attractive method to produce graphene-based polymer composites. It involves the direct inclusion of GS into the melted polymer using a twin-screw extruder by suitably adjusting parameters such

as screw speed, temperature and time [42–43]. Drawbacks of the method include the low density of thermally exfoliated graphene that makes extruder feeding a troublesome task, and the lower degree of dispersion achieved compared to solvent blending. Reduced degree of dispersion typically results in poorer mechanical, electrical and thermal properties.

Properties of graphene-based polymer nanocomposites

In the modern literature, significant improvements in the mechanical, electrical, thermal and barrier properties of graphene-based polymer nanocomposites have been reported, as summarized in several reviews [8–10, 12, 44]. Fang et al. [40], for example, have reported an increase in the tensile strength by 70% and in the Young's modulus by 57% for graphene–polystyrene nanocomposites with polystyrene (PS) chains grafted onto GS by atomic transfer radical polymerization. The experimental studies of Ramanathan et al. [39] and Li and McKenna [45] have shown that behind the extraordinary mechanical properties and the increase in the glass transition temperature (T_g) of poly(methyl methacrylate) (PMMA) nanocomposites filled with functionalized graphene sheets (FGS) are the enhanced interfacial interactions with PMMA chains as driven by oxygen functionalities across the surface of graphene. FGS contain pendant epoxy, hydroxy and/or carboxy groups on their surface, which may form hydrogen bonds with the ester branches of PMMA. However, Liao and coworkers [46–47] have argued that an 80% increase in the PMMA modulus [39] at only 1 wt. % loading of the nanocomposite in FGS, and an increase in T_g by 29 °C [39] at only 0.05 wt.% loading seem unrealistically high. Thus, Liao et al. repeated the experiments carried out by Ramanathan et al. [39] and found an increase of only 25% in the Young's modulus measured [47] and no change in the T_g [46]. These very different observations were attributed to the experimental procedure followed by Ramanathan et al. [39]. In an earlier study [48], significant improvements in the Young's modulus and in ultimate tensile strength had been reported for poly(vinyl alcohol) (PVA) samples enhanced with GO sheets functionalized with PVA chains (PVA chains had been grafted onto the GO surface). The reported enhancement in the mechanical performance reached almost 60% for GO loadings below 0.3 vol.% [48]. For the same nanocomposite, Zhao et al. [49] have reported an improvement of ~150% in the tensile strength and an order of magnitude increase in the Young's modulus for only a 1.8 vol.% loading in graphene.

As already mentioned, graphene-based materials are very promising for the development of new devices with applications in electronics, owing to their high degree of electrical conductivity. In the past, several carbon-based NPs (i.e., carbon filler, carbon nanofibers, expanded graphite, etc.) have been exploited for the production of electrically conductive composites; however, the key advantage of graphene is that the insulator-to-conductor transition (known as the percolation threshold) can

be achieved at significantly lower loadings. Production of electrically conductive polymers has been reported [50–51] upon successful GS dispersion in the host polymer matrix. Stankovich et al. [11, 52] determined the percolation threshold for a polystyrene solvent blended with GO to be 0.1 vol.%, perhaps the lowest percolation threshold ever reported. Eda and Chhowalla [53] studied the electrical properties of solution-processed, semiconducting thin films consisting of FGS as the filler and polystyrene as the host material and found that upon increasing the average size of FGS significantly enhanced carrier mobility and thus device performance. This study demonstrated how a commodity plastic can be used to develop low-cost, macroscale thin-film electronics.

Simulations

In addition to experimental efforts, theoretical and computational works have addressed several aspects of the structure–property–processing relationship in graphene or graphene-based nanocomposite materials. Several simulation techniques and approaches have been employed, extending from the quantum level to the atomistic to the mesoscopic and finally to the macroscopic. The findings of these theoretical studies have significantly improved our understanding of the microscopic mechanisms and interactions governing the macroscopically exhibited properties of these new classes of materials.

Using classical *ab initio* calculations, Van Lier et al. [54] and Liu et al. [55] reported values of graphene’s Young’s modulus equal to 1.11 and 1.05 TPa, respectively, which are in reasonable agreement with the experimentally measured ones [25]. It is worth mentioning that the computational values were reported in 2000 [54] and 2007 [55], respectively, while the experimental one in 2008 [25]. In a recent study that combined density functional theory calculations and classical molecular dynamics (MD) simulations, Kalosakas and coworkers [56] proposed a new force field specifically for graphene that takes into account only bond stretching (described by a Morse-style potential) and bond bending (described by a nonlinear function containing quadratic and cubic terms) interactions between carbon atoms. The new potential was employed in simulations with model graphene systems subject to uniaxial tension or to hydrostatic compression, yielding a value of 0.95 TPa [56] for graphene’s Young’s modulus, which is also consistent with the one measured experimentally [25]. The dependence of graphene’s Young’s modulus on temperature and size of GS was systematically studied by Jiang et al. [57], through MD deformation simulations of SL graphene using progressively larger GS, and an increase in the Young’s modulus was observed with increasing GS size. The plateau value was reached for a GS size equal to $25 \text{ \AA} \times 25 \text{ \AA}$ beyond which no further increase was recorded [57]. The MD deformation experiments were carried out at temperatures ranging from 100 to 600 K; a slight increase in the value of the Young’s

modulus (within the statistical error) was monitored for temperatures up to 500 K, followed by a rapid decrease at higher temperatures.

Ab initio studies of suspended GS are not restricted solely to the estimation of the mechanical properties. Excellent articles have been reported in the literature addressing atom–atom interactions between graphene and popular substrates (e.g., SiC [58] και MoS₂ [59]) that are extensively used for the fabrication of SL graphene. Also important are computational and simulation studies of the mechanical, thermal, barrier and electronic properties of polymers filled with GS. Issues addressed here include microscopic structure, chain conformation and local and terminal dynamics of polymer matrix chains in the presence of graphene. Earlier works focused on the study of the interfacial behavior of graphene-based polymer composites. Awasthi and coworkers [60] carried out atomistic MD simulations with the consistent valence force field to study nanoscale load transfer between polyethylene (PE) and GS and characterize the force-separation behavior between CNTs and a polymer matrix. Separation studies were conducted for opening and sliding modes, and cohesive zone parameters (such as the peak traction and the energy of separation for each mode) were evaluated as a first step toward the development of continuum length-scale micromechanical models for tracking the overall material response by incorporating information about the underlying interfacial interactions. MD simulations have also been employed by Li et al. [61] in their study on the effect of the shape of carbon-based NPs on the viscoelastic properties of a PE matrix. They found that it is the surface-to-volume ratio of the NPs that plays the most important role in the structural, dynamical and viscous properties [61]. More recent MD simulations [62–63] of PMMA/graphene nanocomposite showed strong adhesion of PMMA chains (especially of the side groups) on graphene, and considerably slower segmental and chain mobility in the interfacial area. The MD simulations suggest that local mass density, segmental dynamics and chain terminal relaxation all differ from the bulk behavior up to distances equal to several nanometers from the GS surface. Very similar results have been reported for a different matrix, PE [64], demonstrating large density inhomogeneities due to strong PE chain adsorption on the surfaces of GS, exactly as was reported in the case of PMMA/graphene nanocomposites [62]. Close to graphene, PE chains prefer to stand parallel to the graphene surface [64], and all polymer conformational and dynamic properties [64–65] are significantly affected: (a) the size of polymer chains (as measured by their radius of gyration) increases and (b) their dynamics change dramatically because their orientational relaxation time increases almost by one order of magnitude compared to the bulk value. In a very recent work [66], the effect of GS on the crystallization process of PE, polyvinylidene fluoride (PVDF) and PS oligomers was examined. It was reported that GS tend to act as nucleation sites for the crystallization of PE and PVDF but not for PS, which remains almost amorphous [66]. It was also reported that at high temperatures (e.g., close to 600 K), the crystalline structure of PE is destroyed, a result that is in accordance with the recent MD study of Gulde et al. [67].

Simulations have also addressed polymer nanocomposites enhanced not with pristine GS but with GO. GO is graphene-bearing epoxy, hydroxy and/or carboxy groups on its surface. When GO is used as a nanofiller of a polar (e.g., acrylic) polymer, the interactions between polymer atoms and graphene are intensified due to strong attractive forces that develop between polymer and GO oxygen atoms. Lv et al. [68] examined two different polymers as the host matrix, PMMA and PE, and concluded that with increasing concentration in carboxyl content, the interaction energy between polymer chains and GO sheets decreased (it became more attractive), followed by a significant increase in the value of the shear stress. However, an upper bound in the concentration was found, beyond which no further change in the values of these two properties was observed. This was explained as a saturation effect: high concentrations of functional groups strengthen the interactions between the surface functionalization groups themselves, thus no space is left for interactions with the surrounding polymer chains. Karatasos and Kritikos [69] have reported a strong increase (by 38 °C) of the T_g of GO-based poly(acrylic acid) (PAA) nanocomposites compared to pure polymer (PAA). This strong increase was explained by the strong adsorption of PAA chains onto the surface of GO sheets facilitated by the hydrogen bonds that develop between the hydroxyl groups of GO and the oxygen atoms of PAA branches. Earlier, Xue et al. [70] had studied the T_g of PMMA matrices enhanced either with pristine GS or with GS modified with -COOH and -NH₂ groups. By employing classical MD simulations, they observed a 30 °C increase in the T_g of the PMMA/GS system, whereas for the nanocomposites with the modified GS, the shift was higher (40 °C) [70]. More recently, Azimi et al. [71] showed that the dynamics of a polar (e.g., PVA) matrix is affected more by the presence of GO than by the presence of GS, whereas for an apolar polymer matrix (e.g., poly(propylene)) the effect of the two types of graphene is almost the same. That less polymer is adsorbed on GO than on pristine graphene can be explained by the roughness of GO particles due to OH- and -O- groups on their surface and agrees with a recent detailed MD study by Skountzos et al. [72]. However, the strength of interactions between oxygen atoms of the polar polymer and of GO particles is so strong that despite the smaller adsorbed amount on GO (in comparison to pristine GS), the dynamics of the PVA/GO system is considerably slower than the dynamics of the PS/GS nanocomposite.

In the last years, significant progress has been made in predicting the unique mechanical properties of graphene-based polymer nanocomposites through detailed atomistic-level simulations and understanding the underlying molecular mechanisms behind these properties [55, 72–76]. A typical example is the atomistic simulation work of Skountzos et al. [72] on the effect of pristine graphene and GO on the structure, conformation and mechanical properties of a syndiotactic PMMA (sPMMA) matrix. The atomistic simulations predicted a significant enhancement of all elastic constants (Young's, shear and bulk moduli and Poisson's ratio), especially for the PMMA/GO nanocomposites, which was attributed to the hydrogen

bonds that develop between the oxygen atoms at the branches of PMMA chains and the OH- and -O- groups on the surface of GO particles. Wang et al. [76] have studied the effect of surface functionalization and graphene size on the interfacial load transfer in graphene-PE nanocomposites (by employing the ab initio polymer-consistent force field, PCFF) and showed that oxygen-FGS lead to larger interfacial shear force (than hydrogen-functionalized or pristine ones) during the pull-out process. Increasing the oxygen coverage and graphene size enhanced the interfacial shear force, but further increasing the oxygen coverage to about 7% led to a saturation in the interfacial shear force. Liu et al. [75] studied the effect of shape of carbon-based NPs on the toughening efficiency of a PE matrix by applying pure tensile strain experiments in MD simulations with several model systems. At the same wt. % loading in either CNTs, or fullerenes or GS, they found that the highest toughening was observed for the PE/graphene system; this should be related to the increased surface area that graphene offers for PE chain adsorption. This effect was examined in both the rubbery and glassy states (i.e., above and below the glass transition temperature of PE) and it was found that the nanocomposite in the rubbery state was tougher than the corresponding glassy material [75]. More recently, in a systematic study, Lin et al. [73] investigated how temperature and GS loading affect the mechanical performance of model PMMA/GS nanocomposites. The general trend was that Young's and shear moduli increase with increasing GS loading but decrease with increasing temperature while the temperature dependence of the two moduli is stronger in the nanocomposites with the higher concentration in GS. Comparison of their simulation results with the equations based on the simple rule of mixing for the mechanical properties of microfiber-reinforced composites revealed that the latter do not apply for graphene-reinforced nanocomposites; thus, further research is needed to address this issue [73].

Graphene dispersion

Clearly, among all NPs considered as polymer reinforcing agents, graphene is the most promising due to its outstanding features. However, because of its high specific surface area and tendency for self-adhesion (driven by the very strong van der Waals forces and π - π interactions), GS tend to agglomerate in the form of multi-layer graphitic structures. Significant research has thus been undertaken in the last years to understand and improve GS dispersion, and thus realize its unique properties in practice. The degree of GS dispersion in nanocomposites affects primarily their mechanical performance. Indeed, several studies have shown that the mechanical properties of graphene-based polymer nanocomposites increase as their content in SL graphene increases [39, 77-78]. Motivated by these findings, in the next paragraphs of this chapter we provide a brief overview of the methods employed

nowadays, typically based on covalent or noncovalent graphene functionalization, to achieve homogeneous GS dispersions [79–80].

Techniques based on covalent functionalization make use of small molecules or entire macromolecules that are attached on the surface of GS through covalent bonding. Then, owing to strong chemical interactions developing between the grafted groups and the GS, very homogeneous and stable dispersions can be obtained. However, covalent functionalization disrupts the perfect crystal structure of graphene, which can affect many of its outstanding properties, especially the electrical ones. An attractive alternative is noncovalent functionalization. This is based on the use of functional groups that are attached on the surface of graphene through favorable π – π interactions without disturbing its electronic network. Noncovalent methods are by default nondestructive; however, the forces that develop between the wrapping molecules and the graphene surface are much weaker compared to those in the case of covalent functionalization; this can limit the degree of dispersion eventually achieved.

Covalent functionalization of graphene has been exploited quite widely in the literature for the improvement of the mechanical properties of graphene-based nanocomposites [81–85]. Using mostly peripheral ester linkages that are extensively used in tissue engineering applications, Sayyar et al. [84] managed to successfully link polycarbonate to GO. The fabricated nanocomposite had a very homogeneous and stable GS dispersion and exhibited several good properties: improved Young's modulus, improved tensile strength and high electrical conductivity (~14 orders of magnitude compared to the conductivity of the pure bulk polymer). In an earlier study, Cheng and coworkers [81] had produced PVA nanocomposites by incorporating PVA-grafted GO fillers, which resulted in an enhancement of Young's modulus by 150% and of tensile strength by 88%, for 1 wt.% loading of the nanocomposite in GO.

The tendency of GS to agglomerate and form graphitic structures is witnessed most easily in atomistic or coarse-grained simulations. Park and Aluru [86] have reported GS self-assembly in atomistic MD simulations of GS in water solutions, but this was probably an expected result due to hydrophobic nature of graphene. In a later study, Li and coworkers [61] found that several carbon allotropes (buckyballs, graphenes, etc.) agglomerate in a PE matrix, thus lowering the degree of their interaction (contacts) with the host matrix. Ju et al. [87] studied the degree of GS miscibility in PMMA as a function of NP volume fraction with the help of dissipative particle dynamics (DPD) simulations using different values of the DPD-repulsive interaction parameter to effectively account for surface functionalization. GS agglomeration has also been reported by Karatasos et al. [88–89] in all-atom MD simulations of linear and hyperbranched polymer matrices. Guo et al. [90] have studied the effect of GS agglomeration on the mechanical properties of polymer nanocomposites by examining cases where several GS were intercalated (polymer chains were “sandwiched” between two consecutive GS) or stacked (in the form of graphite-like structure) in the sample. By investigating their mechanical behavior in a series of uniaxial tension experiments, they concluded that intercalated systems exhibit a higher storage modulus compared to

stacked ones due to stronger interactions between the polymer and the GS resulting from the higher surface-to-volume ratio in the intercalated design. More recently [91], atomistic MD simulations were combined with advanced chemistry techniques to produce graphene-based PMMA solutions and nanocomposites of high degree of GS dispersion. Instead of graphene covalent functionalization or incorporation of small molecules as dispersing agents in the solutions, in the new method a fraction of PMMA chains were covalently functionalized by a procedure that allows adding pyrene molecules preferentially to the two ends of the polymer chain [91]. The accompanying MD simulations provided very useful information about the interaction of these functionalized PMMA chains with GS and how these are kept well separated in the polymer matrix, thereby achieving a stable, highly homogeneous dispersion.

5.2 Simulation methods at the atomistic level: the molecular dynamics method

In the last few decades, molecular simulations have emerged as an excellent tool for explaining many of the microscopic mechanisms behind the measured macroscopic properties of complex materials, also for connecting the predictions of theoretical models with experimentally measured properties. Being able, in particular, to predict important material properties from the chemical composition and molecular architecture of the chemical formulation is of paramount importance because it can guide design efforts both at the level of materials synthesis and at the level of materials processing. With their inherent potential to predict important physical properties directly from the underlying atomistic structure, molecular simulations are considered today as very useful, virtual experiments that can replace in many cases actual laboratory measurements.

Molecular simulations encompass two main techniques: MD and Monte Carlo (MC) [92–93]. MD is based on the solution of Newton's equations of motion in an appropriate statistical ensemble. These are numerically integrated, and the result of integration yields the positions and velocities of each atomistic unit in the system in time (this is also known as the trajectory of the system in phase space). In this way, we can monitor how the model system evolves in time (under the macroscopic constraints imposed by the statistical ensemble in which the simulation is carried out) and thus extract information about its thermodynamic, structural, conformational, dynamic and rheological properties. To run an MD simulation, we need initial conditions, namely atomic positions and atomic velocities at zero time. The trajectory followed by the system depends then crucially on the potential energy function describing intra- and intermolecular interactions.

In contrast to MD which is a deterministic method, MC is based on the design of (artificial or even unphysical) moves to sample new states that are selected

randomly with the help of an appropriate acceptance criterion. Thanks, in particular, to the design of some very clever moves, MC helps the system tunnel through large potential energy barriers, and this can accelerate system equilibration by orders of magnitude compared to MD. The major drawback of the method is that it does not offer any dynamic information about the system. This happens because the system evolves stochastically in configuration space based on predefined acceptance criterion for each attempted move. Indeed, in a MC simulation, only atomic positions matter. Our discussion in the remainder of this chapter is devoted solely to the MD method.

In general, the complexity of polymers prohibits the analytical solution of the corresponding statisticochemical problem. Molecular simulations overcome this by solving the corresponding problem numerically, given a mathematical model for the molecular geometry and description of interatomic interactions. Two general types of force fields are typically employed for the molecular simulation of polymers: Explicit atom (EA) models where every atom is considered as an independent interaction site or entity, and united atom (UA) models where hydrogen atoms are neglected by considering a relatively larger, spherically interacting particle that embodies the contributions of both the hydrogen atoms and of the atom (e.g., the carbon) to which the hydrogens are bonded. EA models offer a very detailed and accurate description of the problem. Their main drawback is that, for the same number of total molecules considered in the simulation box, they involve almost twice as many interacting sites as the corresponding UA model; as a result, molecular simulations with EA models are significantly more CPU time demanding than simulations with UA models.

Given the type of molecular model adopted, an initial configuration for the system and initial velocities for all atoms (assigned according to the Maxwell–Boltzmann distribution), what remains to be defined next is the potential energy function describing interatomic interactions. In general, these are distinguished between bonded and nonbonded. Bonded interactions typically include contributions from

- bond length stretching (Figure 5.2a),
- bond angle bending (Figure 5.2b),
- proper dihedral angles (Figure 5.2c) and
- improper dihedral angles (Figure 5.2d).

Nonbonded interactions, on the other hand, include

- inter- and intramolecular van der Waals interactions (Figure 5.2e) and
- inter- and intramolecular Coulomb interactions (Figure 5.2f).

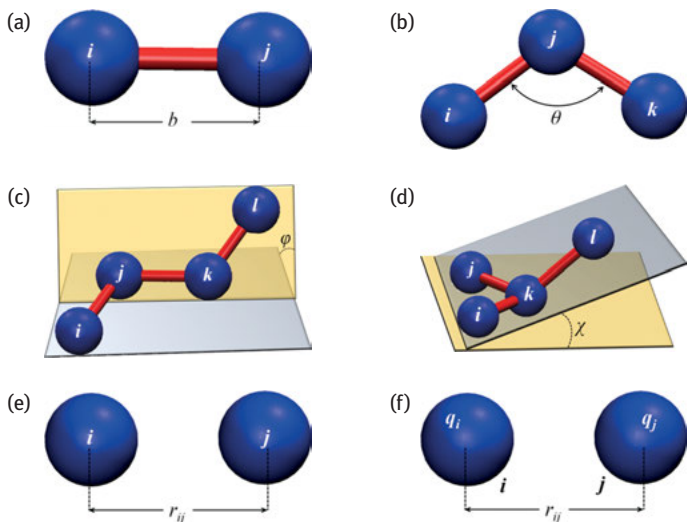


Figure 5.2: Schematic representations of (a) bond length stretching, (b) bond angle bending, (c) proper dihedral, (d) improper dihedral, (e) van der Waals and (f) Coulomb interactions to the potential energy of the system.

A typical mathematical form of the total potential energy function [94] is

$$\begin{aligned}
 U_{\text{pot}} = & \overbrace{\sum_{\text{bonds}} k_b (b - b_0)^2 + \sum_{\text{angles}} k_\theta (\theta - \theta_0)^2 + \sum_{\text{dihedrals}} k_\phi [1 + \cos(n\phi - \delta)] + \sum_{\text{impropers}} k_\chi (\chi - \chi_0)^2}^{\text{Bonded energetic terms}} \\
 & + \underbrace{\sum_{\text{vdW}} 4\epsilon_{ij} \left[\left(\frac{\sigma_{ij}}{r_{ij}} \right)^{12} - \left(\frac{\sigma_{ij}}{r_{ij}} \right)^6 \right] + \sum_{\text{Coulomb}} \frac{q_i q_j}{4\pi\epsilon_0 r_{ij}}}_{\text{Nonbonded energetic terms}}
 \end{aligned} \tag{5.1}$$

where the first and second sums on the right-hand side correspond to a harmonic potential for the description of bond length stretching and bond angle bending contributions, the third term is a cosine function describing contributions from proper dihedral angles (formed by four consecutive atoms along the chain) and the fourth term is a harmonic function describing contributions due to improper dihedral (or out-of-plane) angles formed by four nonconsecutive atoms along the chain (they help maintain the stereoregularity of the fourth atom with respect to the plane of the other three atoms at branch points). The fifth term in eq. (5.1) corresponds to the total van der Waals energy of the system based on a typical 12–6 Lennard–Jones (LJ) potential while the last term is the total electrostatic energy due to Coulomb interactions between charged atoms.

Force fields described by eq. (5.1) are called classical force fields. Some examples are the DREIDING [94], the OPLS [95], the CHARMM [96] and the AMBER [97].

The functional form of eq. (5.1) includes the minimum number of terms (bonded and nonbonded), providing a satisfactory description of the total potential energy of the system. However, during the last 30 years, more detailed atomistic-level force fields have been developed based on ab initio calculations parameterized on the basis of a large body of experimental data for several organic compounds consisting of carbon, oxygen, hydrogen, nitrogen and sulfur atoms. These second-generation potentials are called class II potentials and differ from the classical potentials in that they include extra (coupling) terms between the various contributions in eq. (5.1), thus affording a more accurate representation of the total potential energy. A typical expression reads [98]

$$\begin{aligned}
 U_{\text{pot}} = & \left. \begin{aligned}
 & \sum_b k_2^b (b - b_0)^2 + k_3^b (b - b_0)^3 + k_4^b (b - b_0)^4 \\
 & + \sum_\theta k_2^\theta (\theta - \theta_0)^2 + k_3^\theta (\theta - \theta_0)^3 + k_4^\theta (\theta - \theta_0)^4 \\
 & + \sum_\varphi k_1^\phi [1 - \cos \varphi] + k_2^\phi [1 - \cos 2\varphi] + k_3^\phi [1 - \cos 3\varphi] \\
 & + \sum_\chi k_\chi (\chi - \chi_0)^2
 \end{aligned} \right\} \text{bonded energetic terms} \\
 & + \left. \begin{aligned}
 & \sum_{b,b'} k_{b,b'} (b - b_0)(b' - b'_0) + \sum_{b,\theta} k_{b,\theta} (b - b_0)(\theta - \theta_0) \\
 & + \sum_{b,\varphi} (b - b_0) \left(\sum_{n=1}^3 k_n^{b,\varphi} \cos(n\varphi) \right) \\
 & + \sum_{\theta,\theta'} k_{\theta,\theta'} (\theta - \theta_0)(\theta' - \theta'_0) + \sum_{\theta,\varphi} (\theta - \theta_0) \left(\sum_{n=1}^3 k_n^{\theta,\varphi} \cos(n\varphi) \right) \\
 & + \sum_{\theta,\theta',\varphi} k_{\theta,\theta',\varphi} (\theta - \theta_0)(\theta' - \theta'_0) \cos \varphi
 \end{aligned} \right\} \text{cross-coupling} \\
 & + \underbrace{\sum_{\text{vdW}} \varepsilon_{ij} \left[2 \left(\frac{r_{ij}^0}{r_{ij}} \right)^9 - 3 \left(\frac{r_{ij}^0}{r_{ij}} \right)^6 \right]}_{\text{Nonbonded energetic terms}} + \sum_{\text{Coulomb}} \frac{q_i q_j}{4\pi \varepsilon_0 r_{ij}}
 \end{aligned} \tag{5.2}$$

In general, simulations with class II potentials yield excellent predictions for the majority of the physical properties of system. Their only drawback is that they are computationally more intensive compared to the simpler, classical force fields. Typical examples of class II potentials are the COMPASS [98], the CFF [99] and the PCFF.

Having available a mathematical expression for the calculation of the potential energy of the system under study, the next step is to integrate Newton's equations of motion in the relevant statistical ensemble to sample system configurations in phase space. From this point of view, MD simulations are in many aspects similar to real experiments. When a real experiment is performed, a sample of the material is prepared

and connected to the instrument (a thermometer, a manometer, a viscometer, a spectrometer, etc.) to measure the desired property. The value of a specific property is computed as the average over many different measurements to increase statistical accuracy. In a similar way, in an MD simulation of N interacting atoms described by the potential energy function U_{pot} , the solution of Newton's equations of motion provides snapshots of the system in real time, from the analysis of which one can extract predictions of the relevant physical properties. Newton's equations of motion read

$$m_i \ddot{\mathbf{r}}_i = \mathbf{F}_i, \quad i = 1, 2, \dots, N \quad (5.3)$$

or, equivalently,

$$m_i \frac{d^2 \mathbf{r}_i}{dt^2} = - \frac{\partial U_{\text{pot}}(\mathbf{r}_1, \mathbf{r}_2, \dots, \mathbf{r}_N)}{\partial \mathbf{r}_i}, \quad i = 1, 2, \dots, N \quad (5.4)$$

where i denotes any atom in the system, m_i its mass, \mathbf{r}_i its position vector, \mathbf{F}_i the force acting on it, and t the time. Solving the $3N$ (where N stands for the total number of atomistic units) second-order differential equations (eq. (5.4)), we track the time evolution of the system and obtain its trajectory, that is, the positions and velocities of all its atomistic units in time. Applying then basic principles of statistical mechanics [100], we can obtain estimates of several properties of interest (e.g., thermodynamic, structural, conformational and dynamic), which can be directly compared to experimental data. Figure 5.3 provides the basic structure of a typical MD algorithm.

To solve the equations of motion, a numerical integrator must be employed, which should guarantee efficiency, stability and accuracy. To this, the algorithm must:

- not require an expensively large number of force evaluations per time step (thus, very popular techniques for the solution of ordinary differential equations such as the fourth-order Runge–Kutta method become inappropriate);
- permit the use of a large time step;
- be fast;
- require little memory;
- satisfy the energy conservation law.

Over the years, several algorithms have been proposed that satisfy the above criteria. The most popular are the gear predictor-corrector methods [92], the Verlet algorithms [93, 101] and the multiple time step methods (such as the reversible *RE*ference System *PR*opagator *AL*gorithm or rRESPA [102]). In addition, thanks to the rapid growth of computing power, the development of robust parallelization techniques (based on domain [103–105] and force [106–107] decomposition and CUDA programming) and the availability of supercomputing infrastructures (computer machines with millions of CPU processors), highly complicated systems containing hundreds of thousands or even millions of interacting particles (corresponding to simulation boxes with edge

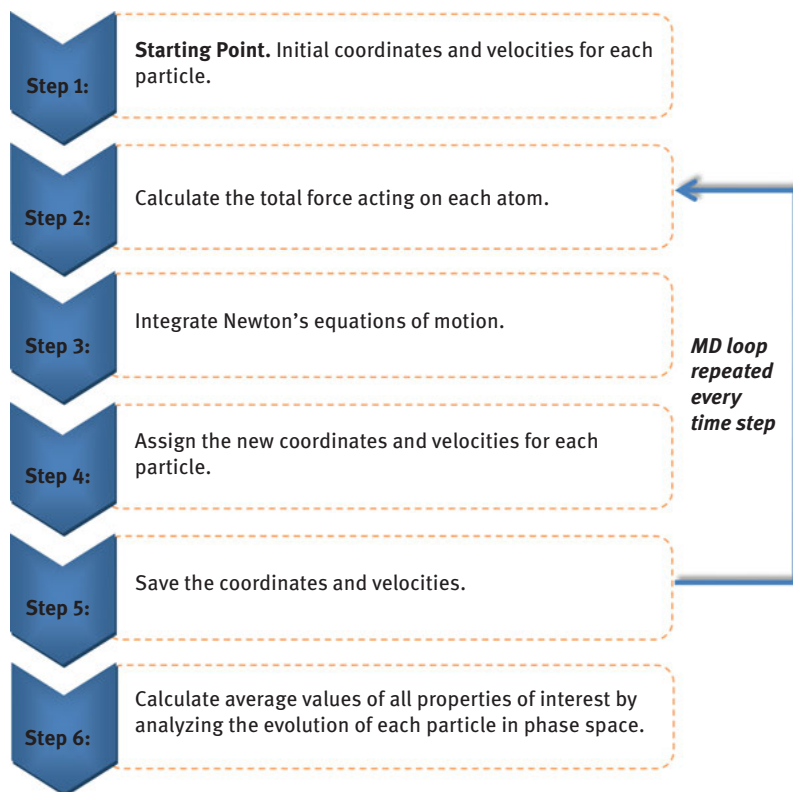


Figure 5.3: Simplified flow diagram of a typical MD algorithm.

lengths equal to hundreds of nanometers) can be simulated today in full atomistic detail for times up to several microseconds. Also, highly parallelized, user-friendly MD simulation packages are commercially available or freely distributed; we mention:

- Large-scale Atomic/Molecular Massively Parallel Simulator, *LAMMPS* [107]
- GRONingen MACHine for Chemical Simulations, *GROMACS* [108]
- Assisted Model Building with Energy Refinement, *AMBER*
- NANoscale Molecular Dynamics, *NAMD* [109]
- Chemistry at HARvard Macromolecular Mechanics, *CHARMM*

5.3 Atomistic MD simulation of graphene-based PMMA nanocomposites

As a model polymer, we have chosen PMMA whose nanocomposites with GS have been studied in detail over the years with several techniques. For example,

Ramanathan et al. [39] used sonication to break rigid nanoplatelets of expanded graphite apart into thinner platelets, which were dispersed next in a PMMA solution using high-speed shearing methods. This led to an increase in the T_g by 29 °C at 0.05 wt.% loading of the matrix in FGS, and up to an 80% enhancement of the Young's modulus at 1 wt.% loading in FGS. Similar observations have been reported by Li and McKenna [45] for GO/PMMA nanocomposites. One reason for the extraordinary mechanical properties of FGS-PMMA nanocomposites is the enhanced interfacial interactions of oxygen functionalities across the surface of graphene with PMMA chains. FGS contain pendant hydroxyl groups, which may form hydrogen bonds with the carbonyl groups of PMMA. Additional enhancement comes from the nanoscale surface roughness of FGS, the defects caused during thermal exfoliation of the precursor graphite oxide and their wrinkled topology at the nanoscale due to their extremely small thickness. These can enhance mechanical interlocking with the polymer chains, which also leads to better adhesion.

Atomistic MD simulations [62–63] have shown strong adhesion of PMMA chains (especially of its side groups) on graphene and considerably slower segmental and chain mobility in the interfacial area. According to simulation data, local mass density, segmental dynamics and chain terminal relaxation differ from the bulk behavior up to several nanometers from the graphene surface.

In the remaining of this chapter, we will focus on a methodology [110], initially proposed for a simpler class of systems (glassy vinyl polymers such as polypropylene and polystyrene) [110], which allows the determination of the mechanical properties of PMMA nanocomposites filled with GS (functionalized or nonfunctionalized), based on small-strain deformation experiments on the computer of microscopically detailed model structures. The procedure involves several modeling and mathematical steps and allows computing the elastic constants (Young's modulus E , bulk modulus B , shear modulus G and Poisson's ratio ν) of a polymeric glass under the assumption that vibrational contributions of the hard degrees of freedom are not significant; as a result, estimates of the elastic constants can be obtained by computing changes only in the total potential energy of static microscopic structures subjected to simple deformation modes. For glassy atactic polypropylene for which the method was first developed and implemented by Theodorou and Suter [110], elastic constants were predicted within 15% of the experimentally measured values.

All the simulations have been performed with an all-atom force field, allowing for a direct comparison of the computed with available experimental data. We chose DREIDING [95] because it combines simplicity with accuracy (for acrylic polymers). Since DREIDING [95] does not provide information about the values of partial charges of PMMA atoms, these were borrowed by the OPLS-AA [96] force field. Additional technical details (such as the parameter values of all bonded and non-bonded interactions describing intra- and interatomic contributions to potential energy) can be found in two published articles [72, 91]. Figure 5.4a–d provides typical

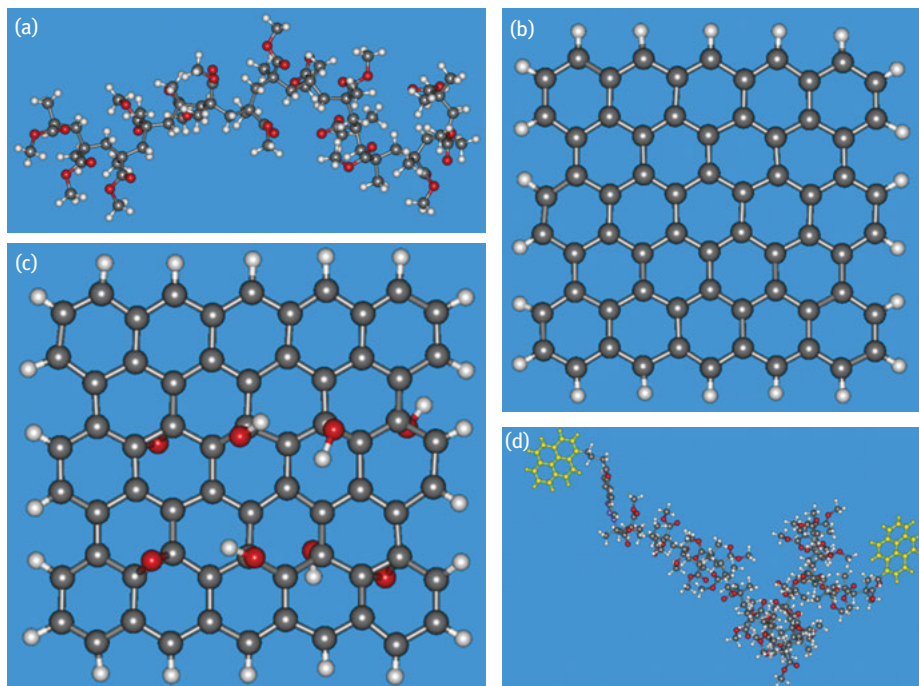


Figure 5.4: Typical atomistic structures of (a) an sPMMA chain, (b) a nonfunctionalized graphene sheet (GS), (c) a functionalized graphene sheet (FGS) and (d) a functionalized (py-sPMMA-py) chain.

atomistic structures of a PMMA chain, a GS, a GO and a functionalized PMMA chain with pyrene groups added to its two ends.

Systems simulated and simulation strategy

We focus on sPMMA, at $P = 1$ atm. The simulations were performed with strictly monodisperse samples with the model system consisting of 27 chains of degree of polymerization $X = 15$ (corresponding to a molecular weight of 1,503.75 g/mol). Unfunctionalized and functionalized GS had lateral dimensions $12 \text{ \AA} \times 12 \text{ \AA}$. Three model systems were studied: (a) the neat sPMMA matrix (no GS added; it will be denoted as sPMMA in the following), (b) its nanocomposite with three unfunctionalized monolayer GS (it will be denoted as GS-sPMMA in the following) corresponding to 5.67 wt.% concentration in GS and (c) its nanocomposite with three functionalized monolayer GS or GO (it will be denoted as FGS-sPMMA in the following) corresponding to 6.54 wt.% concentration in GO. The surface concentration of GO in hydroxyl (-OH) and epoxy (-O-) groups in the latter system was chosen to match as closely as possible the experimentally determined concentration reported by Ramanathan et al. [39] through elemental analysis.

To build initial configurations of all systems we used MAPS [111] and to execute the MD simulations we used LAMMPS [107]. All initial configurations were subjected to static structure optimization using a molecular mechanics algorithm to remove overlaps, and the resulting minimum potential energy structures were annealed to 500 K for several hundreds of nanoseconds to render them completely amorphous prior to quenching them down to room temperature, also to completely equilibrate them at all length scales. We used rectangular parallelepiped simulation cells of initial sides $40 \text{ \AA} \times 40 \text{ \AA} \times 40 \text{ \AA}$ subject to full periodic boundary conditions. Technical details regarding the execution of the MD simulations (type of thermostat–barostat used, calculation of electrostatic interactions, calculation of LJ interactions and of the tail corrections, integration of equations of motion, time step, etc.) can be found in the two relevant publications [72, 91].

Structural and conformational properties

From the equilibration runs at $T = 500 \text{ K}$, we calculated several properties that provided a good picture of the effect of GS and GO on the structural, conformational and thermodynamic properties of the polymer matrix. Figure 5.5 shows a typical atomistic

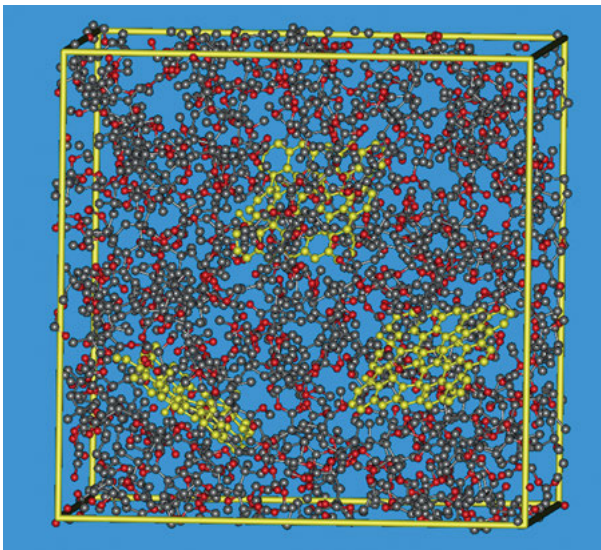


Figure 5.5: Typical atomistic snapshot from the simulation with the FGS-sPMMA nanocomposite at 6.54 wt.% loading. The simulation cell contains 27 PMMA chains and three FGS with five hydroxyl groups and three oxygen atoms on their surface. Initial cell dimensions $40 \text{ \AA} \times 40 \text{ \AA} \times 40 \text{ \AA}$. Carbon (sPMMA), carbon (FGS) and oxygen atoms are represented with gray, yellow and red colors, respectively. Hydrogen atoms have been omitted for clarity.

configuration of the FGS-sPMMA nanocomposite at the end of the MD simulation with this system at $T = 500$ K. A first quantity that can be easily calculated from an MD simulation in the NPT ensemble is the density ρ . Our predictions are $\rho = 1.065$ g/cm³ for the sPMMA, $\rho = 1.082$ g/cm³ for the GS-sPMMA and $\rho = 1.091$ g/cm³ for the FGS-sPMMA system. The experimentally determined value for infinite molecular weight PMMA at the same temperature (500 K) is 1.072 g/cm³ [112].

We also calculated (see Figure 5.6) the variation of polymer mass density with distance from a GS.

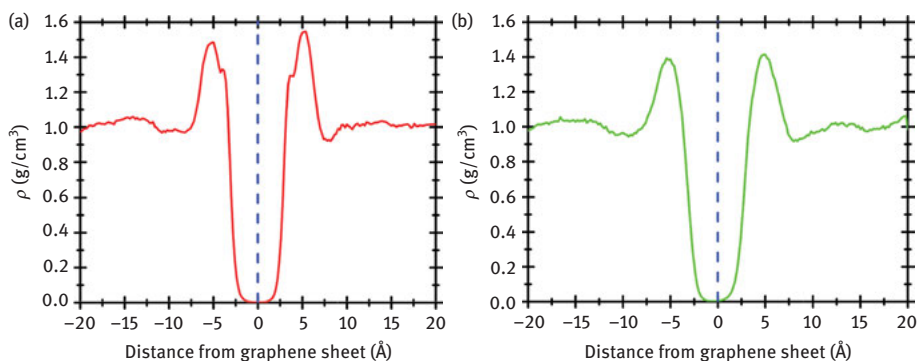


Figure 5.6: Local mass density normal to graphene sheets as obtained from the present MD simulations ($T = 500$ K, $P = 1$ atm) for the cases of pristine graphene sheets (a) and graphene oxide (b). The blue dashed line at the zero value of the horizontal axis denotes the average position of the graphene sheet midplane.

The high-density values (up to ~30% compared to the bulk density value) observed at distances up to ~5 Å from the surface of the GS indicate that sPMMA chains adsorb strongly on GS (either unfunctionalized GS or GO sheets). An example of a typical conformation of an adsorbed sPMMA chain on a GO is displayed in Figure 5.7.

An interesting point is that the local mass density of sPMMA is enhanced less in the FGS-sPMMA system than in the GS-sPMMA system. This should be attributed to the relative roughness of GO sheets (compared to the perfectly smooth surfaces of pristine GS) because of the presence of the characteristic -O- and -OH groups, which leads to the adsorption of less sPMMA molecules on GO than on GS. However, as we will see below, the -OH groups present on the surface of GO help the system develop a non-negligible number of hydrogen bonds with the oxygen atoms of sPMMA ester branches; this will be shown to have a strong impact on the overall mechanical performance of the nanocomposite. Figure 5.8 shows an example of a GO NP, which has developed two hydrogen bonds with one sPMMA chain on its one side and one hydrogen bond with another chain on its other side. The hydrogen bonds are highlighted with dashed circles in the figure. We clarify that the formation

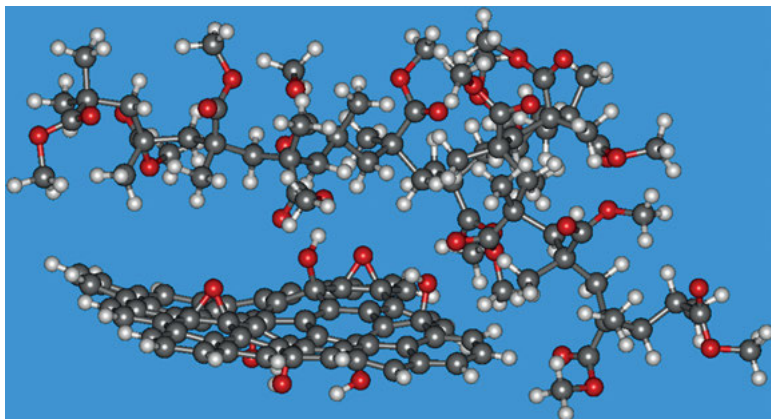


Figure 5.7: Atomistic snapshot from the MD simulation at $T = 500$ K showing a typical sPMMA chain configuration next to a GO.

of hydrogen bonds is not imposed directly in our simulations, but it is the indirect result of the employed force field (particularly of the partial charges assigned to the various atoms).

Mechanical properties

For the estimation of the mechanical properties of the simulated systems, we followed the methodology first proposed by Theodorou and Suter [110] for an amorphous glassy polymer, to which the reader is kindly referred for more details. The method involves the selection of several (about 15) completely equilibrated configurations of the system, which are then submitted to deformation experiments, from which one can calculate in a rigorous way the elastic properties of the sample. At the temperature and pressure conditions of interest here ($T = 300$ K and $P = 1$ atm), sPMMA and its GS- or GO-nanocomposites are in the glassy state, implying that one cannot directly use MD to sample well-equilibrated system configurations because the simulations will be nonergodic (the system will be trapped in configurations characterized by a local minimum in their potential energy). One way to overcome this is to equilibrate the system at a higher temperature (above the melting point), where equilibration is much easier to achieve, select a good number of relaxed configurations from this simulation and subject them to cooling runs down to the lower temperature ($T = 300$ K), followed by a short MD run for the density and local structure to equilibrate further. The resulting glassy structures will then be good candidates to use in the subsequent computational deformation experiments for the estimation of the elastic constants (Young's, bulk, shear moduli and Poisson's ratio). The results can be significantly improved by averaging over all configurations subjected to deformation.

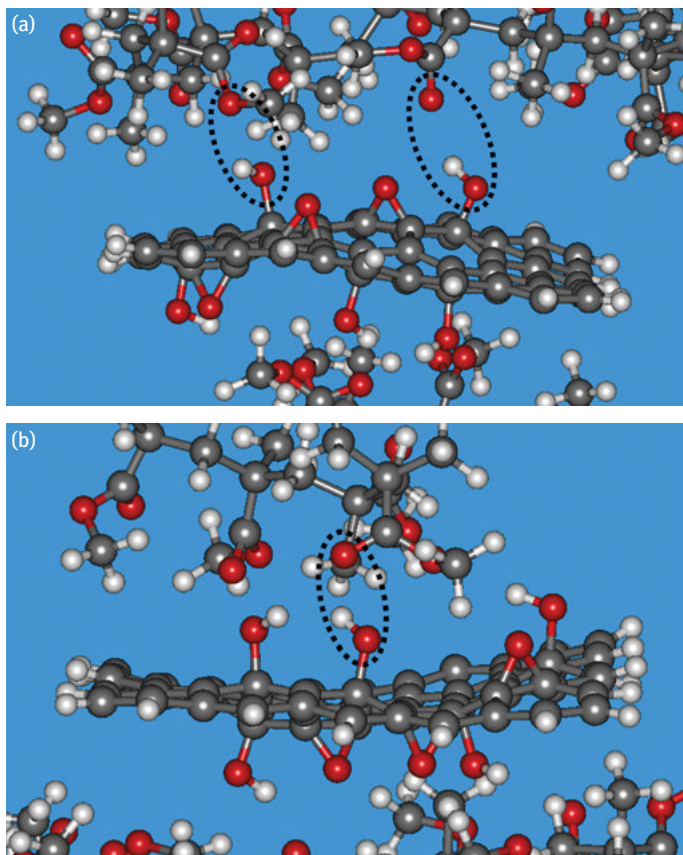


Figure 5.8: An example of a situation where three hydrogen bonds develop between a GO and the surrounding sPMMA chains. We can observe the formation of two hydrogen bonds with the same chain on the one side of the GO (a) and of one hydrogen bond with a different chain on the other side of the GO (b).

Applying the methodology [110] to the systems studied here, we obtained the results shown in Table 5.1. From the numerical data presented in Table 5.1, we can draw several conclusions:

- 1) The predicted values of the Young's modulus, shear modulus, bulk modulus and Poisson's ratio for the pure sPMMA system are in an excellent quantitative agreement with reported experimental values, which are summarized in ref. 72.
- 2) A significant enhancement of the mechanical properties of both types of nanocomposites (GS-PMMA and FGS-PMMA) is observed. This is more pronounced for the FGS-based ones, which should be attributed to the development of hydrogen bonds between the filler (GO) and the polar chains (sPMMA).

Table 5.1: Predicted elastic constants for all simulated systems from our study.

System	Lamé constants		Elastic constants			
	μ (GPa)	λ (GPa)	E (GPa)	B (GPa)	G (GPa)	ν
Pure sPMMA	1.3	3.4	3.4	4.2	1.3	0.36
Experimental values	–	–	2.07–6.2	5.9–6.17	1.78–2.3	0.34–0.36
GS-sPMMA	1.4	3.7	3.8	4.7	1.4	0.36
FGS-sPMMA	2.3	3.5	6.0	5.0	2.3	0.31

To further appreciate the effect of graphene and GO on the mechanical reinforcement of PMMA, we have normalized the predicted values of the four elastic constants with the values corresponding to the pure sPMMA matrix, and the results are shown in Figure 5.9.

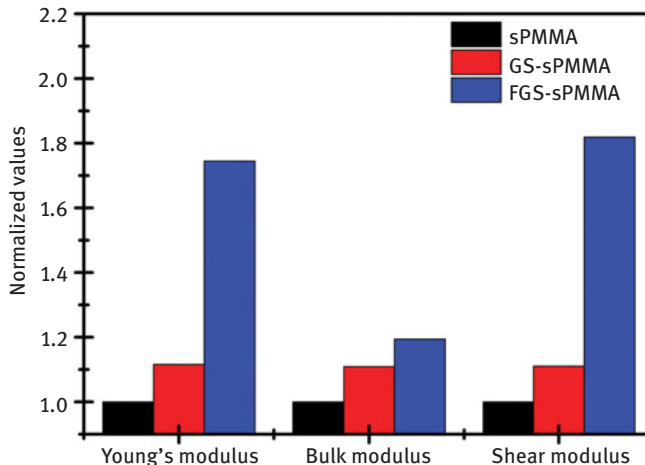


Figure 5.9: Summary of property improvement for the elastic constants of GS-sPMMA and FGS-sPMMA nanocomposites ($T = 300$ K, $P = 1$ atm). Numerical values have been normalized with the corresponding value of the neat PMMA matrix at the same conditions ($E = 3.4$ GPa, $B = 4.2$ GPa, $G = 1.3$ GPa and $\nu = 0.36$).

Overall, our results are in a good qualitative agreement with the experimental work of Ramanathan and coworkers [39] who reported an increase in the Young's modulus of ~80% in PMMA samples modified with FGS. However, a direct comparison of our simulation results with the experimental data is difficult to make because the molecular weight of the polymer matrix and the size of graphene flakes used in the experimental measurements are too large to address with atomistic MD simulations.

Graphene agglomeration in the PMMA matrix and how to prevent it

The homogeneous dispersion of GS in a polymer matrix is perhaps the most important and challenging issue in the fabrication of graphene-based polymer nanocomposites. In principle, GS fine dispersion offers larger areas for the effective adsorption of polymer chains, thus also for the better improvement of the properties of the nanocomposites.

All calculations reported in the previous section were carried out with model systems characterized by a uniform distribution of GS in the polymer matrix. However, several times during the MD equilibrations at $T = 500$ K, GS agglomeration was observed to occur at long times, as GS exhibited a strong tendency to come close to each other and form graphitic (π - π stacking) structures. To gain a better understanding of such a phenomenon, we conducted an additional simulation study with a larger system containing 100 atactic PMMA (aPMMA) chains with degree of polymerization $X = 30$ and six GS of size $60 \text{ \AA} \times 60 \text{ \AA}$ (system 1), and we monitored the time evolution of the positions of the six GS inside the simulation box. The results are shown in Figure 5.10a, where aPMMA chains have been omitted for clarity. We see that already from the first two nanoseconds of the simulation, a pair of GS have come close to each other to form an agglomerate.

To overcome the problem of GS agglomeration, we proposed [91] a novel methodology, which relies on the functionalization not of GS but of a good fraction of PMMA matrix chains by adding pyrene groups to their ends. The functionalized chains are noted as py-PMMA-py (see Figure 5.4d). The key idea is that pyrene groups adsorb strongly on the surface of GS due to very favorable π - π interactions developing between their four benzene rings and the corresponding hexagonal structures of GS; then, the intervening polymer mass between the two GS prevents them from approaching one or the other, thus self-assembly is avoided. To test the idea, we repeated the simulation of system 1 at the same temperature and pressure conditions ($T = 500$ K and $P = 1$ atm) by replacing approximately 40% of the aPMMA chains in the matrix with functionalized py-PMMA-py chains (system 2). The time evolution of the positions of GS for such a system is shown in Figure 5.10b. To enable a one-to-one comparison between the two systems (system 1 and system 2), the initial positions and initial velocities of all atoms in GS in the simulation with system 2 matched exactly those in the simulation with system 1. Then, according to Figure 5.10b, for the entire duration of the simulation (~ 500 ns), the six GS remained homogeneously dispersed in the polymer matrix. It is also clear that many of the pyrene groups of the functionalized py-PMMA-py chains were adsorbed strongly on the surface of GS.

To shed additional light in our MD findings, we calculated the time evolution of the distances between the centers of mass of all GS pairs in the two simulated systems. The results are shown in Figure 5.11a and b for system 1 and system 2, respectively. For system 1, we see that the distances between GS in pairs 1-4, 2-3 and 5-6 suddenly dropped down to 3.4 \AA at $t = 3, 10$ and 120 ns, respectively, which is the

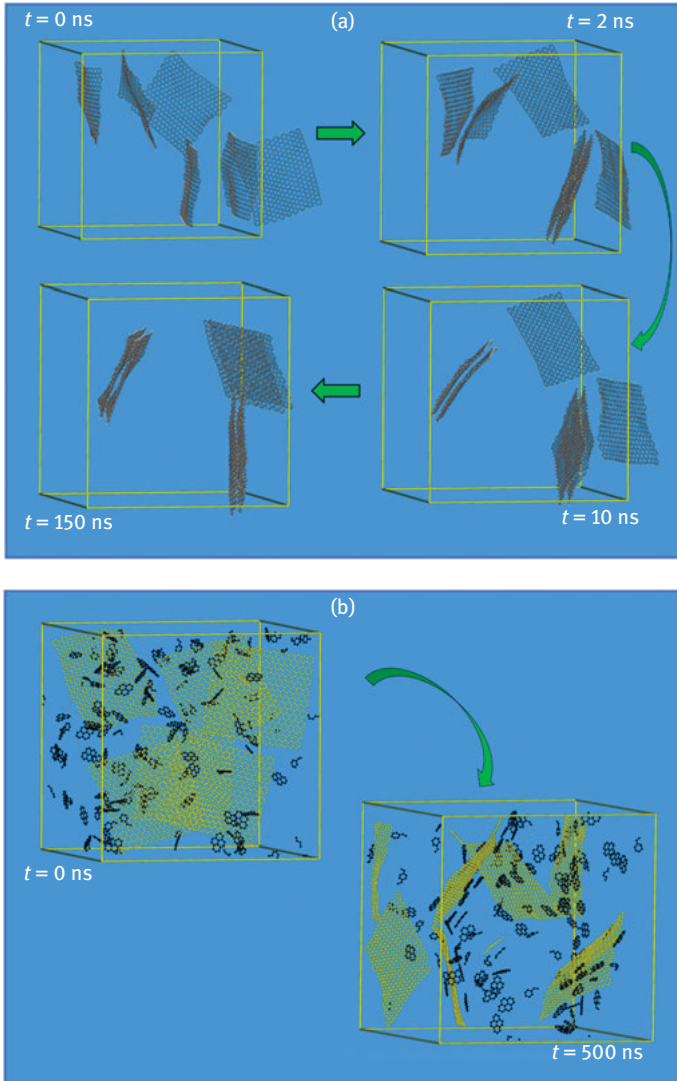


Figure 5.10: (a) Evolution of GS self-assembly during the MD simulation with the aPMMA-GS nanocomposite in the absence of py-PMMA-py chains. (b) Same as with (a) but for the case where 40% of aPMMA chains have been replaced by functionalized py-PMMA-py chains.

characteristic distance between consecutive graphene planes in a typical graphitic structure, and remained to 3.4 \AA throughout the simulation. In contrast, for system 2, no such phenomenon was observed. The reason for this behavior is the strong adsorption of functionalized py-PMMA-py chains on the surface of GS by their end-pyrene groups. A characteristic example is depicted in Figure 5.12, showing a GS on the surface of which 10 pyrene groups from different py-PMMA-py chains have been adsorbed.

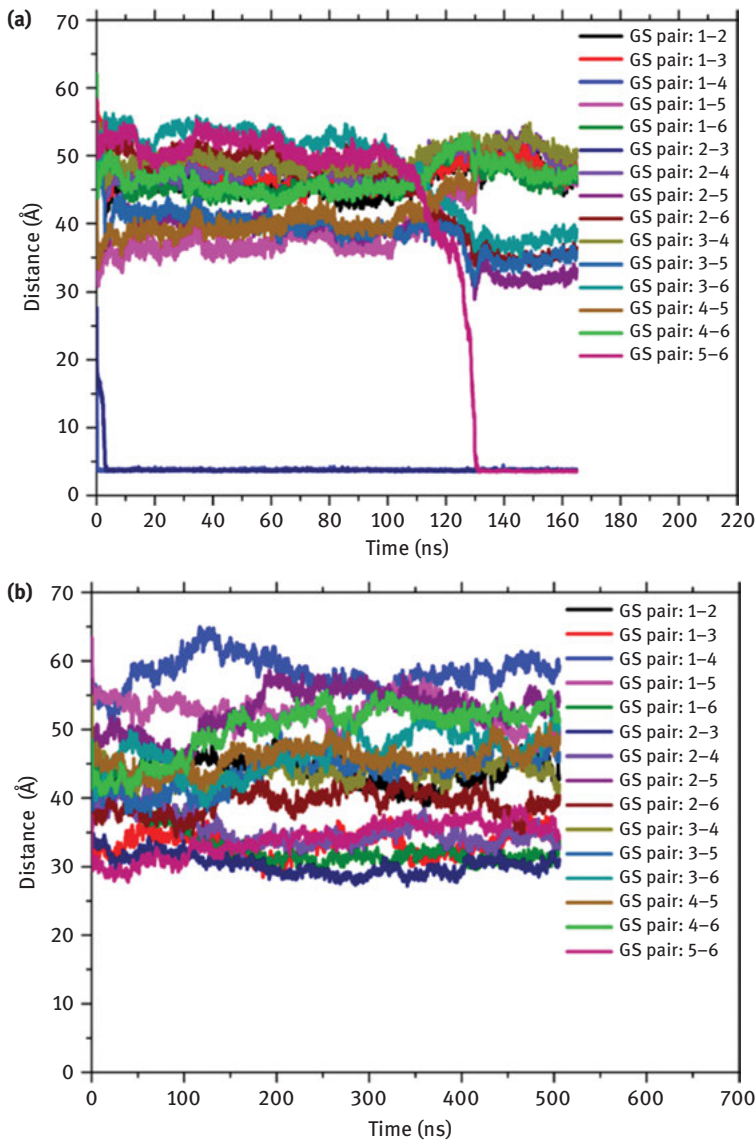


Figure 5.11: Time evolution of the distances between the centers of mass of graphene sheets in all GS pairs in the course of the MD simulation with (a) system 1 and (b) system 2.

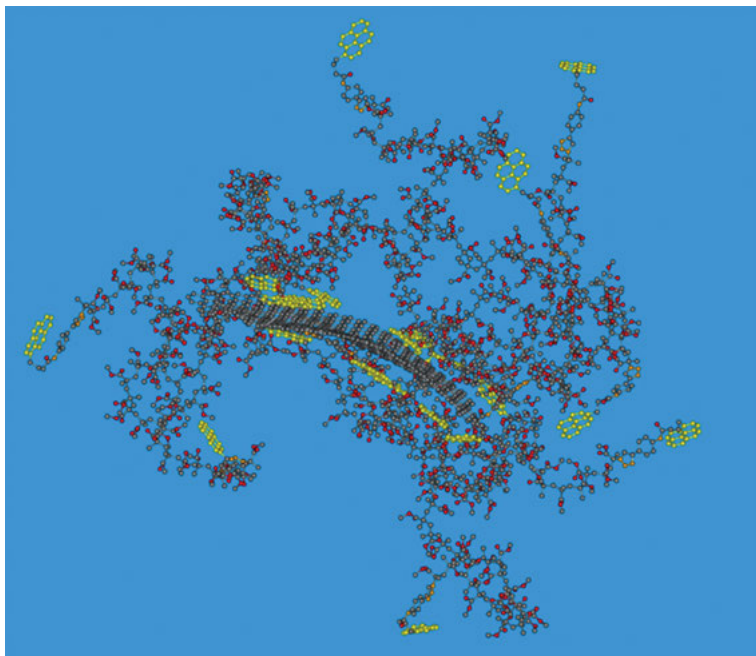


Figure 5.12: Multiple pyrene adsorption on the two faces of a GS. We can discern the parallel arrangement of pyrene groups on the surface of the GS due to π - π stacking, with the rest of the polymer chain extending away from the GS. Hydrogen atoms have been omitted for clarity and adsorbed pyrene groups are depicted in yellow.

A more detailed analysis revealed four different types of adsorbed structures:

- py-PMMA-py chains adsorbed on a GS by only one of their two ends (the other end remains free) forming a *dangling end*. A typical example is shown in Figure 5.13a.
- py-PMMA-py chains adsorbed on the same face of the same GS by both of their end-pyrene groups forming a *loop*. A typical example is shown in Figure 5.13b.
- py-PMMA-py chains adsorbed on both faces of the same GS forming an *extended loop*. A typical example is shown in Figure 5.13c.
- py-PMMA-py chains adsorbed with their end-pyrene groups on two different GS forming a *bridge*. A typical example is shown in Figure 5.13d.

The time evolution of the population of the four different types of adsorbed conformations in the course of the MD simulation is depicted in Figure 5.14. We see that, initially, all py-PMMA-py chains are free (i.e., nonadsorbed). This was done on purpose since we did not want to bias the py-PMMA-py chains to be close to GS.

Then, during the first 15 ns of the simulation with system 2, the population of *dangling ends* increases rapidly, and this continues (albeit with a smoother rate) at

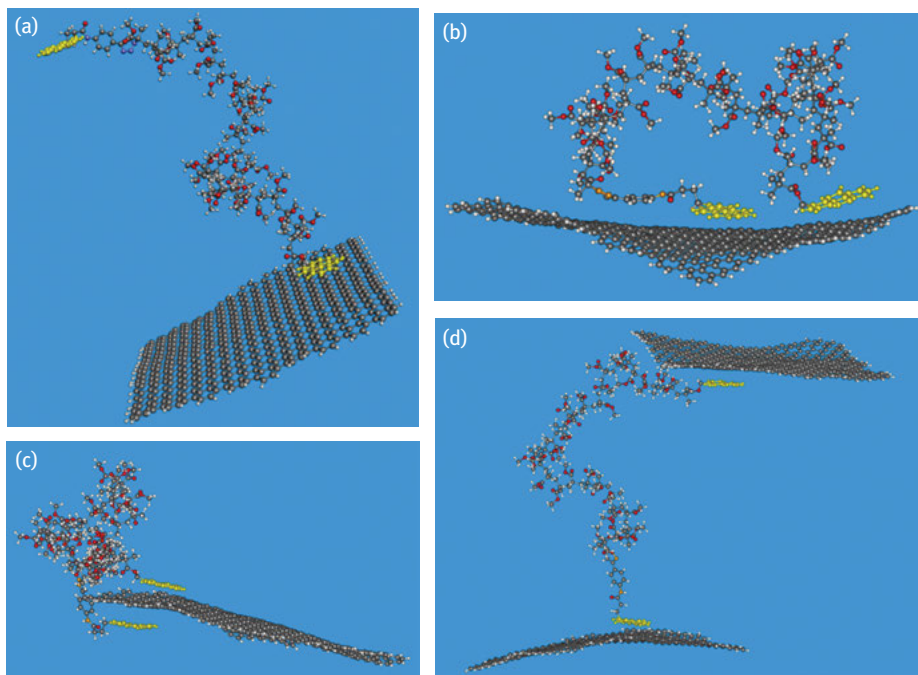


Figure 5.13: Examples of typical py-PMMA-py conformations adsorbed on GS: (a) a *dangling end*, (b) a *loop*, (c) an *extended loop* and (d) a *bridge*.

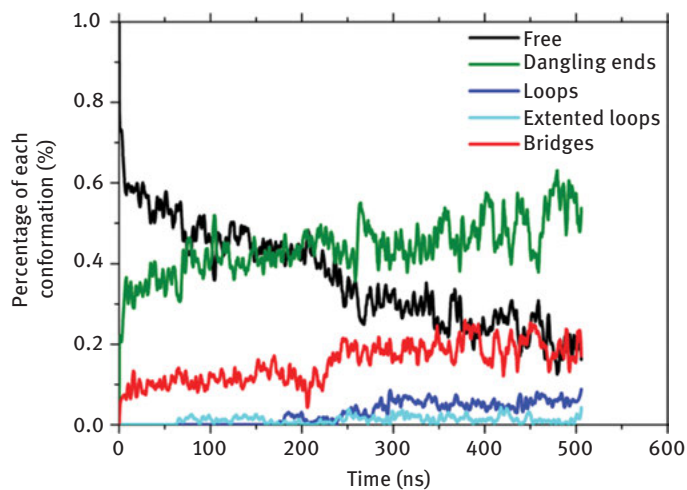


Figure 5.14: Time evolution of the relative population of adsorbed (*dangling ends*, *loops*, *extended loops* and *bridges*) and nonadsorbed (i.e., *free*) py-PMMA-py conformations in the course of the MD simulation.

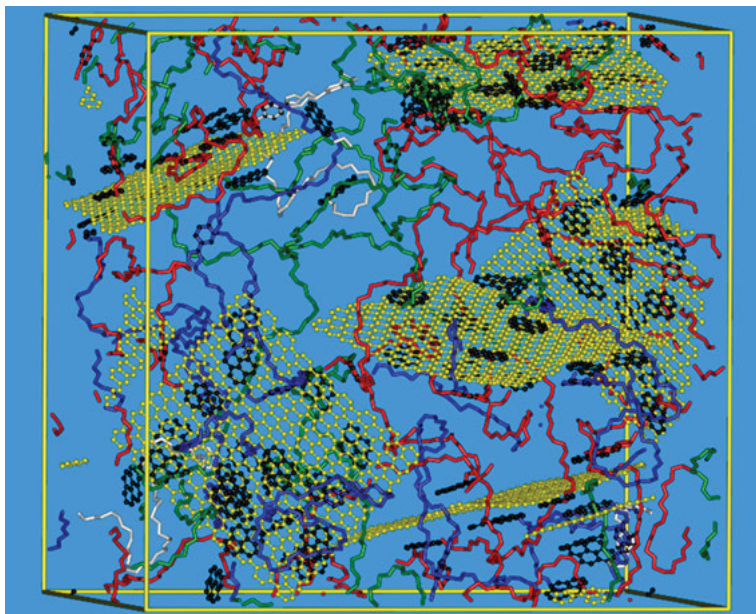


Figure 5.15: Typical conformations of adsorbed and free py-PMMA-py chains on GS (in yellow) in the simulation cell after several nanoseconds of simulation time. Different conformations are shown in different colors: *closed* and *extended closed loops* in blue, *bridges* in red, *dangling ends* in green and *free chains* in white.

all later times. Also increasing with time are the numbers of *loops*, *extended loops* and *bridges*. At the same time, the fraction of nonadsorbed chains decreases.

Figure 5.15 presents the configuration of system 2 at the end of the (approximately 500 ns long) MD simulation. Only graphene, pyrene and backbone atoms of the py-PMMA-py chains are shown for clarity. With blue, red and green colors, we depict the py-PMMA-py chains that participate in *loops*, *bridges* and *dangling ends*, with white color we depict *free* py-PMMA-py chains, and with yellow and black colors we depict carbon atoms in GS and pyrenes, respectively. At the end of the simulation, only few py-PMMA-py chains have remained *free* (i.e., nonadsorbed); the rest have formed *bridges*, *extended bridges* and *dangling ends*.

5.4 Conclusions

Within the space limitations of this chapter we hope that we have given a good account of the unique, extraordinary properties of graphene that have justified why it is widely considered as the material of the future. We have highlighted its great

potential for new applications and have presented the recent progress in the design of graphene-based polymer nanocomposites both from an experimental and a computational point of view.

We have also presented the basic concepts of molecular simulations focusing particularly on the MD technique, and simulation results for the structural, conformational and mechanical properties of a test nanocomposite system based on PMMA filled with two different types of GS: simple (i.e., unfunctionalized) GS and functionalized (i.e., GO). Our study was driven by recent experimental reports according to which addition of a small fraction of GO in a polar polymer matrix such as PMMA can lead to a remarkable enhancement of its elastic constants.

We started with simulations at a high temperature ($T = 500$ K) well above the melting point of PMMA, where system equilibration was easier to achieve and studied several physicochemical properties of the corresponding nanocomposites (density, polymer dimensions, local structure, type and statistics of adsorbed conformations). We found that for both types of fillers, the polymer local density in the proximity of GS is significantly higher than in the pure bulk. In the case of the GO-sPMMA nanocomposite, we observed the formation of a large population of hydrogen bonds between the ester branches of sPMMA and the hydroxyl groups of GO NPs.

In a second step, a good number of selected configurations from these high-temperature simulations were cooled down to room temperature, re-equilibrated and subjected to a rigorous statistico-mechanical analysis which provided predictions of their elastic constants. For the pure glassy sPMMA matrix, these were found to be in very favorable agreement with values measured in the experiment. For the nanocomposites, we found that GO sheets, even when present in very small concentrations in the sPMMA matrix, lead to a remarkable enhancement of the mechanical performance. This is due to the surface chemistry of GO which promotes strong interfacial interactions (mainly through hydrogen bonds) with the polymer matrix, thus significantly increasing the cohesive energy of the system and therefore its mechanical strength. Unfunctionalized GS also enhance mechanical behavior but to a much lesser degree than GO.

We also highlighted the tendency of GS to come close to each other due to very favorable π - π interactions and form stacked (layered) structures in the polymer matrix. To overcome this, a new methodology was discussed based on the end-functionalization of a good fraction of PMMA chains in the nanocomposite with pyrene functional groups to form py-PMMA-py chains. Our atomistic simulations showed that with this new nondestructive and thus highly attractive technique (covalent functionalization of graphene is completely avoided) GS self-assembly is avoided. This happens because pyrene groups adsorb quickly on GS and, owing to the intervening polymer mass, GS are kept separated, forming a stable and uniform dispersion. Our simulations revealed the creation of several interesting adsorbed structures in such a system: (a) *closed loops* (formed by py-PMMA-py chains adsorbed on the same face of a GS through both of their end pyrene groups), (b)

extended closed loops (formed by py-PMMA-py chains adsorbed on the two faces of the same GS), (c) *bridges* (formed by py-PMMA-py chains adsorbed on two different GS) and (d) *dangling ends* (corresponding to the free ends of py-PMMA-py chains adsorbed on a GS with only one of their pyrene groups). All these characteristic structures, especially *loops* and *bridges*, keep GS apart and well separated in the PMMA matrix, even at very high wt.% loadings of the matrix in GS, ensuring a homogeneous GS dispersion in the nanocomposite.

Acknowledgments: The authors are grateful to the Limmat Foundation, Zürich, Switzerland, for generous financial support through the project “Multiscale Simulations of Complex Polymer Systems” (MuSiComPS). The work was supported by computational time granted from the Greek Research & Technology Network (GRNET) in the National HPC facility – ARIS under project name COACERVATE (pr004011).

References

- [1] Geim, A. K., Novoselov, K. S., The rise of graphene. *Nat Mater* 2007, 6, 3, 183 DOI: 10.1038/Nmat1849.
- [2] Novoselov, K. S., Geim, A. K., Morozov, S. V., Jiang, D., Zhang, Y., Dubonos, S. V., Grigorieva, I. V., Firsov, A. A., Electric field effect in atomically thin carbon films. *Science* 2004, 306, 56–96, 666 DOI: 10.1126/science.1102896.
- [3] Allen, M. J., Tung, V. C., Kaner, R. B., Honeycomb Carbon: A Review of Graphene. *Chem Rev* 2010, 110, 1, 132 DOI: 10.1021/cr900070d.
- [4] Castro Neto, A. H., Guinea, F., Peres, N. M. R., Novoselov, K. S., Geim, A. K., The electronic properties of graphene. *Rev Mod Phys* 2009, 81, 1, 109 DOI: 10.1103/RevModPhys.81.109.
- [5] Choi, W., Lahiri, I., Seelaboyina, R., Kang, Y. S., Synthesis of graphene and its applications: A review. *Crit Rev Solid State* 2010, 35, 1, 52 DOI: 10.1080/10408430903505036.
- [6] Geim, A. K., Graphene: Status and prospects. *Science* 2009, 324, 5934, 1530 DOI: 10.1126/science.1158877.
- [7] Zhu, Y. W., Murali, S., Cai, W. W., Li, X. S., Suk, J. W., Potts, J. R., Ruoff, R. S., Graphene and graphene oxide: Synthesis, properties, and applications. *Adv Mater* 2010, 22, 46, 52–26 DOI: 10.1002/adma.201001068.
- [8] Kim, H., Abdala, A. A., Macosko, C. W., Graphene/polymer nanocomposites. *Macromolecules* 2010, 43, 16, 6515 DOI: 10.1021/ma100572e.
- [9] Kuilla, T., Bhadra, S., Yao, D. H., Kim, N. H., Bose, S., Lee, J. H., Recent advances in graphene based polymer composites. *Prog Polym Sci* 2010, 35, 11, 1350 DOI: 10.1016/j.progpolymsci.2010.07.005.
- [10] Potts, J. R., Dreyer, D. R., Bielawski, C. W., Ruoff, R. S., Graphene-based polymer nanocomposites. *Polymer* 2011, 52, 1, 5 DOI: 10.1016/j.polymer.2010.11.042.
- [11] Stankovich, S., Dikin, D. A., Dommett, G. H. B., Kohlhaas, K. M., Zimney, E. J., Stach, E. A., Piner, R. D., Nguyen, S. T., Ruoff, R. S., Graphene-based composite materials. *Nature* 2006, 442, 7100, 282 DOI: 10.1038/nature04969.
- [12] Verdejo, R., Bernal, M. M., Romasanta, L. J., Lopez-Manchado, M. A., Graphene filled polymer nanocomposites. *J Mater Chem* 2011, 21, 10, 3301 DOI: 10.1039/c0jm02708a.

- [13] Young, R. J., Kinloch, I. A., Gong, L., Novoselov, K. S., The mechanics of graphene nanocomposites: A review. *Compos Sci Technol* 2012, 72, 12, 1459 DOI: 10.1016/j.compscitech.2012.05.005.
- [14] de Heer, W. A., Berger, C., Wu, X. S., First, P. N., Conrad, E. H., Li, X. B., Li, T. B., Sprinkle, M., Hass, J., Sadowski, M. L., Potemski, M., Martinez, G., Epitaxial graphene. *Solid State Commun* 2007, 143, 1–2, 92 DOI: 10.1016/j.ssc.2007.04.023.
- [15] Ni, Z. H., Chen, W., Fan, X. F., Kuo, J. L., Yu, T., Wee, A. T. S., Shen, Z. X., Raman spectroscopy of epitaxial graphene on a SiC substrate. *Phys Rev B* 2008, 77, 11 DOI: 10.1103/Physrevb.77.115416.
- [16] Sutter, P. W., Flege, J. I., Sutter, E. A., Epitaxial graphene on ruthenium. *Nat Mater* 2008, 7, 5, 406 DOI: 10.1038/nmat2166.
- [17] Li, X. S., Cai, W. W., An, J. H., Kim, S., Nah, J., Yang, D. X., Piner, R., Velamakanni, A., Jung, I., Tutuc, E., Banerjee, S. K., Colombo, L., Ruoff, R. S., Large-area synthesis of high-quality and uniform graphene films on copper foils. *Science* 2009, 324, 5932, 1312 DOI: 10.1126/science.1171245.
- [18] Wang, Y., Chen, X. H., Zhong, Y. L., Zhu, F. R., Loh, K. P., Large area, continuous, few-layered graphene as anodes in organic photovoltaic devices. *Appl Phys Lett* 2009, 95, 6 DOI: 10.1063/1.3204698.
- [19] Jiao, L. Y., Zhang, L., Wang, X. R., Diankov, G., Dai, H. J., Narrow graphene nanoribbons from carbon nanotubes. *Nature* 2009, 458, 7240, 877 DOI: 10.1038/nature07919.
- [20] Kosynkin, D. V., Higginbotham, A. L., Sinitskii, A., Lomeda, J. R., Dimiev, A., Price, B. K., Tour, J. M., Longitudinal unzipping of carbon nanotubes to form graphene nanoribbons. *Nature* 2009, 458, 7240, 872-U5 DOI: 10.1038/nature07872.
- [21] Bourlinos, A. B., Georgakilas, V., Zboril, R., Steriotis, T. A., Stubos, A. K., Liquid-phase exfoliation of graphite towards solubilized graphenes. *Small* 2009, 5, 16, 1841 DOI: 10.1002/sml.200900242.
- [22] Hernandez, Y., Nicolosi, V., Lotya, M., Blighe, F. M., Sun, Z. Y., De, S., McGovern, I. T., Holland, B., Byrne, M., Gun'ko, Y. K., Boland, J. J., Niraj, P., Duesberg, G., Krishnamurthy, S., Goodhue, R., Hutchison, J., Scardaci, V., Ferrari, A. C., Coleman, J. N., High-yield production of graphene by liquid-phase exfoliation of graphite. *Nat Nanotechnol* 2008, 3, 9, 563 DOI: 10.1038/nnano.2008.215.
- [23] Stankovich, S., Dikin, D. A., Piner, R. D., Kohlhaas, K. A., Kleinhammes, A., Jia, Y., Wu, Y., Nguyen, S. T., Ruoff, R. S., Synthesis of graphene-based nanosheets via chemical reduction of exfoliated graphite oxide. *Carbon* 2007, 45, 7, 1558 DOI: 10.1016/j.carbon.2007.02.034.
- [24] Schniepp, H. C., Li, J. L., McAllister, M. J., Sai, H., Herrera-Alonso, M., Adamson, D. H., Prud'homme, R. K., Car, R., Saville, D. A., Aksay, I. A., Functionalized single graphene sheets derived from splitting graphite oxide. *J Phys Chem B* 2006, 110, 17, 8535 DOI: 10.1021/jp060936f.
- [25] Lee, C., Wei, X. D., Kysar, J. W., Hone, J., Measurement of the elastic properties and intrinsic strength of monolayer graphene. *Science* 2008, 321, 5887, 385 DOI: 10.1126/science.1157996.
- [26] Gomez-Navarro, C., Burghard, M., Kern, K., Elastic properties of chemically derived single graphene sheets. *Nano Lett* 2008, 8, 7, 20–45 DOI: 10.1021/nl801384y.
- [27] Ansari, S., Giannelis, E. P., Functionalized graphene sheet-polyvinylidene fluoride) conductive nanocomposites. *J Polym Sci Pol Phys* 2009, 47, 9, 888 DOI: 10.1002/polb.21695.
- [28] Cai, D. Y., Yusoh, K., Song, M., The mechanical properties and morphology of a graphite oxide nanoplatelet/polyurethane composite. *Nanotechnology* 2009, 20, 8 DOI: 10.1088/0957-4484/20/8/085712.

- [29] Morozov, S. V., Novoselov, K. S., Geim, A. K., Electron transport in graphene. *Phys-Usp+* 2008, 51, 7, 744 DOI: 10.1070/PU2008v051n07ABEH006575.
- [30] Morozov, S. V., Novoselov, K. S., Katsnelson, M. I., Schedin, F., Elias, D. C., Jaszczak, J. A., Geim, A. K., Giant intrinsic carrier mobilities in graphene and its bilayer. *Phys Rev Lett* 2008, 100, 1, DOI: 10.1103/Physrevlett.100.016602.
- [31] Durkop, T., Getty, S. A., Cobas, E., Fuhrer, M. S., Extraordinary mobility in semiconducting carbon nanotubes. *Nano Lett* 2004, 4, 1, 35 DOI: 10.1021/nl034841q.
- [32] Chen, J. H., Jang, C., Adam, S., Fuhrer, M. S., Williams, E. D., Ishigami, M., Charged-impurity scattering in graphene. *Nat Phys* 2008, 4, 5, 377 DOI: 10.1038/nphys935.
- [33] Chen, J. H., Jang, C., Xiao, S. D., Ishigami, M., Fuhrer, M. S., Intrinsic and extrinsic performance limits of graphene devices on SiO₂. *Nat Nanotechnol* 2008, 3, 4, 206 DOI: 10.1038/nnano.2008.58.
- [34] Balandin, A. A., Ghosh, S., Bao, W. Z., Calizo, I., Teweldebrhan, D., Miao, F., Lau, C. N., Superior thermal conductivity of single-layer graphene. *Nano Lett* 2008, 8, 3, 902 DOI: 10.1021/nl0731872.
- [35] Kim, P., Shi, L., Majumdar, A., McEuen, P. L., Thermal transport measurements of individual multiwalled nanotubes. *Phys Rev Lett* 2001, 87, 21 DOI: 10.1103/Physrevlett.87.215502.
- [36] Pop, E., Mann, D., Wang, Q., Goodson, K. E., Dai, H. J., Thermal conductance of an individual single-wall carbon nanotube above room temperature. *Nano Lett* 2006, 6, 1, 96 DOI: 10.1021/nl052145f.
- [37] Seol, J. H., Jo, I., Moore, A. L., Lindsay, L., Aitken, Z. H., Pettes, M. T., Li, X. S., Yao, Z., Huang, R., Broido, D., Mingo, N., Ruoff, R. S., Shi, L., Two-dimensional phonon transport in supported graphene. *Science* 2010, 328, 5975, 213 DOI: 10.1126/science.1184014.
- [38] Moniruzzaman, M., Winey, K. I., Polymer nanocomposites containing carbon nanotubes. *Macromolecules* 2006, 39, 16, 5194 DOI: 10.1021/ma060733p.
- [39] Ramanathan, T., Abdala, A. A., Stankovich, S., Dikin, D. A., Herrera-Alonso, M., Piner, R. D., Adamson, D. H., Schniepp, H. C., Chen, X., Ruoff, R. S., Nguyen, S. T., Aksay, I. A., Prud'homme, R. K., Brinson, L. C., Functionalized graphene sheets for polymer nanocomposites. *Nat Nanotechnol* 2008, 3, 6, 327 DOI: 10.1038/nnano.2008.96.
- [40] Fang, M., Wang, K. G., Lu, H. B., Yang, Y. L., Nutt, S., Covalent polymer functionalization of graphene nanosheets and mechanical properties of composites. *J Mater Chem* 2009, 19, 38, 7098 DOI: 10.1039/b908220d.
- [41] Lee, S. H., Dreyer, D. R., An, J. H., Velamakanni, A., Piner, R. D., Park, S., Zhu, Y. W., Kim, S. O., Bielawski, C. W., Ruoff, R. S., Polymer brushes via controlled, surface-initiated atom transfer radical polymerization (atrp) from graphene oxide. *Macromol Rapid Comm* 2010, 31, 3, 281 DOI: 10.1002/marc.200900641.
- [42] Kim, H., Macosko, C. W., Processing-property relationships of polycarbonate/graphene composites. *Polymer* 2009, 50, 15, 3797 DOI: 10.1016/j.polymer.2009.05.038.
- [43] Steurer, P., Wissert, R., Thomann, R., Mulhaupt, R., Functionalized Graphenes and Thermoplastic nanocomposites based upon expanded graphite oxide. *Macromol Rapid Comm* 2009, 30, 4–5, 316 DOI: 10.1002/marc.200800754.
- [44] Kumar, A., Sharma K., Dixit A. R., A review of the mechanical and thermal properties of graphene and its hybrid polymer nanocomposites for structural applications. *J Mater Sci* 2019, 54, 8, 5992 DOI: 10.1007/s10853-018-03244-3.
- [45] Li, X. G., McKenna, G. B., Considering viscoelastic micromechanics for the reinforcement of graphene polymer nanocomposites. *ACS Macro Lett* 2012, 1, 3, 388 DOI: 10.1021/mz200253x.
- [46] Liao, K. H., Aoyama, S., Abdala, A. A., Macosko, C., Does graphene change T_g of nanocomposites? *Macromolecules* 2014, 47, 23, 8311 DOI: 10.1021/ma501799z.

- [47] Liao, K. H., Kobayashi, S., Kim, H., Abdala, A. A., Macosko, C. W., influence of functionalized graphene sheets on modulus and glass transition of PMMA. *Macromolecules* 2014, 47, 21, 7674 DOI: 10.1021/ma501709g.
- [48] Cano, M., Khan, U., Sainsbury, T., O'Neill, A., Wang, Z. M., McGovern, I. T., Maser, W. K., Benito, A. M., Coleman, J. N., Improving the mechanical properties of graphene oxide based materials by covalent attachment of polymer chains. *Carbon* 2013, 52, 363 DOI: 10.1016/j.carbon.2012.09.046.
- [49] Zhao, X., Zhang, Q. H., Chen, D. J., Lu, P., Enhanced mechanical properties of graphene-based poly(vinyl alcohol) composites. *Macromolecules* 2010, 43, 5, 2357 DOI: 10.1021/ma902862u.
- [50] Kim, H., Macosko, C. W., Morphology and properties of polyester/exfoliated graphite nanocomposites. *Macromolecules* 2008, 41, 9, 3317 DOI: 10.1021/ma702385h.
- [51] Liang, J. J., Wang, Y., Huang, Y., Ma, Y. F., Liu, Z. F., Cai, J. M., Zhang, C. D., Gao, H. J., Chen, Y. S., Electromagnetic interference shielding of graphene/epoxy composites. *Carbon* 2009, 47, 3, 922 DOI: 10.1016/j.carbon.2008.12.038.
- [52] Stankovich, S., Piner, R. D., Nguyen, S. T., Ruoff, R. S., Synthesis and exfoliation of isocyanate-treated graphene oxide nanoplatelets. *Carbon* 2006, 44, 15, 3342 DOI: 10.1016/j.carbon.2006.06.004.
- [53] Eda, G., Chhowalla, M., Graphene-based composite thin films for electronics. *Nano Lett* 2009, 9, 2, 814 DOI: 10.1021/nl8035367.
- [54] Van Lier, G., Van Alsenoy, C., Van Doren, V., Geerlings, P., Ab initio study of the elastic properties of single-walled carbon nanotubes and graphene. *Chem Phys Lett* 2000, 326, 1–2, 181 DOI: 10.1016/S0009-2614(00)00764-8.
- [55] Liu, F., Ming, P. M., Li, J., Ab initio calculation of ideal strength and phonon instability of graphene under tension. *Phys Rev B* 2007, 76, 6 DOI: 10.1103/Physrevb.76.064120.
- [56] Kalosakas, G., Lathiotakis, N. N., Galiotis, C., Papagelis, K., In-plane force fields and elastic properties of graphene. *J Appl Phys* 2013, 113, 13, DOI: 10.1063/1.4798384.
- [57] Jiang, J. W., Wang, J. S., Li, B. W., Young's modulus of graphene: a molecular dynamics study. *Phys Rev B* 2009, 80, 11, DOI: 10.1103/Physrevb.80.113405.
- [58] Mattausch, A., Pankratov, O., Ab initio study of graphene on SiC. *Phys Rev Lett* 2007, 99, 7, DOI: 10.1103/Physrevlett.99.076802.
- [59] Ma, Y. D., Dai, Y., Guo, M., Niu, C. W., Huang, B. B., Graphene adhesion on MoS₂ monolayer: An ab initio study. *Nanoscale* 2011, 3, 9, 3883 DOI: 10.1039/c1nr10577a.
- [60] Awasthi, A. P., Lagoudas, D. C., Hammerand, D. C., Modeling of graphene-polymer interfacial mechanical behavior using molecular dynamics. *Model Simul Mater Sci* 2009, 17, 1, DOI: 10.1088/0965-0393/17/1/015002.
- [61] Li, Y., Kroger, M., Liu, W. K., Nanoparticle geometrical effect on structure, dynamics and anisotropic viscosity of polyethylene nanocomposites. *Macromolecules* 2012, 45, 4, 20–99 DOI: 10.1021/ma202289a.
- [62] Rissanou, A. N., Harmandaris, V., Structure and dynamics of poly(methylmethacrylate)/graphene systems through atomistic molecular dynamics simulations. *J Nanopart Res* 2013, 15, 5, DOI: 10.1007/S11051-013-1589-2.
- [63] Rissanou, A. N., Harmandaris, V., Dynamics of various polymer-graphene interfacial systems through atomistic molecular dynamics simulations. *Soft Matter* 2014, 10, 16, 2876 DOI: 10.1039/c3sm52688g.
- [64] Rissanou, A. N., Power, A. J., Harmandaris, V., Structural and dynamical properties of polyethylene/graphene nanocomposites through molecular dynamics simulations. *Polymers-Basel* 2015, 7, 3, 390, DOI: 10.3390/polym7030390.

- [65] Bacova, P., Rissanou, A. N., Harmandaris, V., Edge-functionalized graphene as a nanofiller: Molecular dynamics simulation study. *Macromolecules* 2015, 48, 24, 9024 DOI: 10.1021/acs.macromol.5b01782.
- [66] Guryel, S., Walker, M., Geerlings, P., De Proft, F., Wilson, M. R., Molecular dynamics simulations of the structure and the morphology of graphene/polymer nanocomposites. *Phys Chem Chem Phys* 2017, 19, 20, 12959, DOI: 10.1039/c7cp01552f.
- [67] Gulde, M., Rissanou, A. N., Harmandaris, V., Muller, M., Schafer, S., Ropers, C., Dynamics and structure of monolayer polymer crystallites on graphene. *Nano Lett* 2016, 16, 11, 6994 DOI: 10.1021/acs.nanolett.6b03079.
- [68] Lv, C., Xue, Q. Z., Xia, D., Ma, M., Xie, J., Chen, H. J., Effect of chemisorption on the interfacial bonding characteristics of graphene-polymer composites. *J Phys Chem C* 2010, 114, 14, 6588 DOI: 10.1021/jp100110n.
- [69] Karatasos, K., Kritikos, G., Characterization of a graphene oxide/poly(acrylic acid) nanocomposite by means of molecular dynamics simulations. *RSC Adv* 2016, 6, 111, 109–267 DOI: 10.1039/c6ra22951d.
- [70] Xue, Q. Z., Lv, C., Shan, M. X., Zhang, H. X., Ling, C. C., Zhou, X. Y., Jiao, Z. Y., Glass transition temperature of functionalized graphene-polymer composites. *Comp Mater Sci* 2013, 71, 66 DOI: 10.1016/j.commat.2013.01.009.
- [71] Azimi, M., Mirjavadi, S. S., Hamouda, A. M. S., Makki, H., Heterogeneities in polymer structural and dynamic properties in graphene and graphene oxide nanocomposites: Molecular dynamics simulations. *Macromol Theor Simul* 2017, 26, 2, DOI: 10.1002/Mats.201600086.
- [72] Skountzos, E. N., Anastassiou, A., Mavrantzas, V. G., Theodorou, D. N., Determination of the mechanical properties of a poly(methyl methacrylate) nanocomposite with functionalized graphene sheets through detailed atomistic simulations. *Macromolecules* 2014, 47, 22, 8072 DOI: 10.1021/ma5017093.
- [73] Lin, F., Xiang, Y., Shen, H. S., Temperature dependent mechanical properties of graphene reinforced polymer nanocomposites – A molecular dynamics simulation. *Compos Part B-Eng* 2017, 111, 261 DOI: 10.1016/j.compositesb.2016.12.0041359-8368.
- [74] Liu, F., Hu, N., Ning, H. M., Liu, Y. L., Li, Y., Wu, L. K., Molecular dynamics simulation on interfacial mechanical properties of polymer nanocomposites with wrinkled graphene. *Comp Mater Sci* 2015, 108, 160 DOI: 10.1016/j.commat.2015.06.023.
- [75] Liu, J., Shen, J. X., Zheng, Z. J., Wu, Y. P., Zhang, L. Q., Revealing the toughening mechanism of graphene-polymer nanocomposite through molecular dynamics simulation. *Nanotechnology* 2015, 26, 29, DOI: 10.1088/0957-4484/26/29/291003.
- [76] Wang, M. C., Lai, Z. B., Galpaya, D., Yan, C., Hu, N., Zhou, L. M., Atomistic simulation of surface functionalization on the interfacial properties of graphene-polymer nanocomposites. *J Appl Phys* 2014, 115, 12 DOI: 10.1063/1.4870170.
- [77] Schopp, S., Thomann, R., Ratzsch, K. F., Kerling, S., Altstadt, V., Mulhaupt, R., Functionalized Graphene and Carbon materials as components of styrene-butadiene rubber nanocomposites prepared by aqueous dispersion blending. *Macromol Mater Eng* 2014, 299, 3, 319 DOI: 10.1002/mame.201300127.
- [78] Yin, B., Zhang, X. M., Zhang, X., Wang, J. Y., Wen, Y. W., Jia, H. B., Ji, Q. M., Ding, L. F., Ionic liquid functionalized graphene oxide for enhancement of styrene-butadiene rubber nanocomposites. *Polym Advan Technol* 2017, 28, 3, 293 DOI: 10.1002/pat.3886.
- [79] Georgakilas, V., Otyepka, M., Bourlinos, A. B., Chandra, V., Kim, N., Kemp, K. C., Hobza, P., Zboril, R., Kim, K. S., Functionalization of graphene: Covalent and non-covalent approaches, derivatives and applications. *Chem Rev* 2012, 112, 11, 6156 DOI: 10.1021/cr3000412.

- [80] Lonkar, S. P., Deshmukh, Y. S., Abdala, A. A., Recent advances in chemical modifications of graphene. *Nano Res* 2015, 8, 4, 1039 DOI: 10.1007/s12274-014-0622-9.
- [81] Cheng, H. K. F., Sahoo, N. G., Tan, Y. P., Pan, Y. Z., Bao, H. Q., Li, L., Chan, S. H., Zhao, J. H., Poly(vinyl alcohol) nanocomposites filled with poly(vinyl alcohol)-grafted graphene oxide. *ACS Appl Mater Inter* 2012, 4, 5, 2387 DOI: 10.1021/am300550n.
- [82] Goncalves, G., Marques, P. A. A. P., Barros-Timmons, A., Bdkin, I., Singh, M. K., Emami, N., Gracio, J., Graphene oxide modified with PMMA via ATRP as a reinforcement filler. *J Mater Chem* 2010, 20, 44, 9927 DOI: 10.1039/c0jm01674h.
- [83] Mallakpour, S., Abdolmaleki, A., Borandeh, S., Covalently functionalized graphene sheets with biocompatible natural amino acids. *Appl Surf Sci* 2014, 307, 533 DOI: 10.1016/j.apsusc.2014.04.070.
- [84] Sayyar, S., Murray, E., Thompson, B. C., Gambhir, S., Officer, D. L., Wallace, G. G., Covalently linked biocompatible graphene/polycaprolactone composites for tissue engineering. *Carbon* 2013, 52, 296 DOI: 10.1016/j.carbon.2012.09.031.
- [85] Xue, Y. H., Liu, Y., Lu, F., Qu, J., Chen, H., Dai, L. M., Functionalization of Graphene Oxide with Polyhedral Oligomeric Silsesquioxane (POSS) for Multifunctional Applications. *J Phys Chem Lett* 2012, 3, 12, 1607 DOI: 10.1021/jz3005877.
- [86] Park, J. H., Aluru, N. R., Self-assembly of graphenes. *Surf Sci* 2011, 605, 17–18, 16–16 DOI: 10.1016/j.susc.2011.02.011.
- [87] Ju, S. P., Wang, Y. C., Huang, G. J., Chang, J. W., Miscibility of graphene and poly(methyl methacrylate) (PMMA): Molecular dynamics and dissipative particle dynamics simulations. *Rsc Adv* 2013, 3, 22, 8298 DOI: 10.1039/c3ra22879g.
- [88] Karatasos, K., Graphene/hyperbranched polymer nanocomposites: Insight from molecular dynamics simulations. *Macromolecules* 2014, 47, 24, 8833 DOI: 10.1021/ma502123a.
- [89] Roussou, R. E., Karatasos, K., Graphene/poly(ethylene glycol) nanocomposites as studied by molecular dynamics simulations. *Mater Design* 2016, 97, 163, DOI: 10.1016/j.matdes.2016.02.078.
- [90] Guo, Y. S., Liu, J., Wu, Y. P., Zhang, L. Q., Wang, Z., Li, Y., Molecular insights into the effect of graphene packing on mechanical behaviors of graphene reinforced cis-1,4-polybutadiene polymer nanocomposites. *Phys Chem Chem Phys* 2017, 19, 33, 22417 DOI: 10.1039/c7cp02945d.
- [91] Papadimitriou, K. D., Skountzos, E. N., Gkempoura, S. S., Polyzos, I., Mavrantzas, V. G., Galiotis, C., Tsitsilianis, C., Molecular modeling combined with advanced chemistry for the rational design of efficient graphene dispersing agents. *ACS Macro Lett* 2016, 5, 1, 24 DOI: 10.1021/acsmacrolett.5b00755.
- [92] Allen, M. P., Tildesley, D. J., Computer simulation of liquids. Clarendon Press, Oxford University Press: Oxford/Oxfordshire/New York, 1987, xix, 385 p.
- [93] Frenkel, D., Smit, B., Understanding molecular simulation: from algorithms to applications. Academic Press: San Diego, 1996, xviii, 443 p.
- [94] Mayo, S. L., Olafson, B. D., Goddard, W. A., Dreiding – a generic force-field for molecular simulations. *J Phys Chem-US* 1990, 94, 26, 8897 DOI: 10.1021/J100389a010.
- [95] Jorgensen, W. L., Maxwell, D. S., TiradoRives, J., Development and testing of the OPLS all-atom force field on conformational energetics and properties of organic liquids. *J Am Chem Soc* 1996, 118, 45, 11225 DOI: 10.1021/Ja9621760.
- [96] MacKerell, A. D., Bashford, D., Bellott, M., Dunbrack, R. L., Evanseck, J. D., Field, M. J., Fischer, S., Gao, J., Guo, H., Ha, S., Joseph-McCarthy, D., Kuchnir, L., Kuczera, K., Lau, F. T. K., Mattos, C., Michnick, S., Ngo, T., Nguyen, D. T., Prodhom, B., Reiher, W. E., Roux, B., Schlenkrich, M., Smith, J. C., Stote, R., Straub, J., Watanabe, M., Wiorkiewicz-Kuczera, J., Yin,

- D., Karplus, M., All-atom empirical potential for molecular modeling and dynamics studies of proteins. *J Phys Chem B* 1998, 102, 18, 35–86 DOI: 10.1021/jp973084f.
- [97] Cornell, W. D., Cieplak, P., Bayly, C. I., Gould, I. R., Merz, K. M., Ferguson, D. M., Spellmeyer, D. C., Fox, T., Caldwell, J. W., Kollman, P. A., A second generation force field for the simulation of proteins, nucleic acids, and organic molecules. *J Am Chem Soc* 1996, 118, 9, 2309, DOI: 10.1021/ja955032e.
- [98] Sun, H., COMPASS: An ab initio force-field optimized for condensed-phase applications – Overview with details on alkane and benzene compounds. *J Phys Chem B* 1998, 102, 38, 7338, DOI: 10.1021/jp980939v.
- [99] Maple, J. R., Hwang, M. J., Stockfisch, T. P., Dinur, U., Waldman, M., Ewig, C. S., Hagler, A. T., Derivation of class-ii force-fields .1. methodology and quantum force-field for the alkyl functional-group and alkane molecules. *J Comput Chem* 1994, 15, 2, 162 DOI: 10.1002/jcc.540150207.
- [100] McQuarrie, D. A., *Statistical mechanics*. Harper and Row: New York, London, 1976, xvii, 641 p.
- [101] Swope, W. C., Andersen, H. C., Berens, P. H., Wilson, K. R., A computer-simulation method for the calculation of equilibrium-constants for the formation of physical clusters of molecules – application to small water clusters. *J Chem Phys* 1982, 76, 1, 637 DOI: 10.1063/1.442716.
- [102] Tuckerman, M., Berne, B. J., Martyna, G. J., Reversible multiple time scale molecular-dynamics. *J Chem Phys* 1992, 97, 3, 1990 DOI: 10.1063/1.463137.
- [103] Brown, D., Clarke, J. H. R., Okuda, M., Yamazaki, T., A domain decomposition parallel-processing algorithm for molecular-dynamics simulations of polymers. *Comput Phys Commun* 1994, 83, 1, 1 DOI: 10.1016/0010-4655(95)00007-3.
- [104] Putz, M., Kolb, A., Optimization techniques for parallel molecular dynamics using domain decomposition. *Comput Phys Commun* 1998, 113, 2–3, 145 DOI: 10.1016/S0010-4655(98)00074-5.
- [105] Wilson, M. R., Allen, M. P., Warren, M. A., Sauron, A., Smith, W., Replicated data and domain decomposition molecular dynamics techniques for simulation of anisotropic potentials. *J Comput Chem* 1997, 18, 4, 478.
- [106] Plimpton, S., Hendrickson, B., A new parallel method for molecular dynamics simulation of macromolecular systems. *J Comput Chem* 1996, 17, 3, 326.
- [107] Plimpton, S., Fast parallel algorithms for short-range molecular-dynamics. *J Comput Phys* 1995, 117, 1, 1 DOI: 10.1006/jcph.1995.1039.
- [108] Lindahl, E., Hess, B., van der Spoel, D., GROMACS 3.0: A package for molecular simulation and trajectory analysis. *J Mol Model* 2001, 7, 8, 306 DOI: 10.1007/s008940100045.
- [109] Phillips, J. C., Braun, R., Wang, W., Gumbart, J., Tajkhorshid, E., Villa, E., Chipot, C., Skeel, R. D., Kale, L., Schulten, K., Scalable molecular dynamics with NAMD. *J Comput Chem* 2005, 26, 16, 1781 DOI: 10.1002/jcc.20289.
- [110] Theodorou, D. N., Suter, U. W., Atomistic modeling of mechanical-properties of polymeric glasses. *Macromolecules* 1986, 19, 1, 139 DOI: 10.1021/Ma00155a022.
- [111] Scienomics, MAPS platform, version 3.4.2, France 2015. See also: <http://scienomics.com/>.
- [112] Brandrup, J., Immergut, E. H., Grulke, E. A., *Polymer handbook*. 4th ed., Wiley: New York, 1999.

Pravin Jagdale, Gemma Rius, Krishna Rajan, Jijeesh Ravi Nair,
Massimo Rovere, Alberto Tagliaferro, Claudio Gerbaldi

6 Carbon from waste source for Li-ion battery

6.1 Introduction

Energy generation and use depends heavily on fossil fuels, and it severely impacts the global economics and living sustainability [1]. Completely shifting to clean energy production and consumption is vital for the present and future generations. Electrochemical energy storage and conversion can be implemented by various devices such as (rechargeable) batteries, fuel cells and electrochemical capacitors (ECs). They are considered fundamental elements for developing a sustainable energy society. In particular, a battery [2] is an electrochemical power source comprising several cells, which are connected in series or parallel or in combination in order to deliver the required output voltage and energy.

In ancient Greece, Thales observed that rubbing amber could generate an electric charge [3]. In between 250 BC and AD 640, there are evidences for the use of a storage system known as the “Baghdad batteries” [4]. In 1748, Benjamin Franklin first coined the term “battery” to describe an array of charged glass plates. In the 1780s, Luigi Galvani demonstrated the electrical basis of nerve impulses, which is widely called as the frog leg experiment. The Italian physicist Alessandro Volta in 1800 invented the chemical battery, Voltaic pile. Volta discovered that an electrical current is generated when metals come in contact with chemicals. John Frederic Daniell in 1820 improved the voltaic cell using copper (Cu) and zinc (Zn) plates as electrodes and sulfates of respective metals as electrolytes, and termed as the Daniell cell, which was later used for operating telegraphs and doorbells. In the 1830s, Michael Faraday conducted experiments with a ferrite ring and device called a battery. Carbon–zinc battery was developed by Georges Leclanché in the 1860s. The wet cell consisted of electrodes that were plunged into a body of electrolyte fluid, which was manufactured easily and exhibited acceptable shelf life [5]. An improved version known as a dry cell was later developed by sealing the cell and changing the fluid electrolyte to a wet paste. Raymond Gaston Planté in the 1860s invented the first practical storage lead acid battery. He immersed two thin solid lead plates separated by rubber sheets in a dilute sulfuric acid solution to make a

Pravin Jagdale, Krishna Rajan, Jijeesh Ravi Nair, Massimo Rovere, Alberto Tagliaferro, Claudio Gerbaldi, Department of Applied Science and technology (DISAT), Politecnico di Torino, Torino, Italy

Pravin Jagdale, Italian Institute of technology (IIT), Torino, Italy

Gemma Rius, Institute of Microelectronics of Barcelona, Bellaterra, Spain

secondary battery. Later in 1900, Thomas Edison developed the nickel (Ni) storage battery and later in 1905 he developed the Ni-iron (Fe) battery [6].

A cell is made of three major components: a positive electrode (cathode), a negative electrode (anode) and a separator. A separator is soaked in organic carbonate-based liquid electrolyte. The electrolyte contains dissociated salts, which facilitate ion transfer between the two electrodes. Once these electrodes are externally connected to a device, the chemical reactions occur at the electrodes. The process generates electrons and enables the current to flow. The terms anode and cathode are applicable generally for primary batteries, but are not suitable for secondary (rechargeable) batteries. During charging and discharging the direction of electron flow changes, however, the electrodes retain their polarity. Thus, the terms negative and positive electrodes are most suited to describe the terminals of a rechargeable battery system.

The energy storage system can be primary or secondary. Primary cells are designed to discharge once and can be discarded after use. If one attempts to recharge a primary cell, then it can present serious safety hazards. The examples of primary cells include carbon–zinc and alkaline cells. Primary cells having lithium (Li) as an anode are called Li cells irrespective of the nature of the cathode. Such cells are separated into two types: cells with solid cathodes (e.g., Li–MnO₂) and cells with liquid cathodes (e.g., Li–SO₂) [7]. Reserve batteries are a special-purpose primary cell, which are used for applications that require a long inactive shelf period followed by intense discharge and unusual operational conditions. The oldest form of a rechargeable battery system in use is the wet cell lead acid battery. It represents one of the worst energy-to-weight ratios. However, it delivers good power-to-weight ratio along with good energy-to-volume ratio compared to other type of batteries. It is cheap and can supply high surge currents needed in starter motors along with low manufacturing cost.

Li metal [8] has been selected as a good choice due to its low mass density, smaller size compared to other known battery materials as charge carrier, and a high mobility and fast transport speed. These features give Li-based secondary batteries a distinct advantage over other battery systems such as Ni-cadmium (Cd) and lead acid batteries. Cd is highly toxic and heavier, and the same problems are applied to lead as well. The discovery (1970s) of several intercalating inorganic compounds was monumental in the development and widespread use of high-energy rechargeable Li-based batteries. Whittingham et al. introduced the concept of electrochemical intercalation and its potential use [9]. The discovery and the understanding of the intercalating compounds led to the development of rechargeable Li batteries using Li insertion compounds as positive electrodes and Li metal as the negative electrode (Li metal battery). The first Li metal battery cell was introduced by Exxon et al. [10] in which they used titanium disulfide (TiS₂) as positive electrode, Li metal as negative electrode and Li perchlorate in dioxolane as the electrolyte. The safety concerns related to the use of Li metal as anode was addressed via

alternative approaches. It led to the modification of either the electrode or the electrolyte. Murphy et al. [11] and Scrosati et al. [12] demonstrated that Li metal can be replaced by an insertion host having low standard reduction potential. In the early 1990s, the concept of using electrodes having Li⁺-ion insertion capabilities led to the development of today's Li⁺-ion batteries. The presence of Li in the anode in ionic form rather than in metallic form of a Li⁺-ion cell resolved the dendrite problem, which was inherited by Li metal cells.

In the 1980s, Goodenough et al. [13, 14] proposed the high-voltage metal oxides (Li_xMO₂, where M = Ni, cobalt (Co) or manganese (Mn)) as cathodes for Li⁺-ion cells. The discovery of highly reversible, low-voltage Li⁺-ion intercalation/deintercalation process in graphite led to the creation of the first Li⁺-ion cell based on C/LiCoO₂, which was commercialized by Sony Corporation. Such cells exhibited an operational voltage of 3.6 V (3 times vs. alkaline systems), gravimetric energy densities of 150 Wh/kg (2–3 times vs. Ni–Cd (cadmium) batteries) and a cycle life of at least 500 discharges.

Presently, Li⁺-ion batteries are the fastest growing storage devices. The salient features of today's commercial Li⁺-ion batteries are

- high operating voltage between 3.6 and 4.2 V,
- compact,
- lightweight,
- high energy density,
- fast charging,
- low self-discharge,
- not suffer from memory effect,
- use between –20 and +60 °C and
- recharge for more than 1,000 cycles.

The Li⁺-ion rechargeable cell working mechanism depends on an “intercalation/deintercalation” process [15]. The storage processes, which do not involve intercalation are called “insertion/de-insertion” process. Indeed, the term “intercalation” is used for layered-type host substances (e.g., graphite, TiS₂, molybdenum disulfide (MoS₂) or lithium cobalt oxide (LiCoO₂)), while “insertion” is used for 3-D materials that have narrow channel cavities. The charge/discharge process is reversible where the Li⁺ ions move back and forth between the anode and cathode. The process presented the Li⁺-ion battery names such as *rocking chair* [16], *swing* [17, 18] or *shuttlecock* [19].

In general, for a Li⁺-ion cell:

- The electrode materials must possess high specific capacity and durability.
- The electrolyte must exhibit high ionic conductivity at ambient and subambient temperatures.
- The electrolyte must have good interfacial properties.
- The materials should be economical, eco-friendly, easily available and safe.

Thus, the selection of right materials is important to produce a sustainable and an efficient battery pack.

A successful electrode should meet a number of criteria:

- The intercalation/insertion compound should have large number of available Li sites.
- The Li^+ ions insertion/de-insertion process should be reversible.
- The host material should not undergo structural changes.
- The host material should be accessing the multiple oxidation states of the transition metals.
- The compounds should possess good electronic and ionic conduction.
- The electrodes must be stable over the working voltage range.
- The electrodes should not undergo dissolution into the electrolyte.
- It should be environmentally friendly and easy to produce.

Li metal is an ideal anode for rechargeable batteries due to its high potential and specific capacity. It is widely used as an anode in primary Li cells. However, dendritic growth, cost, safety hazards and poor recharge ability prevents its practical use in secondary batteries. The issues are addressed by the use of Li alloys (with Al or Si). Unfortunately, the alloy anodes undergo severe volume changes during the cycling process. Nevertheless, the urge for the development of solid-state (ceramic/polymer) electrolytes are a promising approach to realize the use of safe Li metal rechargeable batteries. The standard and commercialized anode for Li^+ -ion batteries is carbon in its different layered structures.

6.2 Role of carbon material in batteries

Li metal anodes with an organic electrolyte result in nonuniform formation of a passive film on the anode surface [20–22], which causes dendrite growth of Li metal. Longer charging–discharging cycles are one of the important requirements for making a commercially viable Li-ion battery. This problem is tackled by utilizing the electrochemical intercalation of Li in carbon. It produces a significant negative potential close to that of Li, but this is less reactive and easily reversible [23].

Various kinds of carbon materials have been employed as anodes in various electrolytes for Li rechargeable batteries. Carbon offers advantages over other types of materials used in rechargeable batteries such as high operating voltage, longer life cycle and lack of “memory” effects [24–26]. The structural characteristics of carbon are believed to be the major factor that controls the performance of Li^+ -ion batteries. The intercalation of Li^+ ion with carbon depends upon many factors such as the preparative history, carbon precursor and structure. The variations in the average layer spacing and the voltage profile for the carbon with intercalating depend

on the degree of graphitization [27]. Literature survey on carbon in battery development revealed that graphite is the most commonly used anode for Li⁺-ion secondary battery. Many studies employed graphite as an anode, which has theoretical capacity of 372 mAh/g based on the stoichiometry of Li carbon [28–34].

6.3 Graphene materials for highly performing electrodes

The widespread interest in graphene includes its potential as a suitable material for energy storage and particularly for Li⁺-ion batteries. Intrinsically, graphene is aimed at providing excellent performance based on a combination of physicochemical properties, its extremely high surface area of 2,630 m²/g [35], high electrical conductivity and chemical inertness [36].

Crystalline carbon nanomaterial, carbon nanotube [37, 38] and graphene had their expected applications in electrochemical energy storage. This was precisely envisioned for both Li⁺-ion and Li-sulfur batteries and supercapacitor devices [39]. Advantageously with respect to carbon nanotube, graphene is the basic unit of sp² carbons (graphitic), which are the most conventionally/commonly used carbons for batteries (or other high surface area applications).

Production wise, the cost of using a certain graphene material could be compared with conventional and cost-efficient traditional macroscopic methods, based on top-down approach or on raw materials, typical chemical or metallurgical approaches to obtain graphite (and graphene-like materials) synthesis and cell-making methods. Examples of current trends and recent achievements include pyrolytic graphite from graphene oxide [40] and kish graphite [41], which are obtained from waste graphite flakes from steel production. Scalable recycling and reusing approach applied to these abundant raw materials will be cited in the following sections.

In the following section, a nonexhaustive collection of bottom-up methods, selected techniques for production of high-quality graphene materials as well as examples of graphene-decorated electrodes are described. For a comprehensive topic review on graphene synthesis, there exist a number of extended resources such as how to achieve specialized morphologies, particularly, those specifically useful/appropriate for EC energy storage [42]. Interestingly, some general vision and hints on using waste and recycled or recyclable carbon sources are included for the described methods. Besides, the quest for valorizing waste materials for energy storage is not new or exclusive for novel nanomaterials [43]. The use of hierarchical structures such as combining graphene with other materials, for example, oxides [44], is beyond the scope of this text.

In summary, graphene is still considered to ultimately outperform existing solutions as it would provide improvements in terms of increased surface area (i.e., enabling higher capacity and also lighter devices), conductivity (faster charge–discharge and efficiency) and increased chemical and mechanical resistance. Relevant evaluation and benchmarking of graphene electrodes as electrochemical energy storage elements in affordable graphite materials, to critically assess their real potential and, eventually, quantify the advantages of graphene in operation that is needed in both energy and power density are carried out. The expected exponential increase in demand and performance of batteries, resulting from their use in electrified vehicles, requires advanced and sustainable solutions. Fundamental investigations on graphitic structure from waste material for electrochemical energy storage are focused on elucidating whether they provide unique features and advantages to affordable carbons, rather than being competitive to existing commercial solutions. Therefore, they are generally based on the “ideal” concept of graphene. High-quality graphene material, in contrast to common graphite/graphitic materials and low-quality graphene materials, can be defined as pure carbon, large crystal domain size and isolated films, that is, typically consisting of monolayer graphene or, eventually, bilayer or few layers’ graphene. In fact, classification of graphene based on these three parameters has been established for proper reference in scientific papers and enabling some standards for industrial purposes, such as production [45]. Advantageously, laser power seems to provide a way to transform a variety of heterogeneous materials into two graphitic forms [46]. Similarly, one could envision that the resources potentially include waste materials.

Recently, attention has been drawn to use disordered carbon materials. It may store Li via a mechanism that is completely different from that associated with graphite. Additional studies indicate that Li insertion into an unorganized carbon loses the layer structure [47]. Variation in the polarization resistance with intercalation revealed the processes in various disordered carbons. It demonstrated the single-phase reactions with different stoichiometry of Li intercalation. Electrochemical intercalation of Li into carbons has been studied using mesophase pitch-based carbon fibers with different heat-treatment temperatures, coke [48] and graphite as anodes [27, 47, 49]. It has been found that the activation energy for the diffusion process decreases by increasing the degree of graphitization [27]. The studies also demonstrated that intercalation of Li with camphor-based carbon nanobeads stabilize the cell for 10–20 days [50, 51]. The reversible Li⁺-ion intercalation capacity was found to be 45–61% of that obtained with graphite [51]. Researchers also reported the result of Li intercalation by carbon nanomaterial obtained from the pyrolysis of biochar such as tealeaves [52].

Research on Li diffusion in carbon is of both theoretical and practical interest. The process was largely studied in connection with the development of Li⁺-ion batteries, whose negative electrode is based on graphite or some other carbon material [27, 53–61]. In some works, Li diffusion was investigated during the reverse process,

that is, the anodic deintercalation [47, 62–66]. A complex impedance model for spherical particles was used to determine the Li^+ -ion diffusion coefficient in graphite as a function of the state of charge and temperature [67]. Practically, in all cases, studies were concentrated on the diffusion of Li, which was electrochemically incorporated during cathodic polarization of a carbon material in an aprotic electrolyte [68].

However, carbon pyrolysis at low temperature shows attractive behavior as their theoretical capacity exceeds that of graphite as anode material [52, 69–75]. This observation indicates that there may be some other different mechanisms operating in these carbons in terms of Li intercalation. However, the density of low-temperature carbon is lower than that of graphite [76]. Therefore, the capacity of low-temperature carbon should be large enough to compensate for its smaller density. The capacity of an anode for Li^+ -ion battery depends on the amount of carbon that can be placed within the limited volume of a typical battery container. Carbon obtained from the same precursor at different temperatures has different structural orientation. Therefore, trial and error is often needed to establish a suitable preparation method for optimizing the properties of carbon [77, 78]. Many researchers studied the relation between the properties of carbon and its electrochemical characteristics relevant to Li^+ -ion rechargeable [79–85].

As for the source of atomic carbon, methane is the commonly used gas as its decomposition products are the simplest. The reuse of greenhouse gases such as the very methane for graphene production would follow automatically. Similarly, green approach is also aimed at reusing carbon dioxide [86], yet it is more complex in terms of chemistry and efficiency of the reaction. Likewise, a number of additional works have actually been reported for the (re)use of greener carbon sources, which include molecules or polymers [87], as well as various recycled waste materials, such as plastics but also organic materials or industrial coal (Figure 6.1) [88–90].

In this study, we examined the effects of carbonization atmosphere on the charge–discharge characteristics of carbon from waste source as an anode for a Li^+ -ion rechargeable battery. This work targeted the “green” approach for energy storage. The carbonaceous materials such as carbon nanowalls (CNWs) and carbon fiber sheet used in this study were made from different precursors such as organic waste (methane) and polymer waste [nanoscale microfibrillated cellulose (NMFC)].

6.4 Vertically oriented micro-mesoporous CNWs

Graphene materials obtained by chemical vapor deposition (CVD) present several limitations for EC energy storage. First, morphologically the effective graphene surface could be reduced up to half of its theoretical value as CVD-obtained graphene is bonded/stuck onto the metal substrate. Besides, the high temperature used in CVD is not desirable to obtain wrinkled or crumbled carbon, especially if power

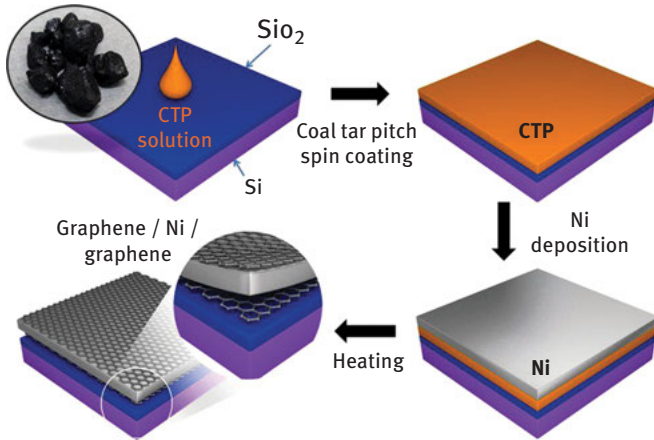


Figure 6.1: Graphene films are converted from coal tar pitch on the top and bottom surface of Ni layer [90]. (Image courtesy: <https://www.nature.com/articles/srep16710/figures/1>)

consumption reduction is aimed, but also for process compatibility, with any substrate such as plastics. Apart from providing better volume–area ratio, an increase in charge storage capacity is expected from the large amount of graphene flake edges to the electrolyte. Consequently, alternatives of producing porous or microstructured carbon materials, ideally based on scalable techniques, have been studied [91].

As an analogy with CNTs, this is the case of using physically assisted CVD systems, such as fitted with radiofrequency and microwave (MW) sources. In particular, for certain solid sources, the reactivity of physically assisted CVD such as based on the use of a powerful MW field may restrict the growth process to be operated in conditions of relatively low pressure. For instrument and operator’s safety in the presence of chemical elements (carbon source), many systems and synthesis principles do make use of hydrogen as a carries gas to avoid oxygen contamination. With the plasma systems, the reuse of methane and other recycled carbon sources may be possible to be applied. Although the compatibility of recycled carbon sources could be more difficult in general, it has actually been achieved [92]. Yet, more examples can be found in the literature [93].

Figure 6.2 provides the image of CNWs deposited on Cu substrate, which has the possibility of being used as anode for Li⁺-ion batteries. Owing to the orientation and morphologies, obtained materials are typically referred in the literature with a variety of terms, including carbon nanosheets [94] or CNWs [95]. These graphene flakes or CNWs are randomly distributed, perpendicularly oriented to the substrate and/or curvy. Their dimensions are maximum of approximately 1–1.5 μm in height and 10–20 nm in thickness, which accounts for multilayered

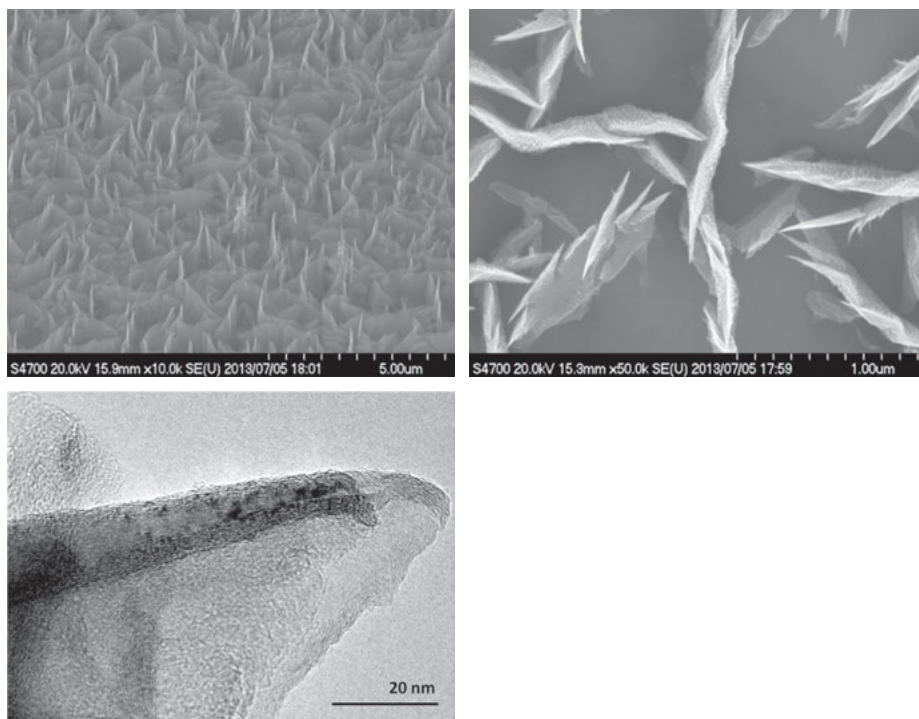


Figure 6.2: Microscopic images of CNWs deposited on Cu: (left and center) FESEM and (right) TEM image.

graphene, and are characterized by very small crystal size, in the order of nanometers. This is further confirmed with micro-Raman analysis.

The observed Raman spectra (Figure 6.3) is typical of a good quality graphitic material. Both first- and second-order Raman effects can be seen. First-order Raman peak is presented as a so-called G-peak around $1,580\text{ cm}^{-1}$. This peak is commonly observed in all graphitic materials being often the sharpest and intense one. It arises from the first Brillouin zone center of the graphene unit cell and it is due to the double degeneration of in-plane transverse optic [96, 97] and longitudinal optic modes [98, 99]. All other peaks are due to second-order Raman effects. The main peak belonging to this category is D-peak around $1,350\text{ cm}^{-1}$. This peak is normally associated with the disorder of the graphitic structure. The principal reasons for the presence of this peak are the combination of grain boundaries, vacancies and other structural defects. The D-peak is particularly intense and very sharp: this can be explained not mainly by the density defects but related to the particular orientation of CNWs, which are vertically aligned or oriented (mainly edges exposed to laser beam). This statement is further confirmed by looking at the D + G peak. It does not show any abnormally great number of defects. In conclusion, D-peak intensity is

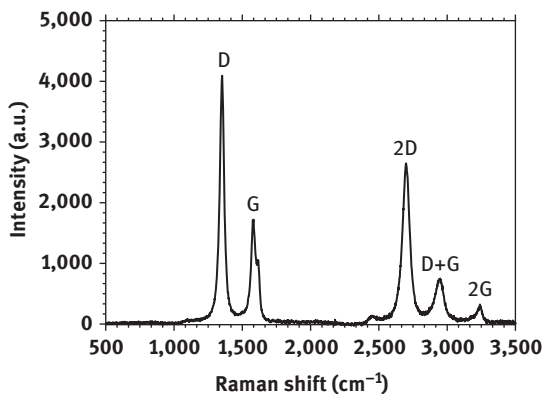


Figure 6.3: Raman analysis of CNWs. (Image courtesy by *Electrochimica Acta* (Elsevier) to reuse in a book under the copyright license number 4454750182186)

correlated with the number of defects in the structure, while the full-width half-maxima of D-peak is correlated with the grain size. The presence of a right-shouldered G-peak around $1,620\text{ cm}^{-1}$ is called second-order D'-peak which appears as a shoulder peak of G-peak. This peak is observed in some disordered graphitic carbon structures, including graphene, but cannot be seen in defect-free structure. Its intensity is usually lower as compared to the G-peak but becomes more important especially in CNW structure. Other second-order features are indicated by the remaining peaks named 2D, D + G, 2G. The peak around $2,700\text{ cm}^{-1}$ is often called 2D. Generally, this peak fall around a zone of the Raman graph where the 2D Raman shift doubles the Raman shift of the D-peak [100, 101]. The origin of peaks is not related to the presence of defects or grain boundary. It arises from the interaction of two phonons. The peak is very intense, especially in planar structure like graphene, CNWs. The peak shape of Raman can give us information about the number of layers present in the structure [102]. The peak around $2,700\text{ cm}^{-1}$ observed here is D + G peak, which is generally associated with the damaged graphene. It is less evident or almost absent in high-quality and defect-free carbon structure [103]. The peak around $3,240\text{ cm}^{-1}$ is sometimes called 2G and is present in both planar (graphene, graphite, CNWs) and nonplanar (CNT) structures [104].

6.5 Growth of CNWs

Vertically arranged graphene materials, arrays of CNWs, can be grown onto as-purchased flexible metal polycrystalline Cu foil. It is directly tested as anode in Li^+ -ion batteries without any prior treatment [70, 105]. A commercial MW plasma-enhanced

CVD technique (CVD-CN-100 from Ulvac, Japan Ltd.) [106–108] is used for the growth of CNWs. The whole process and growth conditions typically consist of, first, exposure of Cu foil to a hydrogen (H_2) flux; then, methane (CH_4) as a reaction gas is introduced in combination with H_2 ($H_2:CH_4$) with the ratio of 20:20 sccm. At growth stage, bias voltage of 200 V is applied. The whole process is done at a constant pressure of 1.5 mTorr pressure. In the process, hydrocarbon gas decomposes into graphitic carbon. The process needs to be catalyzed and is therefore applied on affordable Cu-metal surface, which provides a better control on the number of layers with electrochemically active surface. Figure 6.4 shows the charge–discharge cycling of CNWs on Cu at different current rates. The behavior of current is slightly different from the standard behavior of carbon. This may be due to the presence of disordered carbon in the CNW deposits (*as learnt by Raman spectroscopy*). However, one of the highlights of the material is that even if the current rate is increased to higher orders, the capacity is not dropping down.

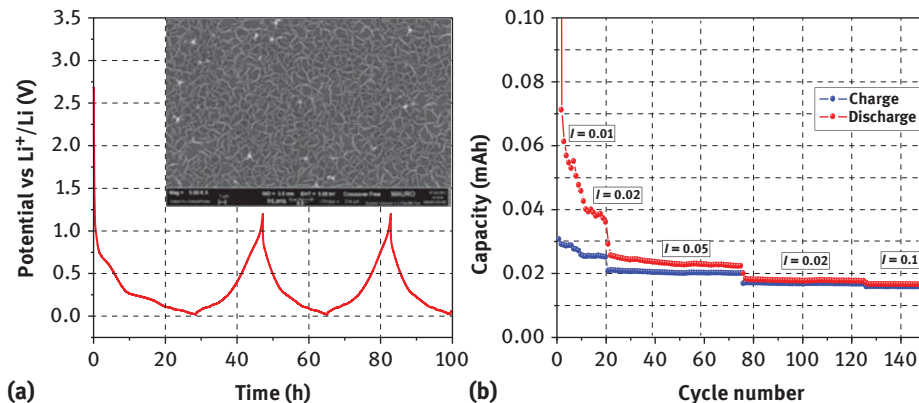


Figure 6.4: (a) Graph showing the galvanostatic charge/discharge curves of CNWs deposited on Cu: inset – morphological characterization of the nanostructured carbons deposited on Cu by FESEM (ZEISS Supra 40); (b) capacity versus number of cycles in a cell Li/electrolyte/CNW-Cu at room temperature. (Image courtesy by *Electrochimica Acta*(Elsevier) to reuse in a book under the copyright license number 4454750182186)

6.6 Carbonized cellulose paper

Use of paper in our everyday life has turned out to be an original answer to the demand of eco-friendly, flexible, lightweight and cost-effective materials for electronics [108, 109] and energy-storage devices [110, 111]. There are promising reports on paper/cellulose-based composite electrodes for supercapacitors and Li batteries

[112, 113]; the rough and porous surface of paper has turned out to be a great advantage, where both high surface area and electrolyte absorption are in demand. Recyclability and biodegradability are significant benefits, considering that cost of waste management and impact on the environment could be considerably low. It has been proven by Liu et al. [109] that paper printed circuit boards have about two orders of magnitude less impact on the environment than the ordinary printed ones.

The work on this material has demonstrated the feasibility of manufacturing graphite-based negative electrodes on a pilot-line exploiting microfibrillated cellulose as binder, through the spray-coating method, and the use of water-based papermaking technologies for large-scale production of Li batteries [114]. Beneventi et al. have successfully assembled a flexible, truly solid Li⁺-ion cell based on self-standing electrodes manufactured using conducting paper as substrate. This approach makes use of a carbonization step of the nanocellulose-binded electrodes at high temperature to obtain conducting carbon nanofiber binder concurrently removing water and impurities, so that no successive drying step was necessary, thus making it more cost-effective in terms of energy and time. An NMFC-reinforced polymeric membrane which was activated by incorporating a freshly prepared room temperature ionic liquid-based green and safe electrolyte solution was used, and the resulting truly solid system assembled in a “pouch cell” envelop demonstrated a remarkably stable cycling behavior upon prolonged cycling at ambient temperature even at elevated current rates as well as in bent configuration. It was also noted that all cell components could be easily recovered using common water-based recycling procedures used in paper mill. The waste was minimal; the process was of low cost and low energy demanding, which led to the worldwide sustainable Li-based battery use and recovery.

6.7 Preparation of self-standing electrodes

Figure 6.5 demonstrates the different processes involved in obtaining pyrolyzed nanocellulose-binded electrodes, which are then used to assemble the solid polymeric Li⁺-ion cell. The anode slurry was made of graphite powder (GP), carbon black (CB), NMFC, carboxy methyl cellulose (CMC) and alum. The cathode slurry was composed of lithium iron phosphate (LiFePO₄)/carbon, CB, NMFC, CMC and alum. Both the slurries, having a dry solid content ranging between 25 and 15 wt.%, were prepared by dissolving CMC in the aqueous NMFC slurry, followed by the addition of CB.

A commercial airless spray system (*Wagner, Project Pro 119*) was used to spray the anode slurry on both sheets and on other substrates (i.e., smooth polyester films and copy paper). An aqueous suspension of carbonized NMFC (2 wt.%) was

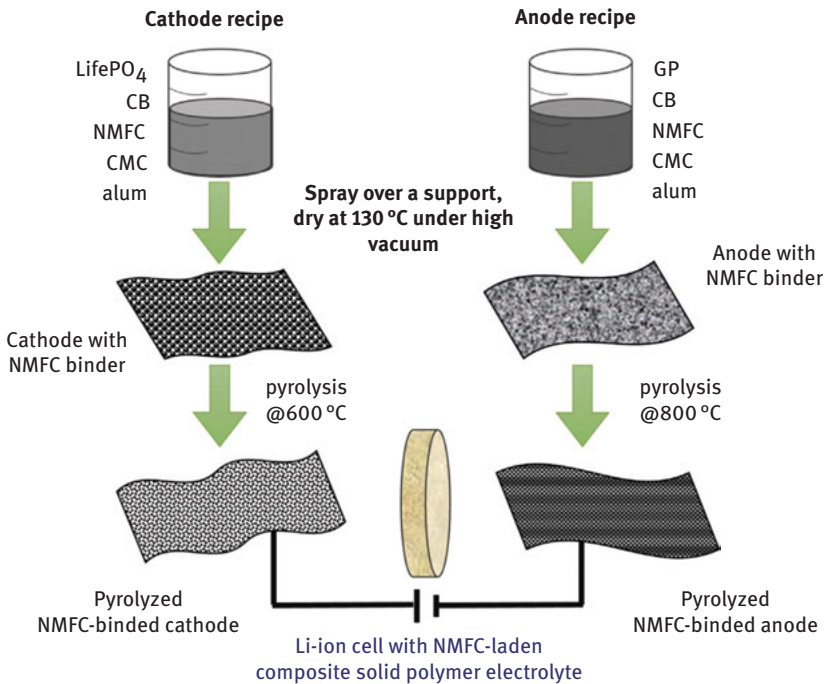


Figure 6.5: Different phases of the process involved in obtaining pyrolyzed nanocellulose-binded electrodes, which are then used to assemble the solid polymeric Li⁺-ion cell. (Image courtesy by Carbon (Elsevier) to reuse in a book under the copyright license number 4454160899455)

prepared for reinforcing the polymer electrolyte and also the same was used as a binder for retaining the active materials within the electrode films (Figure 6.6).

6.8 Pyrolysis of cellulose paper

Pyrolysis method [115] is adopted for carbonization of waste NMFC. This involves the pyrolysis of self-standing anode and cathode samples at 800 and 600 °C, respectively. To avoid thermal degradation of the LiFePO₄ active material, lower pyrolysis temperature was applied to the cathode material. The pyrolysis chamber is normally flushed with argon inert gas to avoid oxygen traces. The furnace is heated with 10 °C/min. Pyrolysis is carried out for 30 min after achieving the required temperature. These steps ensured the completion of the carbonization procedure. Figure 6.7 shows the different forms of an NMFC sheet that has undergone pyrolysis. The pyrolysis method is normally followed by the cooling of the furnace to room temperature to recover the carbonized materials [69].

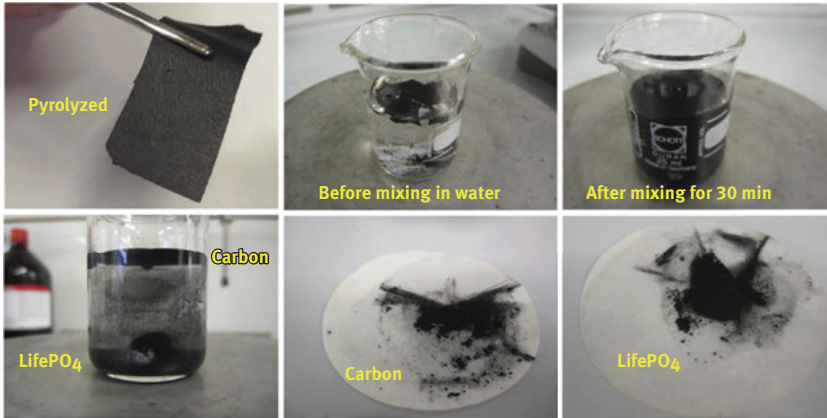


Figure 6.6: Different steps illustrating the facile recovery of pyrolyzed nanocellulose-binded electrode materials by exploiting the standard water-based recycling procedure used in paper industries. (Image courtesy by Carbon (Elsevier) to reuse in a book under the copyright license number 4454160899455)

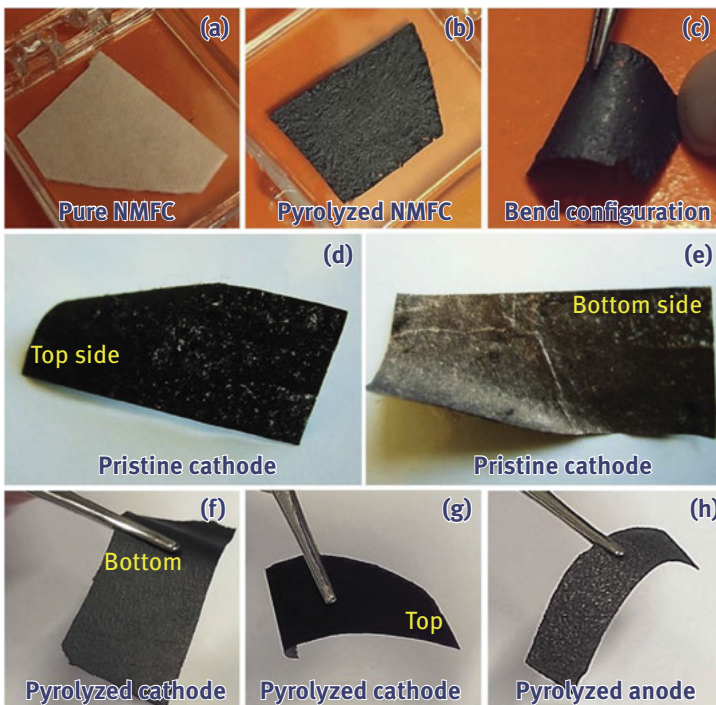


Figure 6.7: Self-standing ability of (a) pristine NMFC paper, (b) pyrolyzed NMFC paper, (c) pyrolyzed NMFC paper in its bend configuration, (d) representative nanocellulose-binded LiFePO_4 -based cathode in its top and (e) bottom side views, (f) pyrolyzed LiFePO_4 -based cathode in its bottom and (g) top side views, (h) pyrolyzed GP-based anode. (Image courtesy by Carbon (Elsevier) to reuse in a book under the copyright license number 4454160899455)

6.9 Analysis of pyrolyzed cellulose paper

Figures 6.8 and 6.9 shows the FESEM images of GP-based anode pyrolyzed at 800 °C and LiFePO_4 -based cathode pyrolyzed at 600 °C. The structure of the carbonized electrode (carbonized anode) is more accessible with respect to the pristine spray-deposited paper electrodes, and the presence of both LiFePO_4 and CB particles is well evidenced. The carbonized cellulose fiber network successfully binds the electrode components effectively, maintaining the preburning structure, despite slight shrinkage. It was observed that LiFePO_4 particles perfectly maintained their characteristics after heat treatment without suffering any kind of modification (Figure 6.9d). The fundamental triphasic system composed of the active material grain (LiFePO_4 particle), the electronic conductivity enhancer (CB spherical particle, locally enhancing the electronic conductivity of LiFePO_4) and the binder (electronic conductive carbonized cellulose fiber, which in turn also ameliorates the electronic conductivity of the system) was still present as highlighted by the yellow circle.

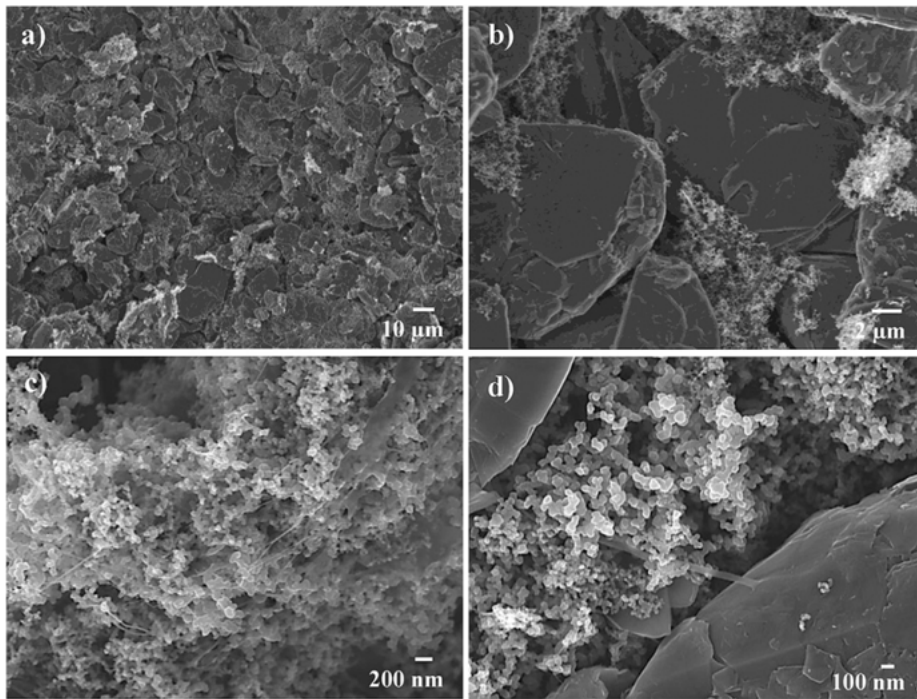


Figure 6.8: FESEM at different magnifications of GP anode pyrolyzed at 800 °C. (Image courtesy by Carbon (Elsevier) to reuse in a book under the copyright license number 4454160899455)

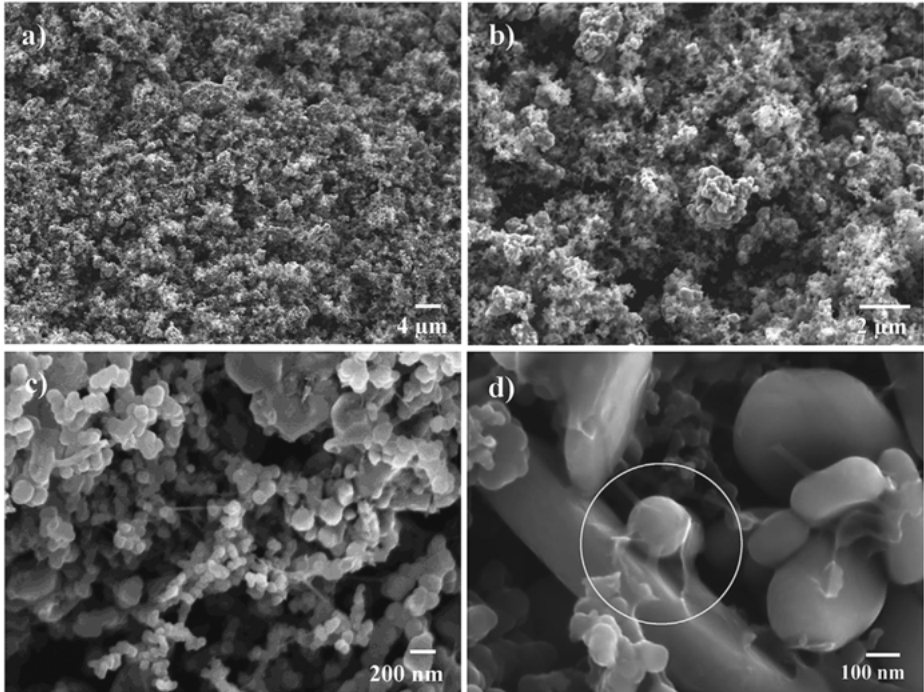


Figure 6.9: FESEM at different magnifications of LiFePO_4 cathode pyrolyzed at $600\text{ }^\circ\text{C}$. (Image courtesy by Carbon (Elsevier) to reuse in a book under the copyright license number 4454160899455)

Figure 6.10 shows the Raman spectrum of GP-based anode, LiFePO_4 -based cathode and NMFC paper. A-800-TS shows a good separation and sharp D, G and G_0 peaks when compared with A-800-BS. It evidences that the carbon material in sample A-800-TS is better graphitized than that of A-800-BS. Raman analysis of top rough (C-600-TS) and bottom smooth (C-600-BS) surfaces of the LiFePO_4 -based cathode shows different behavior (Figure 6.10c and d). Intensity ratios shown in Figure 6.10f indicate that C-600-TS has lower graphitized matrix as compared to C-600-BS. The Raman spectrum of pyrolyzed NMFC paper (Figure 6.10e) shows no peak intensity and positioning variation on either side of the paper due to the uniform characteristics of both the surfaces. In general, the Raman analysis of pyrolyzed NMFC paper shows similar graphitized structure as that of C-600-BS. It can be stated that A-800-TS and C-800-TS have lower degrees of graphitization after analyzing the Raman spectra. Raman analysis also confirmed that the temperature variation did not reflect on the variation of graphitization of the sample. Raman spectroscopy by itself does not provide a complete picture of carbon quality.

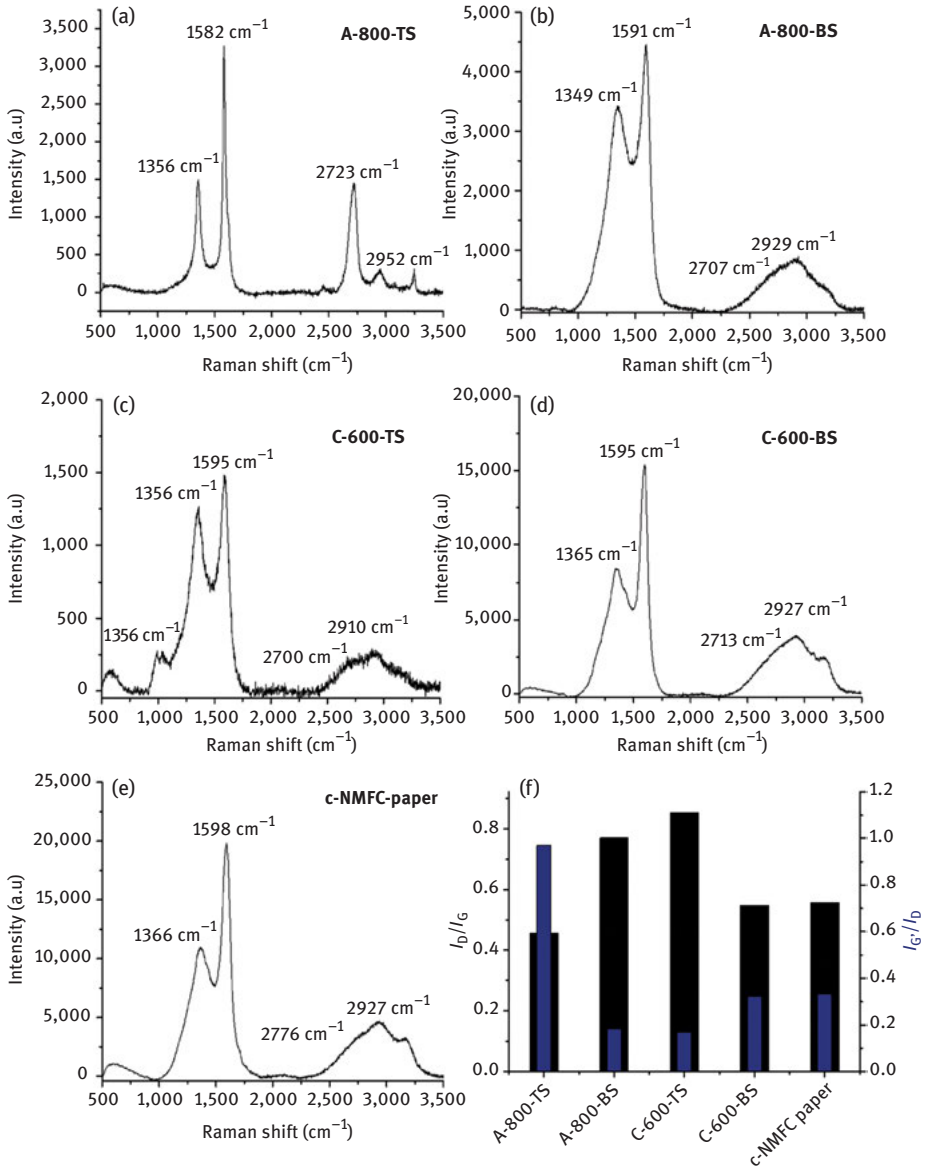


Figure 6.10: Raman spectra of (a) GP-based anode pyrolyzed at 800 °C analyzed on top and (b) bottom surfaces, (c) LiFePO₄-based cathode pyrolyzed at 600 °C analyzed on top and (d) bottom surfaces, (e) NMFC paper carbonized at 600 °C. (f) Samples versus I_D/I_G and I_G/I_D ratios. (Image courtesy by Carbon (Elsevier) to reuse in a book under the copyright license number 4454160899455)

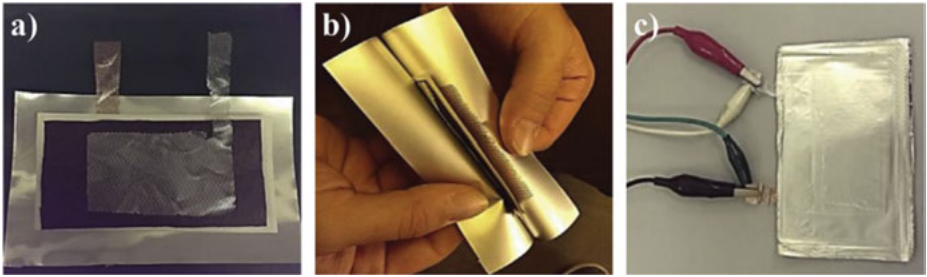


Figure 6.11: Different assembly stages of an all-paper-based solid polymer cell in pouch configuration: (a) assembly of the electrodes on the current collector grids, (b) packing followed by sealing, (c) final Li^+ -ion cell connected to the instrument for testing. (Image courtesy by Carbon (Elsevier) to reuse in a book under the copyright license number 4454160899455)

Figure 6.11 provides the different assembly stages of an all-paper-based solid polymer cell in pouch configuration. The composite polymer electrolyte is sandwiched between the carbonized nanocellulose-binded LiFePO_4 -based cathode and graphite-based anode paper electrodes and housed in a “pouch cell” envelop with Al and Cu grid current collectors (for cathode and anode, respectively). Different phases of the assembly are shown in Figure 6.11a–c. The cell is kept for ambient temperature galvanostatic charge/discharge cycling at various current rates.

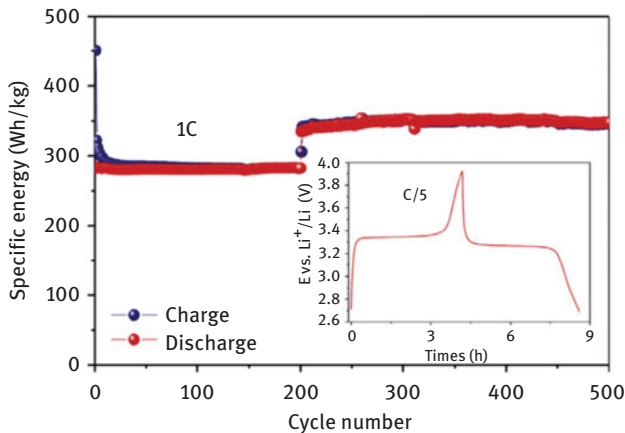


Figure 6.12: Current charge/discharge cycling behavior in terms of specific energy versus cycle number at different current regimes and charge and discharge potential versus time profiles extracted from the 400th cycle at C/5 rate. (Image courtesy by Carbon (Elsevier) to reuse in a book under the copyright license number 4454160899455)

Figure 6.12 provides the electrochemical response of the Li^+ -ion polymer cell in terms of specific energy (Wh/kg calculated on the weight of the active cell components excluding current collectors and packaging) versus cycle number at different rates. The potential versus time profiles (400th constant current charge and discharge profiles at C/5 current rate) are very well consistent with the potential trend of the corresponding cell with natural cellulose bonded electrodes and liquid electrolyte [116]. The potential drop between charge and discharge plateaus was found to be limited, which accounts for low internal resistance, thus good electrode/electrolyte interface. The cell showed good rate capability and high coulombic efficiency approaching 100%. Specific energy values were found to be definitely interesting for a solid polymeric device, approaching 300 Wh/kg at 1 C and even exceeding 350 Wh/kg when reducing the current rate to C/5. Even more important, the cycling response is maintained steady for at least 500 cycles. This observation is definitely remarkable for a solid polymeric device. The exceptional capacity retention indicates that no contact loss occurred between the active material particles. The interface between active material particles and pyrolyzed nanocellulose binder remains intact even after over 500 charge/discharge cycles.

Figure 6.13 provides the electrochemical stability window of the composite polymer electrolyte evaluated by linear sweep voltammetry. It was found to exceed 4.6 V versus Li^+/Li in the anodic region. The Li plating/stripping indicates an overall good cathodic electrochemical stability, which is evident at around 0 V versus Li^+/Li .

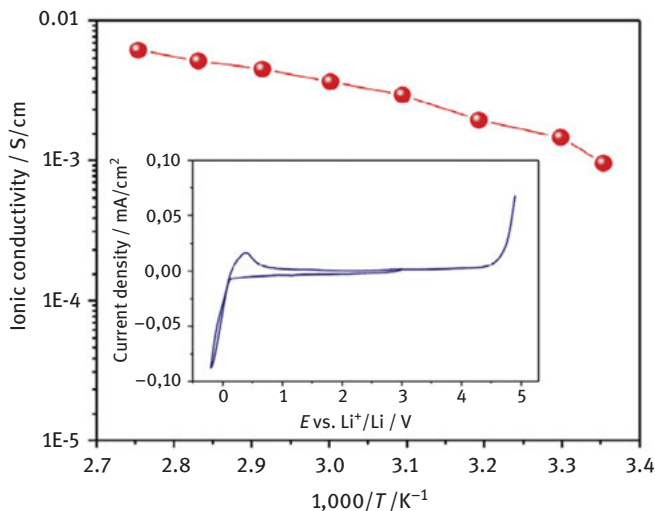


Figure 6.13: Arrhenius plot showing the ionic conductivity versus temperature; inset: electrochemical stability window of the polymer electrolyte. (Image courtesy by Carbon (Elsevier) to reuse in a book under the copyright license number 4454160899455)

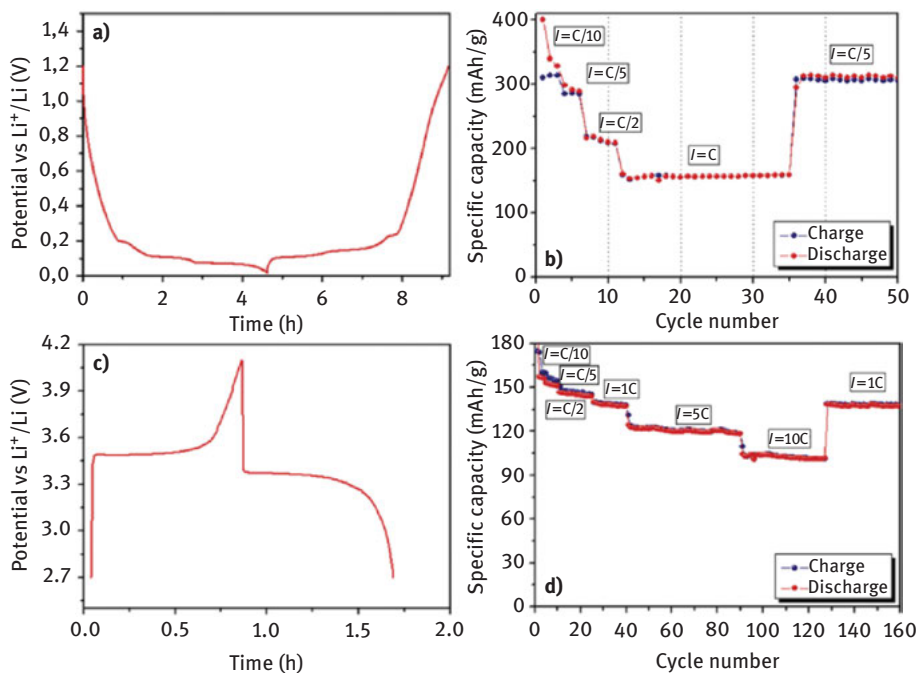


Figure 6.14: Ambient temperature electrochemical characterization of the carbonized electrodes in Li metal cell with standard liquid electrolyte: (a) potential versus time plot of a GP-based anode pyrolyzed at 800 °C showing typical charge and discharge profiles at C/5; (b) specific capacity versus cycle number plot of the same anode at different discharge/charge current regimes; (c) potential versus time plot of a LiFePO_4 -based cathode pyrolyzed at 600 °C showing charge and discharge profiles at 1C; (d) specific capacity versus cycle number plot of the same cathode at different charge/discharge current regimes. (Image courtesy by Carbon (Elsevier) to reuse in a book under the copyright license number 4454160899455)

Figure 6.14 provides the potential versus time plot of the carbonized GP-based anode. Figure 6.14a clearly reflects the characteristics of the electrode active material. It shows the typical discharge (intercalation of Li^+ ions) and charge (deintercalation of Li^+ ions) profiles expected for a highly crystalline graphite material, where the different insertion steps toward the so-called stage-1 Li-graphite intercalation compound, that is LiC_6 , are clearly visible [117]. From the analysis shown in Figure 6.14b, the irreversible capacity loss during the first cycle can be attributed to the expected side reactions with the components of the electrolyte (solid electrolyte interface layer formation). Typically, organic solvent molecules and salt anions are reduced on the active material's surface. Thus, forming insoluble Li salt that precipitates to form a passivating film. This is helpful in preventing further reaction between components of the electrolyte and graphite active material [118].

The reversible specific capacity obtained at low C/10 rate is close to the theoretical value for graphite, reflecting the practical specific capacity of the commercial material used. This can be explained by the fact that the carbon obtained upon cellulose pyrolysis also takes part in the electrochemical process to a certain extent. After the initial cycles, the Coulombic efficiency rapidly increases to above 99%. Subsequently, it remains highly stable throughout the cycles. This indicates that the formed surface film lasted intact and showed excellent reversible cycling after surface reactions were completed. At a relatively high current of 1C, the anode can deliver a capacity of 150 mAh/g, which is definitely higher if compared to the results obtained for the same pristine electrode reported by Beneventi et al. [114]. Thus, it can be summarized that the carbonization procedure at high temperature successfully enhances the electrochemical behavior of paper electrodes. This can be due to the improved electronic conductivity resulting from the presence of the carbonized network of fibers, which contributes to the overall electrode specific capacity. The performance of carbonized LiFePO₄-based cathode in lab-scale Li cell was outstanding in terms of both overall specific capacity and rate capability (Figure 6.14d). The capacity obtained at low C/10 rate was around 160 mAh/g, which is the specific capacity of the commercial material used. It is also interesting to note that after the specific carbonization procedure adopted, this kind of paper-like cathode is able to operate at very high 10C current regime, still providing specific capacity values exceeding 100 mAh/g, thus allowing a higher power output of the final device. These results are difficult to be achieved by the corresponding “as-prepared” spray deposited LiFePO₄-based electrodes as described by Zolin et al. [116]. This signifies the role of pyrolyzed nanocellulose fibers, which combine the functions of strong binder and conducting additive without negatively affecting cycling stability and rate performance [119]. It is worthy to note that this system does not show any performance decay; indeed, reducing the C-rate after more than 120 charge/discharge cycles completely restores the specific capacity, thus achieving excellent stability.

The overall observation concludes that the accomplishment of the “12 principles of Green Chemistry” is a fundamental goal to be pursued by means of designing/optimizing environmentally “conscious” processes, materials and devices to reduce their environmental impact throughout all the phases of their life cycle, thus benefiting the economy, protecting people and achieving the real goal of a truly sustainable world. This goal can be achieved by exploiting carbonized nanocellulosic binders and water-based papermaking coupled with high-performing green composite polymer electrolyte.

Acknowledgments: This work was partially supported by grant 685844 (project MODCOMP) in the framework of European H2020 program. The authors thank Mr. Mauro Raimondo, Politecnico di Torino, for FESEM analysis of the samples.

References

- [1] Winter, M. and Brodd, R. J., What are batteries, fuel cells, and supercapacitors?. *Chem. Rev* 2004, 104, 10, 4245–4270, Oct.
- [2] Linden, David, *Handbook of Batteries*, 3rd ed. McGraw-Hill, New York City, 1994.
- [3] Lacks, D. J. and Mohan Sankaran, R., Contact electrification of insulating materials. *J. Phys. D. Appl. Phys* 2011, 44, 45, 453001, Nov.
- [4] Khundkar, R., Malic, C., and Estela, C., Burned by a battery–coin short circuit: Old concept for a new burn, *Burns* 2010, 36, 1, e4–e5, Feb.
- [5] Seroglou, F., Koumaras, P., and Tselfes, V., History of science and instructional design: The case of electromagnetism, *Sci. Educ* 1998, 7, 3, 261–280
- [6] Whittingham, M. S., History, evolution, and future status of energy storage, *Proc. IEEE* 2012, 100, Special Centennial Issue, 1518–1534.
- [7] George Blomgren, J. H., “Batteries, primary cells,” in *Kirk-Othmer Encyclopedia of Chemical Technology*, Kirk-Othmer, Ed. Wiley, 2004, 880.
- [8] Tarascon, J.-M. and Armand, M., Issues and challenges facing rechargeable lithium batteries, *Nature* 2001, 414, 359, Nov.
- [9] M. S. W.-R. H. and Armand, M., *Fast Ion Transport in Solids*, W. Van Gool, Ed. New York, NY, United States, 1973, 645–665.
- [10] Whittingham, M. S., Electrical energy storage and intercalation chemistry. *Science* (80-) 1976 192, 42–44, 1126–1127.
- [11] Murphy, D. W., Di Salvo, F. J., Carides, J. N., and Waszczak, J. V., Topochemical reactions of rutile related structures with lithium. *Mater. Res. Bull* 1978, 13, 12, 1395–1402, Dec.
- [12] Lazzari, M. and Scrosati, B., A cyclable lithium organic electrolyte cell based on two intercalation electrodes, *J. Electrochem. Soc* 1980, 127, 3, 773, Mar.
- [13] Mizushima, K., Jones, P. C., Wiseman, P. J., and Goodenough, J. B., LiCoO_2 (0. *Mater. Res. Bull* 1980, 15, 6, 783–789, Jun.
- [14] Thackeray, M. M., David, W. I. F., Bruce, P. G., and Goodenough, J. B., Lithium insertion into manganese spinels. *Mater. Res. Bull* 1983, 18, 4, 461–472, Apr.
- [15] Boehm, H. P., Setton, R., and Stumpp, E., Nomenclature and terminology of graphite intercalation compounds. *Carbon N. Y* 1986, 24, 2, 241–245, Jan.
- [16] Armand, M., “Intercalation Electrodes,” in *Materials for Advanced Batteries*, 1st ed., D. Murphy, Ed. New York: Springer US, 1980, 373.
- [17] Brandt, K., Historical development of secondary lithium batteries. *Solid State Ionics* 1994, 69, 3–4, 173–183, Aug.
- [18] Brandt, K., Herr, K., Hoge, D., *DEHEMA Monogr* 1993, 128, 279.
- [19] Ohzuku, T., Iwakoshi, Y., and Sawai, K., Formation of lithium-graphite intercalation compounds in nonaqueous electrolytes and their application as a negative electrode for a lithium ion (Shuttlecock) cell. *J. Electrochem. Soc* 1993, 140, 9, 24–90, Sep.
- [20] Koch, V. R., Specular lithium deposits from lithium hexafluoroarsenate/diethyl ether electrolytes, *J. Electrochem. Soc* 1982, 129, 1, 1.
- [21] Daniel, C. and Besenhard, J. O., *Handbook of Battery Materials*, 2. Auflage. Wiley, 2011.
- [22] Hirai, T., Effect of additives on lithium cycling efficiency, *J. Electrochem. Soc*, 1994, 141, 9, 2300.
- [23] Flandrois, S. and Simon, B., Carbon materials for lithium-ion rechargeable batteries. *Carbon N. Y* 1999, 37, 2, 165–180.
- [24] Z. Q. von S. U. Dahn JR, Sleight AK, Shi H, Way BM, Weydanz WJ, Reimers JN, “Carbons and graphites as substitutes for the lithium anode in lithium batteries: New materials,

- developments and perspectives," in *Industrial chemistry library*, 5th ed., P. G, Ed. London: Elsevier, 1994, 1–47.
- [25] Agubra, Víctor and Fergus, Jeffrey, Review lithium ion battery anode aging mechanisms. *Materials (Basel)* 2013, 6, 1310–1325.
- [26] Kodama, T. and Sakaebe, H., Present status and future prospect for national project on lithium batteries. *J. Power Sources* 1999, 81–82, 144–149, Sep.
- [27] Takami, N., Structural and kinetic characterization of lithium intercalation into carbon anodes for secondary lithium batteries. *J. Electrochem. Soc* 1995, 142, 2, 371.
- [28] Wang, H., Ikeda, T., Fukuda, K., Yoshio, M., Effect of milling on the electrochemical performance of natural graphite as an anode material for lithium-ion battery," *J. Power Sources* 1999, 83, 1–2, 141–147, Oct.
- [29] Liu, Z., Yu, A., and Lee, J. Y., Modifications of synthetic graphite for secondary lithium-ion battery applications. *J. Power Sources* 1999, 81–82, 187–191, Sep.
- [30] McMillan, R., Slegel, H., Shu, Z., Wang, W., Fluoroethylene carbonate electrolyte and its use in lithium ion batteries with graphite anodes. *J. Power Sources* 1999, 81–82, 20–26, Sep.
- [31] Andersson, A. M., Edström, K., Thomas, J. O., Characterisation of the ambient and elevated temperature performance of a graphite electrode. *J. Power Sources* 1999, 81–82, 8–12, Sep.
- [32] Yazami, R., Surface chemistry and lithium storage capability of the graphite–lithium electrode. *Electrochim. Acta* 1999, 45, 1–2, 87–97, Sep.
- [33] W. X. and Dahn, J. R., Study of irreversible capacities for Li Insertion in hard and graphitic carbons. *J. Electrochem. Soc* 1997, 144, 4, 1195–1201.
- [34] Y. I. and K. S. Ohzuku, Tsutomu, Formation of lithium-graphite intercalation compounds in nonaqueous electrolytes and their application as a negative electrode for a lithium ion (Shuttlecock) cell *J. Electrochem. Soc* 1993, 140, 9, 2490–2498.
- [35] Geim, A. K. and Novoselov, K. S., The rise of graphene," *Nat. Mater* 2007, 6, 3, 183–191, Mar.
- [36] Han, J. et al., Engineering graphenes from the nano- to the macroscale for electrochemical energy storage. *Electrochem. Energy Rev* 2018, 1, 2, 139–168.
- [37] Niu, C., Sichel, E. K., Hoch, R., Moy, D., Tennent, H., High power electrochemical capacitors based on carbon nanotube electrodes. *Appl. Phys. Lett* 1997, 70, 11, 1480–1482, Mar.
- [38] Lee, S. W. et al., High-power lithium batteries from functionalized carbon-nanotube electrodes. *Nat. Nanotechnol* 2010, 5, 531, Jun.
- [39] Kim, H., Park, K.-Y., Hong, J., Kang, K., All-graphene-battery: bridging the gap between supercapacitors and lithium ion batteries. *Sci. Rep* 2014, 4, 5278, Jun.
- [40] Cheng, Q. , Okamoto, Y., Tamura, N., Tsuji, M., Maruyama, S., and Matsuo, Y., Graphene-like-graphite as fast-chargeable and high-capacity anode materials for lithium ion batteries. *Sci. Rep* 2017, 7, 1, 14782.
- [41] Wang, S., Kravchyk, K. V, Krumeich, F., and Kovalenko, M. V, Kish graphite flakes as a cathode material for an aluminum chloride–graphite battery. *ACS Appl. Mater. Interfaces* 2017, 9, 34, 28478–28485, Aug.
- [42] Yanwu, Zhu, Shanthi, Murali, Weiwei, Cai, Xuesong, Li, Ji Won, Suk, Jeffrey R, Potts, Rodney S., Ruoff, Graphene and graphene oxide: Synthesis, properties, and applications. *Adv. Mater* 2010, 22, 35, 3906–3924.
- [43] Olivares-Marín, M. et al., Cherry stones as precursor of activated carbons for supercapacitors. *Mater. Chem. Phys* 2009, 114, 1, 323–327, Mar.
- [44] Vivekchand, S. R. C., Rout, C. S., Subrahmanyam, K. S., Govindaraj, A., and Rao, C. N. R., Graphene-based electrochemical supercapacitors. *J. Chem. Sci* 2008, 120, 1, 9–13.
- [45] Wick, P. et al., Classification framework for graphene-based materials. *Angew. Chem. Int. Ed. Engl* 2014.

- [46] Chyan, Y., Ye, R., Li, Y., Singh, S. P., Arnusch, C. J., and Tour, J. M., Laser-Induced graphene by multiple lasing: Toward electronics on cloth, paper, and food. *ACS Nano* 2018, 12, 3, 2176–2183, Mar.
- [47] T. O. and Norio, M. K. Takami, Asako Satoh, Large hysteresis during lithium insertion into and extraction from high-capacity disordered carbons. *J. Electrochem. Soc* 1998, 145, 2, 478–482.
- [48] Pan, Q., Deng, Z., Zhang, X., and Wan, G., Electrochemical characteristics of lithium intercalation into natural gas coke serving as the negative electrode of a lithium battery. *J. Power Sources* 1999, 79, 1, 25–29, May.
- [49] Sato, Y. et al., Characteristics of coke carbon modified with mesophase-pitch as a negative electrode for lithium ion batteries. *J. Power Sources* 1999, 81–82, 182–186, Sep.
- [50] Sharon, M. et al., Camphor-based carbon nanotubes as an anode in lithium secondary batteries. *J. Power Sources* 2002, 104, 1, 148–153, Jan.
- [51] Kumar, M., Kichambare, P., Sharon, M., Avery, N. R., and Black, K. J., Study of camphor-pyrolised carbon electrode in a lithium rechargeable cell. *Mater. Chem. Phys* 2000, 66, 1, 83–89, Sep.
- [52] Sunil Bhardwaj, M. S., Jaybhaye, Sandesh V., Madhuri Sharon, D. Sathiyamoorthy, K. Dasgupta, Jagadale, Pravin, Gupta, Arvind, Patil, Bhushan, Ozha, Goldie, Sunil Pandey, T. Soga, Rakesh Afre, Kalita, Golap, Carbon nanomaterial from tea leaves as an anode in lithium secondary batteries. *Asian J. Exp. Sci* 2008, 22, 2, 89–93.
- [53] Yazami, R. and Touzain, P., A reversible graphite-lithium negative electrode for electrochemical generators. *J. Power Sources* 1983, 9, 3, 365–371, Jan.
- [54] Skundin, A. M., Grigor'eva, O. Y., Kulova, T. L., and Pouchko, S. V., The lithium intercalation into graphite from electrolyte and from solid lithium. *J. Solid State Electrochem* 2003, 8, 1, 11–14.
- [55] A. M. S. O. Yu. Grigor'eva, T. L. Kulova, S. V. Pushko, Lithium Intercalation into Graphite during Direct Contact and Anodic Polarization. *Russ. J. Electrochem* 2002, 38, 12, 1327–1333.
- [56] Kulova, T. L., Skundin, A. M., Nizhnikovskii, E. A., and Fesenko, A. V., Temperature effect on the lithium diffusion rate in graphite. *Russ. J. Electrochem* 2006, 42, 3, 259–262.
- [57] Roh, Y. B. et al., Unique charge/discharge properties of carbon materials with different structures. *J. Power Sources* 1997, 68, 2, 271–276, Oct.
- [58] Morita, M., Nishimura, N., and Matsuda, Y., Charge/discharge cycling behavior of pitch-based carbon fiber in organic electrolyte solutions. *Electrochim. Acta* 1993, 38, 13, 1721–1726, Sep.
- [59] Jean, R. M. M., Desnoyer, C., Tranchant, A., Electrochemical and Structural Studies of Petroleum Coke in Carbonate-Based Electrolytes. *J. Electrochem. Soc* 1995, 142, 7, 2122–2125.
- [60] Takashi Uchida, K. S., Morikawa, Yasuyuki, Ikuta, Hiromasa, Wakihara, Masataka, Chemical Diffusion Coefficient of Lithium in Carbon Fiber. *J. Electrochem. Soc* 1996, 143, 8, 2606–2610.
- [61] Aurbach, D., Levi, M. D., Levi, E., and Schechter, A., Failure and Stabilization Mechanisms of Graphite Electrodes. *J. Phys. Chem. B* 1997, 101, 12, 2195–2206, Mar.
- [62] Levi, M. D. E. Levi, A., and Aurbach, D., The mechanism of lithium intercalation in graphite film electrodes in aprotic media. Part 2. Potentiostatic intermittent titration and in situ XRD studies of the solid-state ionic diffusion. *J. Electroanal. Chem* 1997, 421, 1–2, 89–97, Jan.
- [63] Markovsky, B., Levi, M. D., and Aurbach, D., The basic electroanalytical behavior of practical graphite–lithium intercalation electrodes. *Electrochim. Acta* 1998, 43, 16–17, 2287–2304, May.

- [64] Barsoukov, E., Kim, J. H., Kim, J. H., Yoon, C. O., and Lee, H., Kinetics of lithium intercalation into carbon anodes: In situ impedance investigation of thickness and potential dependence. *Solid State Ionics* 1999, 116, 3–4, 249–261, Jan.
- [65] Churikov, A. V., Chronoamperometric determination of the rate of lithium transfer in carbon electrodes. *Ehlektrókimiya* 2002, 38, 1, 120–125.
- [66] C. D. and S. M. Piao, Tiehua, Parka, Su-Moon, Intercalation of Lithium Ions into Graphite Electrodes Studied by AC Impedance Measurements. *J. Electrochem. Soc* 1999, 146, 8, 2794–2798.
- [67] J. A. R. and R. E. W. Ping Yu, B. N. Popov, Determination of the lithium ion diffusion coefficient in graphite. *J. Electrochem. Soc* 1999, 146, 1, 8–14.
- [68] Lau, K. C., Assary, R. S., and Curtiss, L. A., “Aprotic Electrolytes in Li–Air Batteries BT – Electrolytes for Lithium and Lithium-Ion Batteries,” Jow, T. R., Xu, K., Borodin, O., and Ue, M., Eds. New York, NY: Springer New York, 2014, 445–466.
- [69] Zolin, L. et al., A simple route toward next-gen green energy storage concept by nanofibres-based self-supporting electrodes and a solid polymeric design. *Carbon N. Y* 2016, 107, 811–822.
- [70] Nair, J. R. et al., Remarkably stable high power Li-ion battery anodes based on vertically arranged multilayered-graphene. *Electrochim. Acta* 2015, 182.
- [71] Wang, Y.-G., Chang, Y.-C., Ishida, S., Korai, Y., and Mochida, I., Stabilization and carbonization properties of mesocarbon microbeads (MCMB) prepared from a synthetic naphthalene isotropic pitch. *Carbon N. Y* 1999, 37, 6, 969–976, Jan.
- [72] Guerin, K., Fevrier-Bouvier, A., Flandrois, S., Simon, B., and Biensan, P., On the irreversible capacities of disordered carbons in lithium-ion rechargeable batteries, *Electrochim. Acta* 2000, 45, 10, 1607–1615, Jan.
- [73] Buiel, E. and Dahn, J., Li-insertion in hard carbon anode materials for Li-ion batteries. *Electrochim. Acta* 1999, 45, 1–2, 121–130, Sep.
- [74] Appetecchi, G., Croce, F., Marassi, R., Persi, L., Romagnoli, P., Scrosati, B., Lithium insertion into carbonaceous materials and transition metal oxides from high performance polymer electrolytes. *Electrochim. Acta* 1999, 45, 1–2, 23–30, Sep.
- [75] Sato, E. M. Noguchi, K., Demachi, M, A, Oki N, A mechanism of lithium storage in disordered carbons. *Science (80-)* 1994, 22, 264 (5158), 556–568.
- [76] Walker, S., Holliday AK, Hughes, G., “Comprehensive inorganic chemistry,” in Carbon, T.-D. AF, Ed. Oxford: Pergamon Pres, 1973, 1173–1294.
- [77] Liu, Y., Xue, J. S., Zheng, T., and Dahn, J. R., Mechanism of lithium insertion in hard carbons prepared by pyrolysis of epoxy resins. *Carbon N. Y* 1996, 34, 2, 193–200, Jan.
- [78] Larcher, D., Mudalige, C., Gharghour, M., and Dahn, J. R., Electrochemical insertion of Li and irreversibility in disordered carbons prepared from oxygen and sulfur-containing pitches. *Electrochim. Acta* 1999, 44, 23, 4069–4072, Jul.
- [79] Gong, J., Wu, H., and Yang, Q., “Structural and electrochemical properties of disordered carbon prepared by the pyrolysis of poly(p-phenylene) below 1000 C for the anode of a lithium-ion battery. *Carbon N. Y* 1999, 37, 9, 1409–1416, Jan.
- [80] Buiel, E. R., George, A. E., and Dahn, J. R., Model of micropore closure in hard carbon prepared from sucrose. *Carbon N. Y* 1999, 37, 9, 1399–1407, Jan.
- [81] Dahn, J. R., Xing, W., and Gao, Y., The ‘falling cards model’ for the structure of microporous carbons. *Carbon N. Y* 1997, 35, 6, 825–830, Jan.
- [82] Zheng, T., Xing, W., and Dahn, J. R., Carbons prepared from coals for anodes of lithium-ion cells. *Carbon N. Y* 1996, 34, 12, 1501–1507, Jan.
- [83] Gibaud, A., Xue, J. S., and Dahn, J. R., A small angle X-ray scattering study of carbons made from pyrolyzed sugar. *Carbon N. Y* 1996, 34, 4, 499–503, Jan.

- [84] Zheng, T. and Dahn, J. R., Hysteresis observed in quasi open-circuit voltage measurements of lithium insertion in hydrogen-containing carbons. *J. Power Sources* 1997, 68, 2, 201–203, Oct.
- [85] Zhou, P., Papanek, P., Bindra, C., Lee, R., and Fischer, J. E., High capacity carbon anode materials: Structure, hydrogen effect, and stability. *J. Power Sources* 1997, 68, 2, 296–300, Oct.
- [86] Chakrabarti, A. et al., Conversion of carbon dioxide to few-layer graphene. *J. Mater. Chem* 2011, 21, 26, 9491–9493.
- [87] Seo, Hong-Kyu and Lee, Tae-Woo, Graphene growth from polymers. *Carbon Lett* 2013, 14, 3, 145–151.
- [88] Sun, Z., Yan, Z., Yao, J., Beitler, E., Zhu, Y., and Tour, J. M., Growth of graphene from solid carbon sources. *Nature* 2010, 468, 549, Nov.
- [89] Ruan, G., Sun, Z., Peng, Z., and Tour, J. M., Growth of Graphene from Food, Insects, and Waste. *ACS Nano* 2011, 5, 9, 7601–7607, Sep.
- [90] Seo, H.-K. et al., Value-added Synthesis of Graphene: Recycling Industrial Carbon Waste into Electrodes for High-Performance Electronic Devices. *Sci. Rep* 2015, 5, 16710, Nov.
- [91] Guo, H.-L., Wang, X.-F., Qian, Q.-Y., Wang, F.-B., and Xia, X.-H., A Green Approach to the Synthesis of Graphene Nanosheets. *ACS Nano* 2009 3, 9, 2653–2659, Sep.
- [92] Kim, Y. S. et al., Methane as an effective hydrogen source for single-layer graphene synthesis on Cu foil by plasma enhanced chemical vapor deposition. *Nanoscale* 2013, 5, 3, 1221–1226.
- [93] Shah, J., Lopez-Mercado, J., Carreon, M. G., Lopez-Miranda, A., and Carreon, M. L., Plasma synthesis of graphene from mango peel. *ACS Omega* 2018, 3, 1, 455–463, Jan.
- [94] Wang, J., Zhu, M., Outlaw, R. A., Zhao, X., Manos, D. M., and Holloway, B. C., Synthesis of carbon nanosheets by inductively coupled radio-frequency plasma enhanced chemical vapor deposition. *Carbon N. Y* 2004, 42, 14, 2867–2872, Jan.
- [95] Wu, Y., Qiao, P., Chong, T., and Shen, Z., Carbon nanowalls grown by microwave plasma enhanced chemical vapor deposition. *Adv. Mater* 2002, 14, 1, 64–67.
- [96] Brar, V. W. et al., Second-order harmonic and combination modes in graphite, single-wall carbon nanotube bundles, and isolated single-wall carbon nanotubes. *Phys. Rev. B* 2002, 66, 15, 155–418, Oct.
- [97] Dresselhaus, M. S., Dresselhaus, G., Saito, R., and Jorio, A., Raman spectroscopy of carbon nanotubes. *Phys. Rep* 2005, 409, 2, 47–99, Mar.
- [98] Damen, T. C., Porto, S. P. S., and Tell, B., Raman effect in zinc oxide. *Phys. Rev* 142, 2, 570–574, Feb.
- [99] Galeener, F. L. and Lucovsky, G., Longitudinal optical vibrations in glasses: GeO₂ and SiO₂. *Phys. Rev. Lett* 1976, 37, 22, 1474–1478, Nov.
- [100] Cançado, L. G. et al., Quantifying defects in graphene via raman spectroscopy at different excitation energies. *Nano Lett* 2011, 11, 8, 3190–3196, Aug.
- [101] Graf, D. et al., Spatially resolved raman spectroscopy of single- and few-layer graphene. *Nano Lett* 2007, 7, 2, 238–242, Feb.
- [102] Dresselhaus, M. S., Dresselhaus, G., Saito, R., and Jorio, A., Raman spectroscopy of carbon nanotubes. *Phys. Rep* 2005, 409, 2, 47–99, Mar.
- [103] Ferrari, A. C. and Robertson, J., Interpretation of Raman spectra of disordered and amorphous carbon, *Phys. Rev. B* 2000, 61, 20, 14095–14107, May.
- [104] Tan, P., Dimovski, S., and Gogotsi, Y., Raman scattering of non-planar graphite: arched edges, polyhedral crystals, whiskers and cones. *Philos. Trans. R. Soc. London. Ser. A Math. Phys. Eng. Sci* 2004, 362, 18–24, 2289 LP-2310, Nov.

- [105] Hiralal, P., Rius, G., Andrew, P., Yoshimura, M., and Amaratunga, G. A. J., Tailoring carbon nanostructure for high frequency supercapacitor operation. *J. Nanomater* 2014, 8, 1–7, Jan.
- [106] Rius, G. and Yoshimura, M., Synthesis control for carbon nanowalls on copper supports pro development of green energy applications. *e-Journal Surf. Sci. Nanotechnol* 2012, 10, 305–309.
- [107] Rius, G. and Yoshimura, M., Structured nanocarbon on various metal foils by microwave plasma enhanced chemical vapor deposition. *J. Phys. Conf. Ser* 2013, 417, 012–010, Mar.
- [108] Tobjörk, D. and Österbacka, R., Paper electronics. *Adv. Mater* 23, 17, 1935–1961, May 2011.
- [109] Liu, J. et al., Future paper based printed circuit boards for green electronics: fabrication and life cycle assessment, *Energy Environ. Sci* 2014, 7, 11, 3674–3682, Oct.
- [110] Jabbour, L., Bongiovanni, R., Chaussy, D., Gerbaldi, C., and Beneventi, D., Cellulose-based Li-ion batteries: A review. *Cellulose* 2013, 20, 4, 1523–1545, Aug.
- [111] Berecibar, M., Gandiaga, I., Villarreal, I., Omar, N., Van Mierlo, J., and Van den Bossche, P., Critical review of state of health estimation methods of Li-ion batteries for real applications. *Renew. Sustain. Energy Rev* 2016, 56, 572–587, Apr.
- [112] Sharifi, F., Ghobadian, S., Cavalcanti, F. R., and Hashemi, N., Paper-based devices for energy applications. *Renew. Sustain. Energy Rev* 2015, 52, 1453–1472, Dec.
- [113] Hu, L. and Cui, Y., Energy and environmental nanotechnology in conductive paper and textiles. *Energy Environ. Sci* 2012, 5, 4, 6423–6435, Mar.
- [114] Beneventi, D. et al., Pilot-scale elaboration of graphite/microfibrillated cellulose anodes for Li-ion batteries by spray deposition on a forming paper sheet. *Chem. Eng. J* 2014, 243, 372–379, May.
- [115] Blazsó, M., Pyrolysis for recycling waste composites. *Manag. Recycl. Reuse Waste Compos* 2010, 102–121, Jan.
- [116] Zolin, L. et al., Flexible cellulose-based electrodes: Towards eco-friendly all-paper batteries. *Chem. Eng. trans.* 2014, 41, 361–366.
- [117] Gotoh, K. et al., Properties of a novel hard-carbon optimized to large size Li ion secondary battery studied by ^7Li NMR. *J. Power Sources* 2006, 162, 2, 1322–1328, Nov.
- [118] Peled, E., The electrochemical behavior of alkali and alkaline earth metals in nonaqueous battery systems – the solid electrolyte interphase model. *J. Electrochem. Soc* 1979, 126, 12, 2047–2051, Dec.
- [119] Kirshenbaum, K., et al. Batteries. In situ visualization of $\text{Li}/\text{Ag}_2\text{VP}_2\text{O}_8$ batteries revealing rate-dependent discharge mechanism. *Science* 2015, 347, 6218, 149–54, Jan.

Index

- Activate 17
- Activation treatment 25
- Active screen plasma 18
- Active species 19
- Agglomeration 125, 139
- Anode 164
- Artificial intelligence 68

- Battery 153
- Biochar 158
- Buckypapers (BP) 81

- Carbon 156
- Carbon-based materials 30
- Carbon-based polymer nanocomposites 36
- Carbon fibers 26–27, 52, 159
- Carbon nanofibers 22
- Carbon nanomaterial 157
- Carbon nanotube (CNT) 34, 81, 115
- Carbon nanowalls 159
- Carbon paper 23
- Catalysts 29
- CFRP mirror 81
- Chemical vapor deposition 159
- Circular economy 66
- Class II 129
- CNTs 28
- Coarse-grained 56
- Composite material 27
- Coulombic efficiency 173

- Deformation experiments 121, 132, 136
- Dispersion in nanocomposites 124
- Dissipative particle dynamics 55

- Effective medium approximation 61
- Elastic moduli 48
- Electrical conductivity 52, 54, 157
- Electrical resistance 20
- Electrocatalyst 24
- Electrochemical surface area 25
- Electrode 155
- Electromagnetic compatibility (EMC) 81
- Energy storage 154
- Energy storage devices 22

- Engineered material 66
- Epoxy resins 40

- Fibre Volume Fraction (FVF) 95
- Finite element method 61
- Flexible substrates 13
- Fuel cells 23
- Functional groups 27
- Functionalization 30
- Functionalize 17

- Gas diffusion layer 23
- Generalized Hooke's law 62
- Glass transition 124
- Glass transition temperature 120
- Graphene 1, 20, 34, 157
- Graphene-based devices 1
- Graphene-based nanocomposites 116
- Graphene-based polymer nanocomposites 123
- Graphene oxide 1

- Heterogeneous materials 158
- Hydrogen bonds 120, 123, 132, 135–137, 145

- In situ polymerization 119
- Interfacial characteristics 67
- Ion 155
- Ion bombardment 19

- Kapitza resistance 44

- Lattice Boltzmann method 55
- Lithium 154

- Machine learning 68
- Materials Modelling 38
- MD algorithm 130
- MD simulation packages 131
- Melt processing 119
- Mesoscale 57
- Microscopic structure 67
- Model reduction 67
- Molecular dynamics 39
- Molecular simulations 53, 126–127
- Monte Carlo 39
- Multiphysics modeling 39

- Nanoscale microfibrillated cellulose 159
- Nonequilibrium 40
- Nonvolatile memories 1
- Nonvolatile resistive memories 6

- Optical transparency 20

- Passive Intermodulation (PIM) 81
- Percolation 54
- Phonon 45
- Photoresponsive materials 35
- Piezoelectric materials 34
- Plasma-enhanced CVD (PE-CVD) 29
- Plasma–surface interaction 19
- Plasma technology 18, 30
- Platinum nanowires 25
- Poly(acrylic acid) 123
- Poly(methyl methacrylate) 120
- Poly(vinyl alcohol) 120
- Polyethylene 122
- Polymer electrolyte 165
- Polymer matrix composite 26
- Polystyrene 121, 132
- Polyvinylidene fluoride 122
- Potential energy function 126–128, 130
- Pouch cell 170
- Pyrolysis 159

- Raman 161
- Recyclable carbon 157

- Scotch tape method 116–117
- Shape memory materials 33
- Smart materials 33
- Smoothed particle hydrodynamics 55
- Solvent processing 119
- Space 82
- Space application 13
- Specific energy 171
- Spray-coating 164
- Stress–strain response 48
- Surface conductivity 22
- Surface engineering 17–18
- Surface functionalizations 47

- Technology readiness level (TRL) 112
- Thermal conductivity 40
- Toxicity 68
- Tunneling 53

- VACNT 29

- Waste 157
- Wettability 24, 28